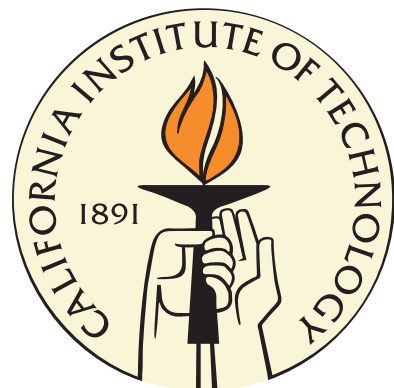# Wrinkling of Dielectric Elastomer Membranes

Thesis by

Ling Zheng

In Partial Fulfillment of the Requirements

for the Degree of

Doctor of Philosophy

California Institute of Technology

Pasadena, California

2008

(Defended September 22, 2008)

Dedicated to my family.

"Scientists study the world as it is; Engineers create the world that has never been."

-Theodore von Kármán

Acknowledgements

After all the confusion and perplexity, joy and elation, finally it comes to the stage when we are humble and grateful, as the last thing to learn from the doctoral studies.

I have been extremely fortunate to work with two advisors, Professor Guruswami Ravichandran and Professor Kaushik Bhattacharya. They introduced me to the enchanting world of mechanics, guided me through the academic challenges and supported me in every aspect of my research and professional endeavors. The discussions with them together were enjoyable and memorable. I was truly inspired by their insights and passion for science, and greatly benefited from all the resources from both groups. As mentors, they shared my happiness during my good times and gave sincere trust and encouragement during my bad times. Over four years I learned from them for being not only a good scientist but also a responsible and considerate person. Thank you for more than I can ever say!

I would like to express my gratitude to the other thesis committee members, Professor Sergio Pellegrino, Professor Chiara Daraio, and Professor Gal deBotton from Ben-Gurion University, Israel, for taking the time to read this thesis and for offering many valuable suggestions and criticisms. Professor Sergio Pellegrino deserves a special thanks for the systematic studies he and his former graduate student Y. Wesley Wong did on thin membrane structure wrinkling, which meant to me a lighthouse in a dark sea. I am also very grateful to Professor Nadia Lapusta for encouraging me to apply for the Mechanical Engineering program at Caltech and persistently supporting me.

Sincere appreciation is extended to my colleagues for their support, company and valuable scientific discussions. I am especially grateful to Dr. Soonsung Hong, who recommended several optical methods for three dimensional shape measurement and a systematic way to evaluate them. With his help I was able to identify the fringe projection method. I would like to express my deep appreciation to our lab technician, Petros Arakelian, who is a very capable and knowledgeable person in engineering and general laboratory work. He provided me with tremendous help in my experimental work. I also want to thank Dr. Christian Franck for lending his knowledge and experience with

finite element analysis using ABAQUS/CAE; and Dr. Winston Jackson for working together on characterizing the membrane material. Many thanks to the former and current group members: Rongjing Zhang, Min Tao, Teresa Kidd, Samantha Daly, HJ Kwon, Hsin-Yi Kuo, Laurent Ponson, Liping Liu, Vikram Gavini, Mike Mello, Sharlotte Kramer, Benny Poon, Xiao Lu. I feel fortunate that I have been in a research group with an active, friendly, and open atmosphere.

There are many others outside the Caltech community who contributed to my success. I am deeply indebted to Professor Todd Allen, who was my advisor in University of Wisconsin-Madison. He provided me the opportunity to pursue science in the United States. I had great experience of working with him and learning professional ways of managing a large research project.

My thanks also go to my friends, Fei Wang, Chunhui Gu, Xiaobai Li, Xiaosong Niu, Xin Guo, Lin Zhu, Jing Yang, Ke Wang, Jet Cheng, Li Liu, Bo Li, Yue Yang, Yong Hao, for sharing my joy and sadness, and offering instant help whenever needed. I treasure every minute I have spent with them.

Finally, I would like to give my special thanks to my family for their unconditional love and for always believing in me. Since I was young, my parents encouraged me to excel and achieve all the goals that I set for myself. Without their encouragement I would never have made it this far and become the first doctor in the family. My husband Yi has been my best friend, my 24/7 tech support, and above all, my source of happiness, and he deserves a special award!

Abstract

Wrinkling of thin membranes due to different in-plane loading and boundary conditions has drawn attention of researchers in structural engineering since the development of thin webs for early aircraft structures. More recently, prestressed lightweight membrane structures have been proposed for future space missions, for example solar sails, the next generation space telescope sunshield and space-based radar systems. These structures are often partially wrinkled during operation. The formation of wrinkles alters the load paths and the structural stiffness of the membranes. More importantly its occurrence degrades the surface accuracy of these structures, which is a key design parameter.

This dissertation focuses on wrinkling of thin rectangular membranes subjected to uniaxial tension and investigates the onset and profiles of wrinkles using both experimental and numerical approaches.

An optical method, which integrates fringe projection method with four-frame phase-shifting technique, pre-conditioned conjugate gradient phase unwrapping algorithm and series-expansion carrier removal technique was developed in order to measure the full-field out-of-plane displacement of membranes, and an optical system was constructed including a uniaxial tension testbed, a LCD projector and a CCD camera. A series of uniaxial tensile tests were carried out on silicone rubber membranes of varying dimensions and aspect ratios in order to investigate the effect of geometric factors such as membrane dimension and aspect ratio on wrinkling onset; and a series of measurements were performed on each membrane at several desired strain levels to understand the evolution of the wrinkles, in particular wrinkle amplitude and wavelength.

A numerical study was carried out using the commercial finite element software ABAQUS to further understand the important characteristics of wrinkling of thin membranes observed in the physical model. Geometrically nonlinear finite element models of membrane structures were constructed with thin-shell elements. A series of simulations were carried out for different membrane dimensions. The critical buckling load and buckling modes was predicted for each dimension using

a pre-buckling eigenvalue analysis. The desirable buckling mode was selected and introduced into the structure as a geometric imperfection. The formation and growth of wrinkles were simulated in the post-buckling analysis.

Finally, an idea of suppressing wrinkle instabilities of dielectric elastomer membranes using through-thickness electric field was proposed and verified in both experiment and numerical simulations.

Keywords: wrinkling; membrane; critical buckling strain; wrinkle onset; wrinkle wavelength; wrinkle amplitude; fringe projection method; finite element; thin shell; dielectric elastomer; dielectric actuation.

Contents

List of Figures

List of Tables

Chapter 1

Introduction

1.1   Wrinkling Phenomenon

Thin membranes wrinkle whenever they are subjected to compressive load. This is due to the inherently small bending resistance of membrane structures which buckle out-of-plane under the action of even small in-plane compressive stress.

This phenomenon is common and it can be observed in many structures in daily use, ranging from umbrellas and temporary tents to large fabric roofs for airports and stadiums. Wrinkling is not a concern for designing small structures because it has no structural consequences. In large scale structures, such as membrane roofs, wrinkling can be counteracted by applying a biaxial stress state by means of cables or compressive rings, as shown in Figure 1.1. More often a compensation scheme is used, in which the fabric is cut to a smaller size than that required to generate purely the geometric shapes that are required according to the form-finding process. Additional stretching of the fabric is thus required in order to eliminate potential wrinkles.

Figure 1.1: Denver International Airport fabric roof (www.flickr.com).

1.2 Types of Wrinkles

Wrinkles due to loading or boundary conditions are completely reversible if the membrane does not yield. These wrinkles are termed structural/elastic wrinkles; their magnitude varies with the loading and boundary conditions. Wrinkles where the material yields are permanent and irreversible, and are termed material/plastic wrinkles. This type of wrinkles can be random and can be thought of as an initial set of very extreme imperfections (Wong and Pellegrino, 2006). Only structural wrinkles are considered in the present study.

1.3 Motivation

Recently the idea of using large and ultra-lightweight membrane space structures to carry out various future interplanetary probes has been put forward by several mission planners. Examples include solar sails, sunshields for the Next Generation Space Telescope (NGST), inflatable antennas and mirrors, as well as structures for Synthetic Aperture Radars (SAR). These structures use thin membranes (having thicknesses of the order of 5 to 200 μm and dimensions of few to hundreds of meters) as their main structural component which carry loads primarily in tension. The main advantage of using thin membranes in deployable structures is their low volume packaging capability and low mass; as well as their ability to be deployed with minimum driving forces. These advantages also suggest the possibility to use several alternative propulsion technologies in addition to those are currently available. Therefore, the use of gossamer structures provides significant advantages for space missions with ambitious goals and tight economic constraints.

Wrinkles may form on these structures due to the boundary conditions they are subjected to or the mechanical forces generated during deployment. On the other hand, wrinkling may also occur due to packing or manufacturing imperfections of the membrane.

However, most of these applications demand very smooth surfaces. For instance, parabolic inflatable reflectors (Figure 1.2) can be used as a large aperture radio frequency (RF) antenna. A typical surface accuracy requirement for an optical quality mirror reflector is 1/20th the wavelength of interest. This means a surface precision of the order of less than 1 μm RMS (root mean square) error may be required. The occurrence of large wrinkles on the surface of these structures is highly undesirable. The surface accuracy of reflectors with lower skin stress may be compromised by diffusion of projected images and scattering of light.

Figure 1.2: Wrinkles on a 3-meter inflatable reflector demonstrator with very low internal pressure and film stress (L'Garde Inc., www.lgarde.com).

Ultra-lightweight solar sail, such as the one shown in Figure 1.3, are prestressed in their operational configuration by applying concentrated corner loads which are likely to cause wrinkling. Surface reflectivity is the main design parameter of solar sails since solar photon pressure is used for propulsion. The occurrence of wrinkles may affect the performance of the sail by changing the angle of reflection of incident photons, thus causing thrust degradation in the sail. Large wrinkles might also cause local concentration of solar energy, thus creating high thermal stress within the structure. This may then result in material creep, and shorten the intended design life-span of a solar sail.
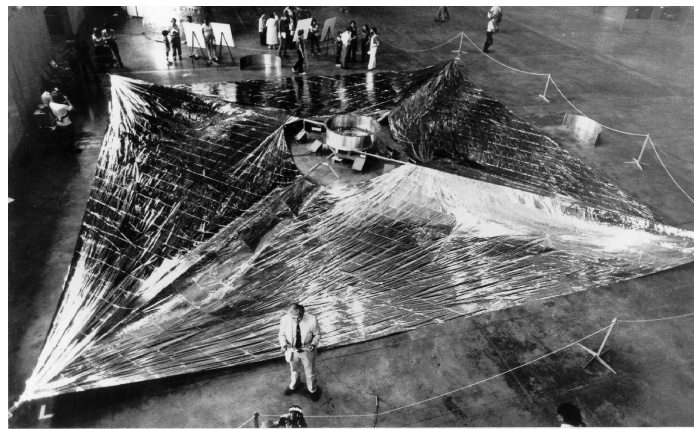
Figure 1.3: Wrinkles on a four quadrant, 20-meter solar sail. The solar sail system is fully deployed during testing at NASA Glenn Research Center's Plum Brook facility in Sandusky, OH (NASA, www.nasa.gov).

The NASA Next Generation Space Telescope (NGST) sunshield (Figure 1.4) consisting of closely spaced layers of insulating membranes, is used to protect the telescope from sunlight. The design requirement is to achieve an operational temperature which is less than 50 K. The thermal efficiency of the sunshield is highly dependent upon the spacing between membrane layers, surface specularity and layer angles. If large scale wrinkles occur, then the surfaces of adjacent membrane layers may touch each other and consequently cause thermal shorts in the structure.

Figure 1.4: Wrinkles on a full-scale sunshield of the James Webb Space Telescope (JWST). The sunshield is undergoing folding and deployment trials to verify its design concept and deployment techniques at Northrop Grumman's Space Technology facility in Redondo Beach, CA (NASA, www.nasa.gov).

The conventional solution of preventing large wrinkles by introducing biaxial stresses or applying higher stress, however, are not feasible for ultra-lightweight thin membrane structures for space applications, because of the potential risks of crack propagation and material creep, and potential increase in the overall cost and mass of the structures. Therefore, engineers now face the task of estimating the extent and amount of waviness and seek ways to control or suppress wrinkling.

1.4 Scope and Layout

The dissertation is organized as follows.

Chapter 2 reviews the existing literature and previous work on wrinkling of thin membranes which can generally be categorized into theoretical, numerical and experimental approaches.

Chapter 3 illustrates the experimental set-up for conducting uniaxial tension test on rectangular membranes. Silicone which is utilized as the membrane material is characterized by stress-strain curves. Experimental procedure is reported with emphasis on the shape measurement of the wrinkled membrane. The fringe projection method combined with phase-shifting technique is introduced to carry the full-field out-of-plane displacement measurement. The experimental observations are discussed which form the basis of the numerical studies in the following chapters.

In Chapter 4, a finite element analysis is performed to model wrinkling of membrane structures in uniaxial tension using thin shell elements in the commercial package ABAQUS. Pre-buckling eigenvalue analysis and post-buckling analysis are carried out on the prescribed model. The onset and growth of wrinkles on membranes of various aspect ratios are discussed.

Chapter 5 compares the experimental results with the numerical simulation results in detail.

Chapter 6 explores a concept of suppressing membrane wrinkling by means of dielectric actuation utilizing properties of dielectric elastomers. A simple analytical model is developed, and experimental and numerical studies are carried out to verify and validate this idea.

Chapter 7 concludes the dissertation and recommends subjects for further investigation.

Chapter 2

Literature Review

2.1 Introduction

The depiction of wrinkles in art is as old as the subject itself. However, the scientific study of wrinkles is a much more recent subject as it involves the large deformation of naturally thin flat sheets whose behavior is governed by a set of nonlinear partial differential equations known as the Föppl-von Karman equations. Yet, interest in the subject has grown rapidly in recent years as evidenced by the number of publications and citations on the Web of Knowledge; these are shown in Figures 2.1 and 2.2 respectively. This chapter reviews important contributions from the existing literature dealing with the wrinkling of thin membranes starting from the beginning of last century, which can be categorized into analytical, numerical and experimental approaches.

2.2 Wrinkling Criteria

Membranes by definition have zero bending stiffness and can only carry loads in pure tension. Therefore, a membrane is unstable when subjected to in-plane compression and tends to deform out-of-plane to form wrinkles. Figure 2.3 shows that the length of the horizontal side of the membrane becomes shorter than its original length after the formation of wrinkles, due to geometric shortening, i.e., $L^{'} < L$. Figure 2.3 also shows schematically the stress redistribution in the membrane after wrinkling.

Generally, a membrane is in one of three different structural states. It is shown in Figure 2.3(a) that a membrane is in a taut state if it is biaxially stressed, i.e. both in-plane major and minor principal stresses denoted by σ_1 and σ_2 are positive. In a wrinkled state, the lowest in-plane principal stress must be zero, i.e., the membrane is stressed uniaxially. Also the troughs and crests - the lines along which the maximum out-of-plane deformation on either side of the membrane is attained - of the
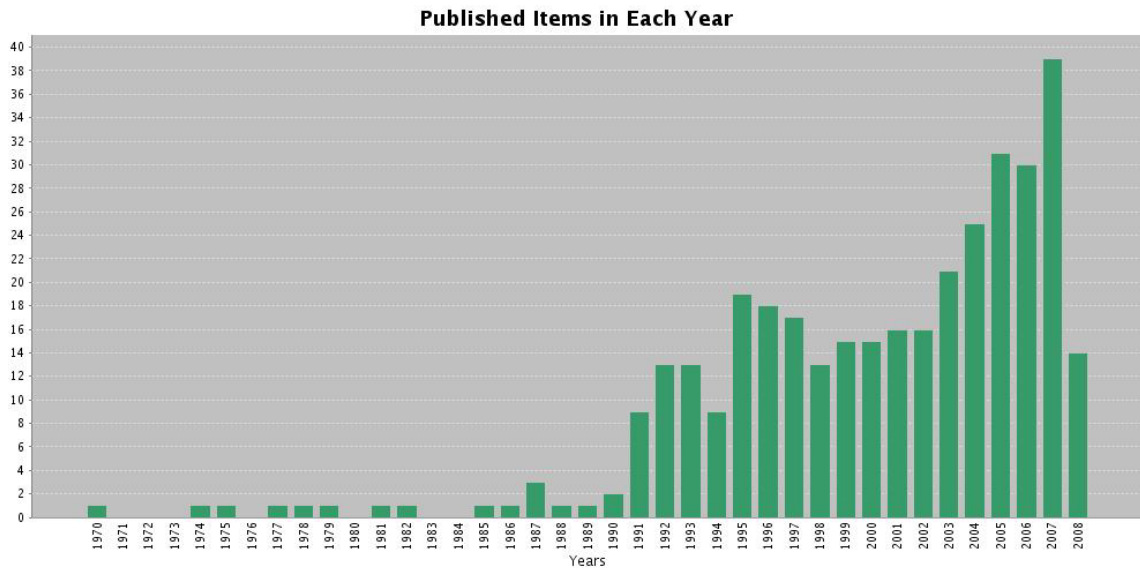
Figure 2.1: Number of publications about membrane wrinkling from 1970 to 2008 (Web of Knowledge).
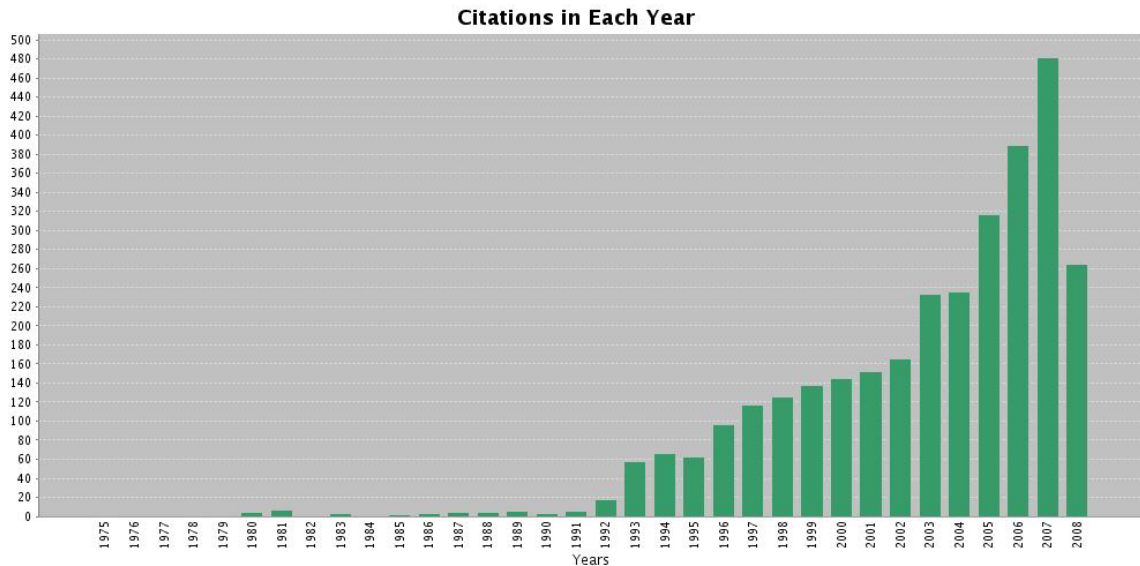
Figure 2.2: Number of citations about membrane wrinkling from 1970 to 2008 (Web of Knowledge).

wrinkles are parallel to the major principal stress direction as shown in Figure 2.3(b). The direction of wrinkles is always perpendicular to this tension line. Finally there is also a slack state, which is the extreme case of a wrinkled membrane where all the stresses are zero (Wong and Pellegrino, 2006).
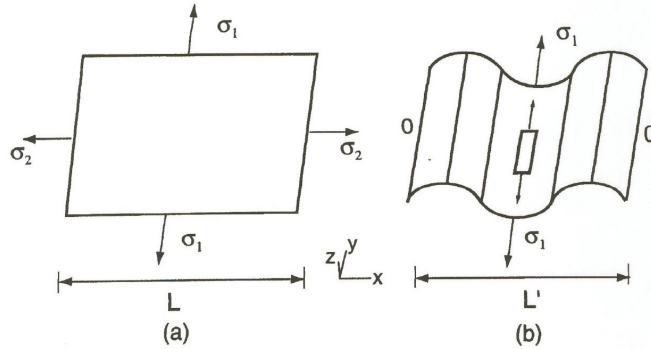
Figure 2.3: A membrane in (a) taut state, (b) wrinkled state (Wong and Pellegrino, 2006).

Note that there is zero stiffness in the direction perpendicular to the major principal stress in the wrinkled regions. Therefore, the membrane becomes softer when these regions grow in size. The overall structural behavior of a partially or fully wrinkled membrane is nonlinear, even if the material constitutive relationship - valid in the taut regions of the membrane - is linear. Further, the fact that the maximum wrinkle amplitudes are always found to run parallel to the maximum tensile stress direction for isotropic material implies that stress concentrations may occur. Together the contribution of softening due to the growth of the wrinkled regions, and the threat of stress concentrations lead to a rather complex behavior.

The above description of the formation of wrinkles based on the sign of the principal stresses is only one of the three wrinkling criteria that have been proposed. The wrinkling criterion based on principal strains is formulated in a similar way to the principal stress criterion: the membrane is in a taut state when the major principal strain is positive (tensile), and the minor principal strain must be greater in magnitude than the strain predicted purely by Poisson's effect if the membrane was under uniaxial stress state (Miller and Hedgepeth, 1982). It is slack if both principal strains are non-positive. In both the taut and slack states there is no wrinkling in the membrane. Thus, a wrinkled state occurs in the membrane when the minor principal strain is less than the strain due to Poisson's effect and the major principal strain is positive.

For wrinkling based on the combined criterion, the membrane is defined to be taut when the minor principal stress is positive. It is in a slack state when both the major principal stress and

strain are non-positive. When the minor principal stress is non-positive and the major principal strain is tensile, the membrane is wrinkled (Roddeman et al., 1987).

The wrinkling criteria described above are summarized below, where σ_1, σ_2 and ϵ_1, ϵ_2 are the major and minor principal stresses and strains respectively (hence $\sigma_1 \geq \sigma_2$ and $\epsilon_1 \geq \epsilon_2$).

1. Principal stress criterion

   Taut: $\sigma_2 > 0$

   Wrinkled: $\sigma_2 \leq 0$, $\sigma_1 > 0$

   Slack: $\sigma_2 \leq 0$, $\sigma_1 \leq 0$.

2. Principal strain criterion

   Taut: $\epsilon_1 > 0$, $\epsilon_2 > -\nu\epsilon_1$

   Wrinkled: $\epsilon_1 > 0$, $\epsilon_2 \leq -\nu\epsilon_1$

   Slack: $\epsilon_1 \leq 0$, $\epsilon_2 \leq 0$.

3. Combined criterion

   Taut: $\sigma_2 > 0$

   Wrinkled: $\sigma_2 \leq 0$, $\epsilon_1 > 0$

   Slack: $\sigma_1 \leq 0$, $\epsilon_1 \leq 0$.

The first two criteria, based on principal stresses or strains only, are fairly easy to apply. However, the slack regions defined by the principal stress criterion may in fact experience positive strain. Whereas, the principal strain criterion may underestimate the taut regions in the membrane since negative strain may exist together with a positive minor principal stress due to Poisson's effects. The combined criterion overcomes the potential shortcomings mentioned above and provides the most accurate description of a wrinkled membrane (Liu et al., 2001).

2.3 Theoretical Approach

The criteria described above provide a quick guide to the presence/absence of wrinkles at a single point. The analysis of an entire membrane subjected to a complex of boundary conditions requires a more complete theoretical approach.

2.3.1 Tension Field Theory

The classical approach to analyzing membrane wrinkling is the tension field theory first introduced by Wagner (1929) for the analysis of thin webs in I-beams that are allowed to go much beyond their

initial buckling load. In its original form, this theory considered a set of parallel wrinkle lines but later a simpler geometrical formulation was proposed (Reissner, 1938), which allowed for nonparallel tension rays. A further generalization (Mansfield, 1968) of this theory showed that the direction of the tension rays maximizes the (stretching) strain energy in the membrane. Closed-form solutions for membranes with different shapes and anisotropic membranes were also developed. A summary of this theory (Mansfield, 1968) is presented next. Note that the notation used here is based on the mentioned reference and hence is not necessarily the same as the general notation defined and employed elsewhere in this dissertation.

Consider an initially flat linear-elastic, isotropic membrane of any shape, with uniform thickness which is subjected to given planar displacements at its boundaries. A tension field is assumed to be generated over the membrane due to this boundary condition. The primary objective in tension field theory is to determine the orientation of the tension rays in a highly wrinkled state of the membrane. Note that a tension ray is referred to as the line of major principal stress.

The strain energy in the membrane is due to only the tensile stresses along the tension rays, since there are no normal and shear stresses across adjacent rays. Mansfield formulated a principle of maximum strain energy by postulating that the true distribution of tension rays maximizes this tensile strain energy. A membrane of constant thickness, t, with reference axis Ox is shown in Figure 2.4. Two adjacent tension rays denoted by LK and $L'K'$, intersect the x-axis at angles α, $\alpha + \delta\alpha$ and meet at the point H. A general point in the membrane is defined by α and η, where η is the distance along the tension ray; it is a function of α and x. Maintaining equilibrium along the tension ray requires the continuity of the tensile load carried by the tapered strip of material enclosed by adjacent rays, with the assumption that there is no stress across, the ray as shown in Figure 2.5 gives

$$\eta\sigma_\eta = \text{constant},\tag{2.1}$$

where σ_η is the normal stress along a ray.

The integral of the strain ϵ_η along line LK is equal to the change in length of LK and will be denoted by Δ_α; its values depends on the given boundary displacements. Therefore, the constant in Eq. (2.1) can be evaluated and

$$\epsilon_\eta = \frac{\Delta_\alpha}{\eta\left(\ln\frac{\eta_2}{\eta_1}\right)},\tag{2.2}$$

where η_1 and η_2 are the boundary values of η, as shown in Figure 2.4. The strain energy in the membrane can then be determined by integrating over an elemental slice bounded by two adjacent
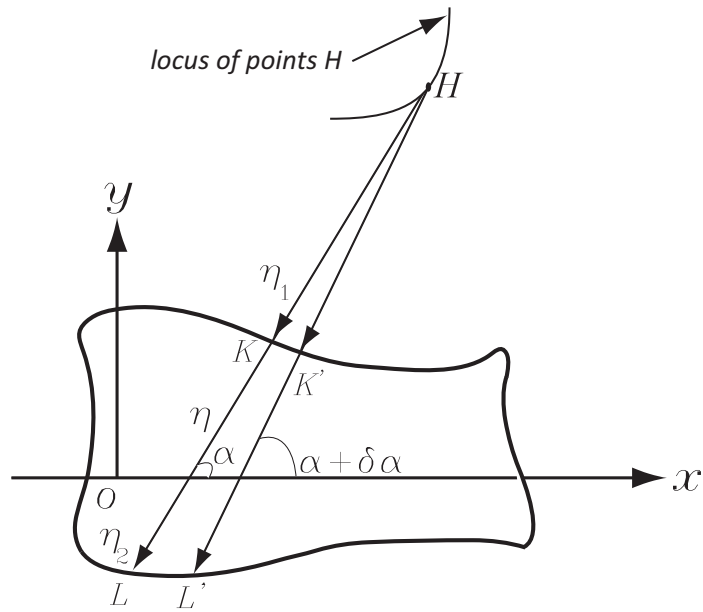
Figure 2.4: An arbitrary membrane with two adjacent tension rays (Mansfield, 1968).
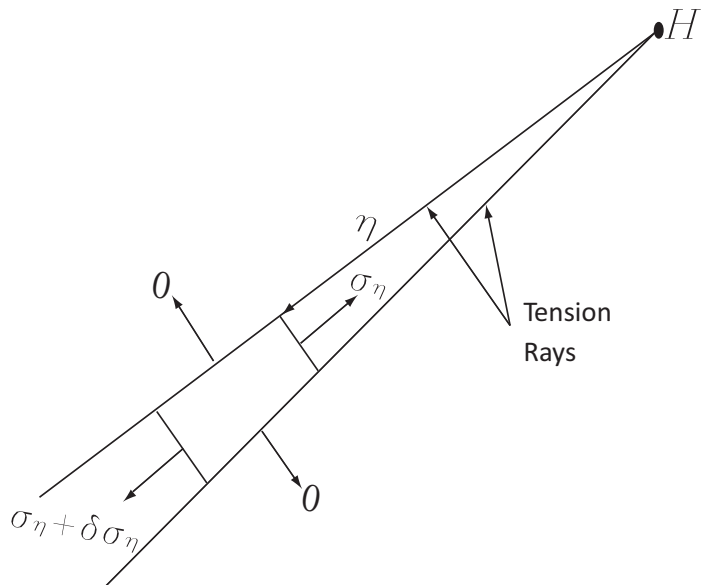
Figure 2.5: Equilibrium of infinitesimal element of membrane defined by two adjacent tension rays (Mansfield, 1968).

rays

$$U = \frac{1}{2}Et \int \int \epsilon^2 d\mathbf{A} = \frac{1}{2}Et \int \int_{\eta_1}^{\eta_2} \eta \epsilon_\eta^2 d\eta d\alpha = \frac{1}{2}Et \int F d\alpha \qquad (2.3)$$

where

$$F = \frac{\Delta_\alpha^2}{\int_{\eta_1}^{\eta_2} \frac{1}{\eta} d\eta}. \qquad (2.4)$$

The value of η on the x-axis, η_x, can be determined by geometrical considerations,

$$\eta_x = \pm \left(\frac{dx}{d\alpha}\right) \sin \alpha, \qquad (2.5)$$

where the sign in Eq. (2.5) depends on the position of point H relative to the x-axis. The relationship between α and x is determined by maximizing U; therefore the general equation is

$$x'' F_{x'x'} + x' F_{xx'} + F_{\alpha x'} - F_x = 0, \qquad (2.6)$$

where $x' = dx/d\alpha$, $x'' = d^2x/d\alpha^2$, $F_x = \partial F/\partial x$, etc. Hence, F is a function of the variables α, x and x'. Note that if F does not contain x explicitly, Eq. (2.6) can be integrated once to give

$$F_{x'} = \text{constant}. \qquad (2.7)$$

From Eq. (2.1)-(2.7), it is seen that the determination of the distribution of tension rays is based solely on the displacement components along the tension rays. This relationship is used to determine the stress distribution in the membrane. Note that the theory is valid only if

$$\Delta_\alpha > 0 \quad \text{and} \quad \epsilon_\alpha + \nu \epsilon_\eta \leq 0. \qquad (2.8)$$

Mansfield extended the general equations developed above to the study of membranes with different strip lengths and boundary conditions and verified this theory with some experimental observations.

This theory was later incorporated into ordinary linear-elastic membrane theory (Pipkin, 1986) by replacing the strain energy density with a special form of strain energy density function, known as a relaxed strain energy. In the wrinkled regions, this function represents the average energy per unit initial area over a region containing many infinitesimal wrinkles. It would then produce a state of a uniaxial stress, i.e., zero minor principal stress if the states of strain in an ordinary, i.e., linear elasticity membrane theory would require compressive stresses. Therefore, the underlying assumptions in tension field theory can be reproduced with this approach.

A further extension of this theory was proposed by Steigmann and Pipkin (1989) to consider finite elastic deformations of membranes subject to in-plane and pressure loading. Roddeman et al. (1987) developed an alternative model to account for large deformation wrinkling problems. Wu and Canfield (1981) were the first to treat wrinkling as a geometrical non-linear problem using plane stress theory but limited only to isotropic material. Roddeman's model is based on deformation gradient tensors obtained from a fictitious, non-wrinkled membrane surface; these tensors are modified so that they are always consistent with tension field theory. This model can be used to analyze both isotropic and anisotropic materials. A generalization of tension field theory in the context of a saturated elasticity theory has been proposed by Epstein and Forcinito (2001).

2.3.2   Variable Poisson's Ratio Theory

An alternative approach has been proposed for partially wrinkled membranes such as a pressurized cylindrical tube in pure bending. This theory, generally known as Wrinkling Theory (Stein and Hedgepeth, 1961), was derived from the linear-elastic, isotropic plane stress theory based on the assumptions given below.

The basic assumptions made in this theory are:

1. Compressive stresses are eliminated completely by the formation of wrinkles. Therefore, the minor principal stress is non-negative everywhere in the membrane.

2. The troughs and crests of wrinkles run in the directions of the local major principal axis.

3. The load in the wrinkled regions is carried only by the wrinkles in the directions of the troughs and crests. Hence, the minor principal stresses in the wrinkled region (perpendicular to the load paths) are zero.

4. There are only taut and wrinkled regions in a partly wrinkled membrane.

In the taut regions, the membrane is assumed to behave according to standard linear-elastic plane-stress theory. In the wrinkled regions, a modified set of constitutive relationships is used, by using a variable Poisson's ratio (which takes into account the over-contraction caused by the wrinkles) determines the membrane behavior. The variable Poisson's ratio must match the material Poisson's ratio at the boundaries between wrinkled and taut regions. The minor principal stresses must be positive in the taut regions and zero in the wrinkled regions.

Stein and Hedgepeth (1961) used this theory to produce closed-form solutions for three simple structures: a biaxially stressed membrane subject to in-plane bending, an internally pressurized My-

lar cylinder in bending, and a stretched circular Mylar sheet attached to a rigid hub that is rotated. Mikulas (1964) generalized this theory and produced a closed-form solution for the rotating circular membrane model. This theory is only capable of estimating an average strain normal to the wrinkle. It is used to determine the regions of a membrane that wrinkle, the pattern those wrinkles take, and the resulting stress field and load paths.
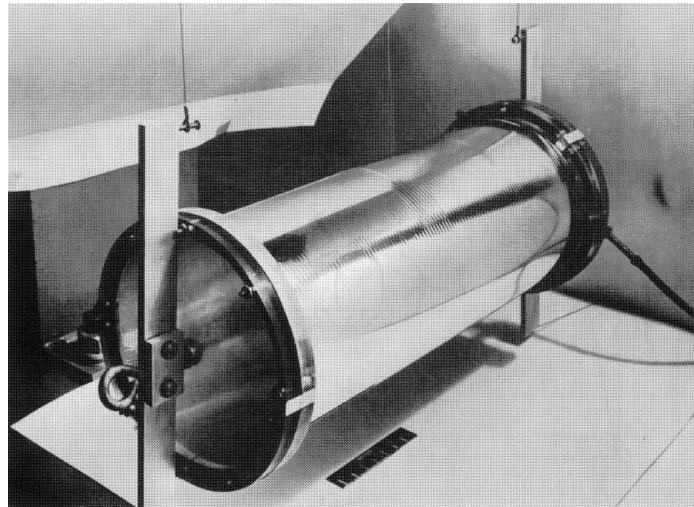
Figure 2.6: Wrinkles on a bent Mylar cylinder (Stein and Hedgepeth, 1961).
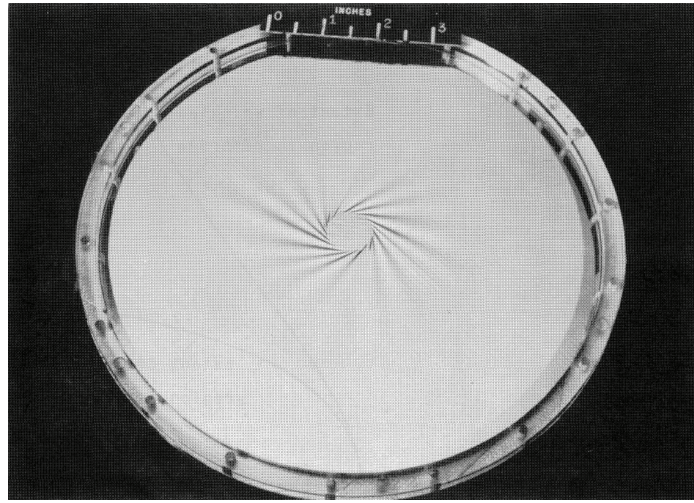
Figure 2.7: Wrinkles on a circular membrane with center attached to a rigid hub and rotated for a certain angle (Stein and Hedgepeth, 1961).

2.3.3 Theories With Finite Bending Stiffness

In the two previous approaches, the membrane is modeled as a non-compressive material with negligible bending stiffness. This amounts to assuming that a wrinkled membrane forms an infinite number of infinitesimally small wrinkles. An analytical solution of the gravity-induced wrinkling in a hanging blanket, for the first time considered a critical compressive stress in the membrane.
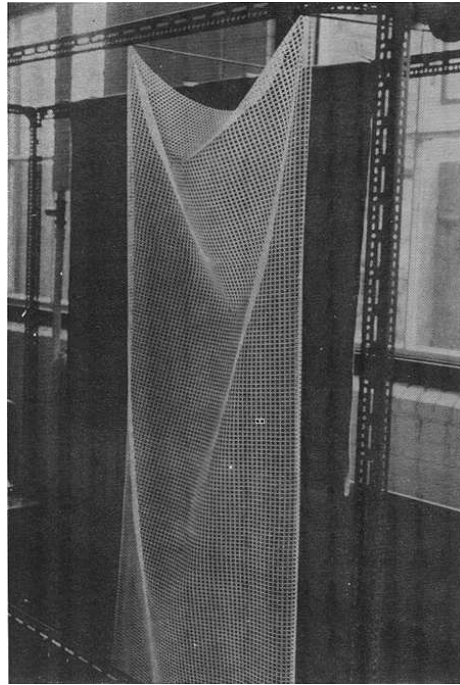
Figure 2.8: Wrinkles on a hanging blanket due to self-weight (Rimrott and Cvercko, 1985).

The effect of in-plane compression on the wrinkling of a thin blanket hung between two level supports was investigated by Rimrott and Cvercko (1985). A series of cosine-shaped wrinkle lines were assumed to form in the blanket due to gravity, as shown in Figure 2.9(a) and each region bounded by two neighboring wrinkle lines was called a tension strip.

Rimrott and Cvercko (1985) noted that equilibrium of the membrane in the out-of-plane distorted configuration requires each finite-size wrinkle to carry a uniform horizontal force component; this horizontal force is equal in each wrinkle. Hence, having shown that the boundaries of the wrinkle lines have amplitudes $a_n, ..., a_0$ that form a geometric progression (a_i/a_{i+1} =constant), it follows that the horizontal stress component, σ_x[1], at the center of the wrinkle is largest in the more closely spaced wrinkles at the top of the membrane. Associated with σ_x, there is a compressive stress σ_y

---

[1]Note that the notation used here is based on the cited reference and hence is not necessarily the same as the general notation defined and employed elsewhere in this dissertation.
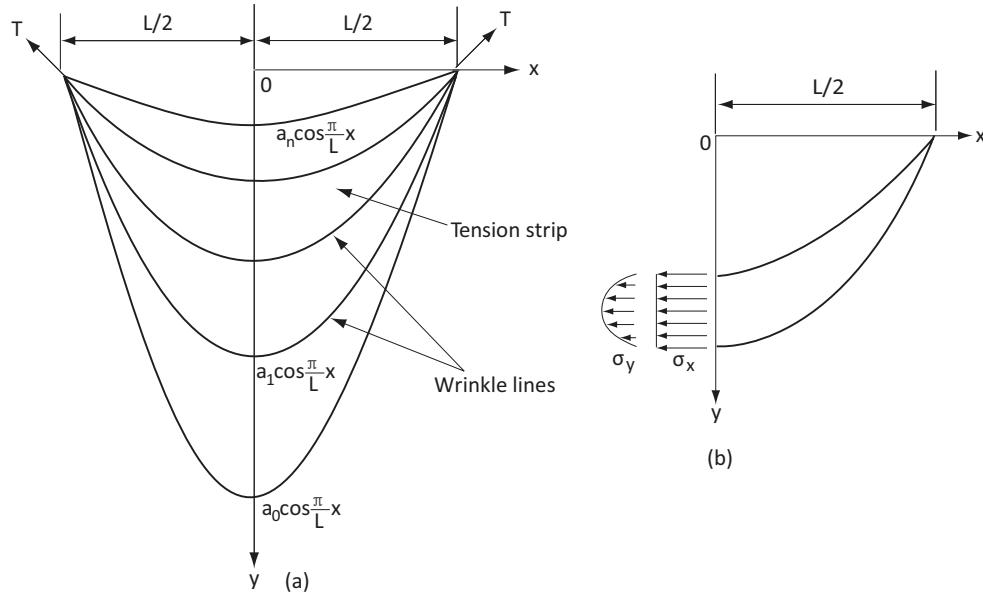
Figure 2.9: (a) Wrinkle lines in a blanket suspended in gravitational field; (b) stress components in the third tension strip (Rimrott and Cvercko, 1985).

that vanishes at the edges of each finite-size wrinkle and reaches a maximum along the center line of the wrinkle. They assume that the critical value, σ_{cr}, of this compressive stress is a characteristic of the blanket material and showed that for any chosen value of σ_{cr}, there is corresponding number of finite-sized tension strips in the membrane.

The assumptions that underlie this approach are different from those in the previous two theories, and can be stated as follows.

1. Bending stiffness is present in the membrane, since a finite number of wrinkle is observed in the experiments. Hence a small compressive stress can be carried and its magnitude is limited by a critical compressive stress in the membrane.

2. The strain energy in tension is zero, as the material is assumed to be inextensible in tension, and is negligible in compression.

3. The bending strain energy in a wrinkled membrane is not negligible.

This study shows that even a small bending stiffness, that certainly exists in any membrane, is responsible for the finite number of wrinkles and corresponding amplitudes that are observed, when a membrane is subjected to in-plane compressive body force.

Epstein (2003) set up an approximate strain-energy analysis of a field of uniform, parallel wrinkles. Having assumed the wrinkles to be of sinusoidal shape longitudinally and to form circular arcs

transversally, Epstein developed a differential equation that describes the wrinkle amplitude in a membrane by relating it to the wrinkling strain determined from the elastic strain energy formulation. This geometric strain is a function of the membrane bending stiffness, wrinkle wavelength and curvatures of a wrinkle. He showed that, given a longitudinal strain ϵ_ξ and a transverse strain ϵ_η, the wrinkle amplitude is

$$A = \sqrt{2kL(\bar{\xi} - \bar{\xi}^2)}, \tag{2.9}$$

where $k = \sqrt{3\epsilon_\eta^2 t^2/2\epsilon_\xi(1 - \nu^2)}$ and $\bar{\xi} = \xi/L$ is a nondimensional length variable along the wrinkle (where L is the length of the wrinkle).

Cerda et al. (2002) studied an elastic sheet under tension and determined the wavelength λ and amplitude A of the parallel wrinkles by minimizing the potential energy

$$U = U_B + U_S, \tag{2.10}$$

where $U_B \approx Et^3(A/\lambda^2)^2 LW$ is the energy due to bending primarily in the transverse direction and $U_S \approx Et\gamma(A/L)^2 LW$ is the energy due to stretching strain γ along the wrinkles, subject to the geometric constraint of transverse inextensibility $(A/\lambda)^2 \approx \nu\gamma$. Minimizing U with respect to λ gives a scaling law for the wavelength

$$\lambda \approx (tL)^{1/2}/\gamma^{-1/4} \tag{2.11}$$

and the amplitude

$$A \approx (\nu tL)^{1/2}\gamma^{1/4}. \tag{2.12}$$

A refined calculation in Cerda and Mahadevan (2003) gives the following expressions for the prefactors: $C_\lambda = \lambda\gamma^{1/4}/(tL)^{1/2} = (4\pi^2/3(1 - \nu^2))^{1/4}$, and $C_A = A/(\nu tL)^{1/2}\gamma^{1/4} = (16/3\pi^2(1 - \nu^2))^{1/4}$. The wrinkle amplitude and wavelength need to be uniform throughout the membrane surface for the above expressions to be valid. Experimental results obtained by stretching polyethylene sheet of thickness 0.01 cm, width 12 cm and three different lengths shows quantitative agreement (Figure 2.10).

Wong and Pellegrino (2006) presented a general analytical framework for predicting the location and pattern of wrinkles in thin membranes, and for making preliminary estimate of their wavelength and amplitude. The key ideas in their analytical model are as follows. First, the wrinkled region and the direction of the wrinkles can be determined from a two-dimensional stress field that admits no compressive stress anywhere, satisfies equilibrium, and provides a reasonably close (upper) bound to the actual complementary strain energy of the membrane. Second, the wavelength of the wrinkles
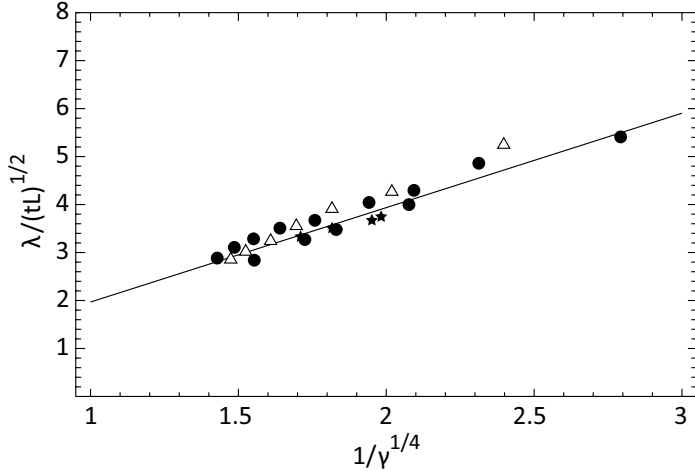
Figure 2.10: Wrinkle in a polyethylene sheet. Plot the dimensionless wavelength $\lambda/(tL)^{1/2}$ against $1/\gamma^{1/4}$ for various lengths of a polyethylene sheet. Lengths: circles, 25.4 cm; stars, 30.4 cm; triangles, 34.5 cm. The data span more than an order of magnitude in strain, with $\gamma \in [0.01, 0.2]$. The line corresponds to the theoretical prediction $\lambda/(tL)^{1/2} = (4\pi^2/3\gamma(1 - \nu^2))^{1/4}$. For polyethylene, $\nu = 0.35$, so that $\lambda/(tL)^{1/2} \approx 2/\gamma^{1/4}$, which is consistent with the results of the experiments (Cerda et al., 2002).

was estimated by considering a (small) compressive buckling stress in the direction transverse to the wrinkles, and by ensuring that this stress component and the longitudinal stress (given by the two-dimensional stress field) are in equilibrium in the out-of-plane direction at the center of the wrinkles. Third, the amplitude of the wrinkles was determined by matching the sum of the material strain and geometric strain due to wrinkling, in the direction transverse to the wrinkles, to the boundary conditions imposed by the nonwrinkled region.

This analytical model has been applied to two different problems, a rectangular membrane under simple shear and a square membrane loaded at the corners. In the first problem, the model predicts the wavelength and the wrinkle amplitude to be inversely proportional and directly proportional to the fourth root of the shear angle respectively as shown in Eqs. (2.13) and 2.14. Both values are directly proportional to the square root of the height, H, and thickness, t, of the membrane, and both are independent of the Young's modulus.

$$\lambda = \sqrt{\frac{\pi H t}{\sqrt{3(1 - \nu^2)}}}, \tag{2.13}$$

$$A = \sqrt{\frac{2Ht}{\pi} \sqrt{\frac{(1 - \nu)\gamma}{3(1 + \nu)}}}, \tag{2.14}$$

where $\gamma = \delta/H$ is the shear angle and ν is the Poisson's ratio.

The same strategy was used in the second problem except that no tension field solution is known for this problem. They first proposed four different, no-compression equilibrium stress fields and then chose the particular distribution that produces the lowest upper bound for the corner deflection (according to the theorem of minimum complementary energy) as the best approximation to the actual stress field in the membrane.

Two wrinkling regimes have been identified. The first is characterized by relatively uniform, small, radial corner wrinkles and occurs for load ratios smaller than $1/(\sqrt{2}-1)$. The number of radial wrinkles, n, determined by considering the out-of-plane equilibrium in the middle of a wrinkle, is proportional to the fourth root of the outer radius of the wrinkled zone, R_w, and the corner forces, T:

$$n = \sqrt[4]{\frac{3\sqrt{2}\pi^2(1-\nu^2)(R_w+a)^3}{64Et^3(R_w-a)^2}T}. \tag{2.15}$$

Here the radius of the wrinkled region is proportional to the radius of the uniaxially stressed wedge field in Figure 2.11. The amplitude of these wrinkles is inversely proportional to this number and
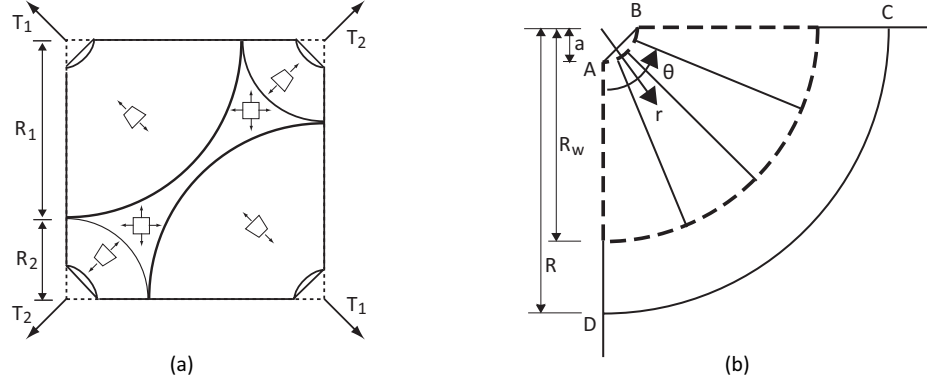
Figure 2.11: (a) Equilibrium stress field. A trapezium denotes a purely radial stress field, (b) radially stressed wedge region (Wong and Pellegrino, 2006).

directly proportional to the square root of the radius of the wrinkled region and to the corner force:

$$A = \frac{1}{n}\sqrt{\frac{R_w+a}{2\sqrt{2}Et}\left(\ln\frac{2R}{R_w+a}-\nu\right)T}. \tag{2.16}$$

The second regime occurs for load ratios larger than $1/\sqrt{2}-1$ and is characterized by a large diagonal wrinkle, plus small radial wrinkles at all four corners.

2.4   Numerical Approach

Closed-form solutions based on the theoretical approaches described in the previous section exist only for simple boundary conditions. For more complex geometries, numerical solutions are the only viable option.

2.4.1   Iterative Membrane Properties (IMP) Method

The first finite element solution to incorporate wrinkling theory was implemented by Miller and Hedgepeth (1982) and Miller et al. (1985) to iteratively modify the membrane stiffness until all compressive stresses had been eliminated. Three different states of the membrane, namely taut, wrinkled, and slack were considered.

A recent extension of this approach has been implemented as a user defined material (UMAT) subroutine that exploits the powerful numerical solvers currently available in commercial finite element packages, e.g., ABAQUS and NASTRAN. Successful predictions of the shape and pattern of the wrinkled regions in a square membrane subjected to point loads and inflated balloons of different shapes were obtained (Adler et al., 2000). The combined wrinkling criterion introduced in Section 2.2 was used in the implementation of this modified material definition. The main problem encountered with this approach is that the solution tends to diverge if there are too many slack regions.

Johnston (2002) used this ABAQUS subroutine to analyze the static and dynamic behavior of a one tenth scale next generation space telescope (NGST) sunshield. The finite element model based on this modified wrinkled material definition was found to predict lower natural frequencies compared to those obtained from standard shell and membrane elements.

2.4.2   Penalty Tension Field Parameter Method

A tension field model was developed by introducing a penalty parameter to approximate the stress state in wrinkled membranes and incorporated into a nonlinear finite element code TENSION6 (Liu et al., 1998). The main difference of this method from IMP is that, instead of modifying the material properties iteratively, the user pre-selects a so-called penalty tension field parameter to provide some stiffness in the wrinkle direction, and thus overcome the numerical singularities due to vanishing diagonal terms in the tangent stiffness matrix. This approach has been implemented to simulate the deployment of a parachute. Modeling issues, including the selection of the penalty term, influence of the order of integration and local remeshing in the wrinkled regions were also discussed.

Liu et al. (2000) used this approach to estimate the wrinkle details in a square membrane subjected to a combination of tension and shear force. The analysis was carried out in two steps. The wrinkled region and directions were determined in the first step using this approach, then a standard eigenvalue analysis was carried out to determine the number of wrinkles. A critical compression coefficient assuming the membrane as a plate was introduced. Wrinkle wavelength and amplitude in this wrinkled region were estimated by correlating the principal strains, the compression coefficient and the stiffness ratio of the membrane.

2.4.3   No-compression Material Method

A different scheme that models the membrane as a no compression material in a non-linear geometrical analysis has been successful in simulating the shapes of inflated air-bags (Contri and Schrefler, 1988), including the formation of some large folds in the surface and also of extensive wrinkled regions.

A similar approach has been implemented in ABAQUS by using the *NO COMPRESSION parameter to define the material properties. The elastic behavior of the membrane is determined, first by solving for the principal stresses, assuming linear elasticity. Then, any compressive principal stresses are set to zero and the associated stiffness matrix coefficients are also set to zero. The directions in which the principal stresses are set to zero are recalculated at every iteration, hence the results are not history dependent.

A three-node triangular isoparametric plane stress wrinkling element was developed based on the Roddeman's model, and made available in DIANA (TNO, 1998), a commercially available finite element package. Also a formulation based on the relaxed energy method (Pipkin, 1986) has recently been incorporated into standard finite element schemes for membrane elements (Barsotti and Ligaro, 2000).

A general feature of all of these numerical approaches is that they adopt a purely two-dimensional model of the membrane. This approach can accurately predict the stress distribution in the membrane, including wrinkled regions, and also the extent of these regions, but it provides little information on wrinkle details. This requires modeling the membrane as a thin shell.

2.4.4   Models Using Thin Shell Elements

Tomita and Shindo (1988) were the first to make use of a three-dimensional shell description of a wrinkled membrane, in a study of the residual wrinkles in a thin metallic plate that has been pulled diagonally. This paper startes with an analysis of the onset of wrinkling, which was assumed to be the outcome of a bifurcation from plane deformation to out-of-plane deformation of the plate. The plate was initially represented by a mesh of thin plate elements, including the effects of material nonlinearity, but the growth of the wrinkles was then traced by switching the model to isoparametric shell elements following bifurcation.

The last five years have seen regular use of the ABAQUS software package, and recently also of ANSYS, to simulate the onset of wrinkling in a tensioned strip and the growth of wrinkles. Friedl et al. (2000) studied the phenomenon of plate buckling under global tension computationally and analytically. They discussed the case in which the instability is a result of clamped boundary condition that prevents lateral displacements along edges being loaded. The origin of the lateral compressive stresses is explained by means of a simple cantilever plate model. The stabilizing effect of the global tension was shown through an investigation of a rectangular plate, simply supported along all four edges. Minimum half wave numbers in lateral direction was estimated. Numerically calculated buckling modes for two different aspect ratios are presented. A novel diagram with critical buckling coefficients as a function of the aspect ratio is introduced, allowing calculation of critical tensile stresses in the same practical way, as used for conventional plate buckling problems.

Three approaches to simulate wrinkle growth have been proposed, differing in the way the out-of-plane deformation is triggered at the beginning of a geometrically nonlinear analysis. Wong and Pellegrino (2002) and Wong et al. (2003) started by extracting a set of eigenvalues/eigenvectors of the tangent stiffness matrix of the structure. Instead, Leifer and Belvin (2003) applied a set of equal and opposite, small magnitude forces perpendicular to the membrane with a resultant of zero. Finally, Tessler et al. (2003, 2004) and Papa and Pellegrino (2005) imposed randomly distributed, out-of-plane imperfections, of similar magnitude to those imposed in Wong and Pellegrino (2002). The choice of the type of elements and the type of analysis are essentially equivalent in the three simulation techniques, so the key difference between the first approach and the other two is the additional burden of the initial eigenvalue/eigenvector extraction. Wong and Pellegrino (2006) showed that this additional computation requires only a small fraction of the total simulation time, and the eigenvector-based perturbation provides better agreement with experimental results than the one based on random imperfections.

2.5   Experimental Approach

Early experimental studies measured the overall response of wrinkled membranes and compared the measurements to predictions from the various theories. Physical measurements of wrinkle details have been attempted more recently following the increased importance attached to this piece of information.

2.5.1   Overall Behavior

Early experiments on wrinkled membranes focussed on the measurement of overall response parameters, such as the end rotation of a pressurized cylinder in pure bending (Stein and Hedgepeth, 1961) or the torque-rotation relationship of a stretched circular membrane attached to a central hub (Stein and Hedgepeth, 1961; Mikulas, 1964). These particular experimental studies were carried out to validate the wrinkling theory outlined in Section 2.3.2, and to confirm that the membrane retained most of its stiffness after wrinkling first occurred, although a notable softening was in fact observed with the growth in the extent of the wrinkled regions. Mansfield (1968, 1970) investigated and determined the orientation of the wrinkle lines in membranes with different shapes and subjected to different boundary conditions. Only qualitative correlations between theory and the experimental observation were given.

2.5.2   Measurement of Wrinkle Details

Performing detailed measurements on thin membranes is not easy, mainly because high accuracy non-contact measurement apparatus is needed. A set of carefully planned experiments, including accurate measurements of wrinkle details by using a capacitance proximity sensor, were carried out on a square Mylar membrane subjected to different combinations of shear and tension forces (Jenkins et al., 1998). These experiments showed that both the wrinkle amplitude and the number of wrinkles increase with the applied shear force, but decrease with the tension force. The reverse relationship was found between wrinkle wavelength and applied forces.

The measurement technique introduced by Jenkins et al. (1998) has been extended to measure the surface profile of a thin, aluminized 0.5 m square Kapton membrane subjected to four corner loads (Figure 2.12(a)), and to include the effect of thermal gradients within the membrane (Blandino et al., 2002). In addition, a complete out-of-plane displacement contour plot (Figure 2.12(b)) was also produced for the membrane with the aid of photogrammetry, and was compared with the measurements made by the capacitance sensor at one corner of the membrane. The experimental data

shows good agreement between the two techniques, with an accuracy of up to ± 0.02 mm for the wrinkle amplitude measurement.

(a)   (b)
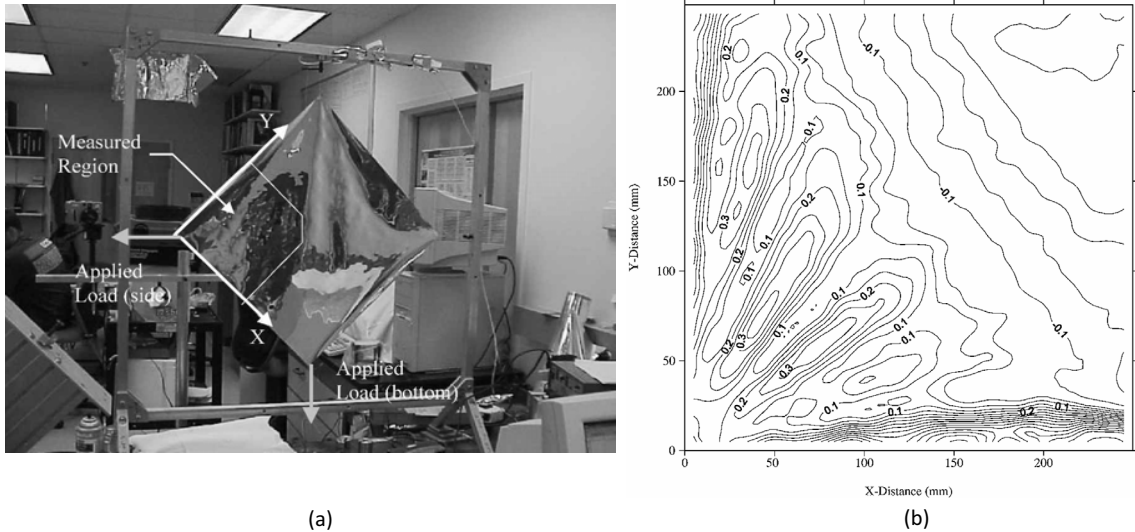
Figure 2.12: (a) Experimental setup of square membrane subjected to symmetric corner loads, (b) contour plot of out-of-plane displacement at the corner section of the membrane; four peaks and five valleys were identified (Blandino et al., 2002).

Wong and Pellegrino (2006) used a charge coupled device (CCD) laser displacement sensor (LK-081, KEYENCE) to measure wrinkle profiles on Kapton membranes subjected to pure shear and point load at corners. A scanning frame was designed as shown in Figure 2.13, on which the laser sensor glides on a linear guide driven by a motor to measure a line profile on the membrane surface. This device provides a measurement range of ± 15 mm and a resolution of 3 μm.

The main disadvantage of capacitance sensors is that they need a metallic surface target and the sensor must be in electrical contact with the membrane. Similarly laser sensors need a surface with sufficient reflectivity and can only acquire a line profile of the wrinkled surface. As for photogrammetry, a large number of target points is required in order to capture fine wrinkle details and the postprocessing of the image can be time-consuming. However, the latest applications of this technique, based on the commercial software package Photomodeler 4.0 (Blandino et al., 2003), have shown that this technique is making rapid advance.
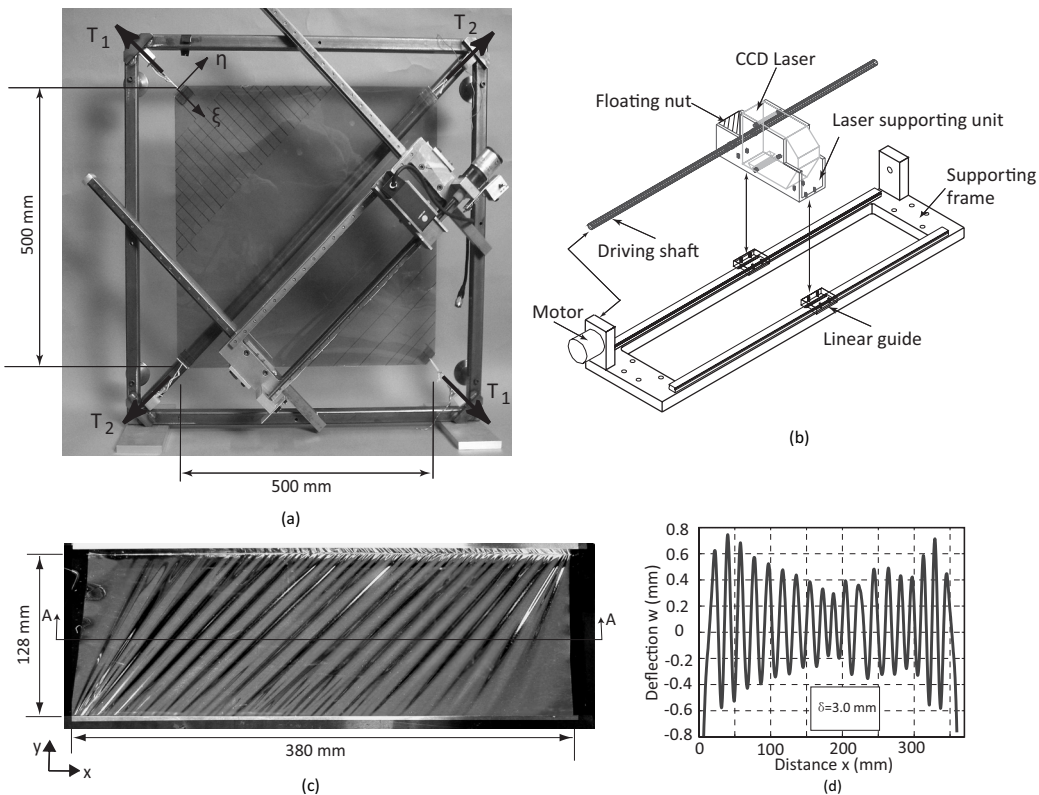
Figure 2.13: (a) Experimental setup of a square Kapton membrane subject to corner loads. A two-dimensional laser scanning frame was built to measure the wrinkle profile at corner; (b) schematic drawing of the laser scanning frame; (c) wrinkle patterns for a 0.025 mm thick Kapton film under shear displacement of 3.0 mm; (d) plot of the displacement along the cross section A-A (Wong and Pellegrino, 2006).

2.6 Optical Methods for 3D Shape Measurement

Optical techniques for 3D shape measurements have been widely studied as the conventional approach using mechanical probes is not suitable for non-contact or full field measurement. Numerous methods, such as those based on the Moiré, interferometry and fringe projection technique, have been developed.

In the Moiré technique, an object profile is coded into a Moiré fringe pattern produced by one (shadow Moiré) or two (projection Moiré) gratings. The phase angle of the fringe pattern is related to the object surface depth and can be extracted to the object surface depth and can be extracted by well-known fringe analysis algorithms, such as phase-shifting and Fourier transform methods. The Moiré technique is useful for measuring small objects but its application for large object measurement is limited by the size of the gratings and the measurement accuracy is dependent on the resolution of the gratings.

Shape measurement techniques based on interferometry, such as those using the Newton, Fizeau and Michelson interferometers, have been known for a long time. Although the basic set-ups of these interferometers are simple, they can be developed into various forms depending on applications. The advantage of interferometry based techniques is that high measurement accuracy, a fraction of the wave length of light, can be achieved. However, the surface of the test object must be highly reflective and monochromatic light source must be used for interference. In recent years, another trend in 3D shape or surface roughness measurement is based on white light (incoherent light) interferometry. The accuracy of the techniques using white light is even higher than that using coherent light because the coherence length of white light is very short and the generation of white light fringe pattern ensures high accuracy. However, since white light fringe pattern is observable only in a small range, it is necessary to scan perpendicularly through an object surface to reconstruct a 3D profile. Hence, the measurement speed is relatively slow and large amount of data is involved in processing.

Fringe projection technique is based on the principle of triangulation. Before the advent of digital fringe projector, gratings served as the source of fringe pattern. The most commonly used is a square wave grating, which is composed of transparent and dark stripes. Takeda and Mutoh (1983) proposed a carrier fringe Fourier transform method to extract phase data from a square wave fringe pattern. Srinivasan et al. (1984) applied phase-shifting algorithm to extract an object surface profile from a projected sinusoidal grating. Similar to the Moiré technique, the accuracy of both methods is dependent on the resolution of the gratings. The advent of the digital fringe projector, such as the programmable liquid crystal display (LCD) projector, has advanced the fringe projection technique.

Any computer generated fringe pattern can be projected. Furthermore, phase shifting, fringe density and intensity can be changed digitally without modifying the physical set-up. A number of papers have reported the use of the digital projection device. Coggrave and Huntley (2000) studied the precision of a shape measurement system based on a LCD projector. Sansoni et al. (1997) developed a gray-code light projection technique which could be used to evaluate objects with discontinuous surface. Quan et al. (2001) applied the LCD projector with long working distance microscope (LWDM) on small object measurement and achieved an accuracy of 1 micron.

2.6.1   Phase Extraction Method

Two phase extraction algorithms for automatic fringe analysis have been developed: Fourier transform method with a single image and phase shifting technique with multiple images. The purpose of these algorithms is to find a phase information at every pixel, and thus to determine a fractional fringe order at every point in the fringe pattern.

Phase-shifting interferometry technique has been exclusively employed for multiple-frame analysis. It requires at least three phase-shifted interferograms each with a known phase shift. It is often the first choice for phase-demodulation whenever atmospheric turbulence and mechanical conditions remain constant during the time of obtaining the interferograms. When the above conditions are not fulfilled, one may use Fourier transform technique provided the image has an added carrier fringe. The most important advantage of the Fourier transform method is that it requires only one interferogram for the analysis. It is ideal for the automatic measurement of full-field displacements. Although ideal in the mathematical description, the Fourier transform method has several practical limitations, such as the lack of capability of handling discontinuities and requirement of exact integer number of the carrier fringes in the digitized image for digital processing.

The phase shifting method utilizes a series of fringe or phase shifted interferograms to compute the fractional fringe orders. The algorithms were originally implemented for classical interferometry. Recently their applications have been extended for other advanced photomechanics methods such as Moiré and fringe projection to increase the surface contour resolution. Experimentally a series of three intensity distributions with a uniform phase shift $\pi/2$ is recorded. The three intensity

measurements may be expressed as

$$
\begin{aligned}
I_1(x,y) &= I_m(x,y) + I_a(x,y)\cos\left[\phi(x,y) + \frac{1}{4}\pi\right] \\
I_2(x,y) &= I_m(x,y) + I_a(x,y)\cos\left[\phi(x,y) + \frac{3}{4}\pi\right] \\
I_3(x,y) &= I_m(x,y) + I_a(x,y)\cos\left[\phi(x,y) + \frac{5}{4}\pi\right],
\end{aligned}
\tag{2.17}
$$

where I is the recorded intensity, x, y are spatial variables, I_m is the average intensity (background), $I_a(x,y)$ is the intensity modulation, and $\phi(x,y)$ is the phase to be determined. The phase at each point is then simply

$$
\phi(x,y) = \arctan\frac{I_3(x,y) - I_2(x,y)}{I_1(x,y) - I_2(x,y)}.
\tag{2.18}
$$

For a phase shift other than $\pi/2$, the phase can be calculated using

$$
\phi(x,y) = \arctan\left(\frac{1 - \cos(\alpha)}{\sin(\alpha)}\frac{I_1(x,y) - I_3(x,y)}{2I_2(x,y) - I_1(x,y) - I_3(x,y)}\right),
\tag{2.19}
$$

where phase shifts of $-\alpha$, 0 and α are assumed.

For a more accurate phase calculation, algorithms using five phase shifted imaged have been developed. The five different intensities are obtained with a symmetric phase shift as

$$
\begin{aligned}
I_1(x,y) &= I_m(x,y) + I_a(x,y)\cos[\phi(x,y) - 2\delta] \\
I_2(x,y) &= I_m(x,y) + I_a(x,y)\cos[\phi(x,y) - \delta] \\
I_3(x,y) &= I_m(x,y) + I_a(x,y)\cos[\phi(x,y)] \\
I_4(x,y) &= I_m(x,y) + I_a(x,y)\cos[\phi(x,y) + \delta] \\
I_5(x,y) &= I_m(x,y) + I_a(x,y)\cos[\phi(x,y) + 2\delta].
\end{aligned}
\tag{2.20}
$$

The phase is given by

$$
\phi(x,y) = \arctan\left[\frac{1 - \cos\delta}{\sin\delta}\frac{I_2(x,y) - I_4(x,y)}{2I_3(x,y) - I_1(x,y) - I_5(x,y)}\right].
\tag{2.21}
$$

If $\delta = \pi/2$,

$$
\phi(x,y) = \arctan\frac{I_2(x,y) - I_4(x,y)}{2I_3(x,y) - I_1(x,y) - I_5(x,y)}.
\tag{2.22}
$$

This algorithm was developed to diminish the cases of denominators with zero or near zero values, and thus to reduce uncertainties in the phase calculation.

With the phase shifting method, uncertainties in phase determination are present when the phase shifting amount δ is not correctly introduced during the measurement. When the three-step algorithm is used, the phase is more sensitive to the phase shift error. Small errors in the phase shift result in significant overestimation or underestimation of the phase. Using more phase steps, the errors in the phase shift can be smoothed out, which produces more stable results. Considering the computational time, the widely used four-frame phase-shifting is selected for this thesis and its details will be presented in Section 3.3.3.

2.6.2 Phase Unwrapping Algorithm

The phase information extracted at each pixel is wrapped within the range of $[-\pi, \pi]$ due to the operation of ARCTAN function. Phase unwrapping is the process in which the absolute value of the phase angle of a continuous function that extends over a range of more than 2π (relative to a predefined starting point) is recovered. Phase unwrapping is illustrated in Figure 2.14.
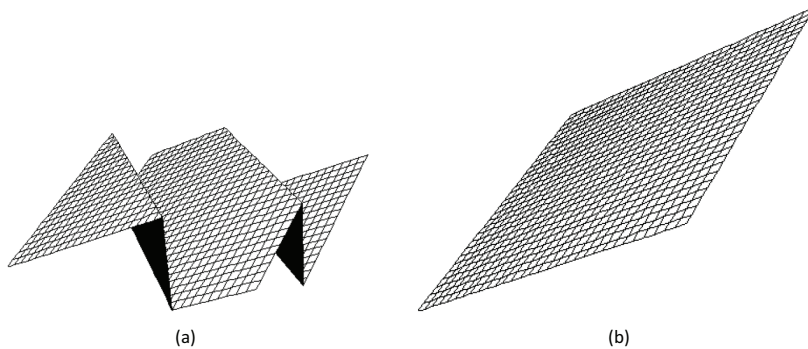
Figure 2.14: Wrapped and unwrapped phase for a linearly changing displacement field: (a) wrapped phase, (b) unwrapped phase (Wang, 2003).

Numerous of phase unwrapping algorithms have been developed and categorized into two categories, path-following algorithms and least-squares algorithms. Path-following algorithms use localized pixel-by-pixel operations to unwrap the phase, while least-squares algorithms minimize a global measure of the differences between the gradients of the input wrapped phase and those of the unwrapped solution. For example, the Quality-guided algorithm (Xu and Cumming, 1996) and the Flynn's minimum discontinuity algorithm (Flynn, 1997) are two typical path-following approaches. The Quality-guided algorithm relies completely on a quality map to determine the order in which the phase data are unwrapped. It begins at a "seed" pixel and "grows" a region of unwrapped pixels, beginning with the highest-quality pixels and ending with the lowest -quality. The resulting unwrapping path depends on the quality map. The best results have been obtained with quality

maps defined by the correlation coefficients or phase derivative variances.

The Flynn's minimum discontinuity algorithm works with or without a quality map. It finds the unwrapped surface that is congruent to the unwrapped phase and whose discontinuities (neighboring pixels whose difference exceeds π radians in magnitude) are minimal in some sense. The algorithm utilizes a tree-growing approach that traces paths of discontinuities in the intermediate unwrapped surface, detects the paths that form loops, and adds multiples of 2π to the phase values enclosed by the loops to reduce the number of discontinuities. It performs this process iteratively until no more loops are detected. The process is guaranteed to converge to an optimal solution.

The path-following algorithms work well when the original wrapped phase values do not have any path inconsistencies (as is the case in virtually all practical 2D problems). Inconsistencies are present when multiples of 2π cannot be added to each wrapped phase sample over a 2D grid to eliminate all adjacent phase differences greater than π radians in magnitude. Least-squares algorithms were developed to attack path-integral discrepancies in a robust manner. Pre-conditioned conjugate gradient (PCG) method (Ghiglia and Romero, 1994) uses fast cosine transforms for 2D unweighed least-squares phase unwrapping and iterative techniques for weighted least-squares phase unwrapping in the case of regional phase noise, aliasing or measurement error, etc.

The choice of algorithm in practice depends on the characteristics of the phase data at hand. In this thesis all three algorithms mentioned above have been tested. The PCG least-squares phase unwrapping algorithm provided the best performance and will be introduced in detail in Section 3.3.4.

2.6.3   Carrier Removal Technique

In fringe projection profilometry, a carrier fringe pattern is projected onto an object surface to encode depth information. A deformed fringe pattern captured by CCD camera can be expressed more realistically as

$$I(x,y) = I_m(x,y) + I_a(x,y)\cos\left[2\pi f(x,y) + \phi(x,y)\right], \tag{2.23}$$

where f is the frequency of the carrier fringe. The continuous phase distribution retrieved by the phase unwrapping process contains both shape-related phases $\phi(x,y)$ and carrier fringe-related phase components $2\pi f(x,y)$. Hence the carrier must be removed from the overall phase distribution for evaluation of the phase, ϕ, of interest.

A number of carrier-removal techniques have been developed, such as spectrum-shift, average-slope, plane-fitting, reference-subtraction, phase-mapping, and series-expansion methods. Depending on the linearity of the carrier phase function $2\pi f(x, y)$, the carrier can be classified into two types: linear carrier with $f(x, y)$ being a first-order function of x or y, and nonlinear carrier with $f(x, y)$ being a higher-order function of x or y. Furthermore, if $f(x, y)$ is related to only x or y, i.e., the carrier fringe is in a specific direction, then it is called a one-dimensional (1-D) carrier; if $f(x, y)$ is related to both x and y, i.e., the carrier fringe is in an arbitrary direction, then it is called two-dimensional (2-D) carrier.

The average-slope approach removes the carrier's phases by subtracting the first derivative (average slope) from an unwrapped phase map. It is applicable to 1-D carrier only. The reference-subtraction approach requires individual measurement of an object and a reference plane. The unwrapped phase maps of the object and reference plane are calculated. The reference phase map contains only the carrier phase component, while the object phase map has both carrier and shape-related phases. Subsequently, the subtraction of the reference phase map from the object phase map gives the phase distribution of the object profile. This method is robust whatever features of a carrier (1-D or 2-D, linear or nonlinear) are obtained by measurement of the reference plane. Hence the method is generally applicable to diverse systems geometries. However the disadvantages of using two sets of recordings hinders application on measurements that require a high data-recording speed. Another undesirable outcome of reference subtraction is that the phase measurement uncertainty is doubled in the subtraction process.

Table 2.1: A comparison of carrier-removal techniques (Quan et al., 2006).

Technique	1-D	2-D	Linear	Nonlinear	Measurement uncertainty	No. of measurements
Spectrum shift	Y	Y	Y	N	Not affected	1
Average slope	Y	N	Y	N	Not affected	1
Plane fitting	Y	Y	Y	N	Not affected	1
Reference subtraction	Y	Y	Y	Y	Magnified	2
Phase mapping	Y	N	Y	Y	Magnified	1
Series expansion	Y	Y	Y	Y	Not affected	1

Table 2.1 shows a comparison of the capabilities of the various carrier-removal techniques. It can be seen that except for the average-slope and phase-mapping approaches, all the other techniques are capable of removing 2-D carriers. Among the techniques that can handle nonlinear carriers, only the series-expansion method does not magnify the phase measurement uncertainty. Generally, if the Fourier-transform method is used to retrieve a phase map and a linear carrier is inherent in

the system geometry, the spectrum-shift approach should be applied for carrier removal because it requires minimal additional computation. If the phase-shifting algorithm is used to extract phase data, the plane-fitting approach becomes a better choice, since a least squares fitting process is normally faster and more accurate than the process of Fourier transform, filtering, and inverse Fourier transform.

In a parallel illumination setup, the carrier phase component is usually linear, and the projected fringes maintain equal spacing. The illumination from an LCD projector is nonparallel (divergent for large objects and convergent for small objects), and fringe spacing is not constant. As far as a nonlinear carrier is concerned, the series-expansion method is considered first, as it outperforms other techniques in several aspects, such as experimental simplicity, accuracy, and automation. A major advantage of the series-expansion approach is that it is generally applicable to different measurement geometries. It also enables a high level of automation that requires little manual intervention. Furthermore, as a series function instead of measurement data is subtracted from the overall phase distribution, the measurement uncertainty will not be affected. However, the series-expansion method is valid only when phase data on a reference plane are retrievable or the measured object has a self-reference. Details of applying the series-expansion technique for carrier phase removal will be described in Section 3.3.5.

Chapter 3

Experimental Studies

This chapter describes the experimental setup and the procedures to examine wrinkle onset and measure wrinkle profiles in rectangular thin membranes under uniaxial tension loading. The properties of the silicone membrane is characterized. The fringe projection method, four-frame phase-shifting technique, PCG phase unwrapping algorithm and series-expansion carrier removal approach are integrated as one inclusive method for non-contact full-field measurement of wrinkling profiles. Membranes of different dimensions were investigated at different levels of tensile strain.

3.1   Membrane Material

Many kinds of dielectric elastomers were pre-selected as membrane candidates, such as polyurethane, polyethylene (LDPE, HDPE and UHMW), polyester (PET), fluoropolymer (PFA, FEP, PTFE and PVDF), and rubber (latex rubber and silicone rubber). After some preliminary tests, the silicone rubber sheets provided by Specialty Silicone Fabricators (Paso Robles, CA) were selected for our study because it has

1. Appropriate thickness. The thickness has to be sufficiently small for membrane structures to exhibit surface instability since the bending stiffness is greatly dependent on the thickness of shell-like structures. However, very thin membranes tend to fold when peeled off from a rigid plastic carrier due to self-adhesion and electrostatic forces, and thus causes difficulty in controlling the unstressed morphology.

2. Low Young's modulus and negligible plasticity and viscoelasticity. Membranes with low Young's modulus have small bending stiffness and thus easily get wrinkled. Our study focuses on the elastic deformation and tries to avoid irreversible wrinkling due to plastic deformation.

3. Appropriate optical properties to provide good sensitivity and accuracy to the optical shape measurement. The ideal surface would be opaquely white and non-reflective for the fringe

projection method.

4. Good dielectric properties. The concept of suppressing wrinkling instability by dielectric actuation will be introduced in Chapter 6. This actuation effect requires membrane material to have large dielectric constant and high breakdown strength.

Table 3.1: Material certification of silicone (SSF-MLTN-950) supplied by Specialty Silicone Fabricators (Paso Robles, CA).

Description	Test results	Units	Specification limits	
			Low	High
Specific gravity	1.14	N/A	1.11	1.16
Durometer[1]	45	Shore A[2]	45	55
Tensile strength	1404	PSI	1000	N/A
Elongation	673	%	400	N/A
Tear strength	218	PPI	200	N/A

[a]Durometer is one of several ways to indicate the hardness of a material, defined as the material's resistance to permanent indentation.

[b]There are several scales of durometer, used for materials with different properties. The two most common scales, using slightly different measurement systems, are the ASTM D2240 type A and type D scales. The A scale is for softer plastics, while the D scale is for harder ones. However, the ASTM D2240-00 testing standard calls for a total of 12 scales, depending on the intended use; types A, B, C, D, DO, E, M, O, OO, OOO, OOO-S, and R. Each scale results in a value between 0 and 100, with higher values indicating a harder material.

Silicone rubber (SSF-MLTN-950, Specialty Silicone Fabricators, Inc.) membranes of thickness ranging from 0.002 inch to 0.05 inch (0.05 mm to 2.00 mm) are available. They are supplied with protective covers on both sides. On one side a rigid plastic sheet is attached as a carrier to keep the silicone film from getting tangled up and stuck together, while on the other side a soft nonsticky plastic film is covered to keep the exposed surface from dust or scratches. Also on this side the rolling direction can be recognized by observing the surface texture (parallel fine lines). Table 3.1 lists several material properties provided by the material vendor. Preliminary tests on different thicknesses showed that 0.004 inch (0.1 mm) is an appropriate thickness for this study. All the membranes are 0.004 inch thick in this study unless specified otherwise. Samples of dimension 20 mm long, 6 mm wide were cut in two orthogonal directions, the rolling direction and the direction normal to it, in order to check for anisotropy.

Figure 3.1 shows the results of the uniaxial tensile test performed on an INSTRON material testing machine at a constant strain rate, 0.01 s^{-1}.[1] In Figure 3.1(a) samples cut in both directions were loaded up to 40% strain and then unloaded. Rubber-like nonlinear material behavior is observed

---

[1]The strain-rate dependence of the stress-strain curve was not tested. However the strain-rate of 0.01 s^{-1} is sufficiently small to achieve repeatability.
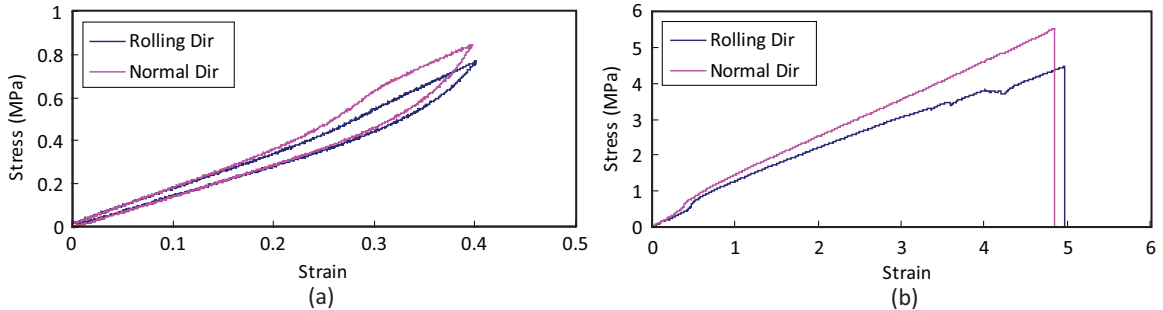
Figure 3.1: Uniaxial tensile test results for silicone rubber (a) tensile strain up to 40%, (b) tensile strain up to failure.

with hysteresis loops between the loading and unloading curves indicating the Mullins effect of the silicone rubber. In Figure 3.1(b) samples cut in both directions were loaded up to failure. Within a larger strain range, the silicone behaves more like a linear elastic material with the rolling direction slightly less stiffer than its orthogonal direction. A linear fit of the stress-strain curve yields the Young's modulus, and Poisson's ratio is determined by evaluating the compressibility of the silicone in ABAQUS using the same set of tensile test data. The details will be discussed in Section 4.4.1. The material properties determined from these tests form the basis of the material models in the later finite element analysis.

3.2   Uniaxial Tension Testbed

3.2.1   Design and Structural Details

A frame was designed and fabricated in polycarbonate to conduct uniaxial tension test on rectangular membranes. For measurement convenience and to avoid sag due to gravity, the membranes are clamped in the vertical plane and stretched upright as shown in Figure 3.2. The clamping boundary condition is enforced on the two short edges of the membrane. Each edge is sandwiched by a pair of grip pads with double-sided adhesive tape attached on interior side and screws fastened from exterior side to ensure that no slippage occurs. The upper grip (moving edge grip) is pinned to a threaded rod through three pin holes as shown in Figure 3.3(a). When the membrane is loaded, the two arms of the upper grip are guided by the side rails to keep the load in-plane. The lower grip (fixed edge grip) is mounted on a supporting unit which is carried by a frictionless linear guide (NDN 1-30.20, Schneeberger) enabling it to glide smoothly to minimize the unwanted shear stress due to misalignment in the mounting process, as shown schematically in Figure 3.3(b). The side rails are graduated so that the tensile strain can be determined from the initial and final position

of the moving edge of the membrane. The design drawings of the testbed is attached in Appendix A.

(a)   (b)
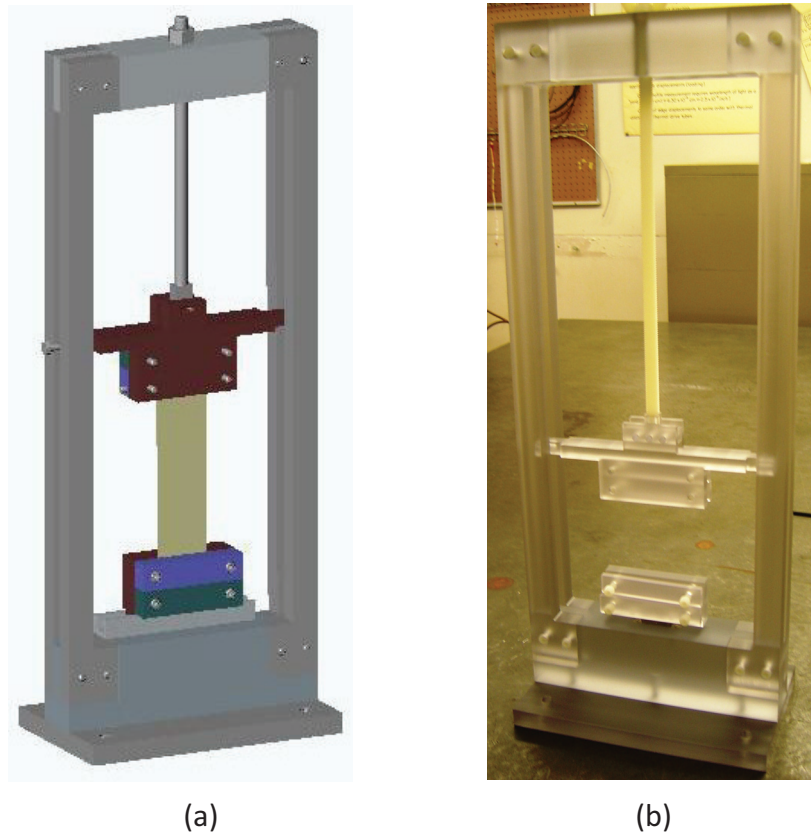
Figure 3.2: The uniaxial tension testbed: (a) 3D schematic assembly drawing, (b) photograph of the apparatus fabricated in polycarbonate.

3.2.2 Membrane Set-up

Membranes were first cut into rectangular shapes using a paper cutter before being peeled off from the carrier. The two short edges were then sandwiched between a pair of plastic strips with double-side tape adhered from both interior sides. The plastic strip was tailored to be a little longer than the membrane width and 10 mm wide, as shown in Figure 3.4. To prevent the membrane from slipping out when stretched, membrane edges were stapled together with the plastic strips. These steps prepare the membrane with rigid edges and make the mounting easier. Next, the membrane sample was mounted on the testbed by clamping the rigid portion with the upper and lower grips. The whole process of preparing and mounting the sample took many attempts because the silicone membrane is very soft and slightly adhesive. Imperfect initial configuration caused by misalignment at the boundary can alter the loading path and wrinkle pattern.
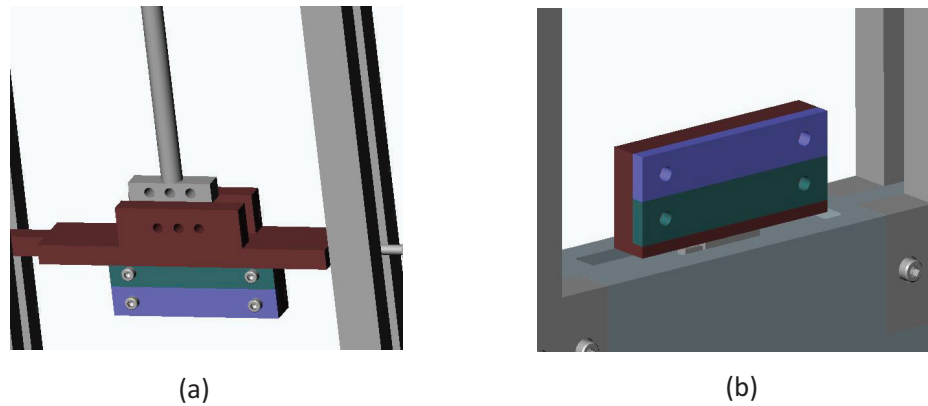
Figure 3.3: (a) The upper and (b) the lower grips.

Figure 3.4: A 101.6×50.8 mm (4×2 inch) membrane sample.

3.2.3 Experimental Procedure

At the beginning of a test, several load-unload cycles were performed to verify that the membrane was still within its elastic range and that no slippage had occurred in the clamping grips. The check was first performed by simple visual inspection, then by optical measurement. It was found that the membranes exhibit more consistent elastic characteristics after being pre-stretched in a few load cycles. After a few initial load cycles, the membrane was loaded. The continuous membrane behavior was recorded in video using a CCD camera (UP-2000, Uniq). At several designated displacement levels (usually every 0.5 inch or 12.7 mm), the out-of-plane displacement was measured.

3.3 Measurement of Wrinkles

3.3.1 Optical system
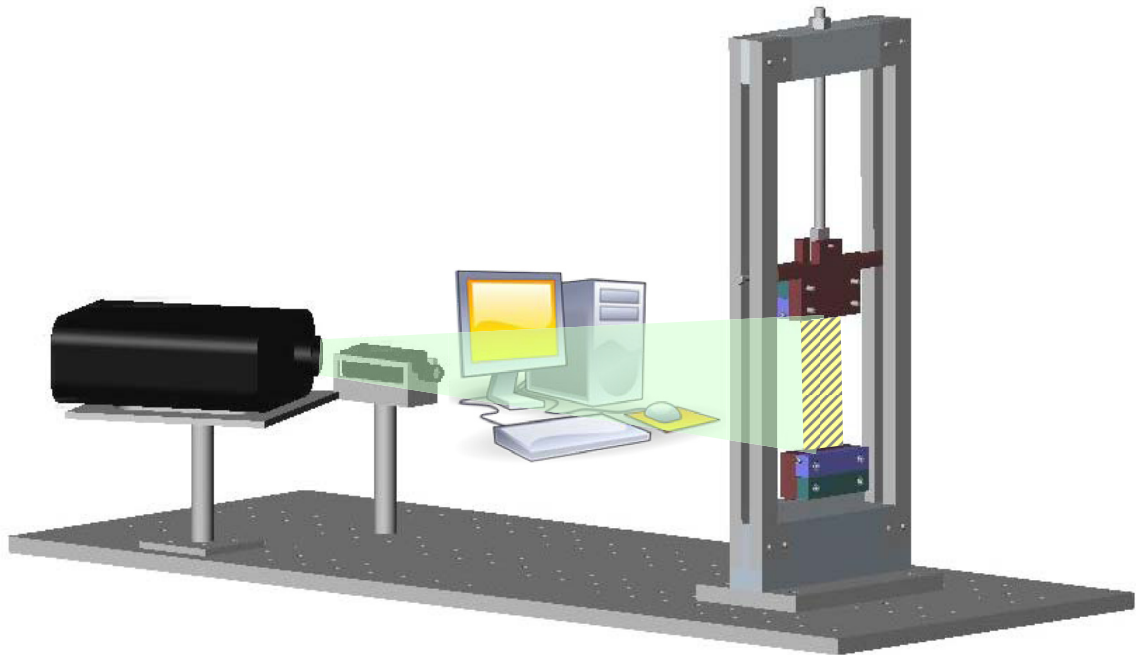
Figure 3.5: A schematic of the experimental setup.

As we discussed earlier in Section 2.6, the fringe projection method was selected for measuring the wrinkle profile. An optical system was assembled comprising of a CCD camera facing the membrane and a LCD projector (EP719, Optoma) projecting from a certain angle, as shown in Figure 3.5. The CCD provides a resolution of 1620×1236 pixels and 16 Hz frame rate. A lens (18-55mm f/3.5-5.6G ED AF-S DX, Nikon) is mounted on the CCD camera to provide adaptable focus and aperture. The

video signal from the CCD camera is received by a digital frame grabber card (R3-CL, Bitflow) and can be displayed on a monitor. The system uses transmitted, white-light illumination generated by a 100 W incandescent light bulb. The LCD projector provides a resolution of 1024×768 pixels, each of which can be set to a relative transparency of $0 - 255$. The matrix display builds up configurable fringe patterns for projection and the fringes can be as small as 1×1 pixel for measurement of small objects.

3.3.2 Fringe Projection Method
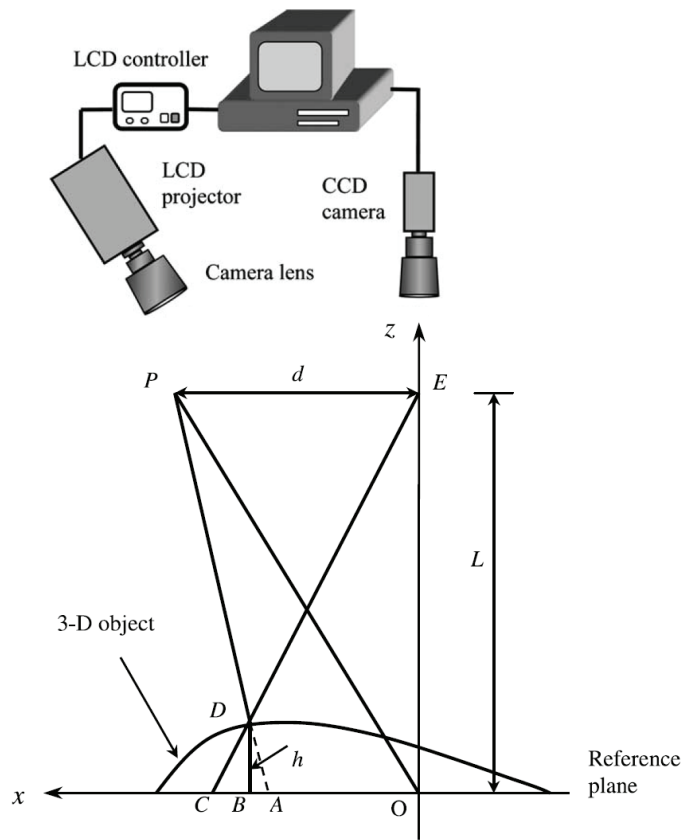
Figure 3.6: The geometry of the optical system for fringe projection method (Quan et al., 2001).

Figure 3.6 shows the optical geometry for projection and imaging system used in the experiment. Points P and E are the center of the exit pupils for projection and the imaging optics respectively. If the distance between the camera and the object reference plane is large compared to the pitch of projected fringes and under normal viewing conditions, the phase and height relationship is readily

derived using the well-known method of triangulation (Quan et al., 2001),

$$h(x,y) = \frac{L}{d}\overline{AC} = \frac{L}{d}\frac{\phi(x,y)}{2\pi f} = k\phi(x,y), \tag{3.1}$$

where L is the distance between the camera and the reference plane, d is the distance between the camera and projector, f is the spatial frequency of the projected fringes in the reference plane, $k = L/(2d\pi f)$ is the coefficient related to the configuration of the optical measuring system and $\phi(x,y)$ is the phase which contains the surface out-of-plane deformation information.

The sensitivity of the system depends on the angle between the axes of the projector and the camera, and the direction from which the fringes are projected. In general the sensitivity increases with the angle. An increase in the angle would however create shadow areas on the object, e.g., behind a crest on a wrinkled membrane. In the experiment, an angle of $30°$ was chosen for the measurement. The fringes were projected to the membrane surface in the direction of $\pm 45°$ to the wrinkles, which were found to be aligned with the tensile load. The projector was placed at a position with minimal distance from the object within its focal range such that the resolution of the projection is optimized. The distance between the camera and the object can be adjusted to attain the desired field of view. Every adjustment of the position of any optical component was followed by a recalibration of the optical system. For better consistency, the configuration of the optical system was fixed for all the tests and the parameters listed in Table 3.2 were achieved for the measurement.

Table 3.2: Summary of measurement parameters.

Field of view	400×300 mm
Spatial resolution	$200\ \mu\text{m/pixel}$
Resolution of measurement	$10\ \mu\text{m}$ (1/10 of the membrane thickness)
Range of measurement	0-5 mm
Dynamic/static measurement?	static or quasi-static

3.3.3 Phase-shifting Technique

To obtain the phase at each pixel $\phi(x,y)$ on the membrane surface we used the four-frame phase-shifting technique. As shown in Figure 3.7 four phase-shifted sinusoidal fringe patterns with phase shifts of 0, $\pi/2, \pi$ and $3\pi/2$ within one period of the fringe were generated in MATLAB, displayed as images slides in computer, projected onto the object surface as seen in Figure 3.8 and captured by the CCD camera.

The following equations describe the four successive intensity distributions from frames with
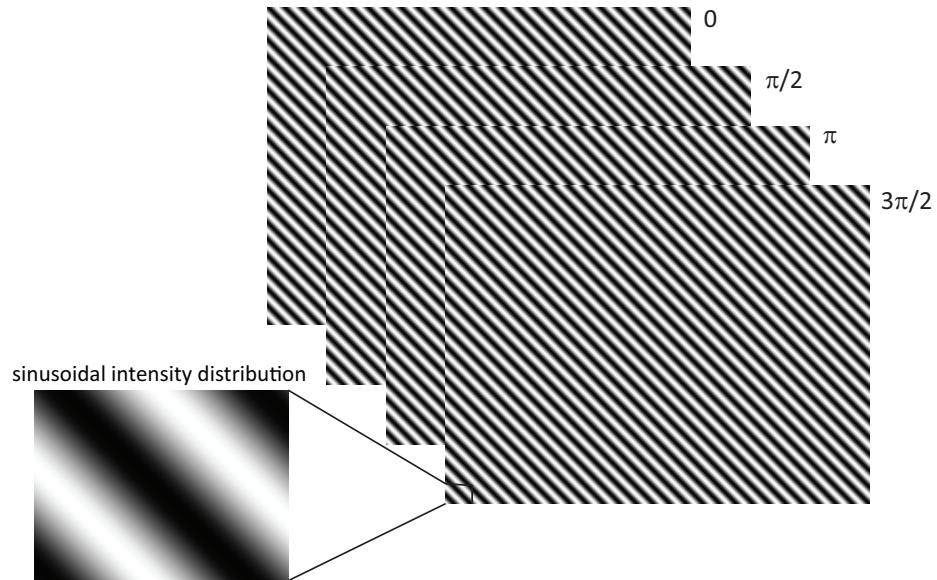
Figure 3.7: Four fringe patterns with sinusoidal intensity distribution and $\pi/2$ phase shift.
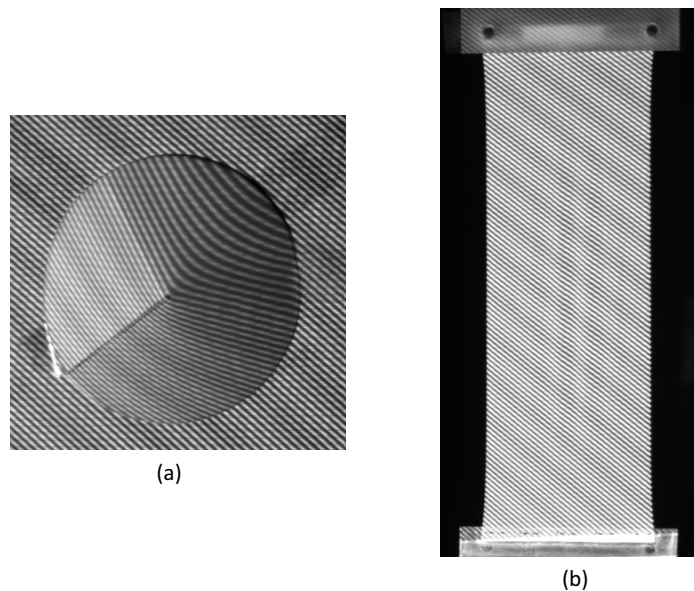
Figure 3.8: Fringes projected onto (a) a cone of known shape on a reference plane (for later calibration), (b) a 254×101.6 mm (10×4 inch) membrane sample on the testbed subjected to 10% strain.

phase shift between each frame:

$$
\begin{aligned}
I_1(x,y) &= I_m(x,y) + I_a(x,y)\cos\left[\phi(x,y)\right] \\
I_2(x,y) &= I_m(x,y) + I_a(x,y)\cos\left[\phi(x,y) + \pi/2\right] \\
I_3(x,y) &= I_m(x,y) + I_a(x,y)\cos\left[\phi(x,y) + \pi\right] \\
I_4(x,y) &= I_m(x,y) + I_a(x,y)\cos\left[\phi(x,y) + 3\pi/2\right], &(3.2)
\end{aligned}
$$

where $I_m(x,y)$ is the average intensity (background), $I_a(x,y)$ is the intensity modulation, and $\phi(x,y)$ is the phase to be determined. By solving the above four equations simultaneously the phase at each detecting point (x,y) in the image can be obtained.

$$
\psi(x,y)^1 = \arctan\frac{I_4(x,y) - I_2(x,y)}{I_1(x,y) - I_3(x,y)}. \tag{3.3}
$$

Figures 3.9 and 3.10 illustrate the wrapped phase of the cone and the wrinkled membrane corresponding to their configurations in Figure 3.8 (a) and (b) respectively. It is noted that periodic 2π discontinuities exist throughout the phase map.
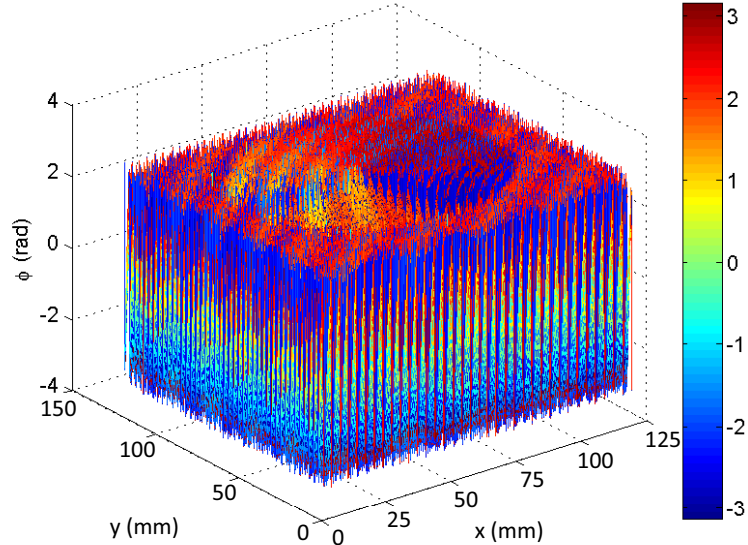
Figure 3.9: Wrapped phase of the cone on a reference plane (Figure 3.8(a)) in the range $[-\pi, \pi]$.

Since phase calculation by the computer gives principal values ranging from $-\pi$ to π, the phase distribution is wrapped into this range and consequently, has discontinuities with 2π phase jumps for

---

[1] ψ is principal values of ϕ in $[-\pi, \pi]$.
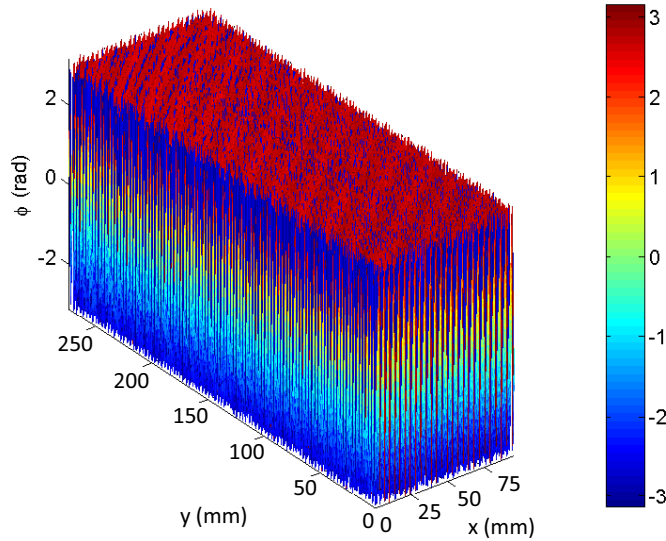
Figure 3.10: Wrapped phase of the 254×101.6 mm (10×4 inch) membrane (Figure 3.8(b)) under 10% strain in the range $[-\pi, \pi]$.

variations larger than 2π. These discontinuities can be corrected by phase unwrapping algorithms.

3.3.4 Phase Unwrapping Algorithm

Given the wrapped phase values $\psi_{i,j}$[1], we wish to determine the unwrapped phase values $\phi_{i,j}$ at the same grid locations by applying a phase unwrapping algorithm. The three typical two-dimensional phase unwrapping algorithms introduced in Section 2.6.2 were tried and the best performance was given by the PCG method.

The PCG method looks for $\phi_{i,j}$ such that the phase differences of $\phi_{i,j}$ agree with those of $\psi_{i,j}$ in the least-squares sense. We define a wrapping operator W that wraps all values of its argument into the range $(-\pi, \pi)$ by adding or subtracting an integer number of 2π rad from its argument. Therefore, for example, $W\{\phi_{i,j}\} = \psi_{i,j}$.

Next we compute two sets of phase differences: those differences with respect to the i index and those with respect to the j index. Specifically, from our known values of the wrapped phase $\psi_{i,j}$, we

---

[1]i, j are used instead of x, y mentioned in the previous section for indexing the pixel.

compute the following wrapped phase differences:

$$
\begin{aligned}
\Delta_{i,j}^{x} &= W\{\psi_{i+1,j} - \psi_{i,j}\}, \quad i = 0...M - 2, j = 0...N - 1, \\
\Delta_{i,j}^{x} &= 0, \quad \text{otherwise;}
\end{aligned}
\tag{3.4}
$$

$$
\begin{aligned}
\Delta_{i,j}^{y} &= W\{\psi_{i,j+1} - \psi_{i,j}\}, \quad i = 0...M - 1, j = 0...N - 2, \\
\Delta_{i,j}^{y} &= 0, \quad \text{otherwise;}
\end{aligned}
\tag{3.5}
$$

where the x and y superscripts refer to differences in the i and j indices, respectively. The solution, $\phi_{i,j}$, that minimizes

$$
\sum_{i=0}^{M-2} \sum_{j=0}^{N-1} (\phi_{i+1,j} - \phi_{i,j} - \Delta_{i,j}^{x})^2 + \sum_{i=0}^{M-1} \sum_{j=0}^{N-2} (\phi_{i,j+1} - \phi_{i,j} - \Delta_{i,j}^{y})^2,
\tag{3.6}
$$

is the least-squares solution.

The solution to the least-squares phase unwrapping problem above is given by the following linear equation:

$$
\phi_{i+1,j} + \phi_{i-1,j} + \phi_{i,j+1} + \phi_{i,j-1} - 4\phi_{i,j} = \Delta_{i,j}^{x} - \Delta_{i-1,j}^{x} + \Delta_{i,j}^{y} - \Delta_{i,j-1}^{y}.
\tag{3.7}
$$

A simple manipulation of Eq. (3.7) yields

$$
(\phi_{i+1,j} - 2\phi_{i,j} + \phi{i-1,j}) + (\phi_{i,j+1} - 2\phi_{i,j} + \phi_{i,j-1}) = \rho_{i,j},
\tag{3.8}
$$

where

$$
\rho_{i,j} = (\Delta_{i,j}^{x} - \Delta_{i-1,j}^{x}) + (\Delta_{i,j}^{y} - \Delta_{i,j-1}^{y}).
\tag{3.9}
$$

Eq. (3.8) is a discretization of Poisson's equation on a rectangular $M \times N$ grid,

$$
\frac{\partial^2}{\partial x^2} \phi(x, y) + \frac{\partial^2}{\partial y^2} \phi(x, y) = \rho(x, y).
\tag{3.10}
$$

It is important to note that Eq. (3.8) is valid for all indices on the rectangular grid, $i = 0...M-1, j = 0...N - 1$, and that the appropriate phase differences that are used to compute $\rho_{i,j}$ in Eq. (3.9) are nonzero only if they come from phases entirely within the rectangular grid. This requirement results directly from the least squares formulation and forms the discrete equivalent of the imposition of

Neumann boundary conditions on Poisson's equation. Specifically we require that

$$\Delta^x_{-1,j} = 0, \quad \Delta^x_{M-1,j} = 0, \quad j = 0...N-1, \tag{3.11}$$

$$\Delta^y_{i,-1} = 0, \quad \Delta^y_{i,N-1} = 0, \quad i = 0...M-1. \tag{3.12}$$

To solve Eq. (3.7) we use a specific form of a cosine expansion that leads to a fast discrete cosine transform (DCT) implementation. A specific form of the 2D discrete cosine transform pair is as follows.

Forward 2D DCT:

$$C_{m,n} = \begin{cases} \sum_{i=0}^{M-1} \sum_{j=0}^{N-1} 4x_{i,j} \cos\left[\frac{\pi}{2M}m(2i+1)\right]\left[\frac{\pi}{2N}n(2j+1)\right], \\ \qquad 0 \leq m \leq M-1; \ 0 \leq n \leq N-1 \\ 0 \quad \text{otherwise.} \end{cases} \tag{3.13}$$

Inverse 2D DCT:

$$x_{i,j} = \begin{cases} \frac{1}{MN} \sum_{m=0}^{M-1} \sum_{n=0}^{N-1} w_1(m)w_2(n)C_{m,n} \cos\left[\frac{\pi}{2M}m(2i+1)\right] \cos\left[\frac{\pi}{2N}n(2j+1)\right], \\ \qquad 0 \leq i \leq M-1; \ 0 \leq j \leq N-1 \\ 0 \quad \text{otherwise.} \end{cases}$$

$$w_1(m) = 1/2, \quad m = 0,$$
$$w_1(m) = 1, \quad 1 \leq m \leq M-1,$$
$$w_2(m) = 1/2, \quad n = 0,$$
$$w_2(m) = 1, \quad 1 \leq n \leq N-1. \tag{3.14}$$

The above cosine expansion imposes the Neumann boundary conditions, $\nabla\phi \cdot \mathbf{n} = 0$, automatically and leads to the exact solution of Eq. (3.8) as shown below.

Let us expand the desired solution $\phi_{i,j}$ in the form of Eq. (3.14):

$$\phi_{i,j} = \frac{1}{MN} \sum_{m=0}^{M-1} \sum_{n=0}^{N-1} w_1(m)w_2(n)\hat{\phi}_{m,n} \cos\left[\frac{\pi}{2M}m(2i+1)\right] \cos\left[\frac{\pi}{2N}n(2j+1)\right], \tag{3.15}$$

and substitute Eq. (3.15) into Eq. (3.7). Performing a similar expansion and substitution for the right-hand side of Eq. (3.8) and rearranging the result yields the following exact solution in the DCT domain:

$$\hat{\phi} = \frac{\hat{\rho}_{i,j}}{2\left(\cos\frac{\pi i}{M} + \cos\frac{\pi j}{N} - 2\right)}. \tag{3.16}$$

Now the unwrapped phase $\phi_{i,j}$ is easily obtained by the inverse DCT of Eq. (3.16).

It is easily shown by simple substitution that the expansion given by Eq. (3.15) automatically imposes the discrete equivalent of the required Neumann boundary conditions:

$$
\begin{aligned}
\phi_{0,j} - \phi_{-1,j} &= 0, \\
\phi_{M,j} - \phi_{M-1,j} &= 0, \quad j = 0...N-1; \\
\phi_{i,0} - \phi_{i,-1} &= 0, \\
\phi_{i,N} - \phi_{i,N-1} &= 0, \quad i = 0...M-1;
\end{aligned}
\tag{3.17}
$$

The 2D unweighted phase unwrapping algorithm is summarized as follows:

1. Perform the 2D forward DCT (Eq. (3.13)) of the array of values, $\rho_{i,j}$, computed by Eq. (3.9), to yield the 2D DCT values $\hat{\rho}_{i,j}$.

2. Modify the values $\hat{\rho}_{i,j}$ (Eq. (3.16)) to obtain $\hat{\phi}_{i,j}$.

3. Perform the 2D inverse DCT (Eq. (3.14)) of $\hat{\phi}_{i,j}$ to obtain the least-squares unwrapped phase values $\phi_{i,j}$.
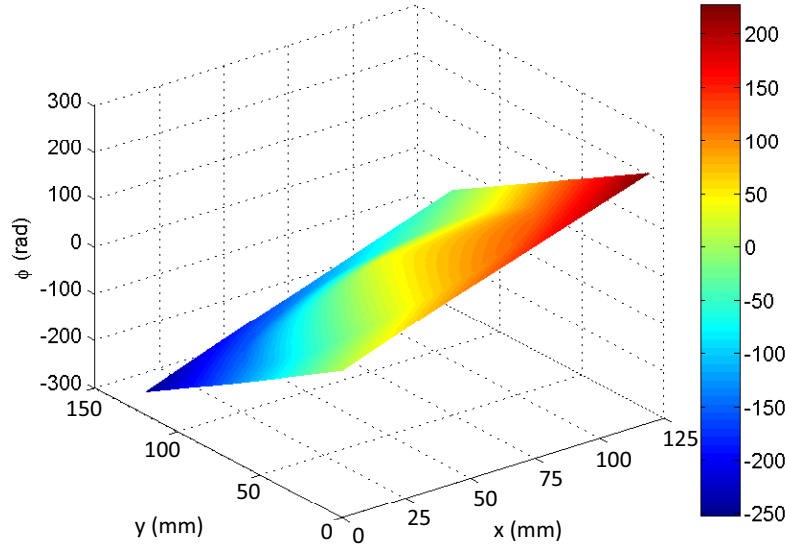
Figure 3.11: Unwrapped phase of the cone (Figure 3.9) on a reference plane.

Figures 3.11 and 3.12 demonstrated the unwrapped phase map of the cone and the 254×101.6 mm (10×4 inch) membrane under 10% tensile strain. The 2π discontinuities have been corrected
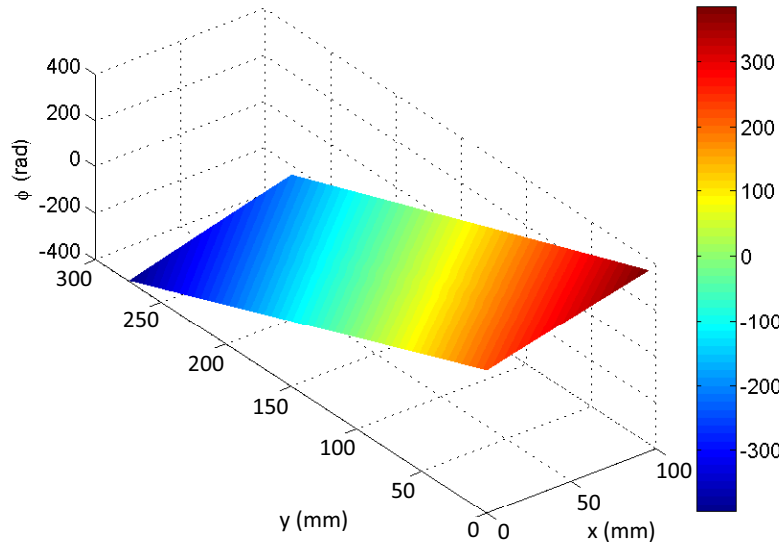
Figure 3.12: Unwrapped phase of the 254×101.6 mm (10×4 inch) membrane (Figure 3.10) wrinkled under 10% strain.

and continuous phase planes are obtained. However the height of the object is not ready to be calibrated according to Eq. (3.1) yet. A nonlinear carrier which originates from the divergent or uncollimated illumination of the projector has to be removed.

3.3.5 Carrier Removal Technique

To cope with the nonlinear carrier problem, the series-expansion technique (Quan et al., 2006) is used to remove the carrier's phase from the unwrapped phase map. The rigorous mathematical expression of a nonlinear carrier is normally complicated and related to various system geometrical parameters. Therefore, it is impossible to quantify unknown geometrical parameters directly. However, it is found that a carrier function can be approximated by a series expansion

$$
\begin{aligned}
\phi_c(x,y) \quad &= a_{0,0} &&+ a_{0,1}x &&+ ... &&+ a_{0,N-1}x^{N-1} &&+ a_{0,N}x^N \\
&+ a_{1,0}y &&+ a_{1,1}xy &&+ ... \\
&+ ... &&+ ... &&+ ... \\
&+ a_{N-1,0}y^{N-1} &&+ a_{N-1,1}xy^{N-1} \\
&+ a_{N,0}y^N,
\end{aligned}
\tag{3.18}
$$

where $a_{m,n}$ are coefficients of elements in the series. Eq. (3.18) is a series expansion of a 2-D carrier. This indicates that whatever the form of a specific carrier function, it can be estimated by fitting a series function to experimentally obtain the phase data on a reference plane. Hence, the quantification of geometrical parameters in various situations can be unified into a simple process of fitting a curved surface (2-D carrier). In Eq. (3.18) the mathematical expression for a curved surface of the Nth order has $(N+1)(N+2)/2$ unknown coefficients. The terms that carry the form $x^{px}y^{py}$ (px and py represent the power of x and y, respectively) take into account the rotation in the direction of the carrier fringes and distinguish the surface fitting from a simple combination of the line fittings in the x and y directions individually. An error function is defined as

$$E_c(a_{0,0}, ..., a_{0,N}, ..., a_{N,0}) = \sum_{(x,y) \in U} \left[\phi_c(x,y) - \phi_{c,\exp}(x,y) \right]^2, \qquad (3.19)$$

where ϕ_c represents the series, U denotes the domain of all points on the reference plane and $\phi_{c,\exp}(x,y)$ refers to the experimentally obtained unwrapped phase value. To minimize the error, the partial derivatives of E_c with respect to each of the unknown coefficients are set to zero. This will produce $(N+1)(N+2)/2$ equations, from which the unknowns can be solved. On substituting the calculated coefficients into Eq. (3.18), one can obtain the estimated carrier phase function in terms of the minimum error. When the carrier phases are subtracted from the overall phase distribution, the carrier phase component is removed.

A higher value of N would provide a better approximation to the nonlinear carrier. However, it should be noted that beyond a certain value of N, the carrier estimation accuracy will not improve any further, since subsequent improvement would be smaller than phase measurement uncertainty. From the study of Chen and Tay (2006), it was found that second-order ($N = 2$) curve fitting provides sufficient accuracy for most applications. It is important to note that data points used for the estimation of the carrier function should be in the vicinity of the reference plane. Hence this would require a certain degree of human intervention to distinguish the reference plane from the test object.

A MATLAB function was developed for $N = 2$ based on the above mechanism. It first displays the image of the object captured by the CCD camera and then requests the user to select the region of interest within which the data points are used for the estimation of the carrier function, and the vicinity is considered as the reference plane or self-reference. Two examples are shown in Figure 3.13. For the cone on a reference plane, a polygon box was drawn to enclose the circumference around the base of the cone tangentially. For the wrinkled membrane, no flat reference plane was placed beneath it. However it was found that membranes neither wrinkle near the two clamped edges nor at the two free edges. Hence a rectangular box can be drawn to separate a narrow joint

border area from the central region of the membrane.

(a)   (b)
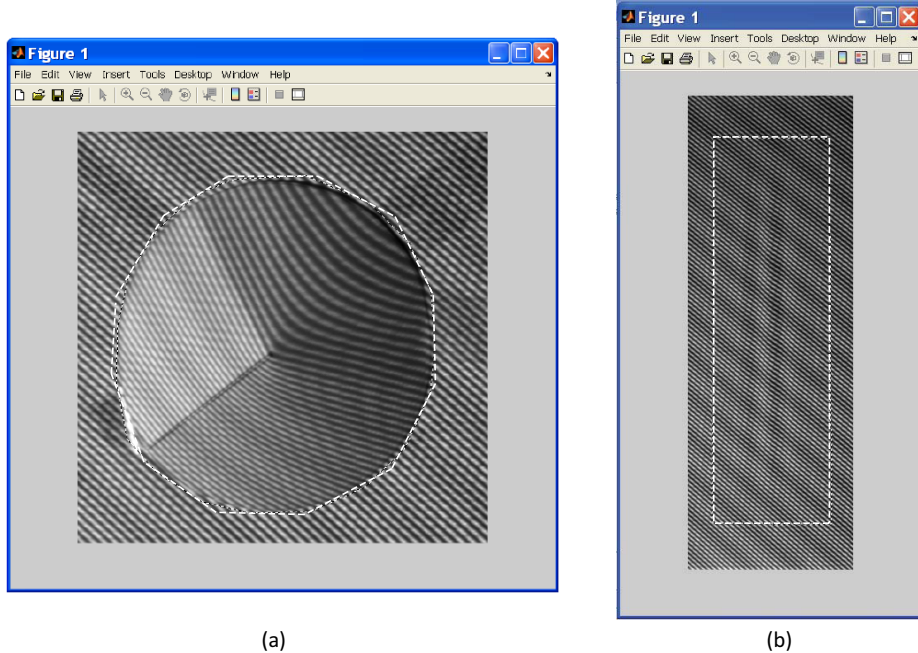
Figure 3.13: Selection of region for the estimation of the carrier phase using polygon tools in MAT-LAB, (a) the standard cone on a reference plane (Figure 3.8(a)), (b) the 254×101.6 mm (10×4 inch) membrane (Figure 3.8(b)) partially wrinkled under 10% tensile strain.

The carrier's phases extracted using the series-expansion method for the two examples are shown in Figures 3.14 and 3.15, which were then subtracted from the unwrapped phase map (Figures 3.11 and 3.12) to obtain the genuine phase information. Figures 3.16 and 3.17 illustrate the phases of the cone and the membrane, which reflect the real shape of the objects.

3.3.6   Calibration Process

The last step of the optical measurement is to find the proportionality k in Eq. (3.1), which relates the height of the object to the phase with carrier removed. One way of calibrating is to shift the object itself by a known distance and measure the corresponding phase change. In this work, however, calibration was achieved by measuring a standard object with known dimensions. A standard cone of diameter 92.8 mm and height 25.4 mm was used for calibrating both the in-plane and out-of-plane shape. By multiplying the calibration coefficient k with the phase, eventually the surface profile of the cone and the membrane were obtained as a 3D contour map as shown in Figures 3.18 and 3.19.

To evaluate the performance of the integrated optical method, a cross-sectional plot of the cone is shown in Figure 3.20. Accuracy on the order of 0.01 mm was achieved, which is sufficient for the
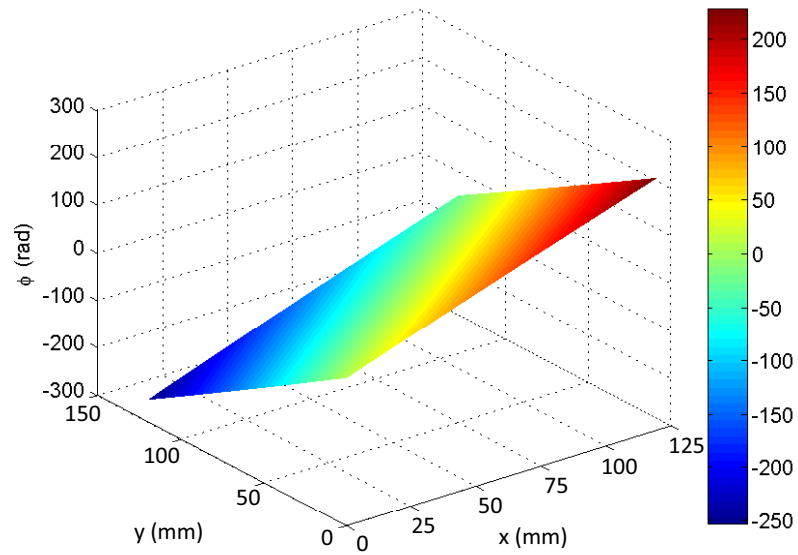
Figure 3.14: Carrier phase of the cone (Figure 3.13(a)) on a reference plane.
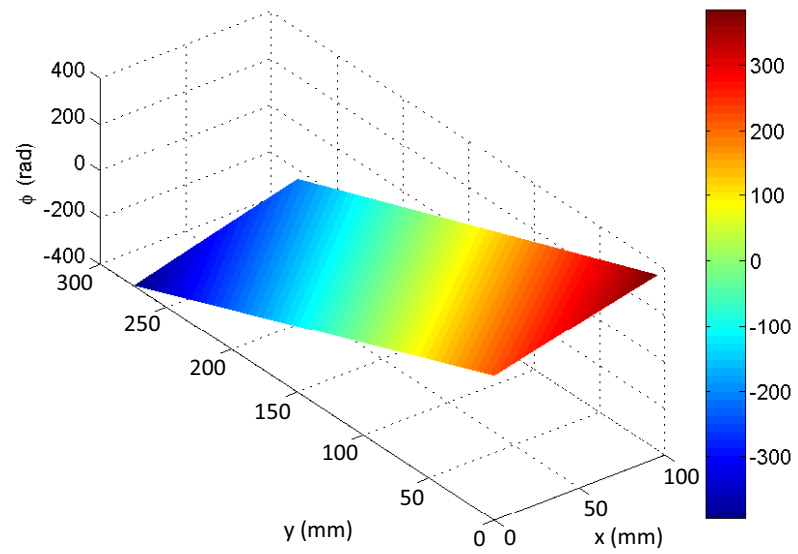
Figure 3.15: Carrier phase of the 254×101.6 mm (10×4 inch) membrane (Figure 3.13(b)) wrinkled under 10% strain.
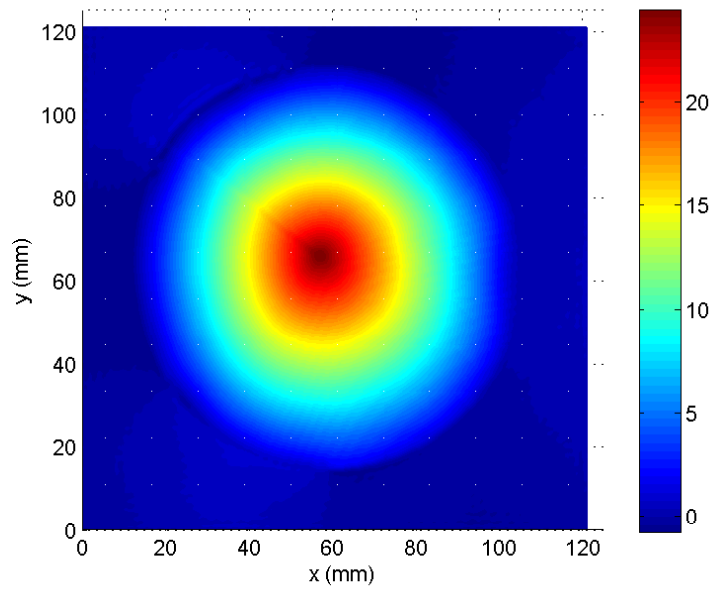
Figure 3.16: Phase of the cone (Figure 3.13(a)) on a reference plane after removal of the carrier - top view.
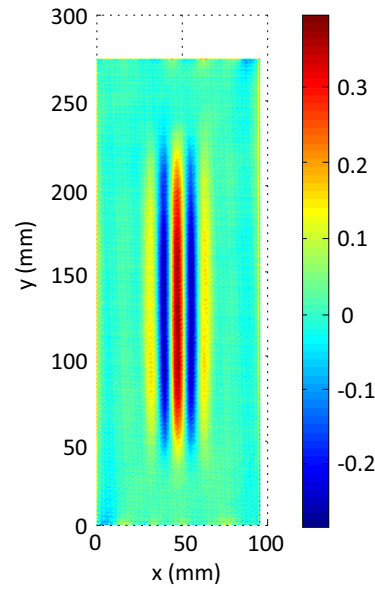
Figure 3.17: Phase of the 254×101.6 mm (10×4 inch) membrane (Figure 3.13(b)) wrinkled under 10% strain after removal of the carrier - top view.
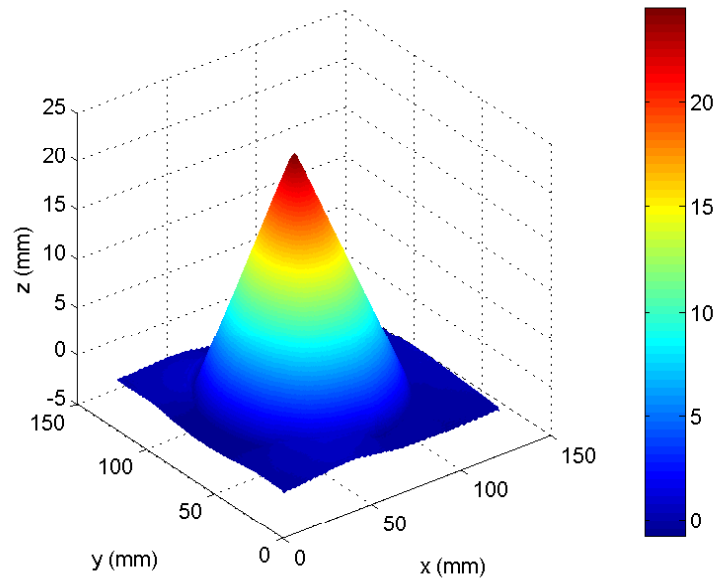
Figure 3.18: Shape of the cone (Figure 3.13(a)) on a reference plane after calibration.
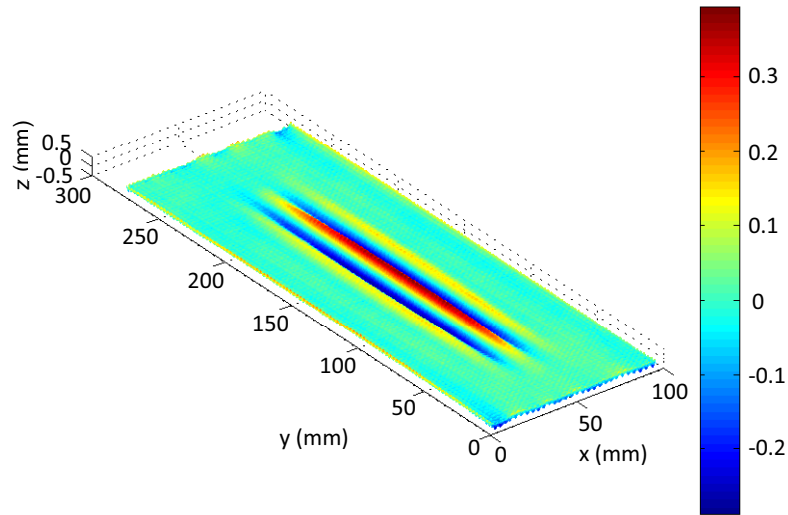
Figure 3.19: Shape of the 254.6 mm (10×4 inch) membrane (Figure 3.13(b)) wrinkled under strain 10%.

study of 0.1 mm membranes. The accuracy can be improved by reducing the pitch of the fringes. However there is a trade-off between the resolution of measurement and the field of view. In order to capture finer fringes in good contrast and avoid Moiré effects, the CCD camera has to be placed closer to the object and record images of a smaller area rather than a full-field.
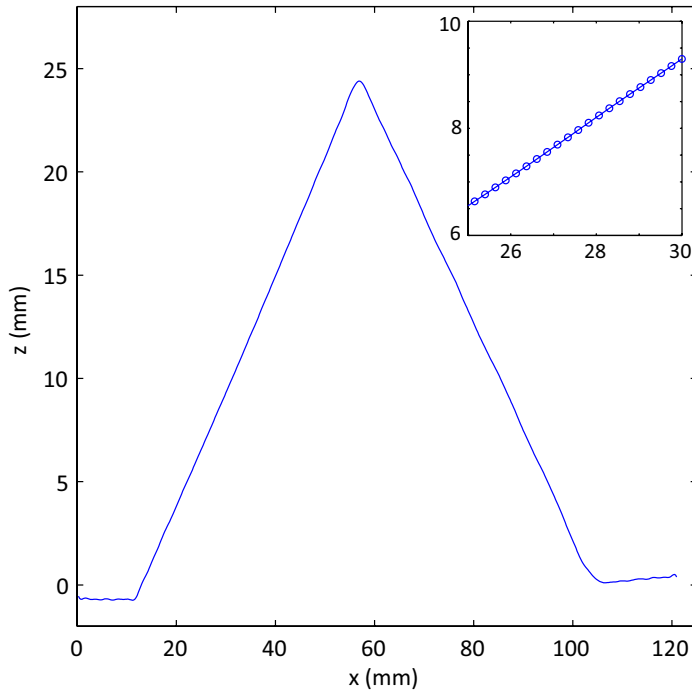
Figure 3.20: Cross section of the cone through the apex.

3.4   Observations

3.4.1   Wrinkle Onset

One interesting question that arises with regard to thin membrane structures is their critical buckling load, which quantitatively describes the resistance of the membrane structure to external loading. In our study the "load" is represented by the tensile strain applied to the membrane, and thus *critical buckling strain* is used instead.

Membrane samples of 27 different in-plane dimensions and uniform thickness of 0.004 inch (0.1 mm) were tested on the uniaxial tension testbed. Ideally the initial configuration of an unstressed membrane is a flat plane, but in reality it is usually partially taut and partially slack due to the imperfections induced in the sample preparation and mounting stages, and the viscous relaxation

from previous loading cycles. This is especially true for large membranes, which appeared to wrinkle immediately after the tensile load was applied. Whereas small membranes became taut and flat once being stressed longitudinally and remained free of wrinkles as they were stretched. Therefore, it was difficult to determine the strain at which the first wrinkle forms. Instead, we qualitatively compared the wrinkling onset among the membranes of different dimensions in Figure 3.21.
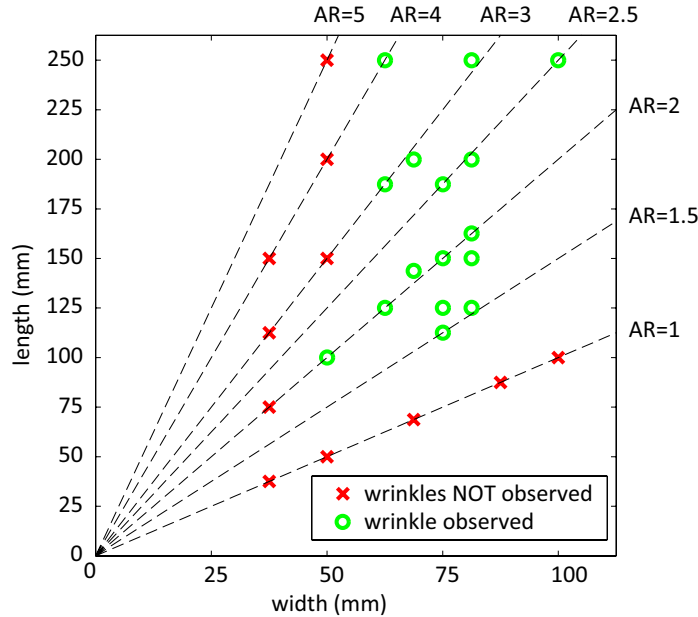
Figure 3.21: Wrinkling onset for membranes of 27 different in-plane dimensions (AR=Aspect Ratio).

Evidence of wrinkling onset is marked at each dimension tested. The green circles represent the dimensions that wrinkled as the tension load was applied; while the red crosses represent the dimensions on which wrinkling was not observed and the membrane surface stayed flat up to 100% strain. The dashed lines of different slopes divide the dimension map into different aspect ratio zones so that one can understand the effect of both the membrane size and the aspect ratio on the wrinkling onset.

At fixed aspect ratio, the membranes in larger sizes exhibited lower surface stability than those in smaller sizes, and were more likely to wrinkle. Membranes in intermediate aspect ratio, i.e., $1.5 \leq AR \leq 4$), exhibited lower surface stability than those in extreme aspect ratios, i.e., AR=1 or AR=5, corresponding to the membranes in square shape and slender shape. Among all the wrinkled samples, the smallest one (101.6×50.8 mm or 4×2 inch) had an aspect ratio of 2.

3.4.2 Wrinkle Profile

For each of the 27 membrane samples, a series of measurements were taken at discrete strain levels during the tests. Let us take a close look at the 254×101.6 mm (10×4 inch) membrane, which was the largest sample among those that have been tested and exhibited the largest wrinkle amplitude. The overall wrinkle pattern is shown in Figure 3.22 by plotting a series of contour maps of the full-field[1] out-of-plane displacement at 0% (initial configuration), 5%, 10%, 15%, 20% and 30% strains.[2] Initially the unstressed membrane is slack in the central region and is not flat. Three wrinkles appear right after the membrane is stretched, and align themselves with the loading direction in a symmetric manner with the largest crest in the middle. This pattern and the number of the wrinkles remained unchanged during the entire loading process.
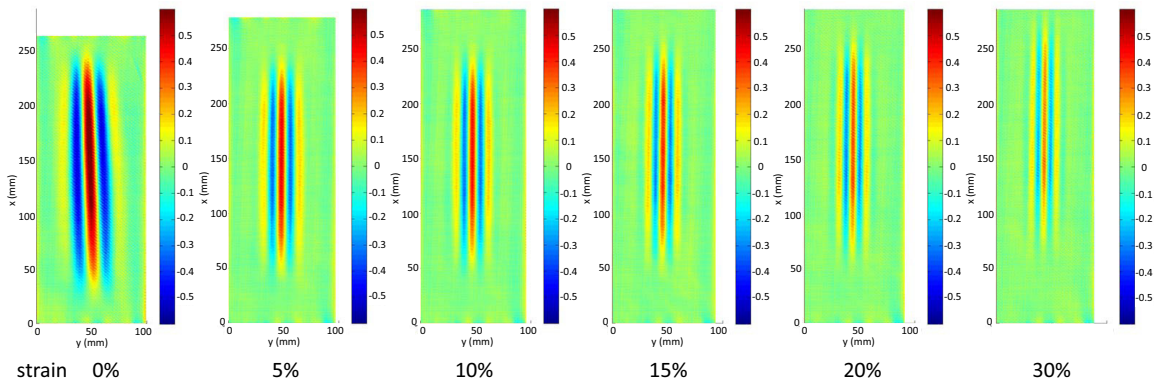
Figure 3.22: Wrinkling profiles of 254×101.6 mm (10×4 inch) membrane under strains up to 30%.

The detailed wrinkle profiles are demonstrated in Figure 3.23 by plotting the cross section along the transverse midplane of the membrane. If the imperfect initial configuration of the membrane is neglected, as the membrane is loaded uniaxially, the wrinkle amplitude suddenly increases and then gradually decreases; whereas the wrinkle wavelength monotonically decreases.

The wrinkles are not of uniform amplitude. Their profiles can be fit into damped sinusoidal functions in the form of $w(x) = A \exp(\beta|x|) \cos(2\pi f x)$, where A is the wrinkle amplitude, β is the damping factor, and f is the frequency. For instance, for the wrinkle profile at 10% strain, $A = 0.46$, $\beta = -0.087$, and $f = 0.076$ as shown in Figure 3.24.

---

[1]At higher strains the upper portion of the membrane was stretched out of the field of view of the CCD camera and thus was not included in the measurement.

[2]Due to the limited length of the side rail, the testbed allows only 30% tensile strain to be applied on the 10 inch (254 mm)long membrane. Also, the field of view of the CCD camera was limited to 400 mm horizontally and 300 mm vertically to achieve good spatial resolution.
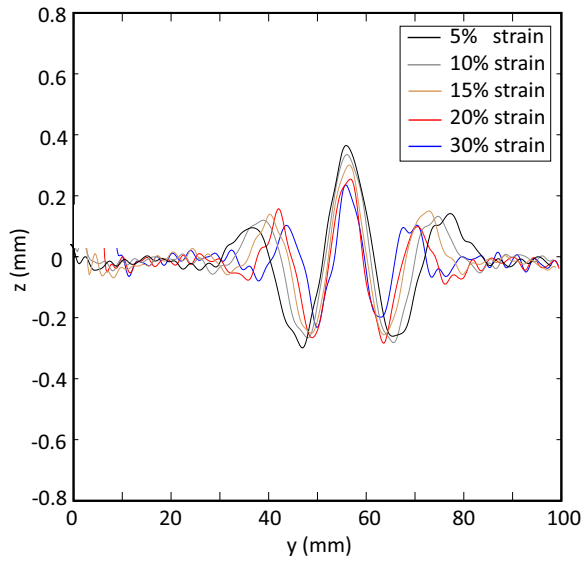
Figure 3.23: Wrinkle profile along the transverse midplane of the 254×101.6 mm (10×4 inch) membrane under several tensile strains.
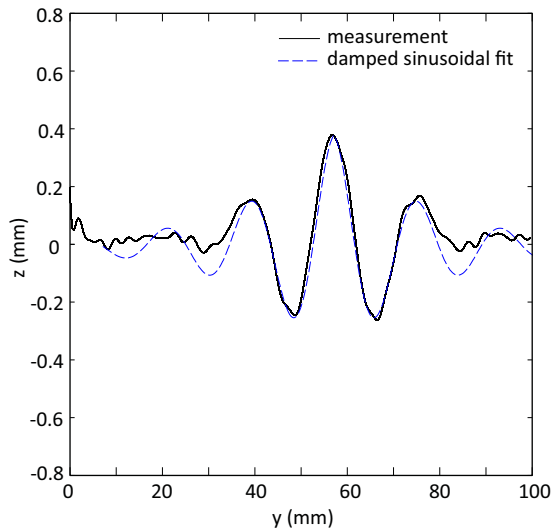
Figure 3.24: The damped sinusoidal fit of the wrinkle profile along the transverse midplane of the 254×101.6 mm (10×4 inch) membrane under 10% tensile strain.

More details of the wrinkles and wrinkle patterns of other membrane dimensions will be revisited and discussed in Chapter 5 when compared with the results from the numerical simulations.

Chapter 4

Numerical Studies

This chapter presents a detailed numerical study of rectangular membranes in uniaxial tension using the commercial finite element software ABAQUS (Hibbitt et al., 2001). This study aims to capture the important characteristics of wrinkling of thin membranes observed in the physical model, using the thin shell finite element model. A three-step analysis is introduced. Preliminary analyses were carried out to address several simulations issues related to modeling of thin silicone membranes, such as material model, element type, mesh density, imperfection sensitivity and stabilizing factor to serve as a benchmark for subsequent analysis. Wrinkle onset and wrinkle profiles of membranes in different dimensions are discussed based on the results of pre-buckling eigenvalue analysis and post-buckling analysis respectively.

4.1   Finite Element Modeling Using ABAQUS

Wrinkling of thin membranes is highly geometrically nonlinear and involves instability in the structure. To simulate this type of problem generally requires a nonlinear solution method and a fully dynamic, transient analysis (or at least a pseudo-dynamic simulation). The main non-linear solution method in ABAQUS is the full Newton-Raphson method. The solution is usually obtained incrementally by solving a sequence of non-linear equilibrium equations with increasing load or displacement. An alternative solution for solving post-buckling snap-through problems is the arc-length method, also known as the modified Riks method in ABAQUS. In this approach, a sequence of equilibrium states is sought in the space defined by the nodal displacement parameters and the loading parameter. Both parameters within each increment are used to obtain equilibrium solutions, instead of only controlling a single load or displacement increment as in the Newton-Raphson method. Previous studies (Wong and Pellegrino, 2006) showed unsuccessful attempts to use the Riks method due to a highly localized instability. Hence monotonic displacement incrementation is the only viable option.

The bending stiffness of a membrane, although small, plays a key role in determining the shape and amplitude of the wrinkles. It is essential that it should be included in any models that aim to capture this kind of detail. Therefore the family of thin shell elements was employed for this study. The specific type of thin shell element will be discussed later in Section 4.4.2.

4.2   Analysis Procedure

The flowchart in Figure 4.1 summarizes the complete simulation procedure.
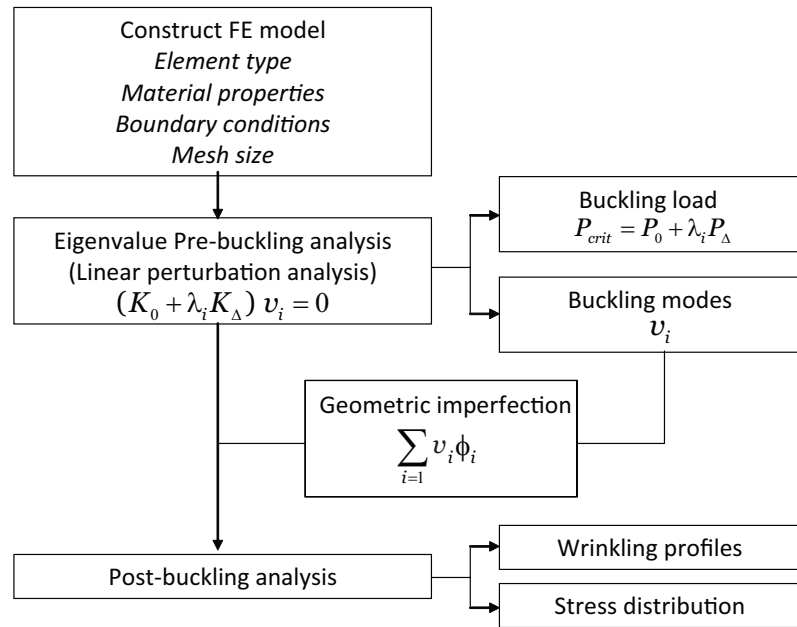
Figure 4.1: Flow chart for wrinkling analysis in ABAQUS.

4.2.1   Initial Conditions

The initial stage of the analysis applies a small uniform prestress to the membrane to stabilize it. The shell elements are thin, hence their bending stiffness is so small that obtaining meaningful results can be a real challenge when in-plane loads are applied. It is important that the amount of prestress applied at this stage should be large enough to successfully steer the subsequent buckling mode analysis, but without significantly affecting the final results.

To apply the prestress, a edge displacement is prescribed to attain the level of prestress required. After applying the initial prestress, a static, geometrically non-linear equilibrium check is performed.

This check allows a small redistribution of the state of prestress, together with small in-plane displacement.

4.2.2 Pre-buckling Eigenvalue Analysis

The next step of the analysis determines the buckling mode-shapes of this lightly pre-stressed membrane. These modes are then used to seed small imperfections that trigger the formation of wrinkles in the subsequent geometrically non-linear analysis.

An eigenvalue buckling analysis in ABAQUS (*BUCKLE) is used to predict the buckling load and possible wrinkling modes of the membrane subject to its actual boundary conditions and loading. Instead of forces, the load here is defined as an edge displacement.

In a general eigenvalue buckling problem we look for the loads for which the model stiffness matrix becomes singular, so that the problem

$$K^{MN}v^M = 0 \tag{4.1}$$

has nontrivial solutions. K^{MN} is the tangent stiffness matrix when the loads are applied; v^M are the nontrivial displacement solutions; M and N refer to degrees of freedom of the whole model. Two eigensolvers are available in ABAQUS to extract the eigenvalues, namely the Subspace iteration and the Lanczos method.

For modeling thin membrane structure, the eigenvalue buckling problem is a little complicated due to the prestress applied in the initial step. A prestress that is not large enough may lead to two consequences: computation fails to converge, or only negative eigenvalues are reported in the eigenvalue buckling analysis. The negative eigenvalues indicate that the structure would buckle if the loads were applied in the opposite direction, e.g., membrane is more likely to buckle when the tensile load is replaced by a compressive one. Such physical negative buckling modes can usually be avoided by applying a sufficiently large preload before the buckling analysis. With Lanzcos eigensolver, one can get positive eigenvalues only by imposing a lower limit to the eigenvalue.

The state of the model at the end of the initial step, during which preload ("dead" loads), P^N, is applied to the membrane as edge displacement, is identified as the base state of the buckling step. The buckling loads are calculated relative to the base state of the structure. An incremental load ("live" load), Q^N, is defined in the eigenvalue buckling prediction step. The magnitude of

this loading is not important; it will be scaled by the load multipliers, λ_i, found in the eigenvalue problem:

$$\left(K_0^{NM} + \lambda_i K_\Delta^{NM}\right) v_i^M = 0, \tag{4.2}$$

where K_0^{NM} is the stiffness matrix corresponding to the base state, which includes the effects of the preloads, P^N if any; K_Δ^{NM} is the differential initial stress and load stiffness matrix due to the incremental loading pattern, Q^N; λ_i are the eigenvalues; v_i^M are the buckling mode shapes (eigenvectors); and i refers to the ith buckling mode. The buckling loads are then

$$P = P^N + \lambda_i Q^N. \tag{4.3}$$

Normally the lowest value of λ_i is of interest. The preload P^N and perturbation load Q^N may be of different types. In this study they are both in the form of edge displacement in the longitudinal direction. The buckling mode shapes v_i are normalized vectors and do not represent actual magnitudes of deformation at critical load. They are normalized so that the maximum displacement component has a magnitude of 1.0. These buckling mode shapes are often the most useful outcome of the eigenvalue analysis since they predict the likely failure mode of the structure.

In an eigenvalue buckling prediction step ABAQUS/Standard first does a static perturbation analysis to determine the incremental stresses, $\Delta\sigma$, due to Q^N. The stiffness matrix K_Δ^{NM} corresponding to $\Delta\sigma$ is then formed. In the eigenvalue extraction portion of the buckling step, the stiffness matrix K_0^{NM} corresponding to the base state geometry is formed. Initial stress and the load stiffness terms due to the preload, P^N, are included and calculated based on the geometry of the base state.

$P^N + \lambda_1 Q^N$ with λ_1 being the lowest eigenvalue generally provide a good estimate for the critical buckling load except for some structures with closely spaced eigenvalues, which can cause numerical problems. A series of closely spaced eigenvalues indicates that the structure is imperfection sensitive. An eigenvalue buckling analysis will not give accurate predictions of the buckling load for imperfection-sensitive structures.

Because buckling analysis is usually done for "stiff" structures, it is not usually necessary to include the effects of geometry change in establishing equilibrium for the base state. However, it was found for some membrane dimensions, the preload has to be large enough in order to obtain positive eigenvalues. In these cases the preload may induce significant geometry change in the base state. Hence geometric nonlinearity feature in ABAQUS (*NLGEOM) is included for the base step and throughout the whole analysis in each simulation.

4.2.3   Post-buckling Analysis

After computing the buckling mode-shapes, a linear combination of some selected eigenmodes is introduced into the structure as a geometric imperfection. The eigenvectors corresponding to the lowest eigenvalues are often those of great interest in a structural analysis, and so normally the imperfections that are seeded in a structure are obtained as linear combinations of these particular eigenvectors. The choice of the imperfection modes that are introduced in the membrane has to be based on the expected, final wrinkling pattern. Hence the chosen eigenmodes should at least resemble the wrinkle pattern that the users aim to predict.

Once the appropriate eigenmodes shapes have been chosen, geometrical imperfections in the form of out-of-plane deformations are introduced using the feature *IMPERFECTION in ABAQUS:

$$\delta z = \sum_i \phi_i v_i \tag{4.4}$$

where v_i is the ith eigenmode and ϕ_i is a scaling factor whose magnitude is chosen as a proportion of the thickness of the membrane. Values between 1% and 100% of the thickness have been used, considering different imperfection magnitudes to test the sensitivity of the predicted response.

A geometrically non-linear (*NLGEOM) incremental analysis is carried out under edge displacement incrementation, using the Newton-Raphson solution method. To go past an instability, a transient analysis was carried out using the stabilize function (*STABILIZE) available in ABAQUS. This option automatically introduces pseudo-inertia and pseudo-viscous forces at all nodes when an instability is detected, and simulates a possible dynamic response of the structure as it snaps in order to obtain the first static equilibrium state after snapping has occurred. Then, instead of continuing with the quasi-static analysis, ABAQUS automatically switches to a dynamic integration of the equations of motion for the structure, thus reducing the likelihood of numerical singularities.

4.3   Description of the Finite Element Model

A finite element model of the rectangular silicone rubber membrane subjected to uniaxial tension was constructed, based on the physical model described in Section 3.2. The dimension and material properties of silicone film determined in Section 3.1 are summarized in Table 4.1. In ABAQUS two sets of units are typically used, SI and SI(mm) as listed in Table 4.2. In our simulation all the prescribed parameters were converted to SI(mm) units before implemented and this set of units has been consistently used.

Table 4.1: Basic parameters of the membrane model.

Parameters	Physical model	Numerical model
Length, L	10 inch	254 mm
Width, W	4 inch	101.6 mm
Thickness, t	0.004 inch	0.1 mm
Young's modulus, E	10^6 Pa	1 MPa
Poisson's ratio, ν	0.5^a	0.5

^{a}The Poisson's ratio is determined by evaluating the compressibility of the material in ABAQUS using the uniaxial tensile test data presented in Section 3.1.

Table 4.2: Two sets of units commonly used in ABAQUS.

Quantity	SI	SI(mm)
Length	m	mm
Force	N	N
Mass	kg	tonne $(10^3$kg)
Time	s	s
Stress	Pa (N/m^2)	MPa (N/mm^2)
Energy	J	mJ $(10^{-3}$J)
Density	kg/m^3	$tonne/mm^3$

Figure 4.2 shows the finite element mesh and the boundary conditions used for a preliminary analysis. It consists of 6477 four noded quadrilateral S4R thin shell elements and each element has an aspect ratio of approximately one. The left edge of the membrane was fully constrained in all its degrees of freedom by using the *BOUNDARY, ENCASTRE option in ABAQUS. On the right edge only the translation in the x-direction was allowed . The top and bottom edges are free edges. This set of boundary conditions remained active in all analysis steps.

4.4   Implementation of Finite Element Analysis

The detailed analysis procedure has been outlined in Section 4.2 and its implementation is given below.

The initial step started by pre-tensioning the membrane by moving the right edge in the x-direction. Then a geometrically non-linear equilibrium check was performed. This displacement plays the role of preload (dead load) ahead of the linear perturbation analysis in order to provide
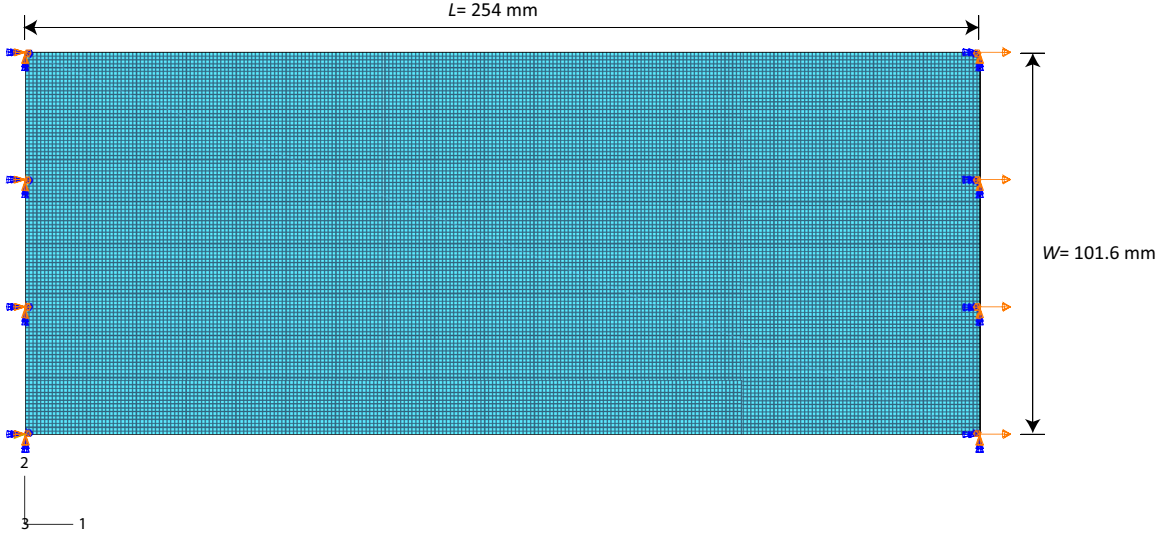
Figure 4.2: The boundary conditions and mesh of the finite element model.

the thin membrane an initial geometric stiffness and enable us to obtain positive eigenvalues. The amount of the preload may vary for different membrane dimensions. The smallest possible preload for each dimension was sought and applied to the model.

In the next step, an eigenvalue buckling analysis, which essentially is a linear perturbation analysis, was carried out with a prescribed horizontal displacement of 1 mm at the right edge as an incremental load (live load). The model boundary conditions were modified in this step by using the *BOUNDARY, OP=MOD option in ABAQUS. The Lanczos solver was set such that only eigenmodes corresponding to the positive eigenvalues are computed.

Several different combinations of eigenmodes and scaling factors were considered to test the sensitivity of the model to the magnitude of the prescribed imperfections to be introduced in the detailed wrinkling analysis. For each set, a complete wrinkling analysis was carried out, which involved the creation of a new input file, with geometrical imperfections seeding to the pristine mesh by the *IMPERFECTION command. The stabilize function was activated to facilitate the solution.

The final step consists of two analysis substeps. The first substep was similar to the initial pretensioning step as described earlier, but this time with the right edge only displaced by 0.1 mm to give an initial prestress of approximately 0.04 MPa. Note that in the initial step, a much higher prestress value was required in order to avoid many localized modes (noise) in the eigenvalue buckling analysis step. However, a smaller prestress was prescribed in the final analysis to provide sufficient initial out-of-plane stiffness to membrane but without affecting the final results. Then in the second

substep, the right edge was translated longitudinally by a prescribed distance to apply the tensile strain, (i.e., 76.2 mm for 30% strain) while all the other degrees of freedom were constrained. An example ABAQUS input file of a complete wrinkling analysis for this model is available in Appendix B.

4.4.1 Material Model

Silicone rubber, like most elastomers (solid, rubberlike materials) has very little compressibility compared to their shear flexibility. ABAQUS provides a powerful tool to evaluate the compressibility of elastomers by incorporating them in hyperelastic material models.

In ABAQUS hyperelastic materials are described in terms of a "strain energy potential", $U(\epsilon)$, which defines the strains energy stored in the material per unit of reference volume (volume in the initial configuration) as a function of the deformation at that point in the material. There are several forms of strain energy potentials available in ABAQUS to model approximately incompressible isotropic elastomers: the Arruda-Boyce form, the Marlow form, the Ogden form, the polynomial form, the reduced polynomial form, the Yeoh form, and the Van der Walls form.

The modified Mooney-Rivlin model is the most typical form in the polynomial class, whose strain energy potential can be expressed as

$$U = \sum_{i+j=1}^{N} C_{ij}(\bar{I}_1 - 3)^i(\bar{I}_2 - 3)^j + \sum_{i=1}^{N} \frac{1}{D_i}(J^{el} - 1)^{2i}, \tag{4.5}$$

where N is a material parameter; C_{ij} and D_i are temperature-dependent material parameters; $\bar{I}_1$ and $\bar{I}_2$ are the first and second deviatoric strain invariants defined as $\bar{I}_1 = \bar{\lambda}_1^2 + \bar{\lambda}_2^2 + \bar{\lambda}_3^2$ and $\bar{I}_2 = \bar{\lambda}_1^{-2} + \bar{\lambda}_2^{-2} + \bar{\lambda}_3^{-2}$, where the deviatoric stretches $\bar{\lambda}_i = J^{-\frac{1}{3}}\lambda_i$ with λ_i being the principal stretches, J being the total volume ratio, and J^{el} being the elastic volume ratio (which equals to J when there is no thermal expansion). The initial shear modulus and bulk modulus are given by

$$\mu_0 = 2(C_{10} + C_{01}), \quad K_0 = \frac{2}{D_1}. \tag{4.6}$$

The modified neo-Hookean model is the simplest (of order 1) form in the reduced polynomial model with strain energy potential,

$$U = \sum_{i=1}^{N} C_{i0}(\bar{I}_1 - 3)^i + \sum_{i=1}^{N} \frac{1}{D_i}(J^{el} - 1)^{2i}, \tag{4.7}$$

where C_{i0} and D_i are temperature-dependent material parameters. The initial shear modulus and

bulk modulus are given by,

$$\mu_0 = 2C_{10}, \quad K_0 = \frac{2}{D_1}. \tag{4.8}$$

Another well-known model is the Ogden form with strain energy potential,

$$U = \sum_{i=1}^{N} \frac{2\mu_i}{\alpha_i^2} (\bar{\lambda}_1^{\alpha_i} + \bar{\lambda}_2^{\alpha_i} + \bar{\lambda}_3^{\alpha_i} - 3) + \sum_{i=1}^{N} \frac{1}{D_i} (J^{el} - 1)^{2i}, \tag{4.9}$$

where μ_i, α_i, and D_i are temperature-dependent material parameters. The initial shear modulus and bulk modulus for the Ogden form are given by,

$$\mu_0 = \sum_{i=1}^{N} \mu_i, \quad K_0 = \frac{2}{D_1}. \tag{4.10}$$

ABAQUS/CAE automatically determines the optimal strain energy potential(s) based on the experimental test data provided, computes all the coefficients in the strain energy potential formula, and creates the stress-strain curve(s) of corresponding hyperelastic model(s) in the same plot with the experimental curve. Usually one needs to obtain test data for the deformation models that are likely to occur in the simulation, and provide more data at the strain magnitudes that the material will be subjected to during the simulation. The four sets of stress-strain data of the silicone rubber from the uniaxial tension test performed in an Instron testing machine, as presented earlier in Figure 3.1, were imported to ABAQUS/CAE *EVALUATION function for four separate evaluations. The evaluation results are shown in Figure 4.3.

All the models except neo-Hookean fit the uniaxial tension test data well within a small strain range ($< 40\%$). Within a large strain range (up to failure strain 500%), the polynomial model of order 1 and 2, and Ogden model of order 2 provide good fit to the experimental data. Among the models which can accurately describe the silicone rubber, the Mooney-Rivlin model is of the simplest form, whose strain energy potential,

$$U_{MR} = C_{10}(\bar{I}_1 - 3) + C_{01}(\bar{I}_2 - 3) + \frac{1}{D}(J^{el} - 1)^2, \tag{4.11}$$

has only three coefficients C_{10}, C_{01} and D. Hence this model is chosen for determination of the Poisson's ratio. From Eq. (4.6), the initial bulk modulus, K_0 and the initial shear modulus, μ_0 can be determined by these coefficients. We can assess the compressibility of the silicone rubber by the ratio in Eq. (4.12), which essentially is the Poisson's ratio of the material,

$$\nu = \frac{3K_0/\nu_0 - 2}{6K_0/\nu_0 + 2}. \tag{4.12}$$
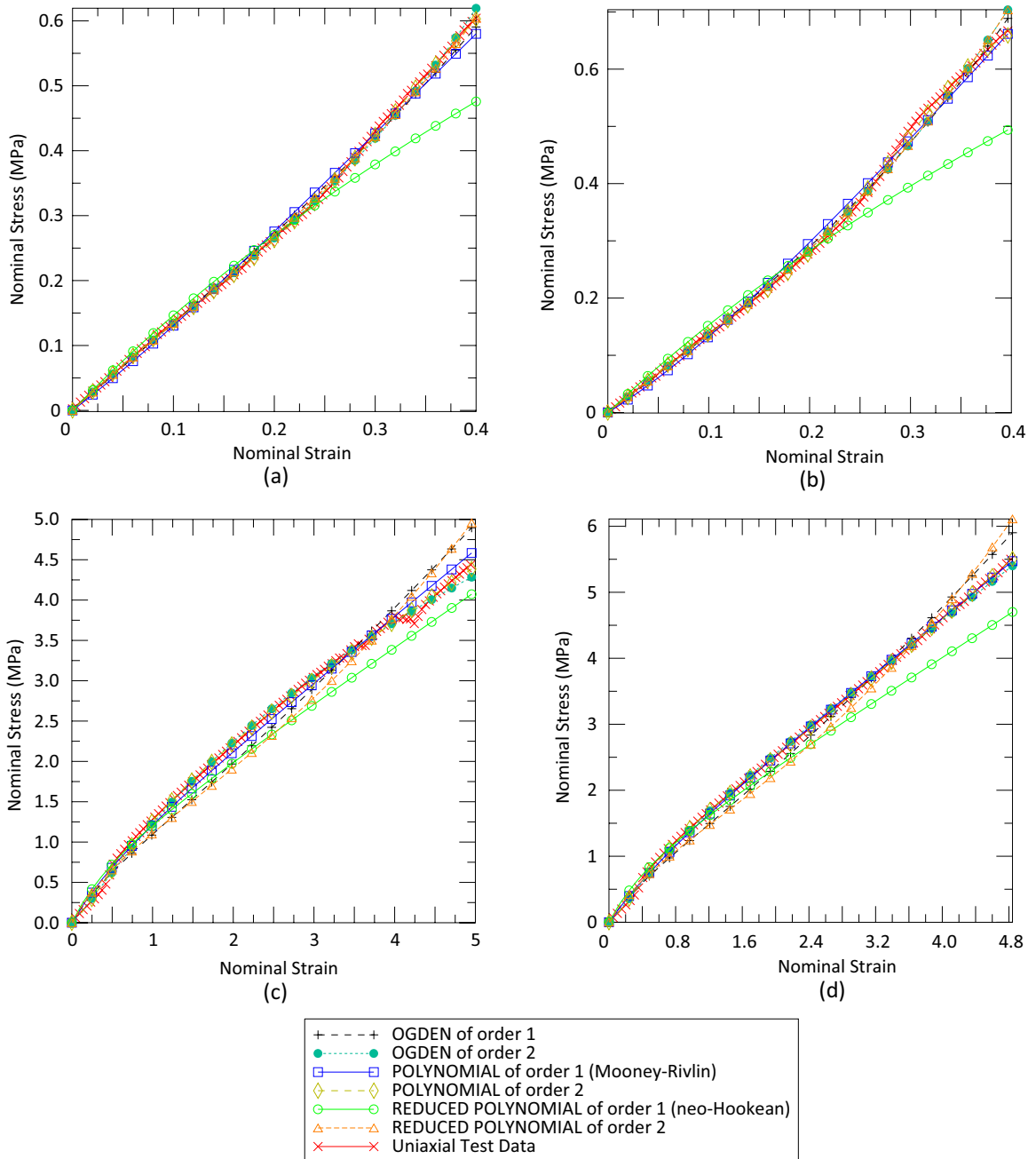
Figure 4.3: Material model evaluation by fitting the experimental stress-strain data of the silicone membrane obtained in uniaxial tension test (a) along the rolling direction up to 40% strain, (b) along the normal direction up to 40% strain, (c) along the rolling direction up to 500% strain, (d) along the normal direction up to 500% strain, into several hyperelastic models provided in ABAQUS.

Table 4.3 lists the evaluation results for the Mooney-Rivlin model, primarily the three coefficients in the strain energy potential and the calculated material properties, based on the four sets of uniaxial tensile test data. A fully incompressible material with Poisson's ratio of 0.5 was suggested.

Table 4.3: Coefficients in the Mooney-Rivlin model evaluated in ABAQUS/CAE and calculated material properties based on four sets of uniaxial tensile test data.

Test		Coefficient			Material parameters		
Direction	Strain range	C_{10}	C_{01}	D	μ_0	K_0	ν
Rolling	0-40%	646111.865	-448263.257	0	395697.216	∞	0.5
Rolling	0-500%	407411.710	-122799.772	0	569223.876	∞	0.5
Normal	0-40%	863076.127	-682611.888	0	360928.478	∞	0.5
Normal	0-500%	507376.129	-214563.479	0	585625.300	∞	0.5

However, when using the Mooney-Rivlin model or any other hyperelastic material model in ABAQUS, it is not possible to assume that the material is fully incompressible because the program has no mechanism for imposing such a constraint at each material calculation point. Instead, we must provide some compressibility. The difficulty is that, in many cases, the actual material behavior provides too little compressibility for the algorithms to work efficiently. By default ABAQUS assumes Poisson's ratio of 0.475. An upper limit of 0.495 is suggested since larger values introduce high frequency noise into the dynamic solution.

In general hyperelastic materials are highly unstable during simulations compared to linear elastic ones. All the attempts of using the evaluated Mooney-Rivlin material model in buckling analysis were unsuccessful. Hence, linearly elastic material model with Young's modulus 1 MPa and Poisson's ratio 0.5 is used for all the numerical simulations in this study.

4.4.2 Element Choice

Another important issue in computational simulations is the selection of element types that are used to discretize the structure. ABAQUS offers a number of structural element types, of which thin shell[1] elements were identified as potential candidates for modeling membrane structures.

ABAQUS provides a number of three dimensional shell elements, which can be classified into two types, conventional shell element and continuum shell element. Conventional shell elements dis-

---

[1]Thin shell refers to the homogeneous shells with thickness less than about 1/15 of a characteristic length on the surface of the shell, such as the distance between supports for a static case or the wavelength of a significant natural mode in dynamic analysis.
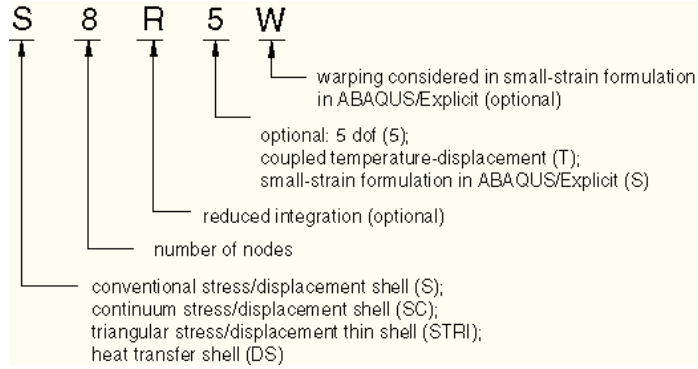
Figure 4.4: Three dimensional shell element name convention in ABAQUS (Hibbitt et al., 2001).

cretize a body by defining the geometry at a reference surface, and have displacement and rotational degrees of freedom. In contrast, continuum shell element discretize an entire three-dimensional body, and have only displacement degrees of freedom. For general purposes, the former provides robust and accurate solutions to most applications.

Conventional shell elements include both finite-strain and small-strain elements. Element types in ABAQUS such as S3, S3R, S4, and S4R account for finite membrane strains and arbitrarily large rotations; therefore, they are suitable for large-strain analysis. Elements S4R5, S8R, S8R5 and S9R5 are provided for shell problems with small membrane strains and arbitrarily large rotations. The small-strain shell elements in ABAQUS provide a computationally efficient alternative to the finite-membrane strain elements for appropriate application although solution accuracy may degrade as membrane strains become large. Depending on the amount of membrane in-plane stretching and compression, problems of shell structures undergoing large-scale buckling behavior may use either of the two types of elements.

Three dimensional shell elements in ABAQUS are named as shown in Figure 4.4. For example, S4R is a 4-node, quadrilateral, stress/displacement shell element with reduced integration and a large-strain formulation; and SC8R is an 8-node, quadrilateral, first-order interpolation, stress/displacement continuum shell element with reduced integration.

Among the three dimensional conventional shell elements provided in ABAQUS/Standard, some use five degrees of freedom (three displacement components and two in-surface rotation components) such as S4R5, S8R5 and S9R5, while others use six degrees of freedom (three displacement components and three rotation components) at all nodes. The elements that use five degrees of freedom can be more economical. However, they are available only as "thin" shells and they cannot be used

for finite-strain applications.

For conventional shell elements in ABAQUS/Standard one must specify a section Poisson's ratio as part of the shell section definition to allow for the shell thickness in finite-strain elements to change as a function of the membrane strain. If the section Poisson't ratio is defined as zero, the shell thickness will remain constant and the elements are therefore suited for small-strain analysis. For typical large-strain applications with rubber-like materials, the section Poisson's ratio should be set to 0.5 (the default value) to reproduce the incompressible response of the material at large plastic or hyperelastic deformation. The change in thickness is ignored for the small-strain shell elements.

Having understood the difference among the the three dimensional thin shell elements, elements S3, S4, S4R, S4R5 and S8R5 were selected as candidates and investigated in preliminary analyses as described in Section 4.2. Table 4.4 summarizes the primary results of both pre-buckling and post-buckling analyses of a 254×101.6 mm (10×4 inch) membrane, based on each type of element.

Table 4.4: Effect of element type on the results of pre-buckling and post-buckling analysis.

Element type	S4R[a]	S4R5	S4	S8R5
No. elements	6477	6477	6477	6477
Critical buckling strain	3.82%	3.27%	3.9%	3.22%
Computation time[b] (s)	1639	3725	3129	6497
No. of wrinkles	3	3	3	3
Amplitude at strain 5% (mm)	0.1720	0.2363	0.1557	0.2378
Amplitude at strain 10% (mm)	0.2912	0.2977	0.2848	0.2961
Maximum amplitude (mm)	0.2938	0.3013	0.2878	0.3000
Strain@$w_{\max}$[c]	11.06%	8.82%	11.17%	8.70%

[a]The S4R element reduces the four integration locations of S4 element to only one integration location.
[b]The time is for the post-buckling analysis only.
[c]$w_{\max}$ is the maximum wrinkle amplitude.

Simulations built with all the four elements produced the same number of wrinkles and approximately the same maximum wrinkle amplitude. The critical buckling strain computed by S4R5 and S8R5 elements is smaller than the one by S4R and S4 elements, as well as the tensile strain at which the maximum wrinkle amplitude was reached. This is not surprising because the S4R5 and S8R5 are both small-strain elements and may underestimate the membrane strain. Consequently they overestimated the wrinkle amplitude at small strain, i.e., 5%. Another problem associated with these small-strain shell elements is that the cross-sectional thickness change is ignored, and thus they are incapable of reproducing thickness strain induced by thermal field or electric field, which will be discussed in Chapter 6. Both the S4R and S4 elements can model fairly accurately and S4R

was chosen since it is computationally more economical. Shell element S3 was also tested, but failed probably because the mesh of 6477 elements was not fine enough. Therefore, S4R was adopted for all following wrinkling analyses.

4.4.3 Mesh Density

To investigate the effect of mesh density on the numerical results, S4R element of different mesh densities were seeded in the model of a 254×101.6 mm (10×4 inch) membrane. In order to properly resolve the wrinkles, the element size had to be at least smaller than the wrinkle half-wavelength. Table 4.5 compares several representative results of both the pre-buckling and post-buckling analyses for different mesh densities.

Table 4.5: Effect of mesh density on the results of pre-buckling and post-buckling analysis.

No. of elements	1600	2890	6477	11492	25908
Computation time[a] (s)	9	20	74	98	233
Critical buckling strain	3.85%	3.72%	3.64%	3.61%	3.59%
Computation time[b] (s)	180	584	1639	2600	5231
No. of wrinkles	3	3	3	3	3
Amplitude at 5% strain (mm)	0.1354	0.1706	0.1720	0.1724	0.1772
Amplitude at 10% strain (mm)	0.2759	0.3091	0.2912	0.2880	0.2942
Maximum amplitude (mm)	0.2800	0.3132	0.2938	0.2921	0.2972
Strain@$w_{\max}$[c]	11.29%	11.41%	11.06%	11.41%	11.29%

[a]This time is for the pre-buckling analysis only.
[b]This time is for the post-buckling analysis only.
[c]$w_{\max}$ is the maximum wrinkle amplitude.

In both the pre- and post-buckling analyzes it was found that the solution becomes mesh-independent after a particular level of refinement. Since the computational time increases roughly proportionally to the number of elements, it would be pointless to use a mesh finer than that in the analysis. Therefore the finite element model comprised of 6477 elements was chosen, whose mesh density is approximately 0.028 mm^{-2} and mesh size is about 35 mm^2. The results presented and discussed in the following sections were all based on this mesh density.

4.4.4 Imperfection Sensitivity

In ABAQUS the exact post-buckling problem often cannot be analyzed directly due to the discontinuous response (bifurcation) at the point of buckling. To analyze a post-buckling problem, it must be converted into a problem with continuous response instead of bifurcation, which can be

accomplished by introducing a geometric imperfection pattern in the perfect geometry so that there is some response in the buckling mode before the critical load is reached.

Imperfections are introduced by perturbations in the geometry. Typically there are two ways to define an imperfection in ABAQUS: a linear superposition of buckling eigenmodes from the displacements of a static analysis or specifying the node number and imperfection values directly. ABAQUS then calculates the normals using the usual algorithm based on the perturbed coordinates. Usually the first approach is used unless the precise shape of an imperfection is known.

The response of some structures depends strongly on the imperfections in the original geometry, particularly if the buckling modes interact after buckling occurs. By adjusting the magnitude of the scaling factors of the various buckling modes, the imperfection sensitivity of the structure can be assessed. Usually (if the structure is not imperfection sensitive) the lowest buckling mode should have the largest factor. The magnitudes of the perturbations used are typically a few percent of a relative structural dimension, i.e., shell thickness. Normally, a number of analyses should be conducted to investigate the sensitivity of a structure to imperfections. Structures with many closely spaced eigenmodes tend to be imperfection sensitive.

In our study it was found in a series of preliminary analyses that the eigenmodes always came in pairs, one is symmetric (about the longitudinal midplane) and the other is antisymmetric, both of which correspond to the same eigenvector. However, the eigenvalues for adjacent pair of eigenmodes are not closely spaced. Prior experimental observations and measurement of wrinkle patterns of membrane in different dimensions may provide us with some insight on choosing the eigenmodes. For example, in experimental studies the 254×101.6 mm (10×4 inch) membrane demonstrated a symmetric wrinkling pattern with the largest wrinkle in the center of the membrane and remained in this pattern during the entire loading process. Hence only the symmetric eigenmode corresponding to the lowest eigenvalue was selected instead of a pair as imperfection. A wide range of scale factors were chosen, from 0.25% to 10% of the membrane thickness t in order to test the sensitivity of the model to the geometric imperfection. For each magnitude, a complete wrinkling simulation was carried out, which involved the creation of a new input file, with geometrical imperfections seeding to the pristine mesh by the *IMPERFECTION command. The stabilize function was activated to facilitate the solution. In Table 4.6 several principal results from the post-buckling analysis are listed and compared.

The maximum wrinkle amplitude and corresponding strain are not sensitive to the magnitude of the geometric imperfection even though the largest scale factor differs from the smallest one by

Table 4.6: Effect of imperfection magnitudes on of results of post-buckling analysis.

Scale factor	$w_{\max}$ (mm)	strain@$w_{\max}$	strain@wrinkle onset
$0.0025t$	0.3000	11.46%	4.0%
$0.01t$	0.2997	11.28%	2.9%
$0.025t$	0.2995	11.58%	2.0%
$0.1t$	0.2972	11.28%	0.8%

two orders of magnitude. Whereas wrinkling onset, characterized by the tensile strain at which the first wrinkle forms, is quite different. Here the formation of wrinkles is defined to be the moment at which the maximum out-of-plane displacement of the membrane surface reaches 1% of the maximum wrinkle amplitude $w_{\max}$. For small imperfection, the deformation is quite small (relative to the imperfection) below the critical load. The response grows quickly near the critical load, introducing a rapid change in behavior. On the other hand, a large imperfection tends to trigger the structural instability at an earlier stage, and the post-buckling response will grow steadily before the critical load is reached. In this case the transition into post-buckled behavior will be smooth and relatively easy to analyze. A reasonable intermediate scale factor of 1% of the membrane thickness was adopted for all following wrinkling analyses.

4.4.5 Stabilizing Factor

Buckling problems are unstable due to the nonlinear geometrical nature. ABAQUS/Standard provides an automatic mechanism for stabilizing unstable quasi-static problems through the automatic addition of volume-proportional damping to the model. The mechanism is triggered by including automatic stabilization in any nonlinear quasi-static procedure.

It is assumed that a problem is stable at the beginning of the step and that instabilities may develop in the course of the step. While the model is stable, viscous forces and, therefore, the viscous energy dissipated are very small. Thus the additional artificial damping has no effect. If a local region goes unstable, the local velocities increase and, consequently, part of the strain energy then released is dissipated by the applied damping. ABAQUS/Standard can, if necessary, reduce the time increment to permit the process to occur without the unstable response causing very large displacement. ABAQUS/Standard calculates the damping factor based on the solution of the first increment of a step. In most applications the first increment of the step is stable without the need to apply damping. The damping factor is then determined in such a way that the extrapolated dissipated energy for the step is small fraction of the extrapolated strain energy. The fraction, called the dissipated energy fraction, has a default value of 2.0×10^{-4} and can be prescribed.

To achieve good accuracy, it is generally desirable to set this parameter to the lowest possible value for which convergence can still be achieved. This parameter was adjusted almost continuously, according to the level of difficulty of converging to a solution, by using the *RESTART option. This approach allows the numerical damping to be made very small initially to minimize the deviation between the computed equilibrium path and the actual path, and to be increased only when necessary. As listed in Table 4.7, the principal results of the post-buckling analysis with different stabilizing factors imposed are almost the same except for the computational time. Typically, a smaller stabilizing factor requires a longer computation time. The smallest factor chosen for the simulations was 1×10^{-8}.

Table 4.7: Effect of stabilizing factor on the results of post-buckling analysis.

Stabilizing factor	Computation time (s)	$w_{\max}$ (mm)	strain@$w_{\max}$
2×10^{-4} (default)	1920	0.2974	11.28%
1×10^{-6}	2734	0.3002	11.47%
1×10^{-7}	3452	0.3002	11.43%
1×10^{-8}	5254	0.3000	11.24%

4.5 Discussion

4.5.1 Wrinkling Onset

In Section 3.4.1 we have shown that wrinkling onset in terms of the critical buckling strain was very difficult to capture and measure in experiments. However observations suggested that membrane dimensions (i.e., in-plane dimensions, L, W, thickness t, and aspect ratio L/W) play important roles in determining the membrane structural instability in the event of in-plane tensile loading. To understand these roles in a more quantitative and efficient way, numerical tools were employed. A series of simulations have been designed and carried out for various membrane dimensions in the pre-buckling analysis stage. 144 dimensions with lengths ranging from 1.75 inch to 10 inch (44.45 mm to 254 mm), widths ranging from 0.9 inch to 7.5 inch (22.86 mm to 190.5 mm) were selected such that they can be compared with experimental results.

A contour map of the critical buckling strains for all the dimensions was generated by interpolating[1] the 144 data points which are listed in Table C.1 in Appendix C and is shown in Figure 4.5. The coordinates of each data point on the contour map specify the length and width of membrane that it corresponds to. Each isoline connects the dimensions with the same critical buckling strain

---

[1]Using a surface fitting tool, Gridfit, developed by John D'Errico in MATLAB language. (URL:http://www.mathworks.com/matlabcentral/fileexchange/loadFile.do?objectId=8998)

value. For example, the isoline representing the critical buckling strain value of 2% encloses all the dimensions with which membranes wrinkle under 2% tensile strain or less.
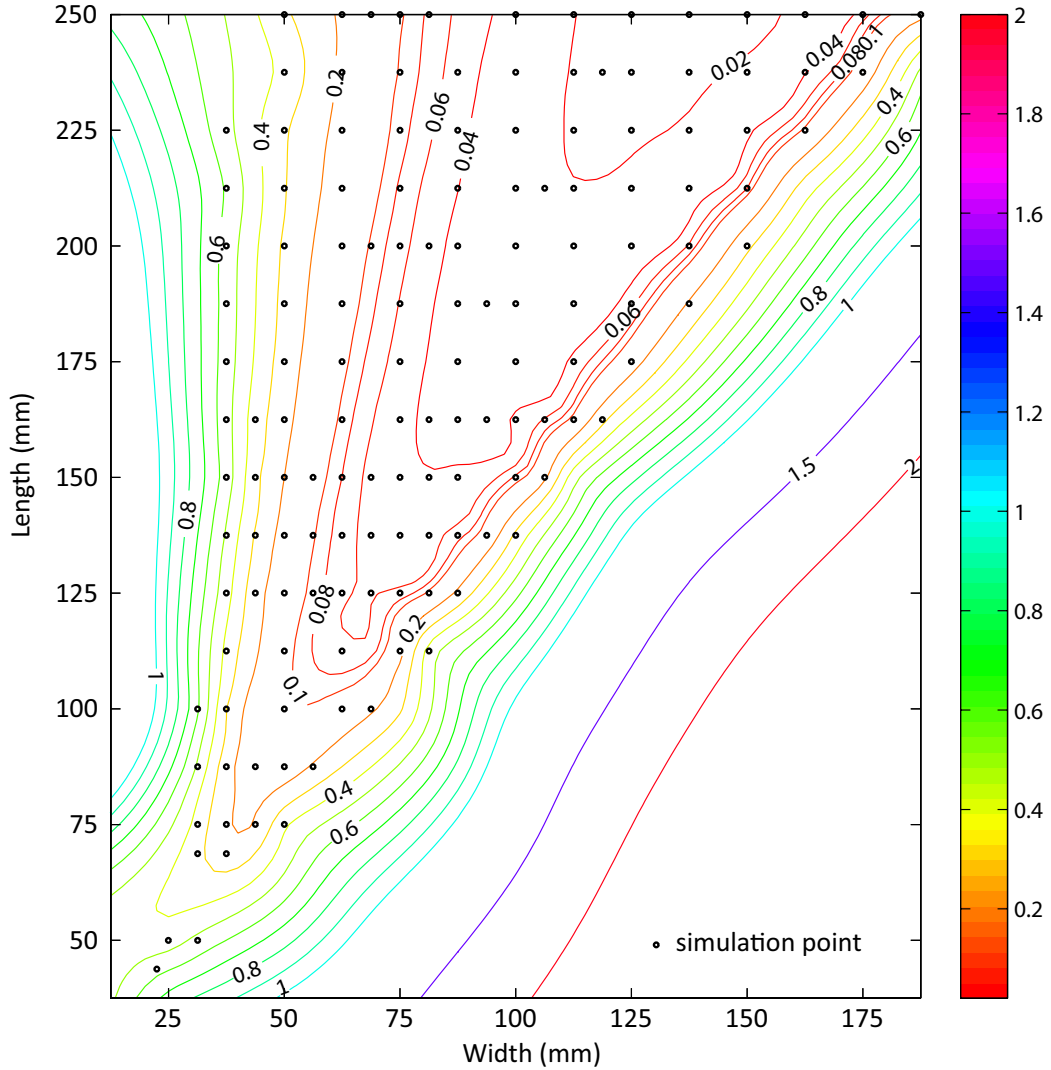
Figure 4.5: Contour map of the computed critical buckling strain for 0.1 mm (0.004 inch) membranes.

Some interesting trends are observed on this contour map. Generally wrinkles are more likely to occur on large membranes than small ones. Among all the tested dimensions, the 10×5.5 inch (254×139.7 mm) membrane has the lowest critical bucklings strain, 1.5%, while the 4×1.25 inch membrane has the highest value, 62.2%. In addition, wrinkles are more likely to occur on membranes with intermediate aspect ratios than those with extreme ones. It is noticed that these contours are self-similar. The valley of each isoline points out the smallest dimension among all the membranes with the same critical buckling strain. If these valleys are connected, a straight line with a slope of

about 2 emerges, which reflects the fact that rectangular membranes with aspect ratio 2 have lower instability to in-plane tension load than those with the same surface area but other aspect ratios.

The effect of individual factors (i.e., membrane thickness t or aspect ratio L/W) is also investigated. The thickness has been nondimensionalized by dividing it by the width since membrane strain is only a function of dimensionless parameters instead of absolute geometries. For example, a $203.2 \times 101.6 \times 0.1$ mm ($8 \times 4 \times 0.004$ inch) membrane has almost the same critical buckling strain as a $101.6 \times 50.8 \times 0.05$ mm ($4 \times 2 \times 0.002$ inch) one in simulation with small discrepancy due to computational uncertainties. Therefore, it makes more sense to use a dimensionless thickness t/W when comparing the critical buckling strains than to use an absolute thickness. The previous simulation results of the 144 dimensions were sorted by their aspect ratio. For each aspect ratio, quadratic dependence of the critical buckling strain on the dimensionless thickness, t/W, was found as shown in Figure 4.6.
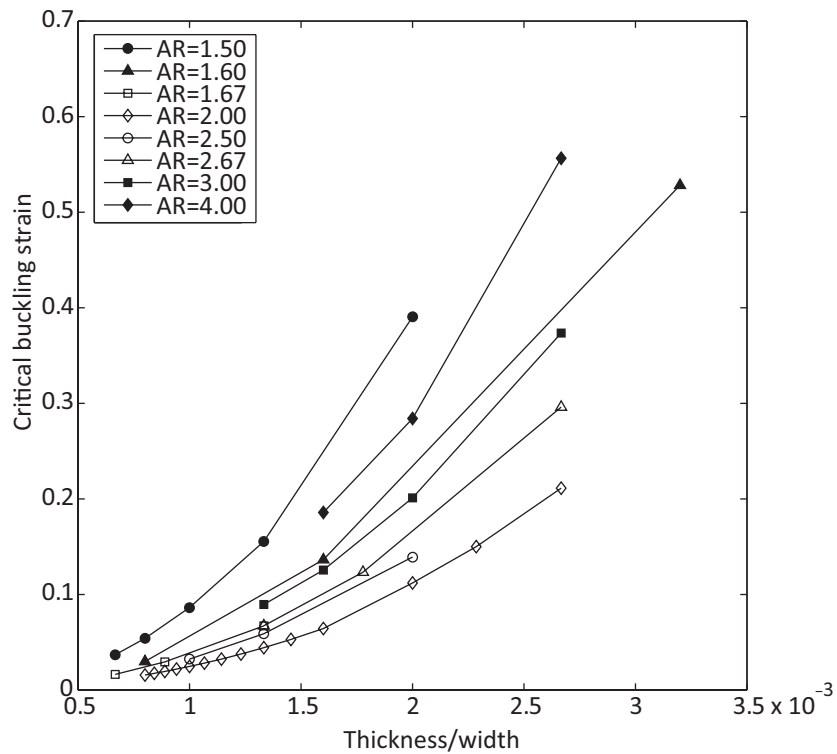
Figure 4.6: Critical buckling strains vs. dimensionless membrane thickness, t/W, for different aspect ratios.

Given this quadratic relationship, now it is simple to predict the critical buckling strains of 0.05 mm (0.002 inch) thick membranes with different dimensions based on the contour map of the 0.1

mm (0.004 inch) thick membrane. Figure 4.7 overlaps the two contour maps for comparison. The threshold for wrinkling has been significantly lowered by reducing the membrane thickness t by one half, which is equivalent to doubling both in-plane dimensions, L and W. The information provided in this kind of contour maps is comprehensive and thus they can serve as a guide to design or to failure analysis in many applications of thin membranes in tension.
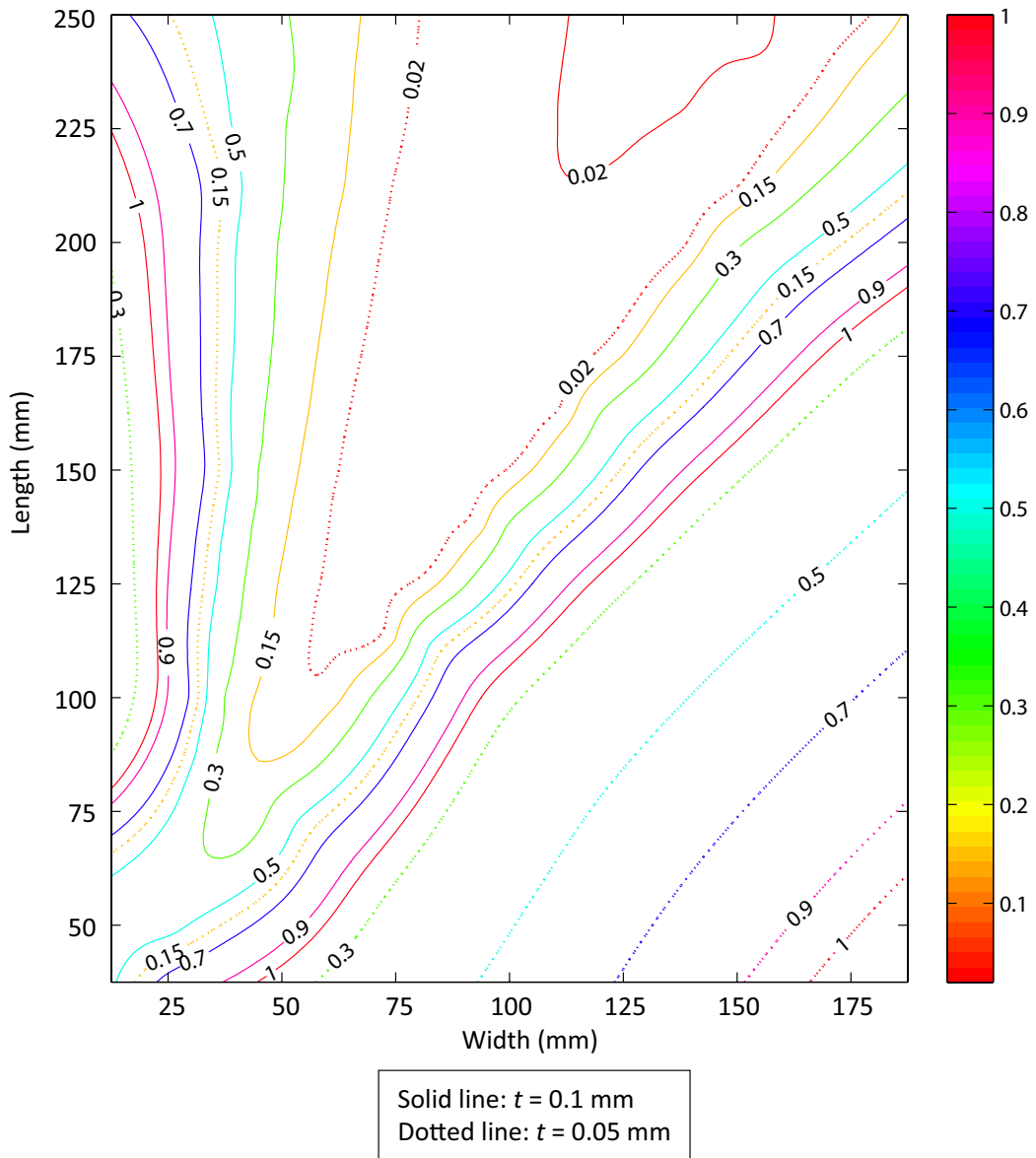
Figure 4.7: Contour maps of critical buckling strains for 0.05 mm (0.002 inch) and 0.1 mm (0.004 inch) thick membranes of various dimensions.

Furthermore, dependence of the critical buckling strain on membrane aspect ratio, L/W, is discovered. In Figure 4.8 the critical buckling strain is normalized by $(t/W)^2$ and plotted as a

function of the aspect ratio, which ranges from 1.33 to 6.0. The normalized critical buckling strain is a non-monotonic function of the aspect ratio and reaches its minimum when the membrane aspect ratio equals to 2 approximately. As the aspect ratio increases from 2, the normalized critical buckling strain increases gradually and stays almost constant for $L/W \geq 4.25$; on the other hand when the aspect ratio decreases from 2, the normalized critical buckling strain increases rapidly. At $L/W = 1.33$, this value becomes 25 times higher than the minimum value at $L/W = 2$. The pre-buckling analysis failed to converge for models with $L/W < 1.33$ based on the implementation parameters we adopted in the computation.
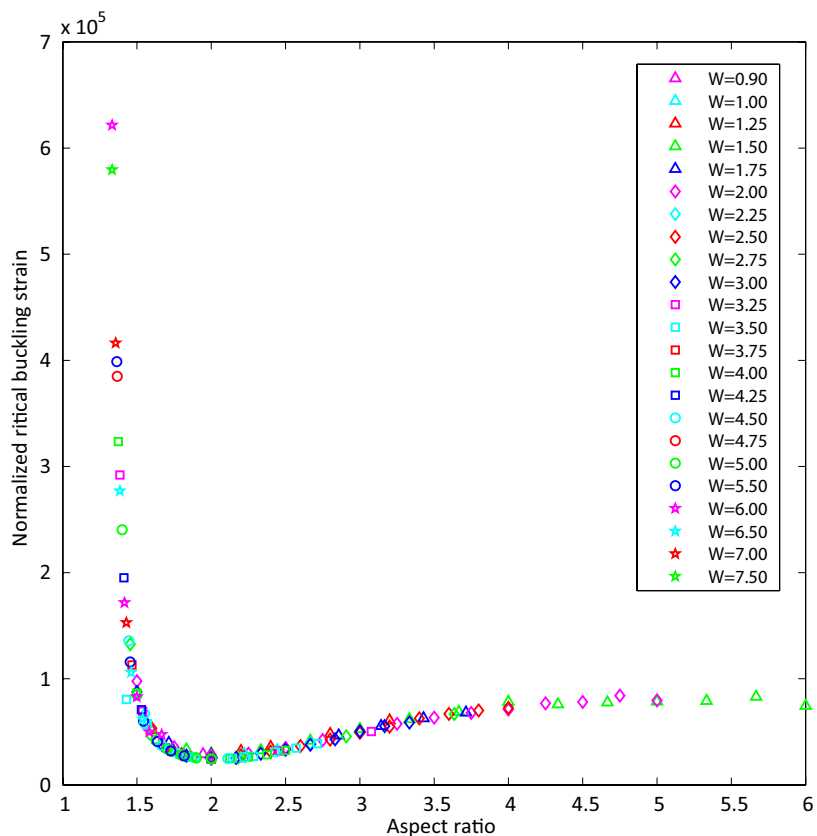
Figure 4.8: Normalized critical buckling strain vs membrane aspect ratio, L/W. The critical buckling strain is normalized by the $(t/W)^2$. Data points corresponding to 144 membrane dimensions are sorted by the length of the membrane.

The eigenvalue buckling analysis predicts not only the critical buckling load (eigenvalue) but also the buckling modes (eigenvectors). Figures 4.9-4.13 illustrate the first symmetric wrinkling modes corresponding to the lowest eigenvalues of membranes with different aspect ratios.[1]

---

[1]The corresponding membrane dimensions were 76.2×50.8 mm (3×2 inch), 101.6×50.8 mm (4×2 inch), 152.4×50.8 mm (6 × 2 inch), 254 × 50.8 mm (10 × 2 inch), and 406.4 × 50.8 mm (16 × 2 inch).
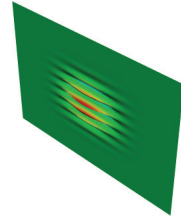
Figure 4.9: First buckling mode of membrane with aspect ratio $L/W = 1.5$.
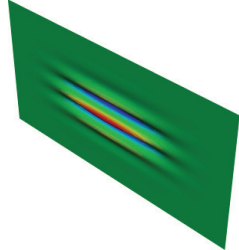
Figure 4.10: First buckling mode of membrane with aspect ratio $L/W = 2$.
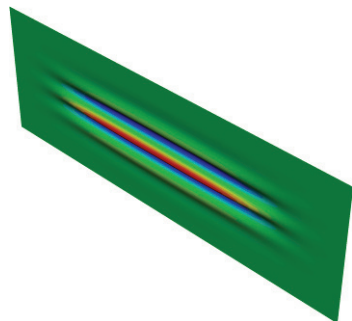
Figure 4.11: First buckling mode of membrane with aspect ratio $L/W = 3$.
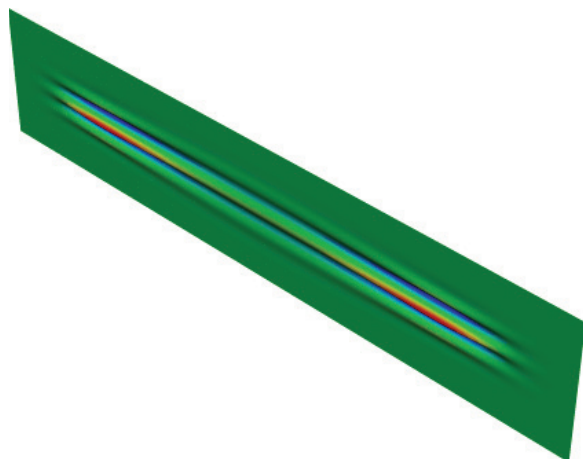
Figure 4.12: First buckling mode of membrane with aspect ratio $L/W = 5$.
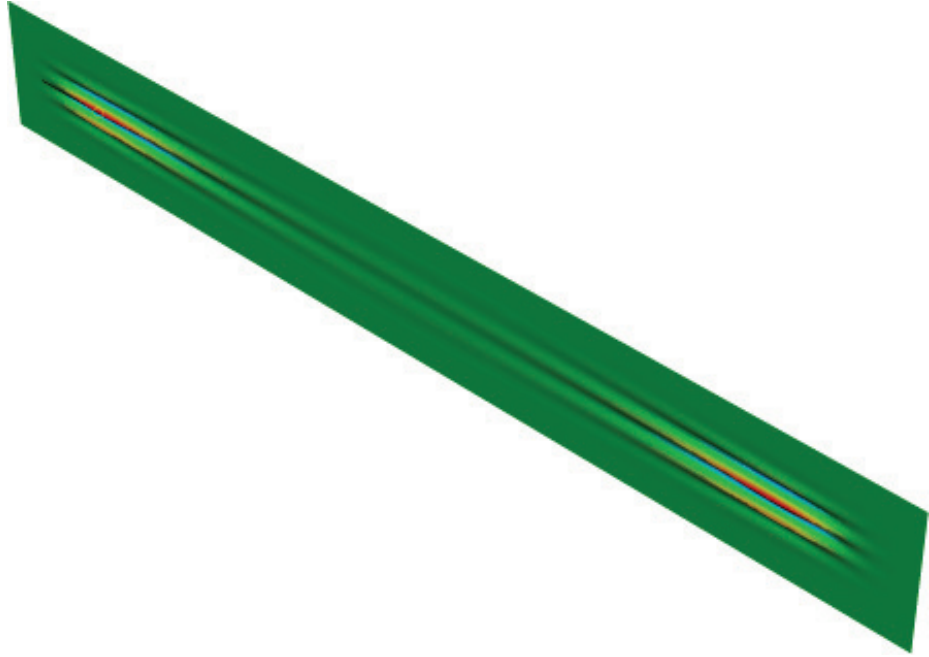
Figure 4.13: First buckling mode of membrane with aspect ratio $L/W = 8$.

These normalized wrinkling modes provide constructive ideas about the potential deformation that membranes may form into upon the critical buckling strain. Wrinkles form parallel to the loading direction. In most cases, three major wrinkles were predicted in the first mode except for the case of extremely small aspect ratio (i.e., $L/W = 1.5$) where five wrinkles were predicted. It is also found that the locations at which wrinkling first occur on the membrane vary with the aspect ratio though they are always on the longitudinal midplane for symmetric modes. This is suggested by the locations of the maximum magnitude of the eigenvectors, whose dependence on membrane's aspect ratio is illustrated in Figure 4.14. For membranes with aspect ratio $L/W \leq 2.8$ wrinkles initiate at the center of the membrane; whereas for membrane with $L/W \geq 2.9$ wrinkles occur at two separate points equally apart from the center. The larger the membrane aspect ratio is, the further they are apart from the center.

The wrinkling modes usually come in pairs, one being symmetric and the other being anti-symmetric. The first two modes correspond to the lowest eigenvalue, indicating that in numerical simulation membrane has an equal chance to deform into each mode beyond the critical buckling load. Figure 4.15 compares the first two eigenmodes of three membrane models with the same width and aspect ratios of 1.5, 2 and 4 by plotting the transverse cross sections through the point of maximum amplitude[1]. The membrane with aspect ratio 2, which has the lowest critical buckling strain

---

[1]The corresponding membrane dimensions were 254×63.5 mm (10×2.5 inch), 127×63.5 mm (5×2.5 inch) and 95.25×63.5 mm (3.75×2.5 inch).
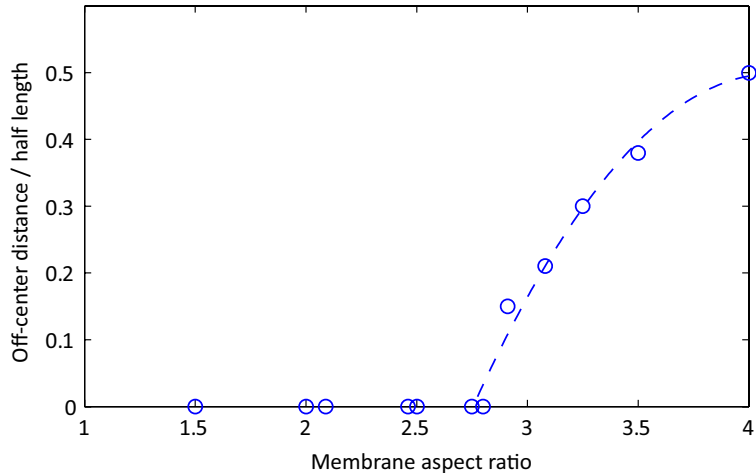
Figure 4.14: The ratio of the longitudinal off-center distance of the point of the maximum amplitude to membrane half length, $L/2$, vs. membrane aspect ratio.

among the three, tends to form wrinkles with larger wavelength than the other two.

Higher wrinkling modes may also be of interest later on when membrane heavily loaded is studied. Figure 4.16 shows the cross-sections of the first six wrinkling modes of a membrane with aspect ratio $L/W = 2$. In high modes, the total number of wrinkles increases, and the maximum normalized wrinkling amplitude moves towards the lateral side.

4.5.2 Stress Distribution

Compressive stress or shear stress is the driving force of most buckling phenomena. A two dimensional static analysis was carried out prior to the buckling analysis to study the stress distribution on thin rectangular membranes when clamped at two ends and subjected to uniaxial loading. 4-node bilinear plane stress quadrilateral element with reduced integration (CPS4R) was used in the model. The material properties remained the same as in the eigenvalue buckling analysis. The analysis procedure was comprised of two steps. In the first step, clamping boundary conditions were applied to both ends of the membrane such that there is no lateral contraction at the end. In the second step, one end was fixed while the other end was imposed an edge displacement in the longitudinal direction to produce a 50% tensile strain.

The normal stresses in the transverse direction, σ_{22}, for membranes with different aspect ratios are shown in Figures 4.17-4.21(a). To show the exact position of the maximum compressive stress, negative σ_{22} is plotted along the horizontal centerline in Figures 4.17-4.21(b). On each contour map
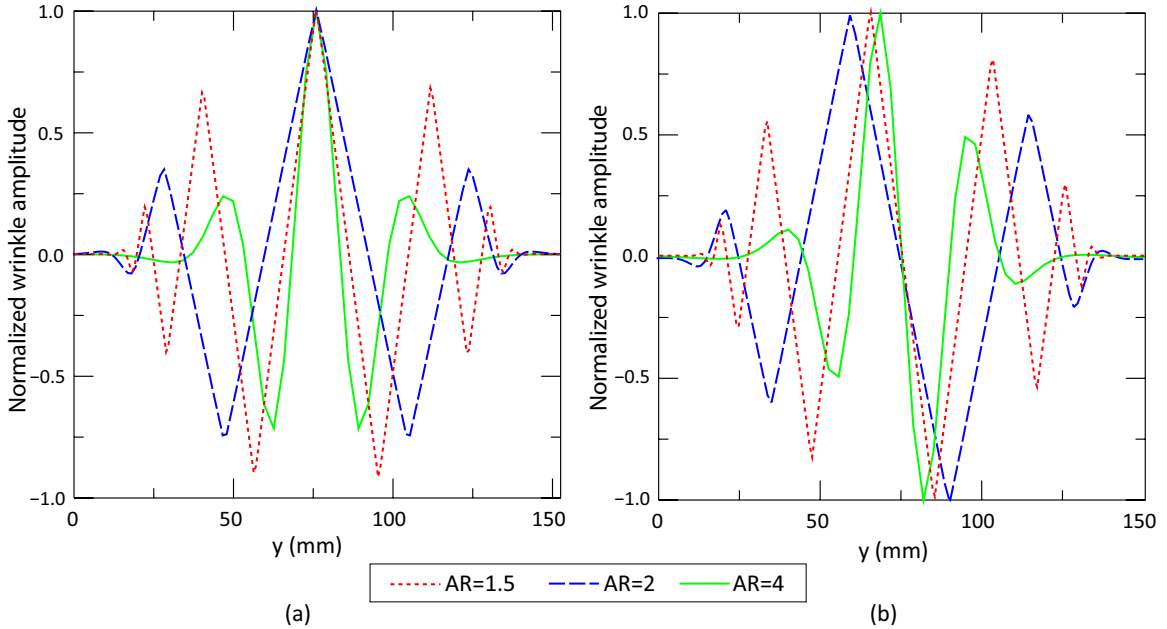
Figure 4.15: The cross section of (a) the first symmetric mode, and (b) the first anti-symmetric mode, corresponding to the lowest eigenvalue through the point of the maximum amplitude for membranes with aspect ratios $L/W = 1.5$, $L/W = 2$ and $L/W = 4$.

the values of the isolines are not scaled uniformly, i.e., the difference between adjacent isolines in the tension region is 300 times larger than the one in the compression region, because compressive stress is smaller than the tensile stress by 2-3 order of magnitude. However the compressive stress is crucial to the onset of the wrinkling phenomenon.

The distribution of σ_{22} is symmetric about both the longitudinal and transverse centerlines of the membrane with the maximum tensile σ_{22} concentrated at the four corners, and the maximum compressive σ_{22} at the center of the membrane (for small aspect ratios) or separated at two points equally apart from the center along the horizontal centerline. This is consistent with the locations where wrinkles first form on membranes with these aspect ratios. For large aspect ratios (i.e., $L/W = 5$ and $L/W = 8$), the central area of the membrane does not feel the existence of the clamping boundary condition and behaves as if the membrane was free to contract laterally everywhere due to the Poisson's effect. Therefore σ_{22} becomes zero in the central area.

We also generated contour maps of the shear stress σ_{12} for membrane with different aspect ratios in Figures 4.22-4.26. The distribution of σ_{12} is antisymmetric about both the longitudinal and transverse centerlines, along which $\sigma_{12} = 0$ as well as the closed loop in the center. At the corners
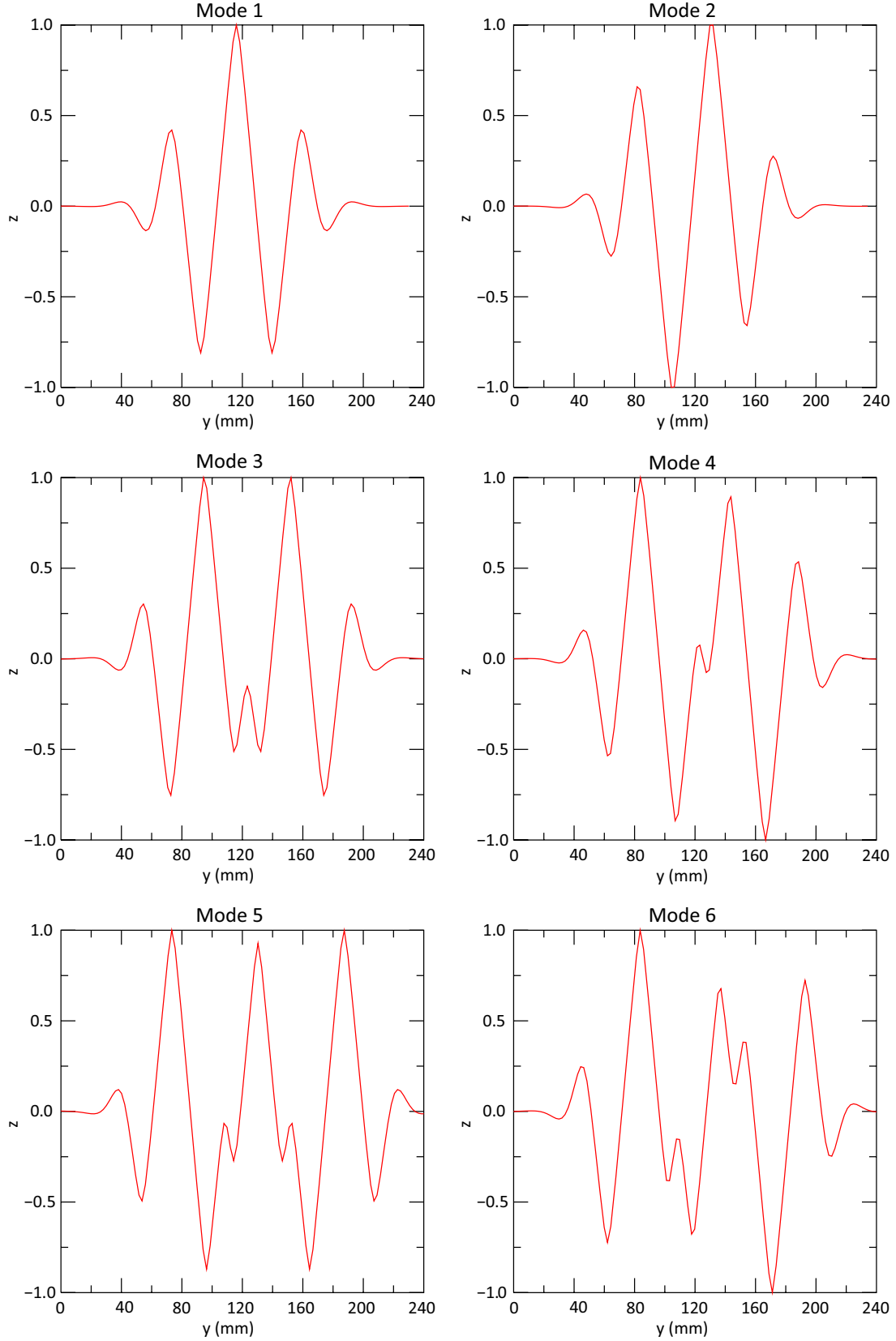
Figure 4.16: The first six wrinkling modes of the membrane with $L/W = 2$. The cross section is through the point of maximum amplitude.
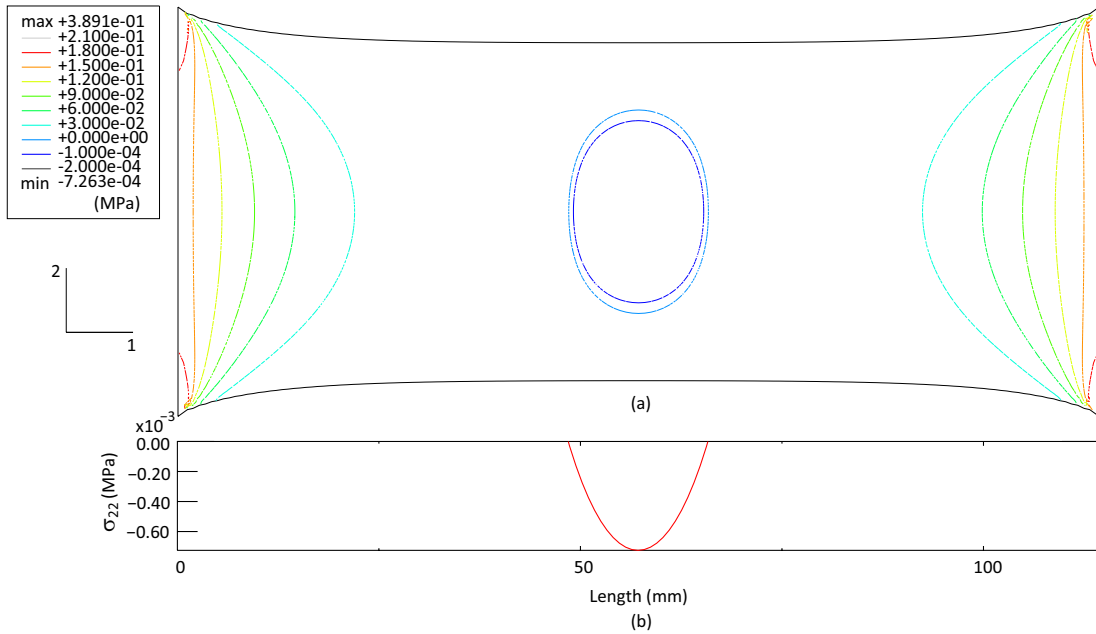
Figure 4.17: The distribution of the normal stress σ_{22} of membrane with aspect ratio $L/W = 1.5$ subjected to 50% tensile strain. (a) isolines of σ_{22}, (b) σ_{22} along the horizontal centerline in the region $\sigma_{22} \leq 0$.
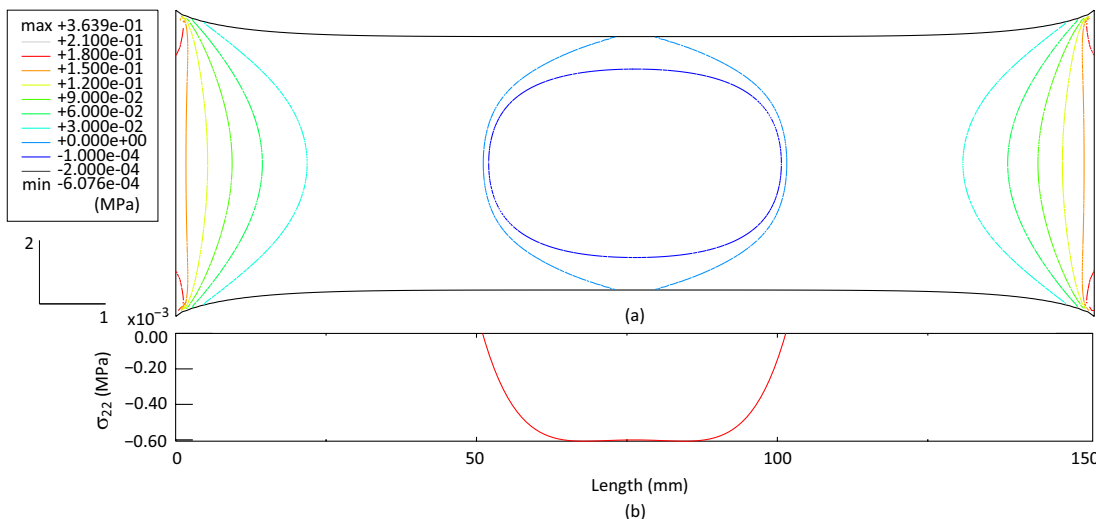
Figure 4.18: The distribution of the normal stress σ_{22} of membrane with aspect ratio $L/W = 2$ subjected to 50% tensile strain. (a) isolines of σ_{22}, (b) σ_{22} along the horizontal centerline in the region $\sigma_{22} \leq 0$.
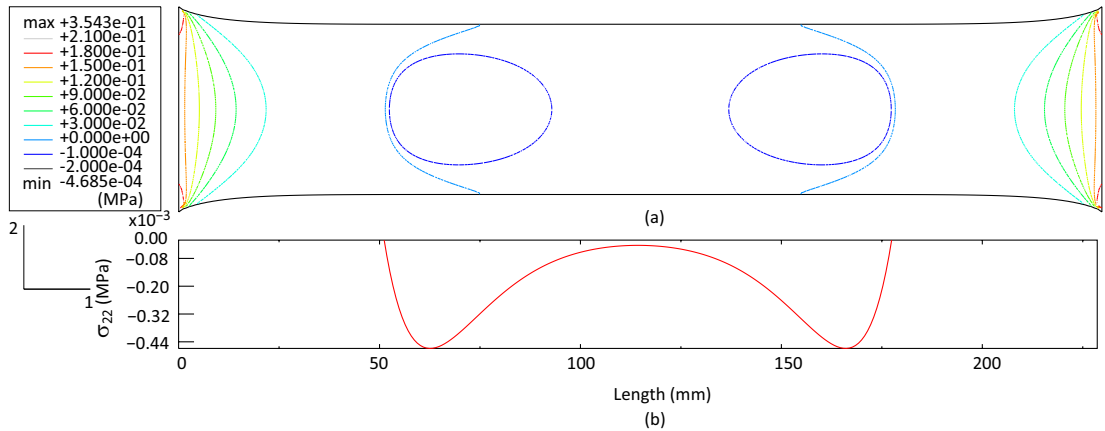
Figure 4.19: The distribution of the normal stress σ_{22} of membrane with aspect ratio $L/W = 3$ subjected to 50% tensile strain. (a) isolines of σ_{22}, (b) σ_{22} along the horizontal centerline in the region $\sigma_{22} \leq 0$.
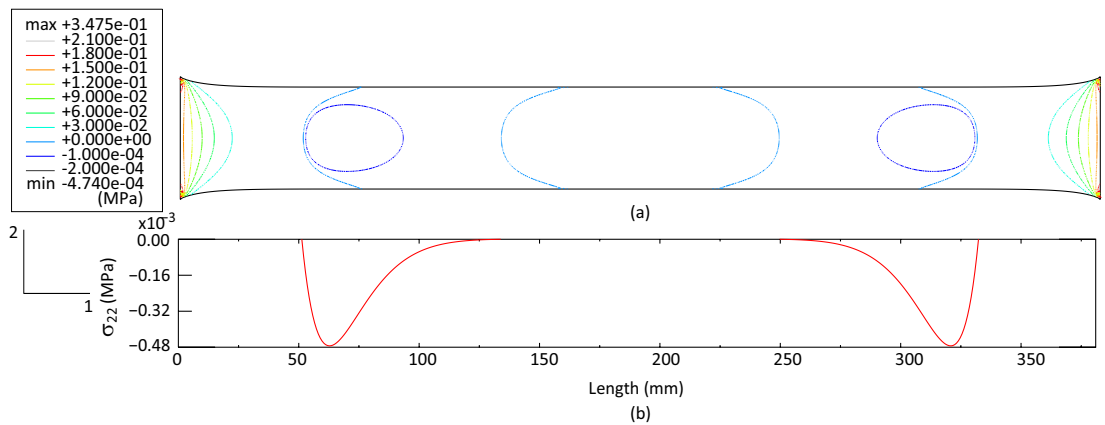
Figure 4.20: The distribution of the normal stress σ_{22} of membrane with aspect ratio $L/W = 5$ subjected to 50% tensile strain. (a) isolines of σ_{22}, (b) σ_{22} along the horizontal centerline in the region $\sigma_{22} \leq 0$.
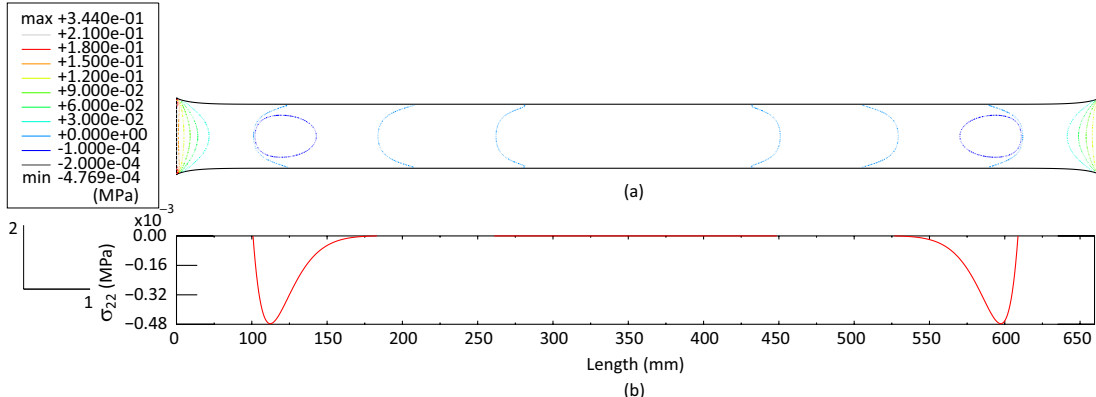
Figure 4.21: The distribution of the normal stress σ_{22} of membrane with aspect ratio $L/W = 8$ subjected to 50% tensile strain. (a) isolines of σ_{22}, (b) σ_{22} along the horizontal centerline in the region $\sigma_{22} \leq 0$.

of the membrane σ_{12} is concentrated, while the central area is free of shear stress.
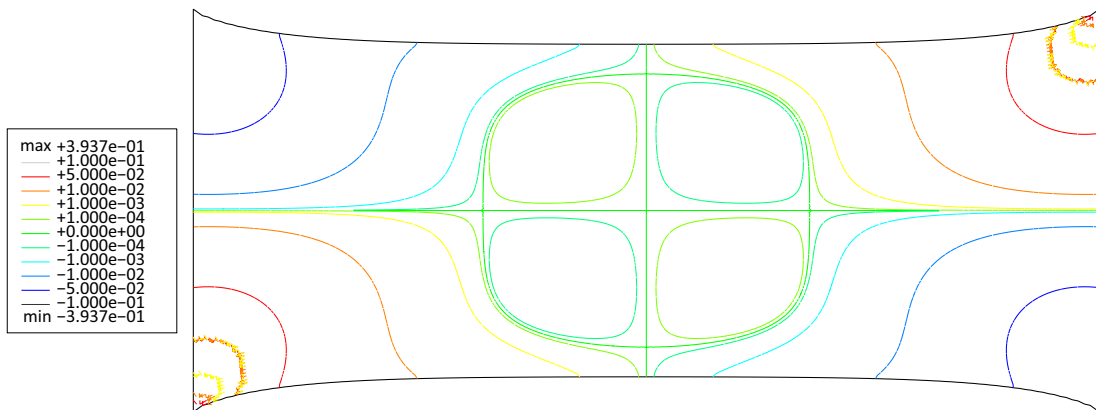
Figure 4.22: The distribution of the shear stress σ_{12} of membrane with aspect ratio $L/W = 1.5$ subjected to 50% tensile strain.

4.5.3 Wrinkling Profile

After we identified the wrinkling mode(s) from all the eigenmodes computed in the pre-buckling eigenvalue analysis, a geometric imperfection was determined and seeded into the post-buckling analysis to study the wrinkling profile on membranes of different dimensions.

The incremental solution method allows us to vary the edge displacement by a prescribed small amount[1] at each frame and thus provides us a continuous image of the deformation. Figure 4.27

---

[1]The lower and upper limits were prescribed for the increments. Usually the increments are not equally spaced.
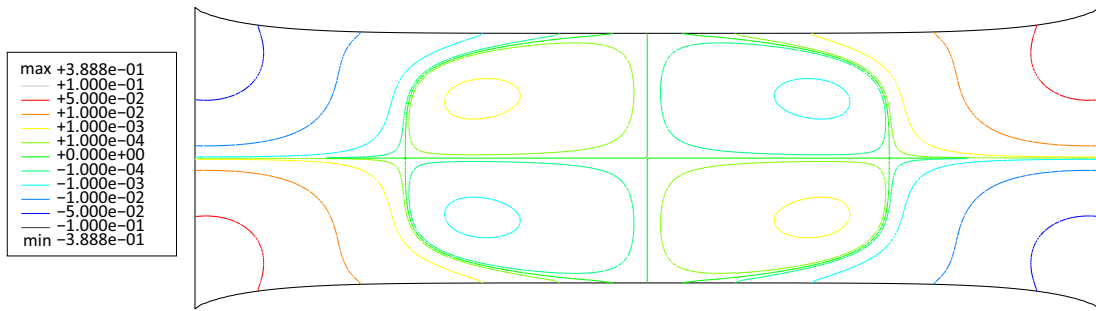
Figure 4.23: The distribution of the shear stress σ_{12} of membrane with aspect ratio $L/W = 2$ subjected to 50% tensile strain.
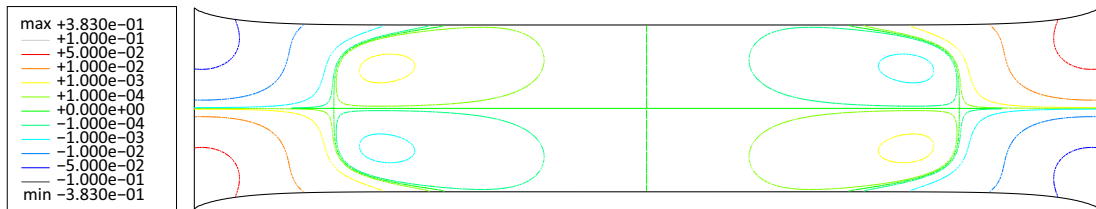
Figure 4.24: The distribution of the shear stress σ_{12} of membrane with aspect ratio $L/W = 3$ subjected to 50% tensile strain.
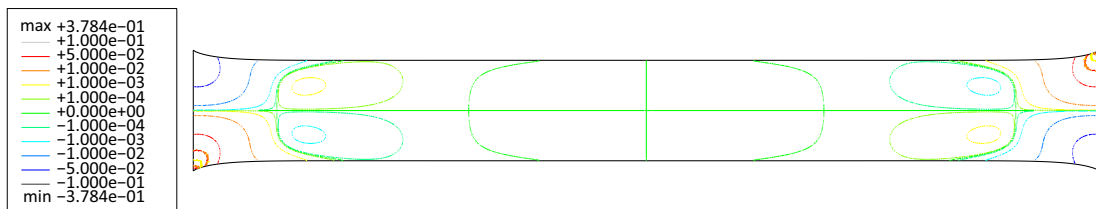
Figure 4.25: The distribution of the shear stress σ_{12} of membrane with aspect ratio $L/W = 5$ subjected to 50% tensile strain.
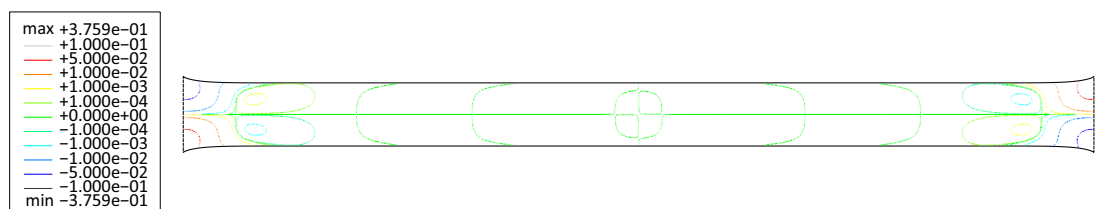
Figure 4.26: The distribution of the shear stress σ_{12} of membrane with aspect ratio $L/W = 8$ subjected to 50% tensile strain.

demonstrates the out-of-plane displacement of the 254×101.6 mm (10×4 inch) membrane model. Over 100 frames were generated in the loading step for the 30% strain, among which six frames were picked at the desired strains levels. The color schemes of the contour maps are adjusted so that they are comparable with the optical measurement results which we have shown earlier in Figure 3.22. Detailed comparison will be discussed in Chapter 5.
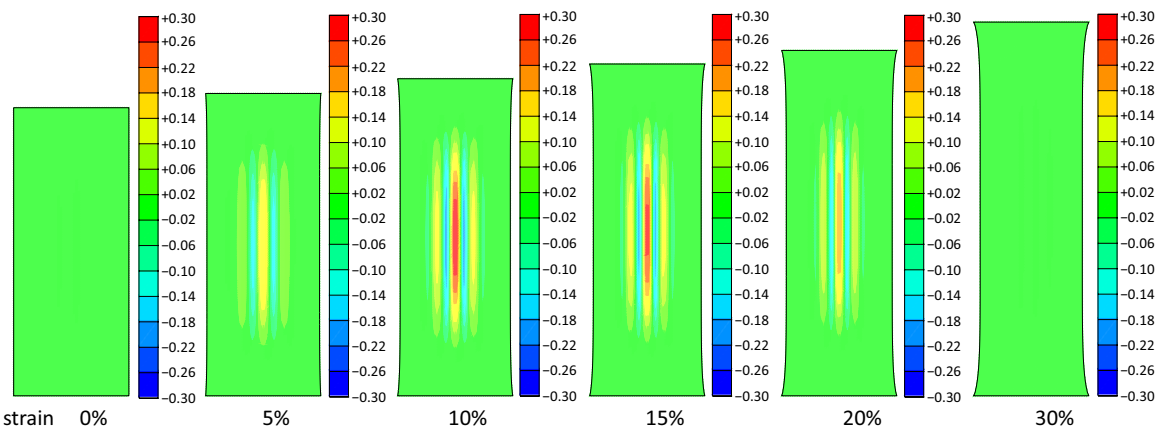
Figure 4.27: Out-of-plane displacement of the 254×101.6 mm (10×4 inch) membrane model at different tensile strains.

The wrinkle profile is symmetric about both the longitudinal and transverse midplanes. The line profiles along the cross section of the membrane midplanes are shown in Figure 4.28. The maximum wrinkle amplitude remains at the center of the membrane.

Figure 4.29 shows the variation of the amplitude and wavelength of the central wrinkle at the transverse midplane section with the applied tensile strain. The wrinkles initiate at the center of the membrane when the tensile strain reaches 2.9%.[2] Then the wrinkle amplitude increases rapidly and reaches its maximum 0.29 mm when membrane is stretched by approximately 11.3%. Beyond this point, further tensile strain reduces the wrinkle amplitude at a slightly slower rate. At 30% tensile strain the wrinkles almost disappear. On the other hand, the wavelength of the central wrinkle decreases monotonically with the tensile strain. At 5% strain the wavelength is approximately 17 mm and reduced to 15 mm at about 10% strain when the amplitude is maximal. At 30% strain when the wrinkles become very shallow, the wavelength decreases by roughly 30%, to 12 mm.

The distributions of the major and minor principal stresses, σ_1 and σ_2, were obtained at different strain levels as shown in Figures 4.30 and 4.31. σ_1 and σ_2 along the midplanes were also obtained

---

The analysis begins with the smallest increment prescribed and ends with the largest one which is subjected to change to achieve convergence.

[2]The pre-buckling analysis computed the critical buckling strain is 3.2% for membrane of this dimension.
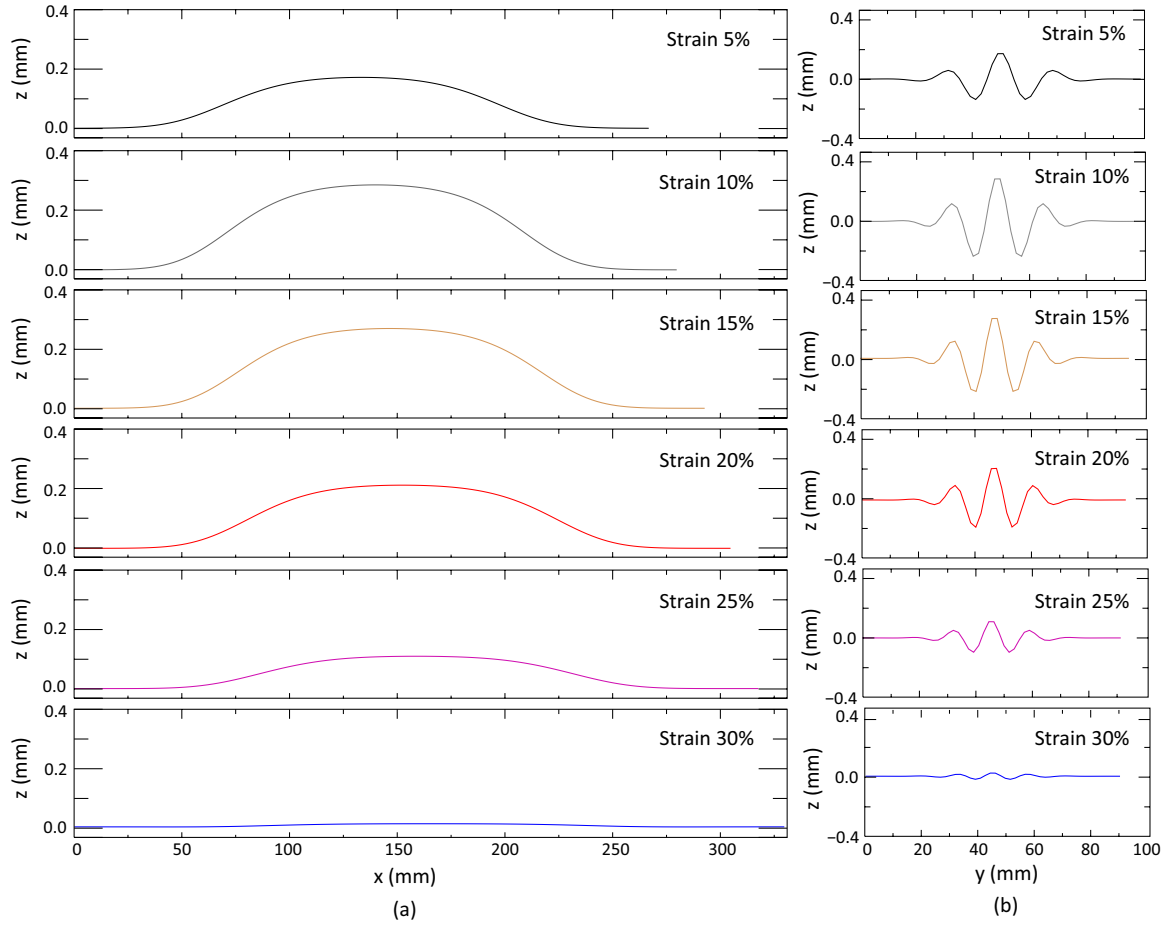
Figure 4.28: Wrinkle profiles of the 254×101.6 mm (10×4 inch) membrane along (a) the longitudinal midplane, (b) the transverse midplane under different tensile strains.
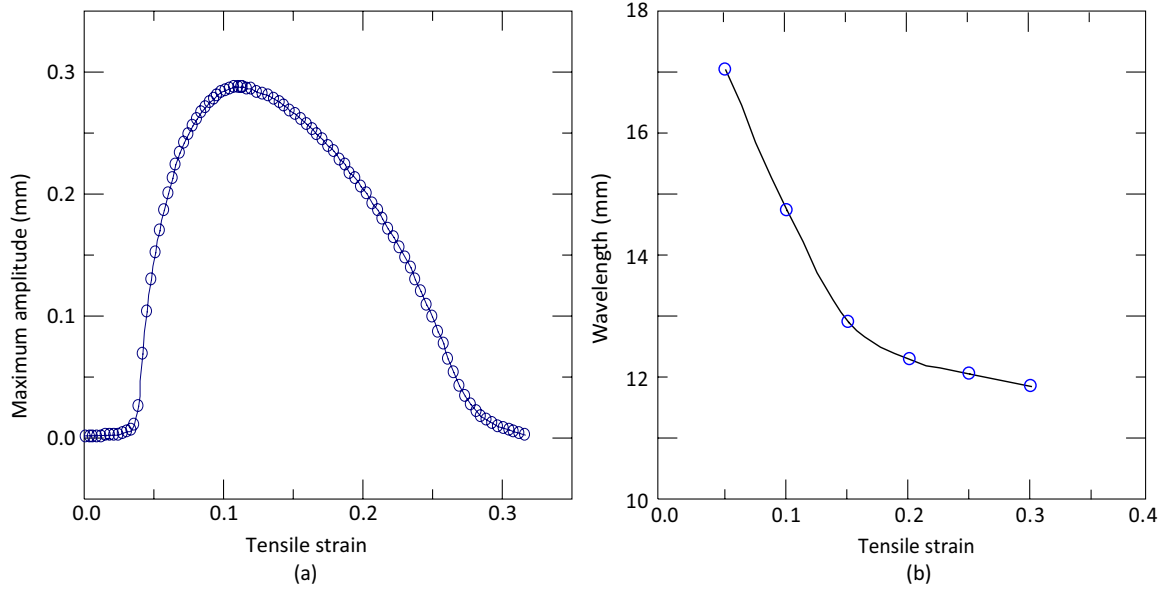
Figure 4.29: (a) The maximum wrinkle amplitude vs. the tensile strain for the 254×101.6 mm (10×4 inch) membrane. 104 data points were extracted from the computational results of 104 increments directly and fit into a curve; (b) the wavelength of the central wrinkle vs. the tensile strain. 6 data points at the six desired strain levels were extracted manually and fit into a curve.

at strain of 11.3% when the wrinkle amplitude is maximal as shown in Figure 4.32. The major principal stress is positive throughout the membrane surface at all strain levels. Whereas the minor principal stress is positive at the two clamped ends and fluctuates around zero in a wavelike pattern in the central region. According to the wrinkling criteria introduced earlier in Section 2.2, the taut region and the wrinkled region are distinguished by the contour of $\sigma_2 = 0$, and there is no slack region in the membrane.

The relationship is found between the distribution of the minor principal stress and the out-of-plane displacement of the membrane in Figure 4.33, which compares the wrinkle profile with the minor principal stress along the transverse midplane at 11.3%. The crests and troughs fit in the regions where the compressive stress and tensile stress are localized respectively.
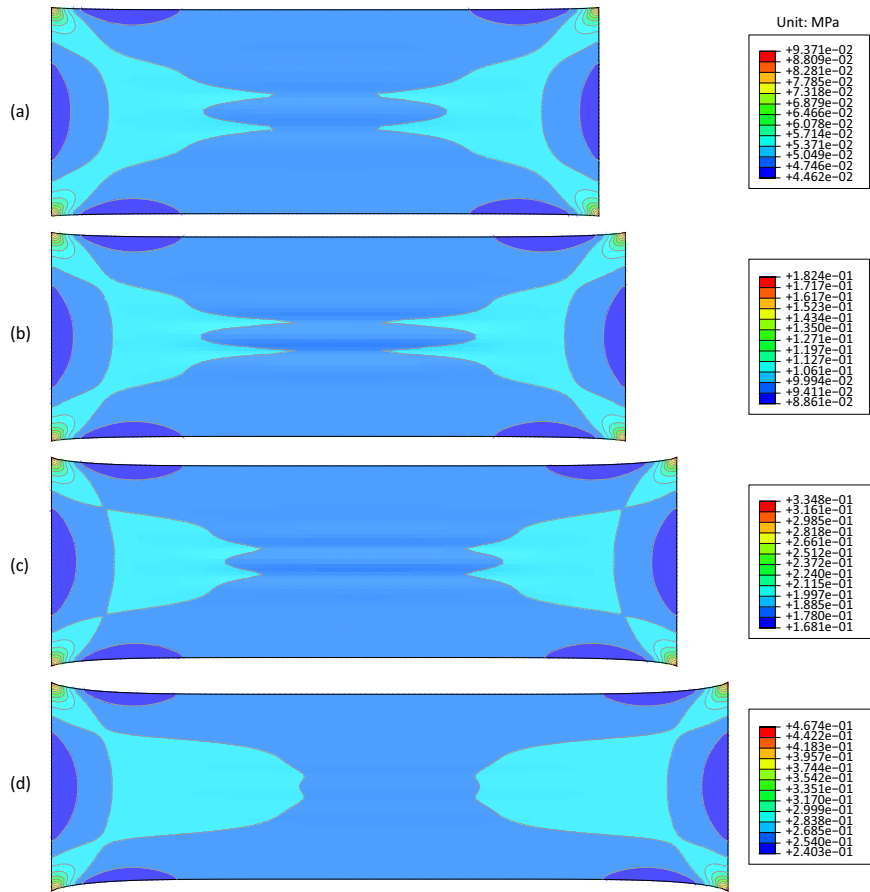
Figure 4.30: The major principal stress of the 254×101.6 mm $(10 \times 4$ inch) membrane subjected to tensile strain (a) 5%, (b) 10%, (c) 20%, (d) 30%.
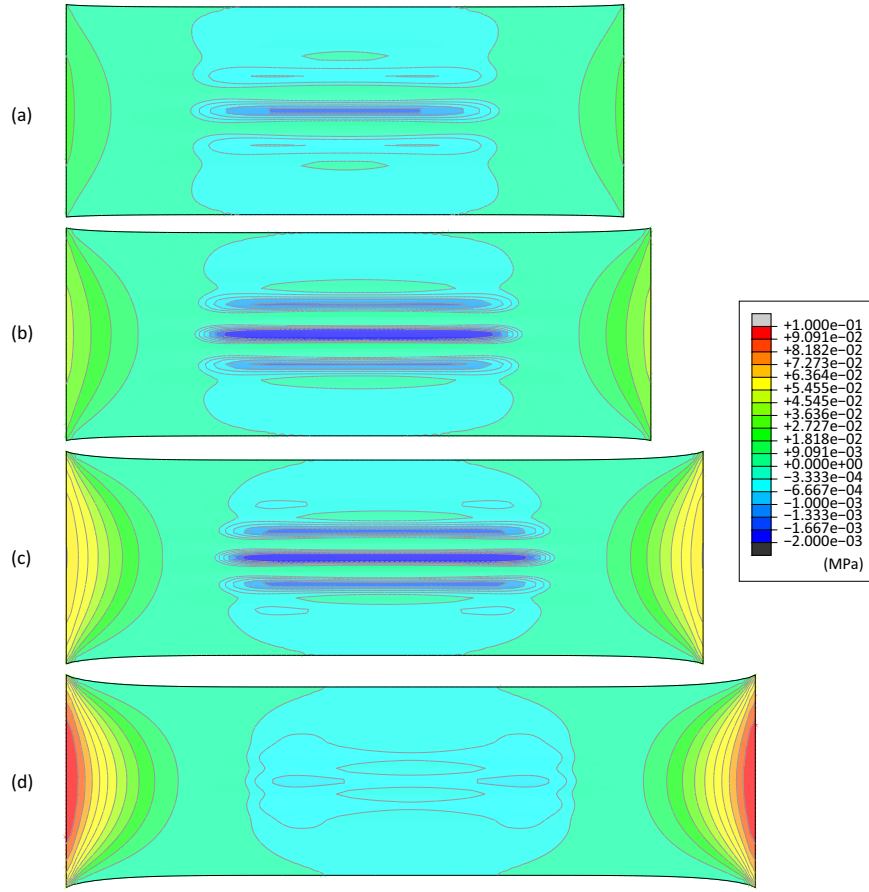
Figure 4.31: The minor principal stress of the 254×101.6 mm $(10 \times 4$ inch) membrane subjected to tensile strain (a) 5%, (b) 10%, (c) 20%, (d) 30%.
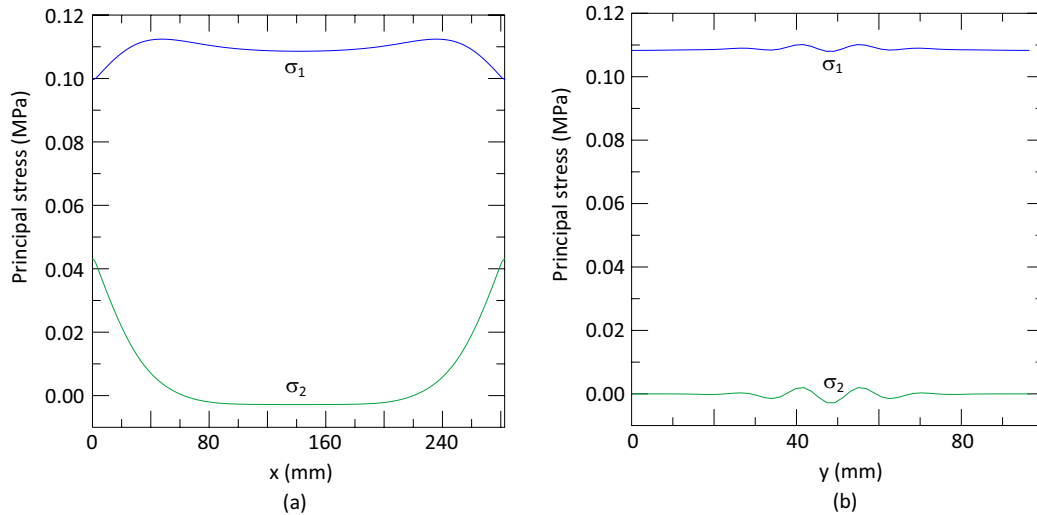
Figure 4.32: Principal stresses at 11.3% strain along (a) the longitudinal midplane, and (b) the transverse midplane.
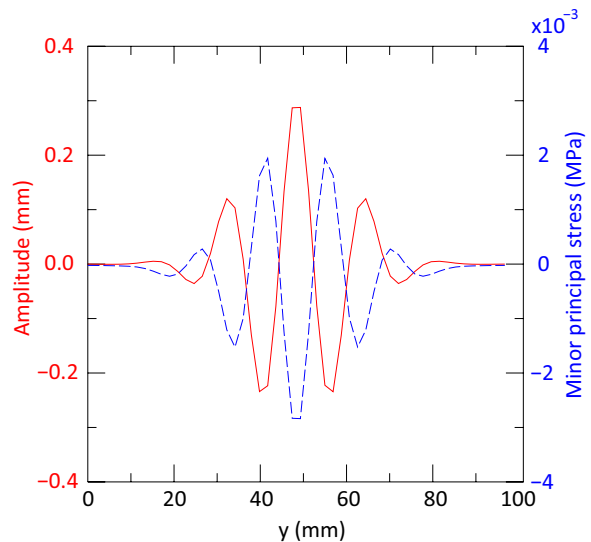
Figure 4.33: The wrinkle amplitude (solid line) and the minor principal stress (dashed line) along the transverse midplane on the 254×101.6 mm (10×4 inch) membrane at tensile strain of 11.3%.

Chapter 5

Comparison and Discussion

This chapter compares the experimental observations and measurements with the results of numerical simulation from the aspects of wrinkling onset and wrinkle profile.

5.1 Comparison

5.1.1 Wrinkling Onset

Figure 3.21 showed the experimental observation of the (non)existence of wrinkles in membranes with 27 different dimensions. Figure 4.5 showed the numerical prediction of wrinkling onset of membrane with 144 different dimensions. The axes of both maps are identical, which are membrane length and width respectively. The overlap of the two maps is shown in Figure 5.1. An envelope (the dashed line in the figure) is drawn to distinguish the dimensions of the membranes which wrinkled in experiment from those which did not wrinkle. The shape of this envelope coincides with the isolines of the 20% critical buckling strain computed in simulations. This agreement can be understood as follows. Numerical simulations always provide the critical buckling strain (eigenvalue) to a membrane structure as long as the convergence can be achieved. However in reality, the silicone membranes behave in a more complicated manner. They either form wrinkles at a very small strain or do not wrinkle at all. No onset of wrinkles at intermediate strain levels was observed in the experiments. The contour map may not predict the absolute value of the critical buckling strain for a specific membrane dimension, but it successfully predicts the relative structural instabilities in membranes subjected to in-plane tension load.
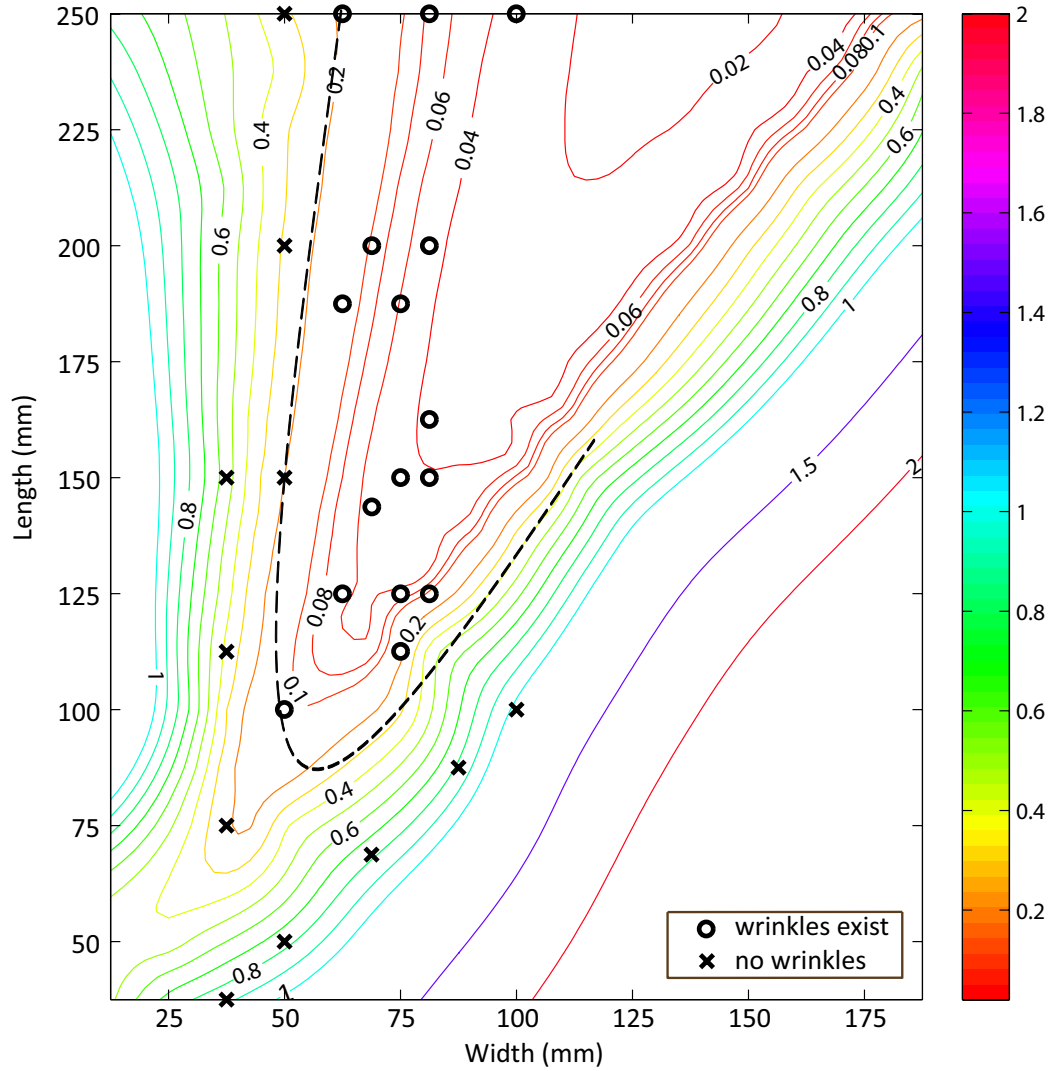
Figure 5.1: Contour map of the computed critical buckling strain of various membrane dimensions overlapped with wrinkle existence map obtained from experiments. The dashed line is the trendline separating the wrinkled and non-wrinkled regions.

5.1.2 Wrinkle Profile

We have shown the contour plots of the out-of-plane displacement of the 254×101.6 mm (10×4 inch) membrane under a series of tensile strains based on both the calibrated measurement results in Figure 3.22 and the computational results from the post-buckling analysis in Figure 4.27. The overall wrinkling behaviors, including the symmetric wrinkle pattern and the total number of wrinkles, predicted in the simulation agree with those observed in the experiments. In order to compare the wrinkling details, wrinkle profiles along the transverse midplane are plotted in Figure 5.2. The changes of the maximum wrinkle amplitude and the wavelength with the tensile strain are plotted in Figure 5.3.
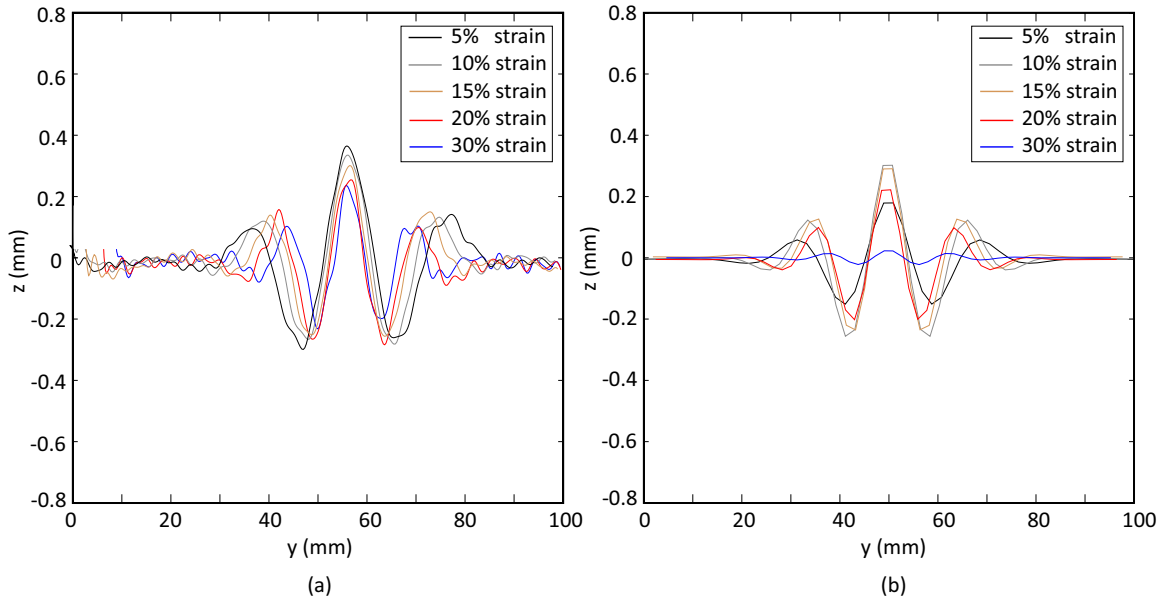
Figure 5.2: Wrinkling profiles along the transverse midplane of the 254×101.6 mm (10×4 inch) membrane under different tensile strains obtained from (a) the experimental measurement and (b) the numerical simulation.

Due to complexities involved in dealing with the thin silicone sheet, the bifurcation at small strain predicted in the simulation was not observed in experiment. The maximum wrinkle amplitude shows the same trend for the experimental and numerical results when the tensile strain is between 10% and 20%, and the numerical one is smaller than the experimental one by about 15%. The amplitude at 30% strain is significantly underestimated in the simulation. Numerically, wrinkles almost disappear at about 32% strain, whereas experimentally membrane may require a much larger tensile load to smooth out the wrinkles. Wrinkle disappearance was not observed in experiment because the limited length of the side rails on the testbed allows only 10% tensile strain to be applied to a 10 inch long membrane. The monotonically decreasing wrinkle wavelength obtained in the simulation
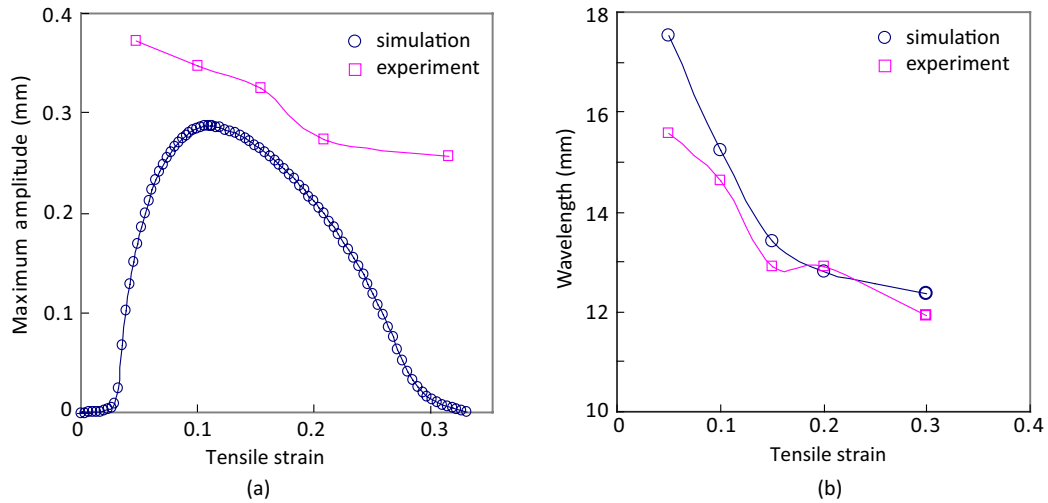
Figure 5.3: Comparison of the experimental and numerical results for (a) the maximum wrinkle amplitude, and (b) the wavelength of the largest wrinkle, of the 254×101.6 mm (10×4 inch) membrane vs. tensile strain.

matches the experimental data fairly well.

5.2 Discussion

So far we have been consistently using the 254×101.6 mm (10×4 inch) membrane for discussion, which was actually the the largest membrane sample among all the samples that have been tested. It also exhibited the largest out-of-plane deformation when wrinkling, indicating the wrinkle profiles are scaled with the membrane in-plane dimensions. Wrinkling behaviors of thin membrane structures in other dimensions were also studied using both the experimental and numerical tools. Here we restrict our discussion to only the overall wrinkling behavior, primarily the wrinkle patterns and growth under tensile strain.[1]

Figures 5.4-5.17 demonstrate the wrinkle of membranes of several other dimensions at different strain levels in the form of contour plots generated from both experimental measurement and finite element analysis as comparison.

Some common features were observed from all the dimensions tested. As the membrane is loaded uniaxially, the wrinkle amplitude first increases and then decreases; whereas the wrinkle wavelength decreases monotonically. Membranes typically deform into either a symmetric or an anti-symmetric

---

[1]For some membranes of small size, the comparison and discussion become difficult because the measurement uncertainties and computational error may not be negligible compared with the wrinkle amplitudes.

wrinkling patten, whose profiles can be characterized by damped cosine function and damped sine function respectively. Dimensions like 254×101.6, 254×82.55 and 165.1×82.55 mm (10×4, 10×3.25 and 6.5×3.25 inch) exhibit the symmetric pattern with the largest wrinkle along the longitudinal midplane; other dimensions like 203.2×69.85, 190.5×76.2 and 146.05×69.85 mm (8×2.75, 7.5×3 and 5.75×2.75 inch) exhibit anti-symmetric pattern with the largest crest and trough at either side of the longitudinal midplane.
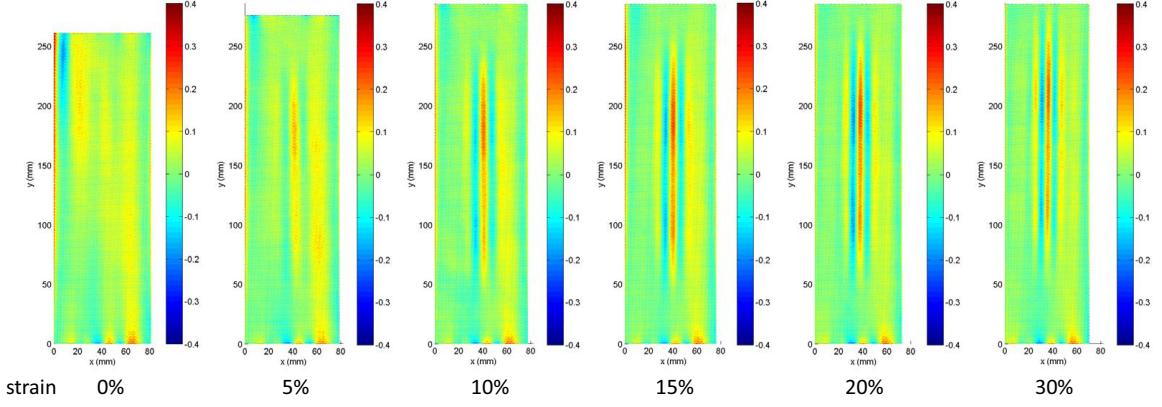
Figure 5.4: Experimental wrinkling profiles of the 254×82.55 mm (10×3.25 inch) membrane under strain of up to 30%.
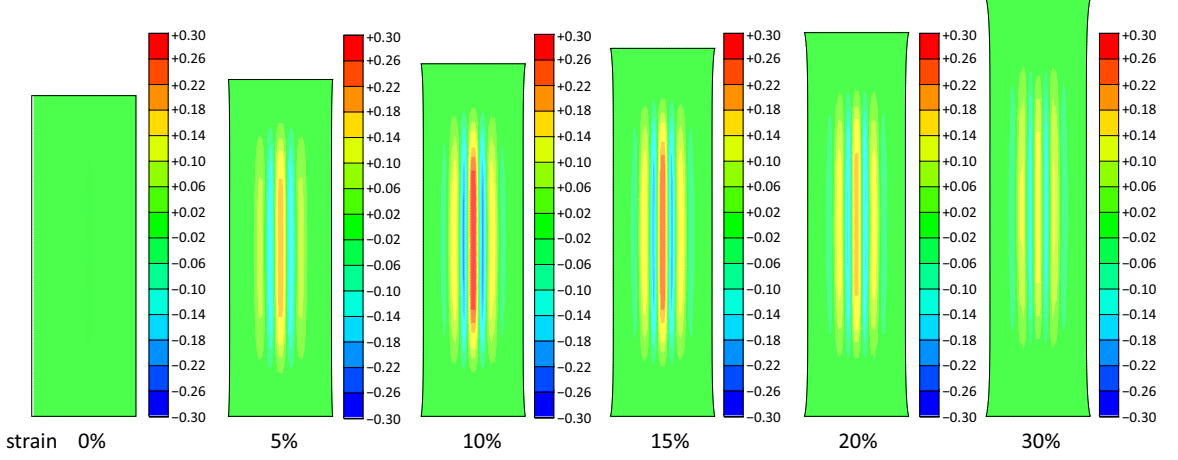
Figure 5.5: Numerical wrinkling profiles of the 254×82.55 mm (10×3.25 inch) membrane under strain of up to 30%.

For the 254×82.55 mm (10×3.25) inch membrane (with aspect ratio $L/W \simeq 3.0$), the maximum wrinkle amplitude initially occurs at the center of the membrane. As the tensile strain becomes large, the elongation of the membrane in the longitudinal direction exceeds its contraction in the

transverse direction, and thus its aspect ratio changes. Beyond a certain strain, the point of the maximum amplitude split into two and moves toward the clamped edges. This trend was observed on the membranes with aspect ratio close to 3. Typically, for membranes with aspect ratio less than 3 (i.e., the 254×101.6 mm one), the maximum wrinkle amplitude remains at the center of the membrane even when tensile strain becomes large; while for membranes with aspect ratio larger than 3 (i.e., the 254×63.5 mm one), the maximum wrinkle amplitude initially occur at two points equally apart from the center.
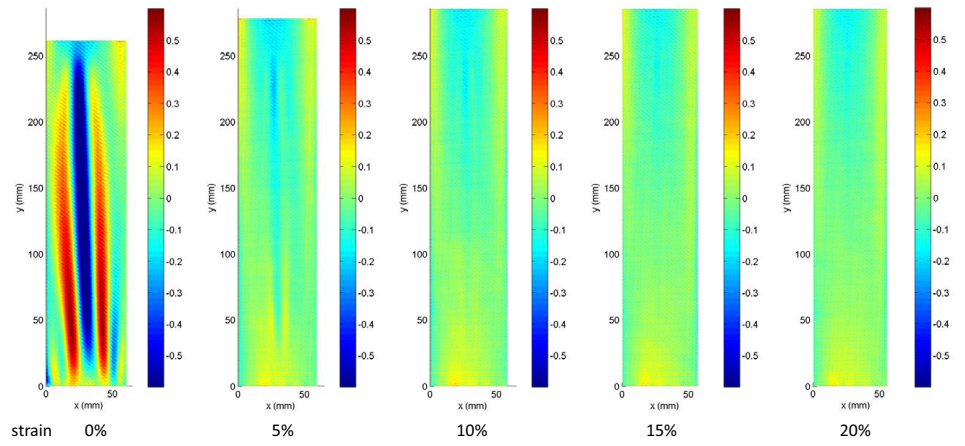
Figure 5.6: Experimental wrinkling profiles of the 254×63.5 mm (10×2.5 inch) membrane under strain of up to 20%.
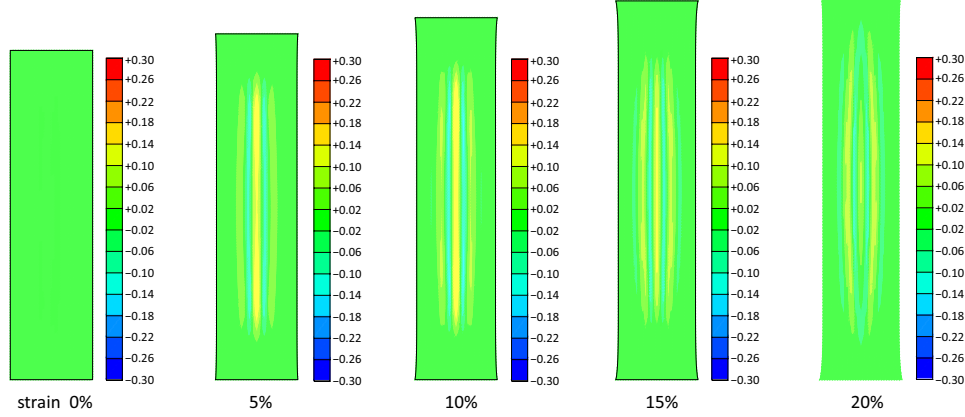
Figure 5.7: Numerical wrinkling profiles of the 254×63.5 mm (10×2.5 inch) membrane under strain of up to 20%.

For the 203.2×82.55 mm (8×3.25 inch) membrane, the out-of-plane deformations shown in the measurement results and the numerical results were in the opposite direction. Conventionally the numerical model always chooses to display the maximum wrinkle amplitude on its front side. However in the experiment the maximum wrinkle amplitude has equal chance to occur on either side of the membrane, not necessary on the front side which is facing the camera. This also reflects the bidirectional nature of bifurcation phenomena.
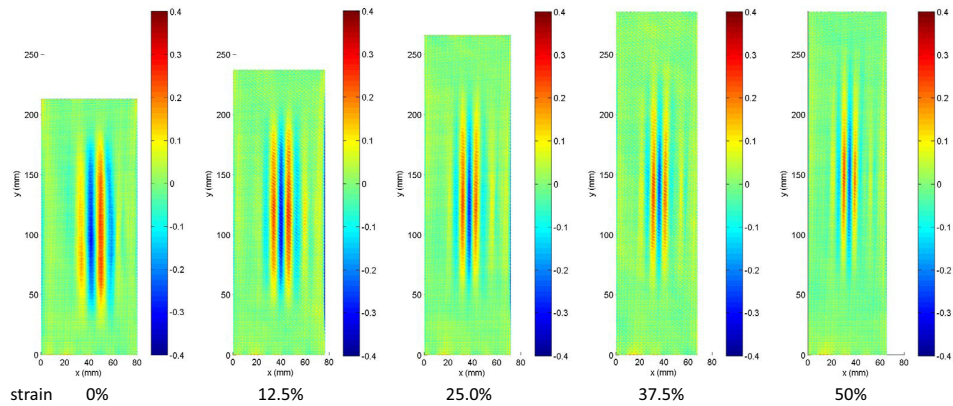
Figure 5.8: Experimental wrinkling profiles of the 203.2×82.55 mm (8×3.25 inch) membrane under strain of up to 50%.
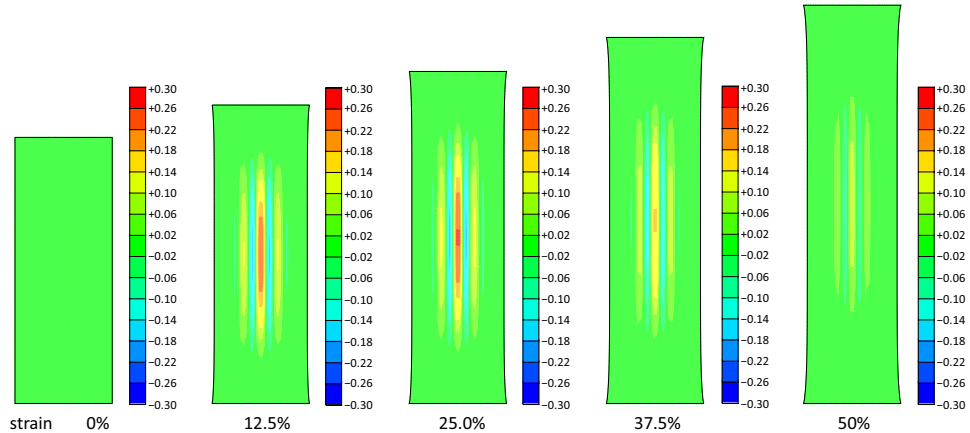
Figure 5.9: Numerical wrinkling profiles of the 203.2×82.55 mm (8×3.25 inch) membrane under strain of up to 50%.
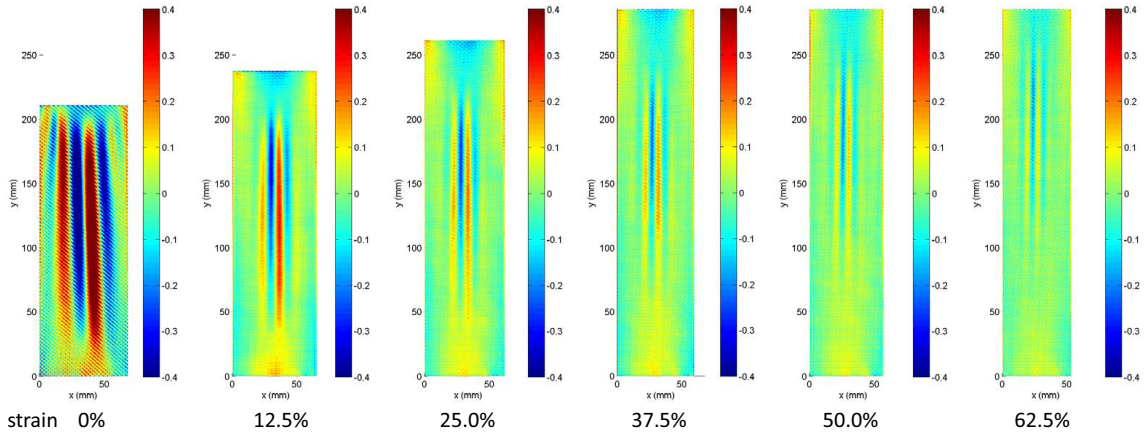
Figure 5.10: Experimental wrinkling profiles of the 203.2×69.85 mm (8×2.75 inch) membrane under strain of up to 62.5%.
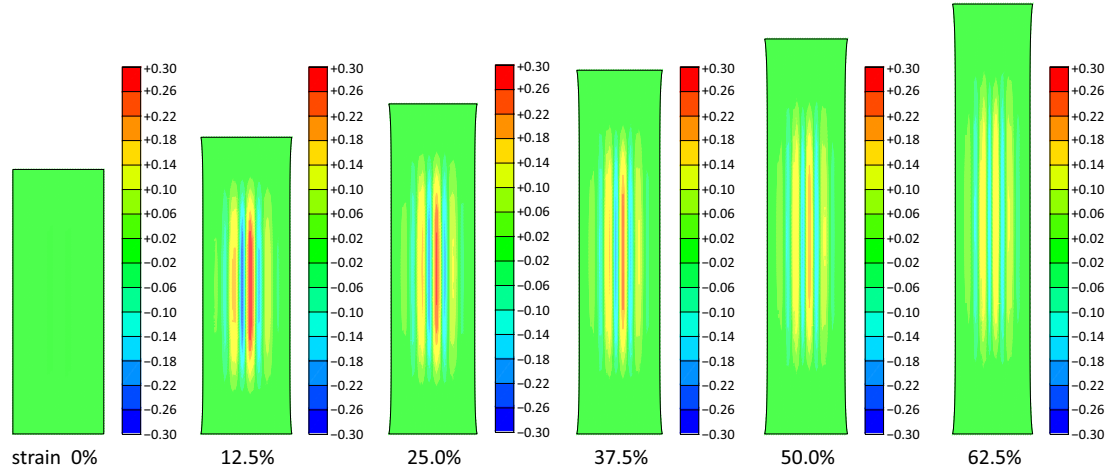
Figure 5.11: Numerical wrinkling profiles of the 203.2×69.85 mm (8×2.75 inch) membrane under strain of up to 62.5%.
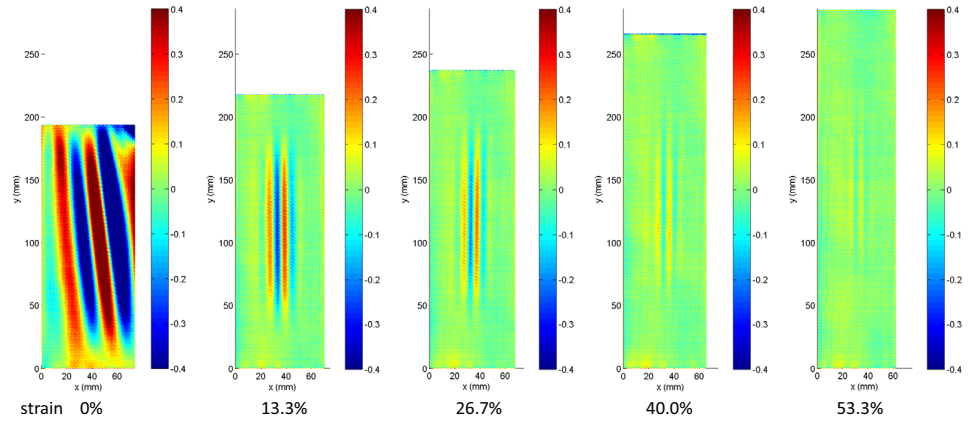
Figure 5.12: Experimental wrinkling profiles of the 190.5×76.2 mm (7.5×3 inch) membrane under strain of up to 53.3%.
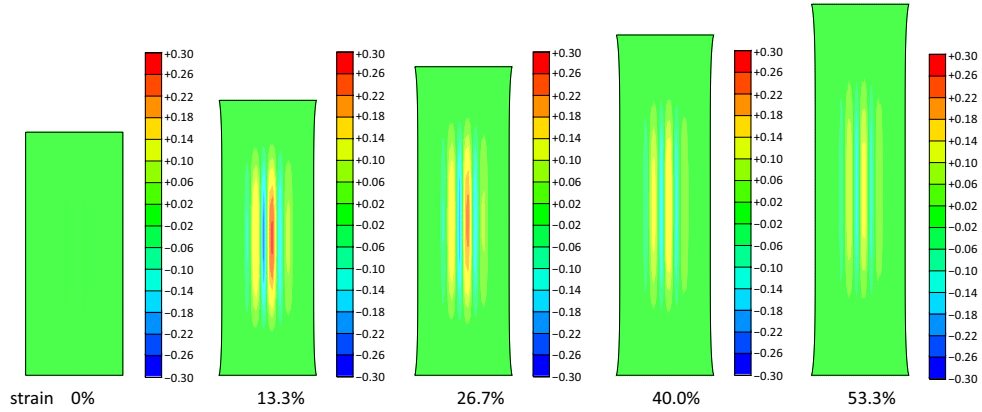
Figure 5.13: Numerical wrinkling profiles of the 190.5×76.2 mm (7.5×3 inch) membrane under strain of up to 53.3%.
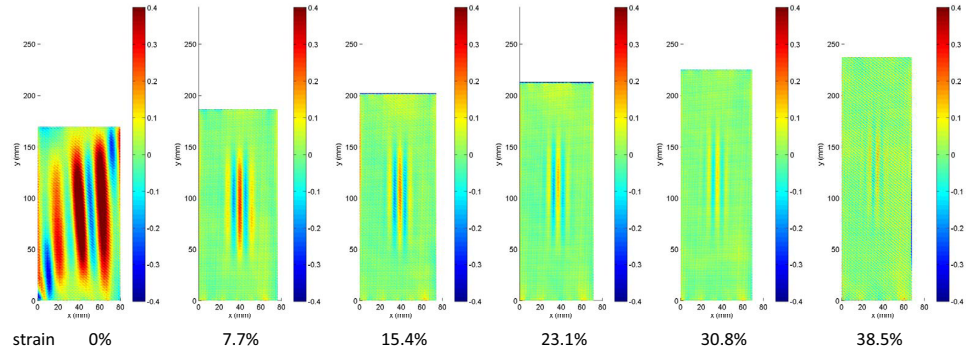
Figure 5.14: Experimental wrinkling profiles of the 165.1×82.55 mm (6.5×3.25 inch) membrane under strain of up to 38.5%.
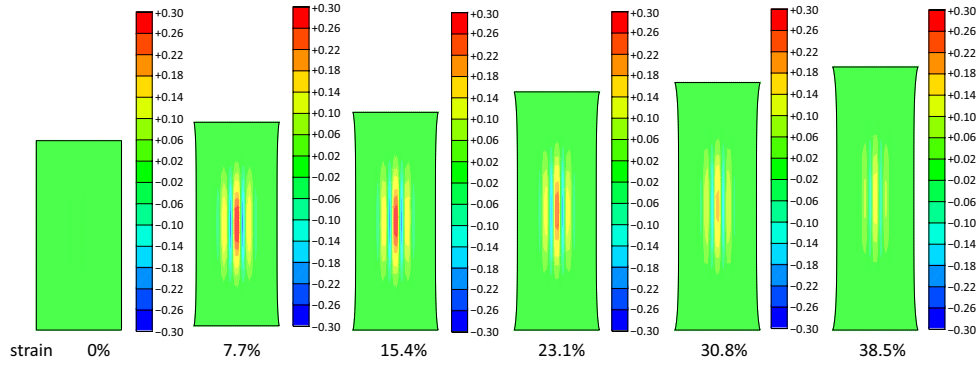
Figure 5.15: Numerical wrinkling profiles of the 165.1×82.55 mm (6.5×3.25 inch) membrane under strain of up to 38.5%.
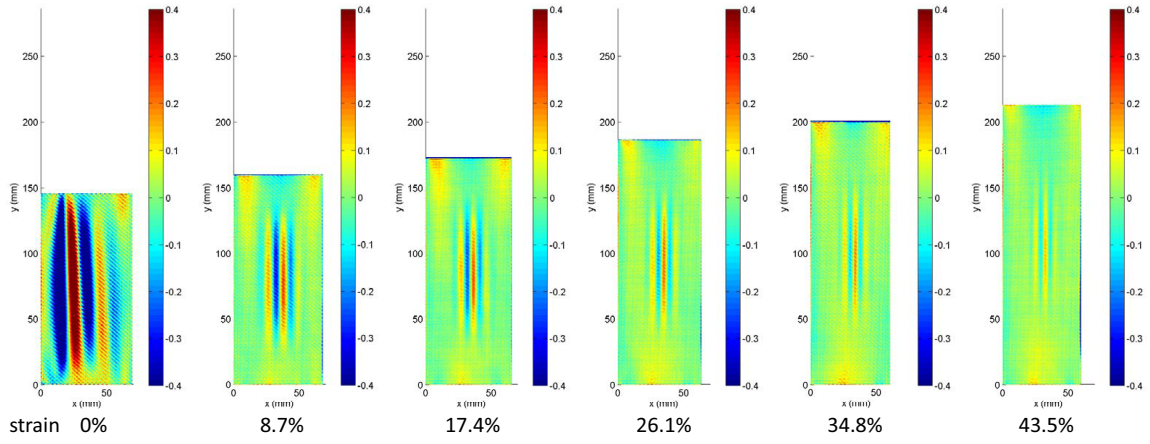
Figure 5.16: Wrinkling profiles of the 146.05×69.85 mm (5.75×2.75 inch) membrane under strain of up to 43.5%.
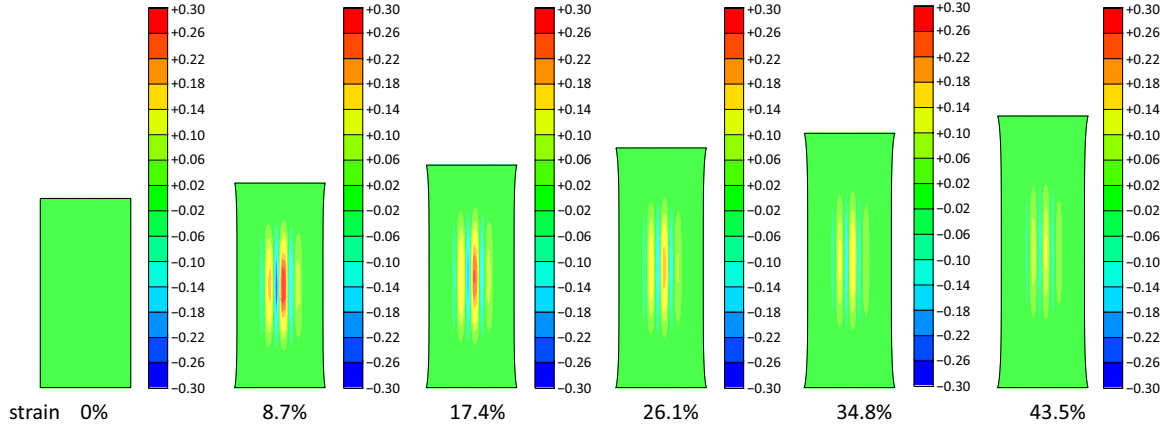
Figure 5.17: Wrinkling profiles of the 146.05×69.85 mm (5.75×2.75 inch) membrane under strain of up to 43.5%.

Chapter 6

Suppression Wrinkling by Dielectric Actuation

In this chapter, we examine the conceptual idea proposed in Chapter 1 about suppressing wrinkling on thin membrane structures by means of dielectric actuation which was verified.

6.1 Literature Review: Dielectric Elastomers as actuators

6.1.1 Electroactive Polymers (EAPs)

Fundamental and technological interest in electroactive polymers (EAPs), a broad class of organic actuators that exhibit large dimensional changes relative to their inorganic counterparts upon electrical stimulation, has grown tremendously over the past decade or so. Electroactive polymers can best be described as soft, flexible materials that are capable of converting electrical energy to mechanical energy and thus imparting a force or motion. EAPs are considered smart materials due to their responsive and often tunable properties, and they behave as actuators since they convert electrical energy into mechanical energy much in the same fashion as an electric motor can be used to generate torque. Since EAPs are also lightweight, flexible, tough, shape-processable and inexpensive (unlike their rigid and often fragile inorganic counterparts), they afford tremendous promise in emerging technologies ranging from micro air vehicles and flat-panel speakers to active video displays and artificial muscles (Shankar et al., 2007).

The EAP family includes two large categories: ionic EAPs and electronic EAPs. Examples of ionic EAPs are carbon nanotubes (CNTs), conductive polymers (CPs) and ionic polymer-metal composites (IPMCs). The electronic EAPs commonly are distinguished on the basis of their actuation mechanism as either electrostrictive (ferroelectric polymers) or electrostatic (dielectric elastomers).

6.1.2 Dielectric Elastomers

In dielectric elastomers (D-EAPs, also referred to as electroelastomers or electrostatically stricted polymers, ESSPs), the electric field-induced actuation response is initiated by the electrostatic attraction between oppositely charged conductive layers applied to the opposing surfaces of a thin elastomeric film.
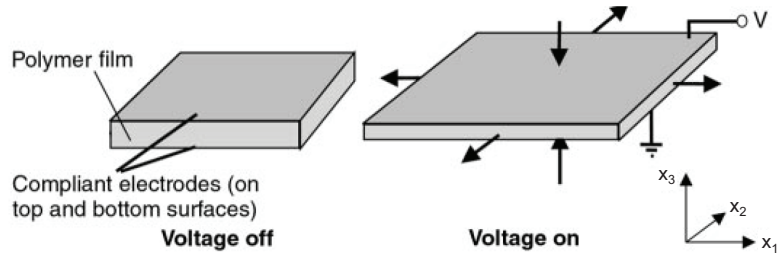
Figure 6.1: Schematic illustration of the operational principle of D-EAPs. Prior to actuation, the elastomer film is coated on each side with a compliant electrode. An applied electric field promotes attraction of the oppositely charged electrodes, thereby introducing a compressive Maxwell stress along the x_3 direction (Pelrine et al., 2000).

Upon application of a transverse electric field via compliant electrodes coated on opposing film surfaces (Figure 6.1), the D-EAP film compresses along the x_3 direction and expands laterally due to attractive electrostatic charges across the electrodes and repulsive like charges along each electrode. The Maxwell stress, commonly regarded as an electrostatic pressure acting perpendicular to the D-EAP film surfaces can be expressed as:

$$p = \epsilon_0 \epsilon (V/t)^2 \tag{6.1}$$

where ϵ_0 is the free-space dielectric permittivity ($\epsilon_0 = 8.85 \times 10^{-12}$ F/m) and ϵ is the dielectric constant of the silicone rubber (Pelrine el at., 2000).

Two parameters are commonly used to characterize the actuation performances of D-EAPs, the transverse strain (or thickness strain) and the in-plane strain (or areal strain). The transverse strain ε_{33} reflects a dimensional change in the thickness direction of an EAP film due to the normal pressure induced by an electrostatic Maxwell stress and is defined as $(t-t_0)/t_0$, where t and t_0 are the current thickness and original thickness respectively. If the strain is sufficiently small (i.e., $< 20\%$) such that the deformation due to actuation can be presumed to be linearly elastic, Hooke's law can be used to directly relate the transverse strain to the applied electric field:

$$\varepsilon_{33} = -\epsilon_0 \epsilon \frac{V^2}{Et^2}. \tag{6.2}$$

The in-plane strain is defined as $(A - A_0)/A_0$, where A denotes the active area of actuation in the $x_1 - x_2$ plane and the subscript 0 denotes pre-actuation. Compared with the transverse strain, the in-plane strain is relatively large and easy to measure. using a circular test configuration illustrated by diagrams and images displayed in Figure 6.2. Areal strain of 380% has been reported for acrylic D-EAPs as shown in Figure 6.3.
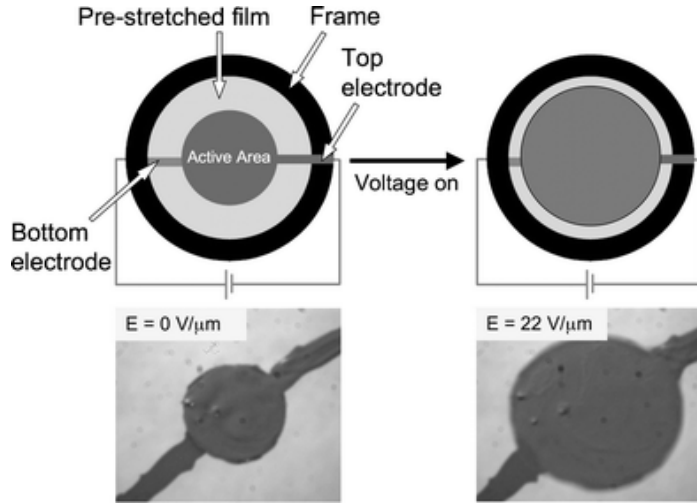
Figure 6.2: Circular experimental setup used to measure the electromechanical behavior of D-EAPs in the presence of an electric field and corresponding optical images. An elastomeric film is commonly subjected to a mechanical pre-strain and subsequently fixed to a frame prior to coating the active area on both film surfaces with a compliant electrode. Actuation upon electrical stimulation results in an increase in the active area, which is digitally measured and quantified (Shankar et al., 2007).

Figure 6.3: 380% in-plane strain of an acrylic based dielectric elastomer film due to an applied voltage (Kornbluh et al., 2000).

As seen from Eq. (6.1), the ideal dielectric elastomer material has a high dielectric constant ϵ, a high breakdown strength (V/t), and a low elastic modulus E. Desirable material also have low viscoelastic losses, large strain energy density and high electromechanical coupling efficiency. The electromechanical coupling efficiency is defined as the ratio of energy converted to mechanical work per cycle and electrical energy applied per cycle. Table 6.1 summarizes the performances of some typical dielectric elastomers.

Table 6.1: Representative dielectric elastomer materials performance (Pelrine el at., 2000).

Elastomer	Elastic energy density (J/cm^3)	Actuation pressure (MPa)	Thickness strain (%)	Young's modulus (MPa)	Electric field $(\text{V}/\mu\text{m})$	Dielectric constant	Coupling efficiency (%)
Silicone	0.22	1.36	32	1.0	235	3.2-9.8	54
Polyurethane	0.087	1.6	11	17	160	7.0	21
Fluoroelastomer	0.0046	0.11	8	2.5	32	12.7	15
Latex rubber	0.0059	0.11	11	0.85	67	2.7	21

One of the most important actuation metrics is the voltage- or field-induced actuation strain, and its dependence on applied voltage is presented in Figure 6.4 for various EAPs. The acrylic elastomer and some silicone elastomers exhibit the highest in-plane and transverse strains upon electrical stimulation and can sustain high electric field.
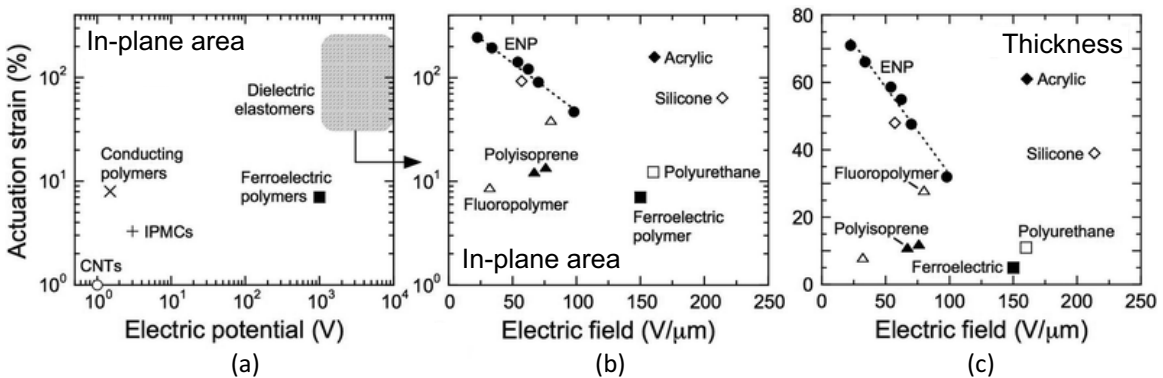
Figure 6.4: Comparison of the actuation-strain levels achieved for (a) various EAPs as a function of electric potential, and (b, c) D-EAPs and ferroelectric polymer as a function of electric field. The actuation strains are labeled in each part and include (a) in-plane areal strain, (b) in-plane area strain, and (c) thickness strain. The dotted lines serve as guides for the eye (Shankar et al., 2007).

Elastomer films can be made by casting, dipping, spin coating, or spraying. Spin coating generally yields the best-performing films because the spin coating process is able to fabricate films of high uniformity. Spin coating is also the preferred process for the thinnest films.

6.1.3 Compliant Electrodes

A key feature of dielectric elastomer technology is the use of compliant electrodes. If the electrodes cannot stretch in at least one planar direction of the film while its thickness contracts, actuation

is dramatically reduced because the polymer is essentially incompressible, i.e., its bulk modulus is much greater than its elastic modulus. Fortunately, the compliant electrodes need not be very conductive, due to the high voltage, low current drive situation.

The selection of electrode materials remains an area of ongoing research. Ideally we want a thin, extremely low-modulus electrode that provide uniform charge distribution over the surface of the film under the electrodes. The most successful materials have typically been based on small particles of carbon such as ultrafine graphite powder, carbon black and carbon grease.These materials can be deposited directly on the film in a screen-printing process, or they can be sprayed on the film with a fast-evaporating carrier liquid. In this study, carbon black grease CW7200BLK from Circuit Works is brushed on to the surface of the film through a stencil. It is difficult to get a smooth and uniform electrode layer. For many of the silicones that are capable of undergoing extremely large strains, it was necessary to coat these electrodes with a mixture of silicone-polymer-based graphite grease and carbon-filled silicone (Chemtronics CW7200 and Stockwell RTV 60-CON respectively) in order to ensure full coverage at large strains.

6.1.4 Applications of EAP Membranes

Macro-scale EAP membranes can perform specific out-of-plane displacements under activation, and thus is promising to drive lightweight structures with continuous surfaces to accomplish large active shape changes. Potential applications include drag and/or oscillation reduction of wind-exposed objects (i.e., bridges, buildings and ropeway gondolas) or fish-like propulsion of vehicles through air or water (Figure 6.5).
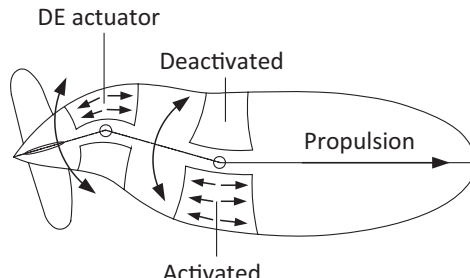
Figure 6.5: Inspired by the continuous shape changes of stingray wings for locomotion, a fish-like propulsion of a blimp with EAP membranes was proposed by Lochmatter et al. (2007).

Very large spherical or paraboloidal space telescope mirrors are designed by connecting segments of stretchable membrane with electrostatic curvature (SMEC). Each of the membrane segment forms a slight concave curvature under electrostatic pressure. The electric potential can be spatially and temporally controlled to obtain uniform curvature despite the non-uniform tension in the membrane. In this way a deployable space telescope of very long focal length can be made and rolled up for launch.
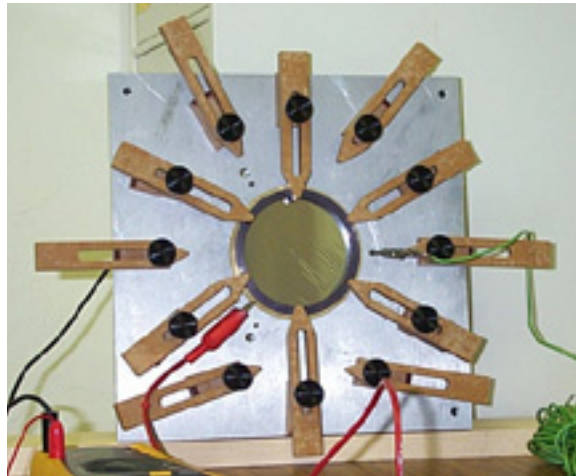
Figure 6.6: A three-inch stretched circular membrane mirror with electrostatic curvature. Here the out-of-plane deformation on membrane surface is favorable for the purpose of optical focal plane (Stamper et al., 2000).

6.2 Simple Analytical Models

As we discussed previously, wrinkling of thin membrane is essentially caused by in-plane compression, which may be suppressed by in-plane strain induced by electrostatic pressure. This forms the basis of the idea of suppressing wrinkling of dielectric elastomers by means of dielectric actuation.

We consider a piece of silicone rubber with material behavior described by the Mooney-Rivlin model occupying the space $\{\Omega : (-\frac{L}{2}, \frac{L}{2}) \times (\frac{W}{2}, \frac{W}{2}) \times (\frac{t}{2}, \frac{t}{2})\}$ and subjected to a uniaxial tension load in x_1 direction up to a certain stretch λ_1. Due to Poisson's effect, the rubber contracts in the x_2 and x_3 directions uniformly[1]. Now we fix the stretch in x_1 direction and apply an electric field such that at equilibrium the contraction in the x_2 direction can be canceled by the expansion due to the dielectric actuation, that is,

$$\lambda_2 = 1. \tag{6.3}$$

---

[1]For simplicity, the clamping boundary conditions are not considered.

In Section 4.4.1 we have shown the material behaviors of the silicone rubber can be described by the Mooney-Rivlin model through the material evaluation tool in ABAQUS. Eq. (4.11) gave the general expression of the strain energy potential of Mooney-Rivlin materials, in which the coefficients were determined based on experimental tensile test data and listed in Table 4.3. Due to the incompressibility, the last term in Eq. (4.11) can be eliminated. Ep. (4.11) can be rewritten as

$$
\begin{aligned}
U_{MR} = \quad & C_{10} \quad \left[\frac{\lambda_1^2}{(\lambda_1\lambda_2\lambda_3)^{2/3}} + \frac{\lambda_2^2}{(\lambda_1\lambda_2\lambda_3)^{2/3}} + \frac{\lambda_3^2}{(\lambda_1\lambda_2\lambda_3)^{2/3}} - 3)\right] \\
+ \quad & C_{01} \quad \left[\frac{(\lambda_1\lambda_2\lambda_3)^{2/3}}{\lambda_1^2} + \frac{(\lambda_1\lambda_2\lambda_3)^{2/3}}{\lambda_2^2} + \frac{(\lambda_1\lambda_2\lambda_3)^{2/3}}{\lambda_3^2} - 3\right],
\end{aligned}
\tag{6.4}
$$

where λ_i are the stretches along x_i directions.

By solving the equilibrium problem we try to find the relation between the uniaxial tensile stretch λ_1 and the applied voltage V. Given the strain energy potential in Eq. (6.4), the normal stress in each direction is

$$
\begin{aligned}
\sigma_{11} &= \frac{\partial U_{MR}}{\partial \lambda_1} + \bar{p}, \\
\sigma_{22} &= \frac{\partial U_{MR}}{\partial \lambda_2} + \bar{p}, \\
\sigma_{33} &= \frac{\partial U_{MR}}{\partial \lambda_3} + \bar{p}, \\
\sigma_{ij} &= 0, \quad i \neq j,
\end{aligned}
\tag{6.5}
$$

where $\bar{p}$ is the hydrostatic pressure and can be solved by letting $\sigma_{22} = 0$. Combining Eq. (6.3) with incompressibility, we have

$$
\lambda_3 = \frac{1}{\lambda_1}.
\tag{6.6}
$$

The equilibrium equation in the x_3 direction can be written as

$$
\sigma_{33} = -\epsilon\epsilon_0 \left(\frac{V}{t\lambda_3}\right)^2.
\tag{6.7}
$$

Substituting conditions Eqs. (6.3) and (6.6) into Eq. (6.7) yields an implicit relation between V and λ_1

$$
-\epsilon\epsilon_0 \left(\frac{\lambda_1}{t}\right)^2 V^2 = \frac{2}{3}C_{10}\left(-\lambda_1^3 + \lambda_1^2 - \lambda_1 - 2 + \frac{2}{\lambda_1} + \frac{1}{\lambda_1^2}\right) + \frac{2}{3}C_{01}\left(-2\lambda_1^3 - \lambda_1^2 + \lambda_1 + 2 + \frac{1}{\lambda_1} - \frac{1}{\lambda_1^2}\right).
\tag{6.8}
$$

Figure 6.7 illustrates the relationship between the tensile stretch and the voltage that needs to be applied to the silicone rubber through its thickness direction such that at equilibrium the membrane has no contraction in the transverse direction. Here the coefficients $C_{10} = 863076.127$ and

$C_{01} = -682611.888$ are used, which are calculated based on the tensile test along the normal direction up to 40% strain (Table 4.3). The two curves correspond to $\epsilon = 3.2$ and $\epsilon = 9.8$ respectively, between which typical dielectric constant of silicone rubbers ranges.
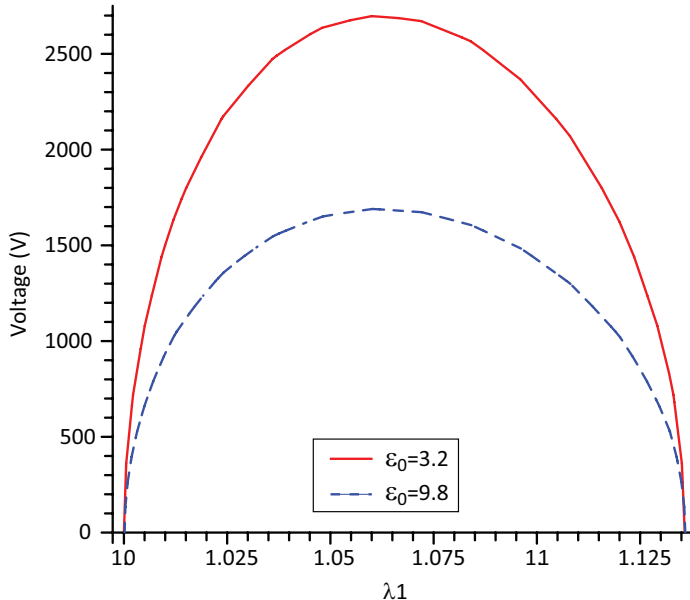
Figure 6.7: The voltage that needs to be applied to the silicone rubber through its thickness direction such that at equilibrium membrane has no contraction in the transverse direction vs. the uniaxial tensile stretch based on Mooney-Rivlin model.

6.3   Experimental Studies

6.3.1   Experiment Set-up

The uniaxial tension testbed introduced earlier in Section 3.2.1 was used for the experiments of membrane wrinkling under electric field. The testbed was made in polycarbonate material and assembled using plastic fasteners so that it is nonconductive. Membrane specimens were prepared in the same way as we mentioned in Section 3.2.2. A stencil ink brush was used to brush the compliant conductive grease (Molykote 41 Extreme High Temperature Grease, Dow Corning)[1] on the membrane surface, and then a stencil ink roller was used to smooth out the grease such that the compliant electrode layers becomes more uniform, though the absolute thickness was very difficult to measure and control. The grease was painted on the central area of the membrane to prevent shorting between the two electrodes at the edges. As seen in Figure 6.8(a) a copper wire was clamped between

---

[1]Chemical component of the grease: 40-70 wt% Phenylmethyl siloxane, trimethyl-terminated, 15-40 wt% Dimethyl, phenylmethyl siloxane, trimethyl-terminated, 15-40 Carbon black, 1-5 wt% mixed zinc carboxylates.

the grips at each end of the membrane from different sides in contact with the grease layer. The high-voltage input signal was generated by a programmable digitally synthesized function generator (Global Specialties, Inc. Model 2003) connected to a high voltage power amplifier (Trek, Inc. Model 10/10B) with a voltage range of ± 10 kV DC or peak AC as shown in Figure 6.8(b). The amplifier takes a low voltage input of the function generator and amplifies it to provide a high-voltage output with a gain of $1000\times$. A voltmeter was used to monitor the voltage change.

(a)   (b)
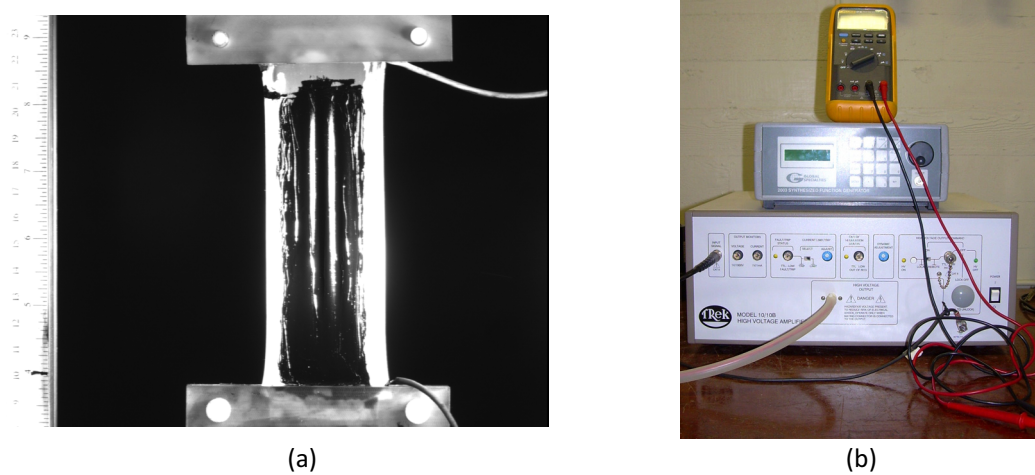
Figure 6.8: The experimental setup of suppressing membrane wrinkling using dielectric actuation, (a) membrane with electrodes on both sides clamped on the uniaxial tension testbed, (b) high voltage amplifier, function generator and voltmeter (from bottom to top).

6.3.2   Observations

As we discussed earlier in Section 3.4.1, it is very difficult to experimentally capture the moment of wrinkling onset and quantitatively determine the critical buckling load. With carbon grease electrode on the membrane surface becomes more unfavorable in terms of reflectivity and the fringe projection method is no longer capable of wrinkling shape measurement due to the lack of contrast on the fringes and the gain of reflectivity on membrane surfaces. The reflectivity of the surface finish plays a negative role in the optical measurement using fringe profilometry. Some regions on the wavy surface of the membrane may reflect the light from the LCD projector too much to carry the fringe information. Based on the above concerns, therefore, only post-buckling membrane response to the electric field was tested.

In order to capture the membrane's response to the through-thickness electric field, a sinusoidal mode with frequency 0.25 Hz and initial amplitude 3 V was chosen as the output signal from the

function generator. This signal then was amplified to 3 kV by the high-voltage amplifier and applied to the membrane electrodes. Amplitude of the sinusoidal signal was raised by 0.5 kV each time up to 8.5 kV. About 10 membrane specimens of different dimensions were tested under electric field, most of which failed at the initial voltage by burning at a point on the surface covered with grease. Failures were most likely to occur at a point where the membrane is thinner than the surrounding areas such that the electric field is higher. Among all the specimen the highest DC voltage that a membrane sustained was 8 kV. As the voltage was raised to 8.5 kV, the membrane immediately broke down. This indicates the breakdown strength of the silicone rubber we used is about 80 V/μm . Figures 6.9(a)-(c) demonstrate three snapshots of the wrinkling profiles of a 127×63.5 mm $(5 \times 2.5 \times 0.004$ inch) membrane at 20% strain in one period of the sinusoidal voltage with amplitude 8 kV. The snapshots were captured by the CCD camera at a rate of approximately 2 images/s.
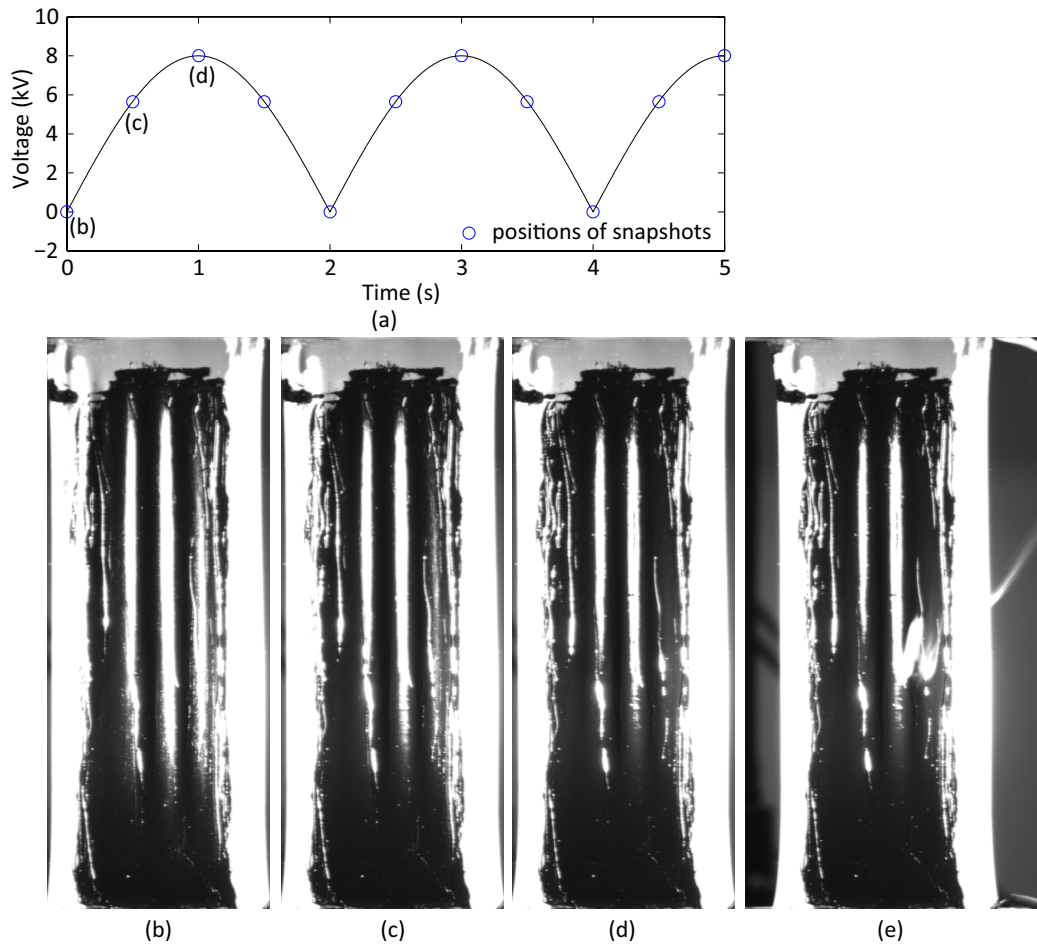
Figure 6.9: Membrane with conductive grease as compliant electrodes on both sides subjected to (a) a voltage in sinusoidal mode with amplitude 8 kV and frequency 0.25 Hz, (b)-(e) snapshots of wrinkling profiles on a 127×63.5 mm $(5 \times 2.5$ inch) membrane at three moments within a sinusoidal period, (d) breakdown of the membrane at 8.5 kV amplitude.

6.4 Numerical Studies

6.4.1 Simulation Techniques

ABAQUS limits the types of load that can be applied on a thin shell model. Unfortunately electrostatic pressure is not among those allowed. Hence an equivalent way by replacing the electric field with a thermal field is proposed. ABAQUS can analyze buckling due to thermal strain/stress. In an eigenvalue buckling analysis, nodal temperature can be specified, and the incremental thermal strain will be generated given the thermal expansion coefficient of the material. Both the incremental thermal strain and incremental tensile strain contribute to the incremental stiffness matrix, whose eigenvalues will be computed and used to predict the critical buckling load.

A simple analysis was developed to verify this equivalence and find out the relation between a voltage difference ΔV and a temperature difference ΔT for subsequent simulations.

We begin with the constitutive relation (Hooke's law) of a linearly elastic material for the three dimensional shell model under an electrostatic pressure,

$$\sigma_{ij} = \lambda \epsilon_{kk} \delta_{ij} + 2\mu \epsilon_{ij}. \tag{6.9}$$

For simplicity we neglect the boundary effect and assume the membrane is contracted uniformly under tension load, thus $\sigma_{13} = \sigma_{23} = 0$. The constitutive relation is rewritten as

$$\sigma_{11} = \lambda(\epsilon_{11} + \epsilon_{22} + \epsilon_{33}) + 2\mu \epsilon_{11}, \tag{6.10}$$

$$\sigma_{22} = \lambda(\epsilon_{11} + \epsilon_{22} + \epsilon_{33}) + 2\mu \epsilon_{22}, \tag{6.11}$$

$$\sigma_{33} = \lambda(\epsilon_{11} + \epsilon_{22} + \epsilon_{33}) + 2\mu \epsilon_{33}, \tag{6.12}$$

$$\sigma_{12} = 2\mu \epsilon_{12}. \tag{6.13}$$

From (6.12),

$$\epsilon_{33} = \frac{1}{\lambda + 2\mu} \left[\sigma_{33} - \lambda(\epsilon_{11} + \epsilon_{22}) \right]. \tag{6.14}$$

Here the σ_{33} is the prescribed electrostatic pressure, $p = \epsilon \epsilon_0 \left(\frac{V}{t} \right)^2$. By plugging (6.14) in (6.10), (6.11) and (6.13), and replace σ_{33} with p, we eliminate the thickness strain, ϵ_{33}, and get

$$\sigma_{11} = \left(\lambda + 2\mu - \frac{\lambda^2}{\lambda + 2\mu} \right) \epsilon_{11} + \left(\lambda - \frac{\lambda^2}{\lambda + 2\mu} \right) \epsilon_{22} + \frac{\lambda}{\lambda + 2\mu} p, \tag{6.15}$$

$$\sigma_{22} = \left(\lambda + 2\mu - \frac{\lambda^2}{\lambda + 2\mu}\right)\epsilon_{22} + \left(\lambda - \frac{\lambda^2}{\lambda + 2\mu}\right)\epsilon_{11} + \frac{\lambda}{\lambda + 2\mu}p, \tag{6.16}$$

$$\sigma_{12} = 2\mu\epsilon_{12}. \tag{6.17}$$

Similarly we can write the constitutive relations of a three dimension shell model subjected to a thermal field given the thermal expansion coefficient of the material, α, Young's modulus, E' and the Poisson's ratio ν' of another linearly elastic material,

$$\sigma_{ij} = \lambda'\epsilon_{kk}^{\alpha}\delta_{ij} + 2\mu'\epsilon_{ij}^{\alpha}, \tag{6.18}$$

where $\epsilon_{ij}^{\alpha} = \epsilon_{ij} - \epsilon_{ij}^{T}$, and and $\epsilon_{ij}^{T} = \alpha\Delta T\delta_{ij}$ is the thermal strain. In the case of thermal load, the model is in a plane stress state. Write Eq. (6.18) explicitly,

$$\sigma_{11} = \left(\lambda' + 2\mu'\right)\epsilon_{11} + \lambda'\epsilon_{22}, -2(\lambda' + \mu')\alpha\Delta T \tag{6.19}$$

$$\sigma_{22} = \left(\lambda' + 2\mu'\right)\epsilon_{22} + \lambda'\epsilon_{11}, -2(\lambda' + \mu')\alpha\Delta T \tag{6.20}$$

$$\sigma_{12} = 2\mu'\epsilon_{12}. \tag{6.21}$$

Compare the stress state under electrostatic pressure described in Eqs. (6.15)-(6.17) and the stress state under thermal field described in Eqs. (6.19)-(6.21), we find the conditions on which the two kinds of loading are equivalent. The temperature and voltage satisfy,

$$\alpha\Delta T = -\frac{\lambda}{2(\lambda + 2\mu)(\lambda' + \mu')}\epsilon\epsilon_0\left(\frac{V}{t}\right)^2, \tag{6.22}$$

and a new linear elastic material needs to be defined which satisfies,

$$E' = E\frac{1 + 2\nu}{(1 + \nu)^2}, \tag{6.23}$$

$$\nu' = \frac{\nu}{1 + \nu}. \tag{6.24}$$

6.4.2   Finite Element Model

The previous finite element model and the analysis procedure discussed in Chapter 4 were employed with several minor changes. The material property was modified to include a thermal expansion coefficient 10^{-6} K^{-1}; the Young's modulus and Poisson's ratio became 0.89 MPa and 0.33 respectively instead of 1 MPa and 0.5. In the initial step, besides the pre-stress, a uniform temperature field equivalent to the desired electric field was prescribed to the entire model as the base state of the buckling step. A larger pre-stress may be required to generate positive eigenvalues. In

the post-buckling analysis, the membrane was first stretched to reach a maximum amplitude and subjected to an electric field through the thickness direction while the two clamped edges were fixed.

6.5 Discussion

6.5.1 Wrinkle Onset

In Section 4.5.1 the influence of membrane dimension, thickness and aspect ratio on wrinkling onset were discussed. In this section this influence will be reexamined, this time under an electric field of 5×10^7 V/m (5 kV voltage across 0.1 mm membrane) by conducting the eigenvalue buckling analysis on the same 144 membrane dimensions.

The contour map of the critical buckling strains is revisited. In Figure 6.10 the dotted isolines representing the results with electric field show similar shapes as the solid isolines representing the previous results without electric field but enclose smaller area than the solid isolines of the same value. The dimensions which fall between a solid isoline and the dotted isoline of the same critical buckling strain value are the ones that wrinkle beyond that strain without electric field but do not wrinkle any more with electric field. In short, the electric field raises the threshold of the wrinkling instability.

Table C.1 in Appendix C compares the critical buckling strains without electric field and with 5×10^7 V/m electric field for each membrane dimension simulated.

An interesting consistency is found between the two sets of results. Among all the dimensions simulated, the 254×139.7 mm (10×5.5 inch) membrane consistently has the lowest critical buckling strain, 1.5% without electric field versus 10.0% with electric field; while the 101.6×31.75 mm (4×1.25 inch) membrane consistently has the highest critical buckling strain, 62.2% versus 72.0%. Their threshold of wrinkling are raised by 591% and 15% respectively. Considering all the dimensions, the increase of the critical buckling strain due to the emergence of electric field spans from 11% to 610%, and is more significant for those dimensions which originally exhibit lower structural stability without electric field.

For a specific dimension, this threshold of wrinkling can be further raised by turning up the applied voltage. Figure 6.11 shows a nonlinear monotonic relation between the critical buckling strain and the applied voltage. The critical buckling strain under 8 kV voltage is almost 6 times the one under 1 kV voltage. The plateaus at the two ends of the trend curve indicates that the
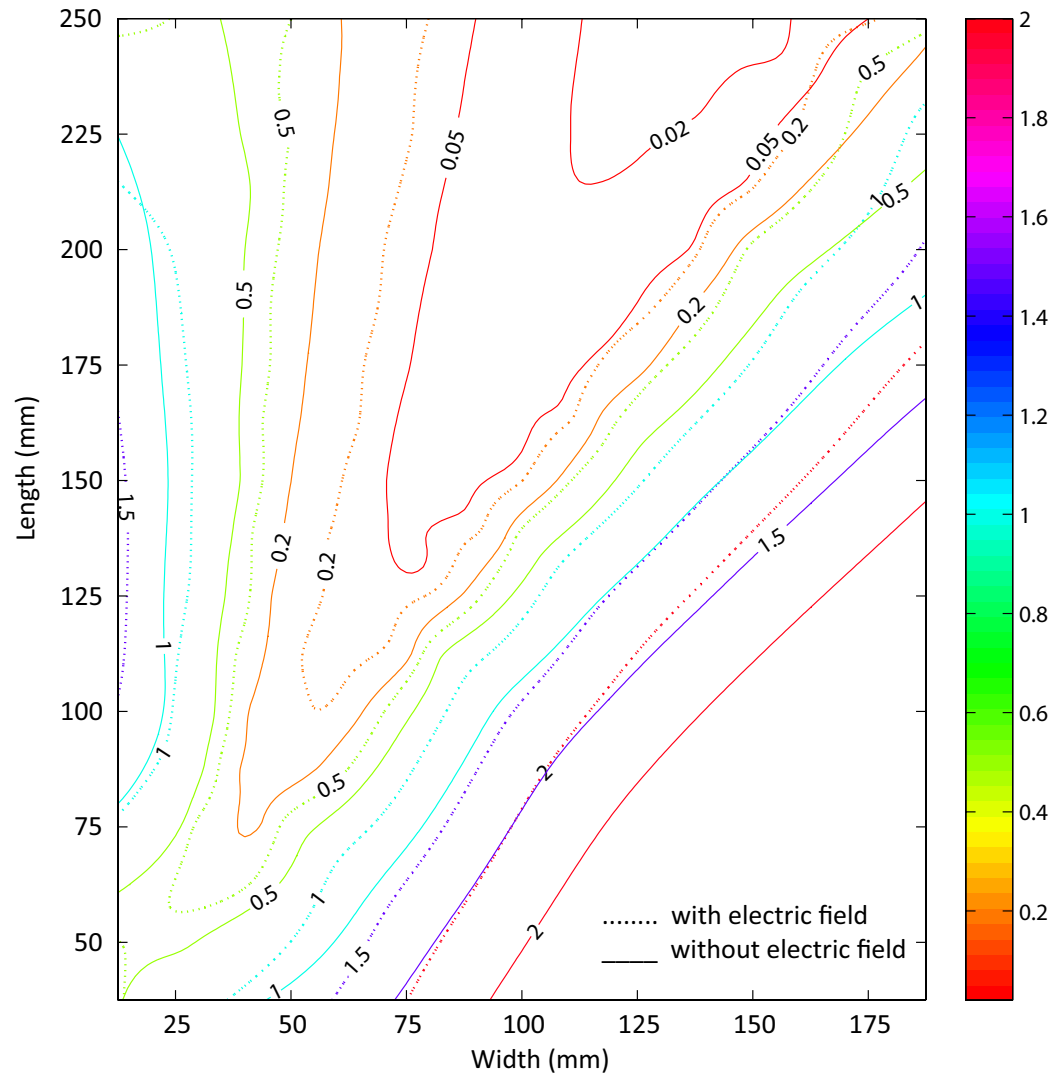
Figure 6.10: Contour maps of critical buckling strain for thickness $t = 0.1$ mm (0.004 inch) under 0 V (solid line) and 5 kV (dotted line) voltage.

applied voltage has to be large enough to be effective, and beyond a certain voltage the effect may be saturated.
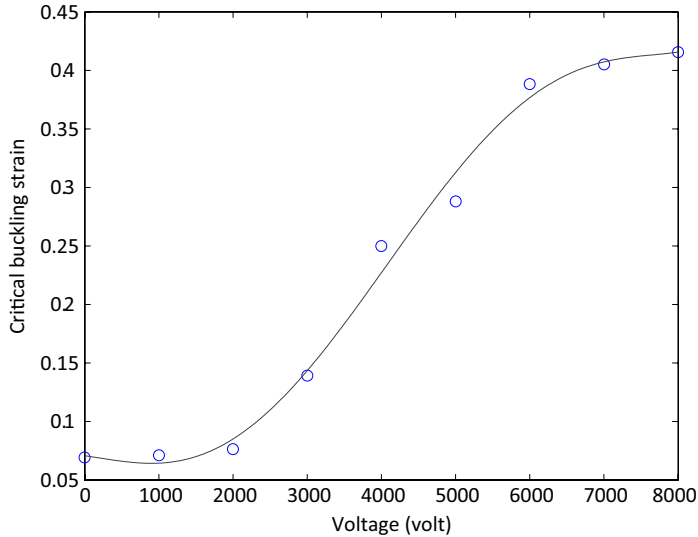
Figure 6.11: The critical buckling strain versus the applied voltage for the 127×63.5 mm (5×2.5 inch) membrane.

Next we reduced the thickness of the model by one half and repeated the simulations for all the dimensions. Now we have four sets of critical buckling strain results for the combinations of membrane thickness (0.05 mm and 0.1 mm) and voltage (0 V and 5 kV), all of which are listed in Tables C.1 and C in Appendix C. The contour map in Figure 6.12 compares the critical buckling strain under 0 V and 5 kV voltages for membrane of 0.05 mm, and once again confirms with electric field dielectric elastomer membranes need a larger tensile load to pass the barrier of bifurcation. We also compared the critical buckling strains of the 0.05 mm membrane with the 0.1 mm one under 5 kV voltage in another contour map in Figure 6.13. In general thicker membranes have larger bending stiffnesses and thus higher structural stabilities.

In the previous analysis in Section 4.5.1 the dependence of the critical buckling load on normalized membrane thickness, t/W, was studied and a quadratic relation was discovered. Here this dependence under 5 kV applied voltage is reexamined and compared with the previous one in Figure 6.14. In the presence of electric field a quadratic dependence of the critical buckling strain on t/W is established. Note that only curves corresponding to membrane aspect ratio 2 are shown in this figure. For other aspect ratios the quadratic relation are also valid. The difference between the two quadratic curves is non-uniform, and is larger for thickness membranes, indicating that the same voltage has greater influence on thicker membranes.
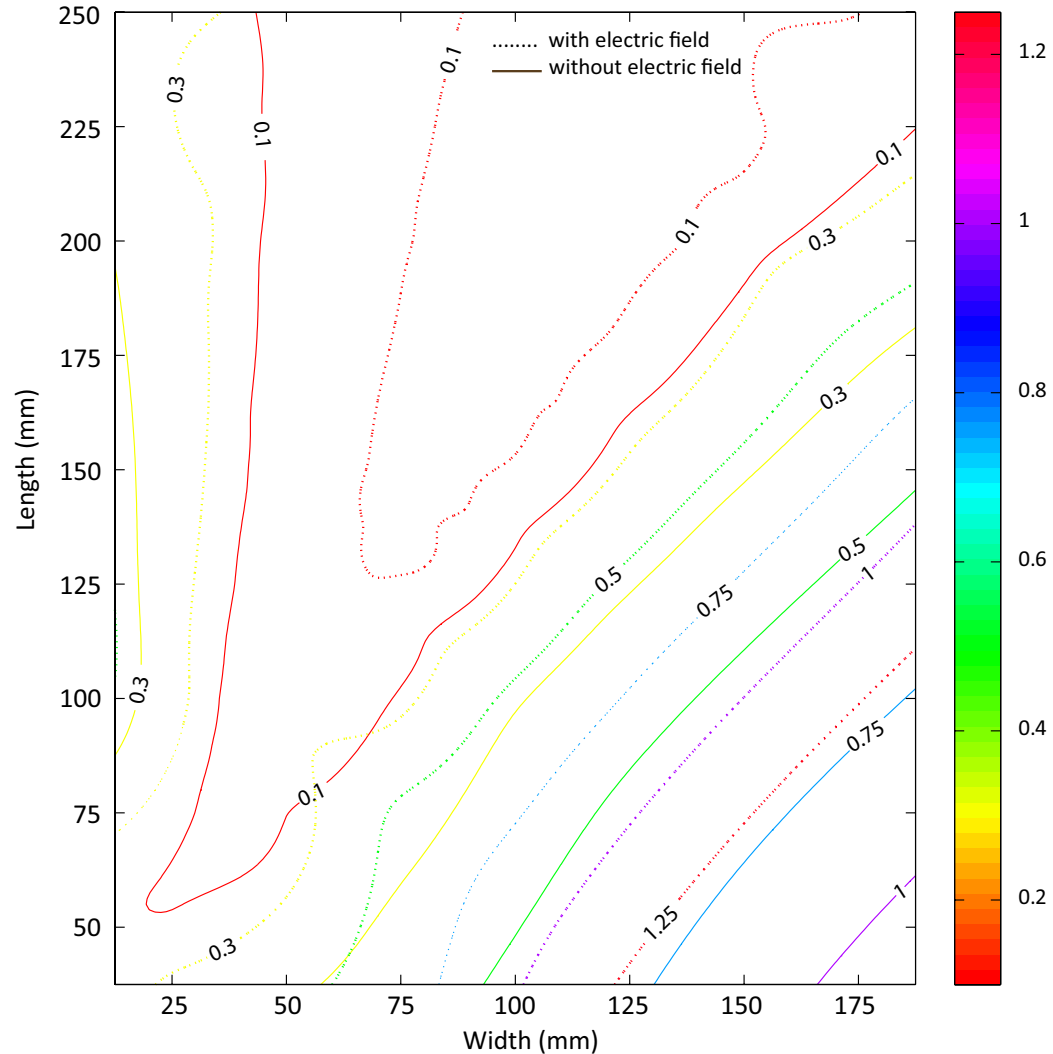
Figure 6.12: Contour maps of critical buckling strain for thickness $t = 0.05$ mm (0.002 inch) under 0 V (solid line) and 5 kV (dotted line) voltage.
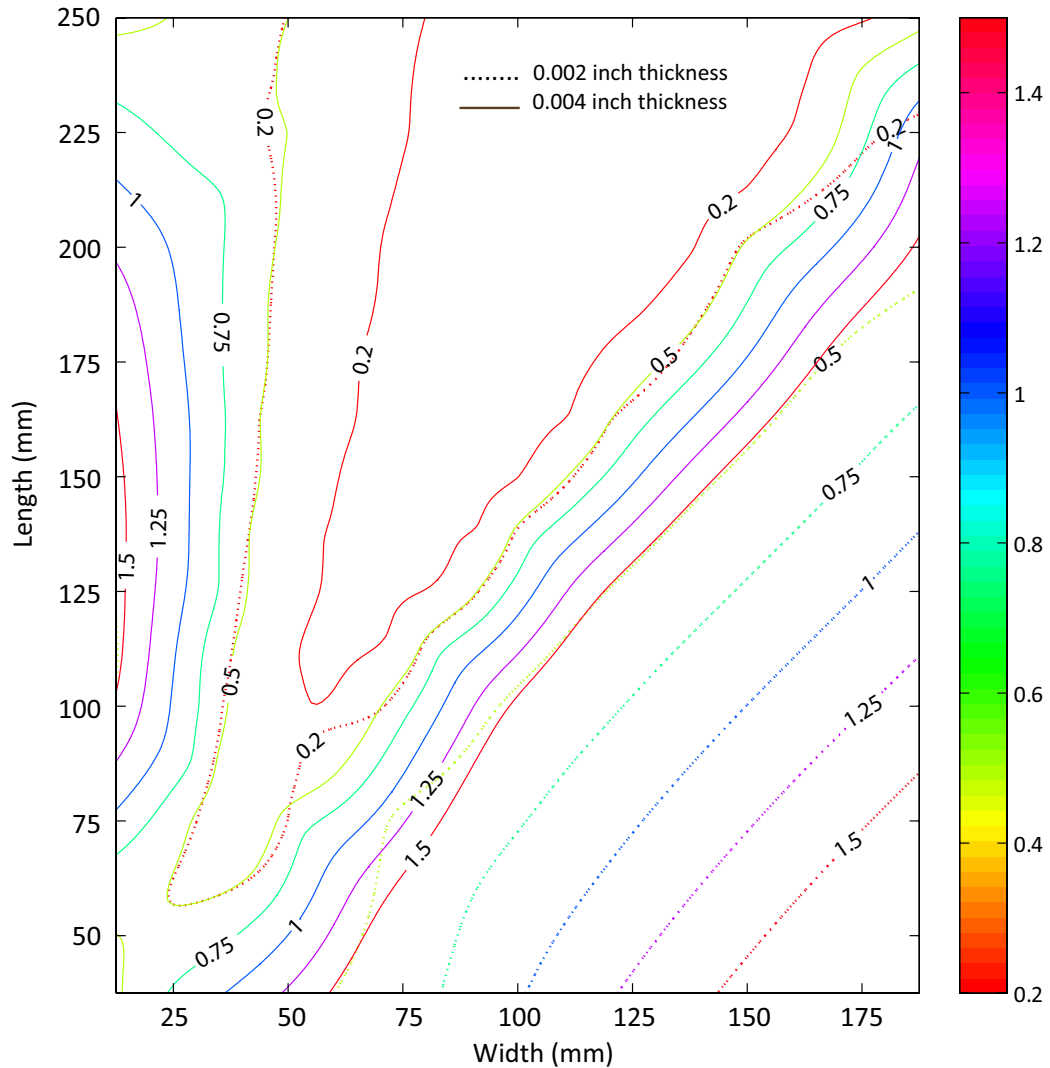
Figure 6.13: Comparison of the contour maps of critical buckling strain under 5×10^7 V/m electric field for thickness $t = 0.05$ mm (dotted line) and thickness $t = 0.1$ mm (solid line).
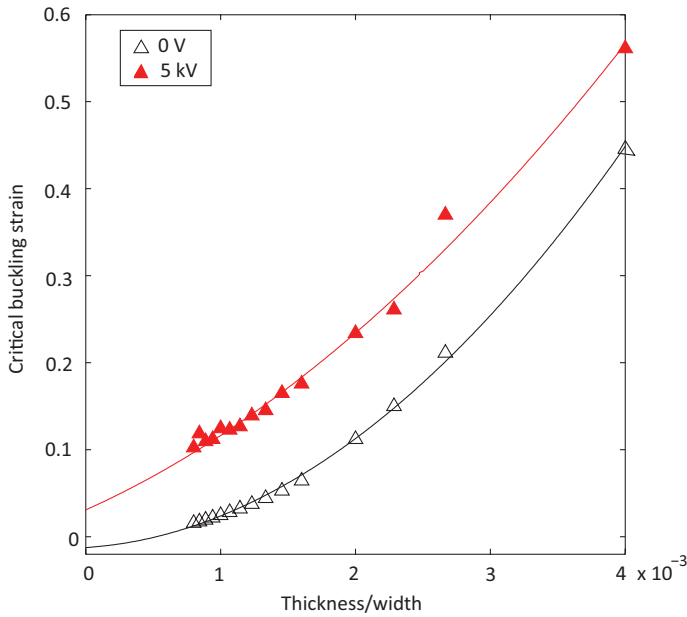
Figure 6.14: Critical buckling strain vs. normalized membrane thickness t/W for fixed aspect ratio $L/W = 2$ without and with 5×10^7 V/m electric field.

Lastly the dependence of the critical buckling strain on membrane aspect ratio is reexamined. The critical buckling strains of the 144 dimensions are first normalized by $(t/W)^2$ and then plotted as a function of the membrane aspect ratio L/W. In Figure 6.15, two sets of results are compared: the results with electric field in color markers sorted by the width of the membrane and the previous results without electric field in black dots. Prior to the application of electric field the dependence of the normalized critical buckling strain on the aspect ratio can be described in the form of a single function, which is nonlinear with a minimum at around $L/W = 2$. This means the critical buckling strain once normalized is unique for any given aspect ratio. However, it is a different story when there is an electric field. Instead of one curve, a band of curves emerge, each of which corresponds to a t/W ratio and a minimum at $L/W = 2$. This can be understood better by looking at one specific aspect ratio, $L/W = 2$. In our simulation there are 14 different dimensions corresponding to this aspect ratio. In the case of no electric field their normalized critical buckling strains are the same because their critical buckling strain is proportional to $(t/W)^2$ with zero offset as seen in Figure 6.14. While with electric field, the 14 data points shift upward by different amount and spread out vertically, because the quadratic relation between the critical buckling strain and t/W is offset by the electric field in different amount as seen in Figure 6.14. Hence, a simple normalization cannot take their critical buckling strain to the same value.
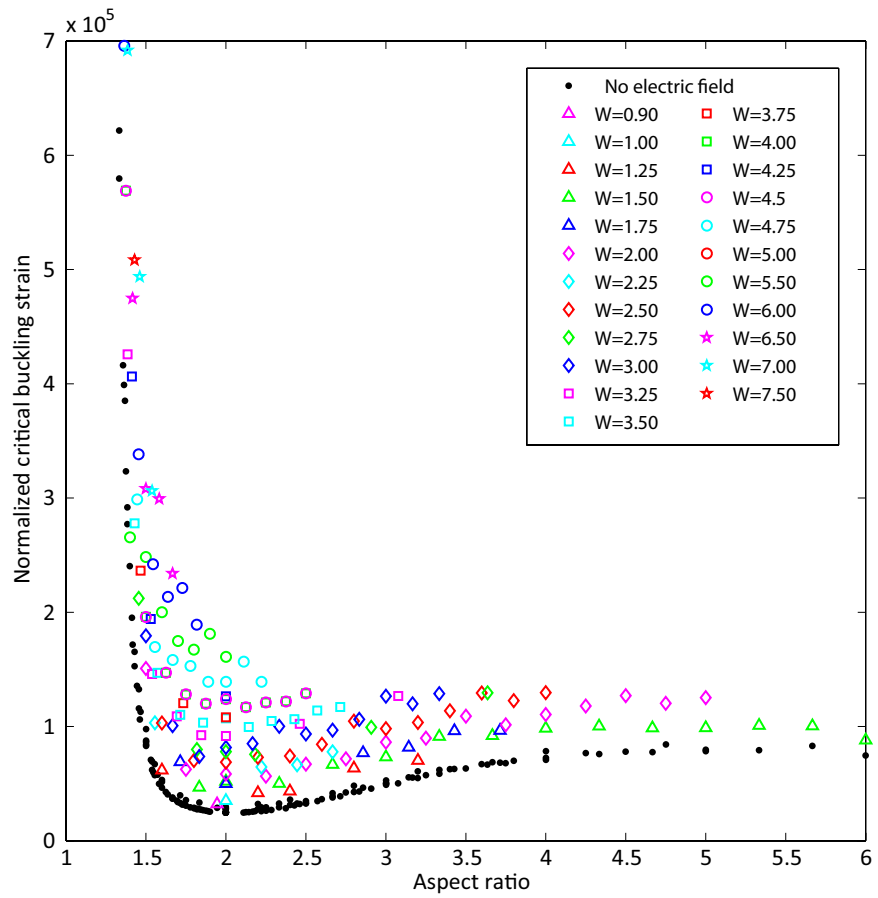
Figure 6.15: The normalized critical buckling strain vs. membrane aspect ratio L/W without and with 5×10^7 V/m electric field. The critical buckling strain is normalized by $(t/W)^2$.

6.5.2 Stress Distribution

Similar to the two-dimensional static analysis we discussed in Section 4.5.2 a two-dimensional static analysis was conducted prior to the post-buckling analysis to study the influence of electric field on the stress distribution of dielectric elastomer membranes. Previously we have found that generally the magnitude of the compressive stress does not increase monotonically with the uniaxial tensile load. For example, for the 127×63.5 mm (5×2.5 inch) membrane, the maximum compressive stress occurred when tensile strain applied reached 19.1%. Further stretch leads to a decrease in the compressive stress and the wrinkling amplitude accordingly. Therefore, a numerical test was designed as follows. A uniform zero temperature field was predefined in the initial step; following which a tensile load was applied to membrane in terms of edge displacement up to the point where the maximum compressive stress is reached. In the third step, the predefined temperature was ramped up to a certain value representing the desired voltage with the relation defined in Eq. (6.22). The material properties and element type remained the same as the previous stress analysis except a thermal expansion coefficient was introduced. We restrict our discussion to the 127×63.5 mm (5×2.5 inch) membrane in the present section and next section.

Figures 6.16-6.20 demonstrate the evolution of the normal stress σ_{22} on the 127×63.5 mm (5×2.5 inch) membrane under electric field. As the strength of the electric field increases, both the magnitude of the compressive stress and the region it covers decrease. Accompanied with the reduction of the compressive stress, the magnitude of the tensile stress near the clamping boundary is also reduced, and the membrane is expanded laterally. When the voltage reaches 8785 volts (Figure 6.20), the membrane surface becomes almost stress free and the lateral contraction due to the Poisson's effect is canceled by the expansion due to the dielectric effect.

As the incompressible membrane is squeezed in thickness direction by the Maxwell stress, it expands laterally and recovers its original rectangular shape. As a result, the magnitude of the σ_{22} is significantly reduced in both the tensile and compressive portions, which can be clearly viewed in Figure 6.21 by plotting σ_{22} along the entire longitudinal centerline. The compressive portion of σ_{22} is 2 orders of magnitude smaller than the tensile one and thus its variance is hardly observed in this figure.

Should the applied voltage be further raised, the membrane would overexpand laterally and the region of compressive and tensile σ_{22} would switch, that is, tension appears in the central area while the compression stress of one order of magnitude higher appears near the clamping boundary as shown in Figure 6.22.
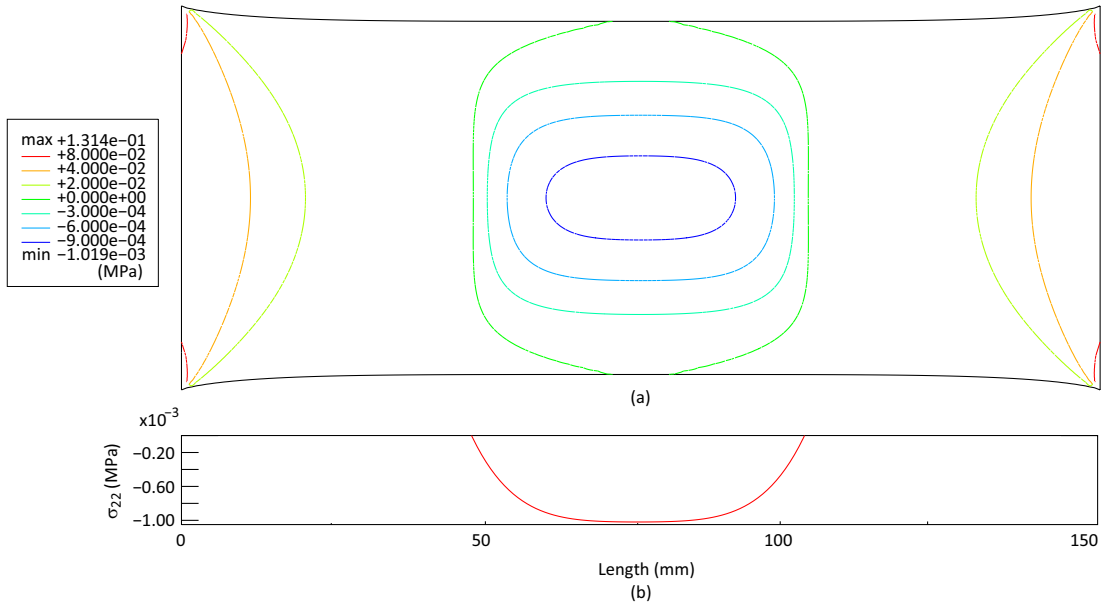
Figure 6.16: The distribution of the normal stress σ_{22} on a 127×63.5 mm (5×2.5 inch) membrane subjected to 20% tensile strain. (a) isolines of σ_{22}, (b) σ_{22} along the longitudinal centerline in the region $\sigma_{22} \leq 0$ only.
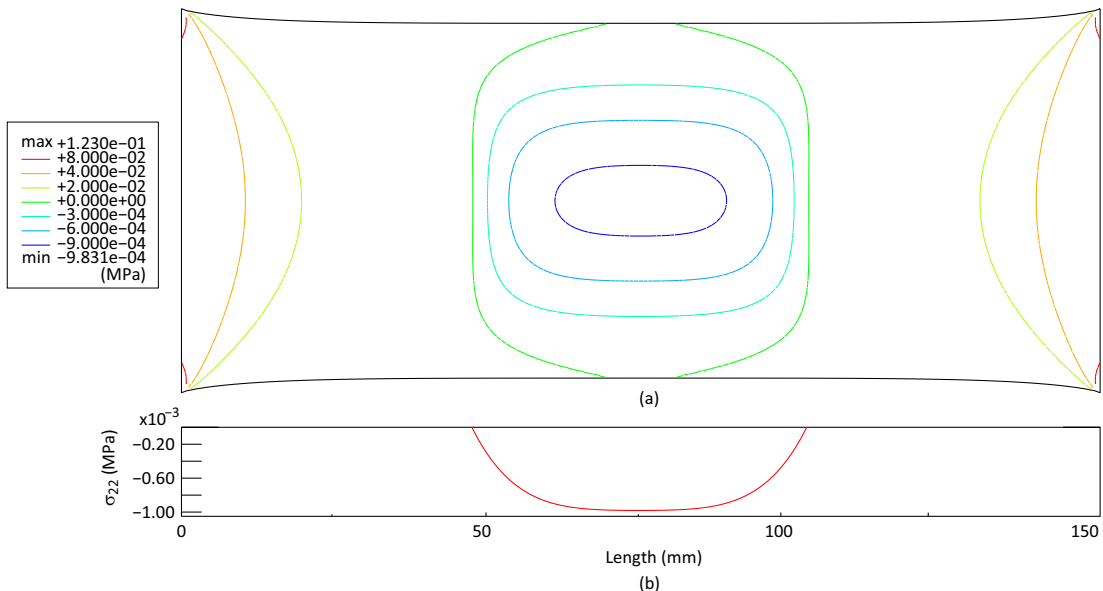
Figure 6.17: The distribution of the normal stress σ_{22} on a 127×63.5 mm (5×2.5 inch) membrane subjected to 20% tensile strain and 2000 V voltage subsequently. (a) isolines of σ_{22}, (b) σ_{22} along the longitudinal centerline in the region $\sigma_{22} \leq 0$ only.
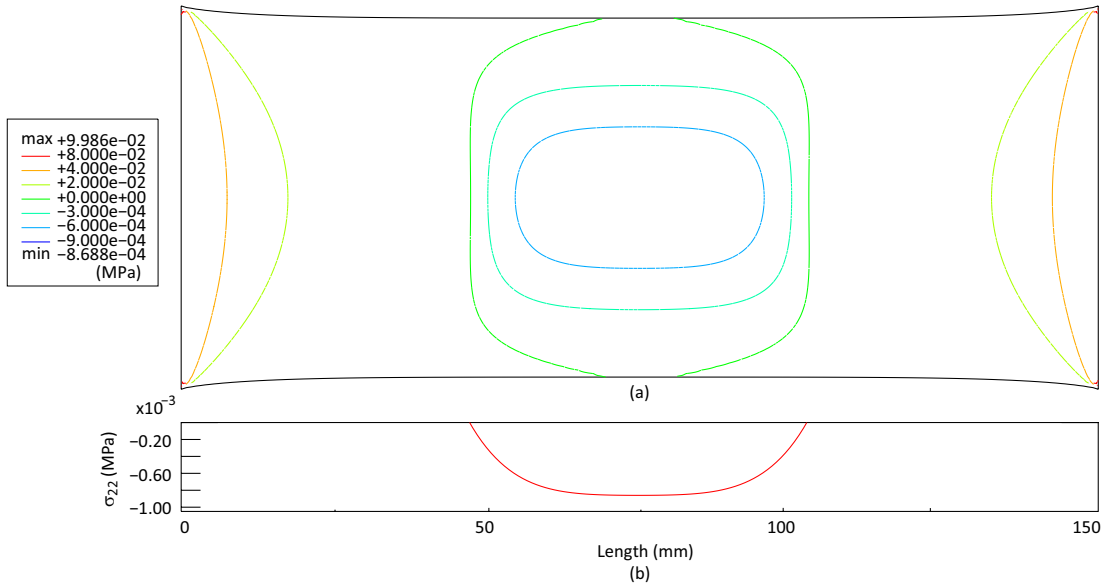
Figure 6.18: The distribution of the normal stress σ_{22} on a 127×63.5 mm (5×2.5 inch) membrane subjected to 20% tensile strain and 4000 V voltage subsequently. (a) isolines of σ_{22}, (b) σ_{22} along the longitudinal centerline in the region $\sigma_{22} \leq 0$ only.
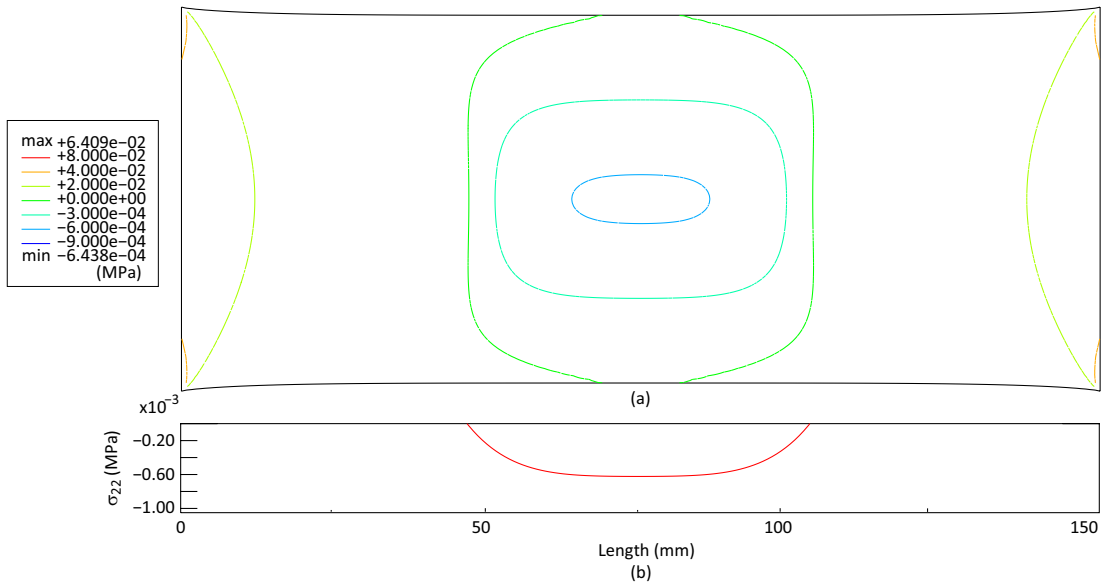
Figure 6.19: The distribution of the normal stress σ_{22} on a 127×63.5 mm (5×2.5 inch) membrane subjected to 20% tensile strain and 6000 V voltage subsequently. (a) isolines of σ_{22}, (b) σ_{22} along the longitudinal centerline in the region $\sigma_{22} \leq 0$ only.
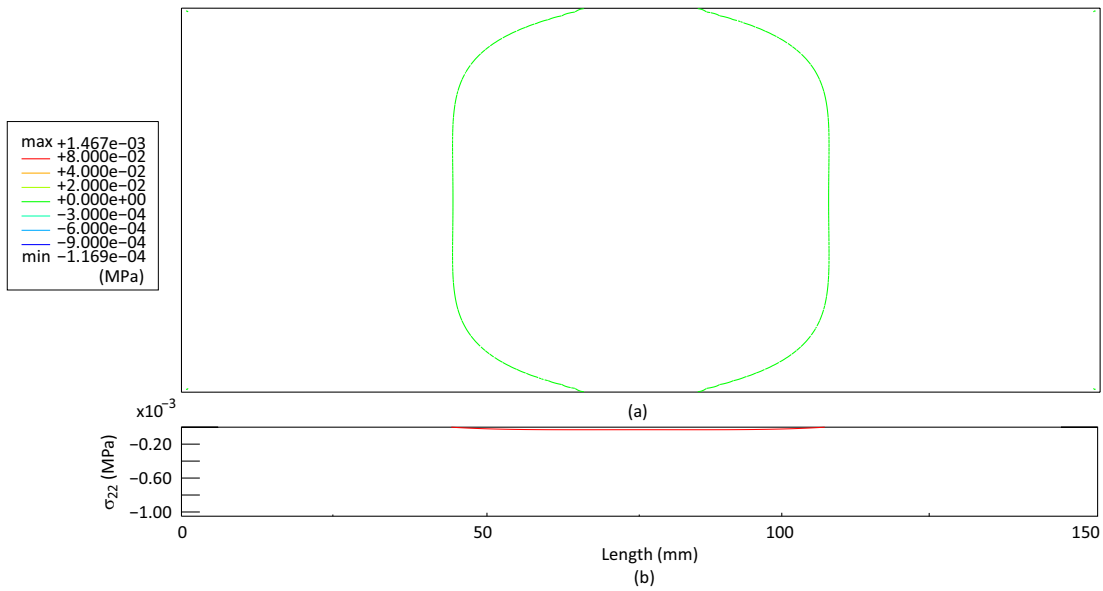
Figure 6.20: The distribution of the normal stress σ_{22} on a 127×63.5 mm (5×2.5 inch) membrane subjected to 20% tensile strain and 8785 V voltage subsequently. (a) isolines of σ_{22}, (b) σ_{22} along the longitudinal centerline in the region $\sigma_{22} \leq 0$ only.
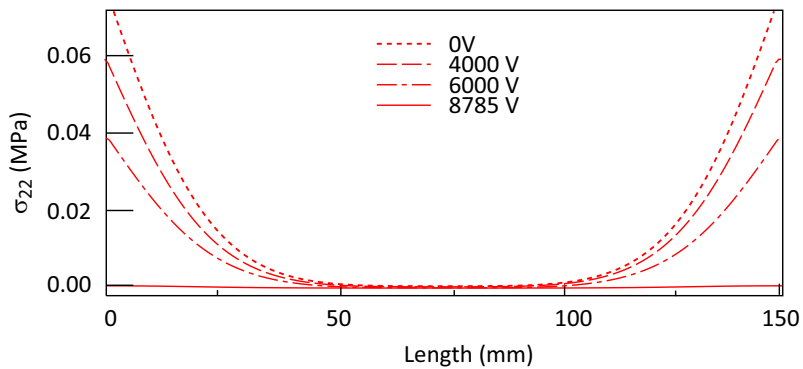
Figure 6.21: Comparison of the normal stress σ_{22} along the horizontal centerline on a 127×63.5 mm (5×2.5 inch) membrane in 20% tensile strain under different voltages.
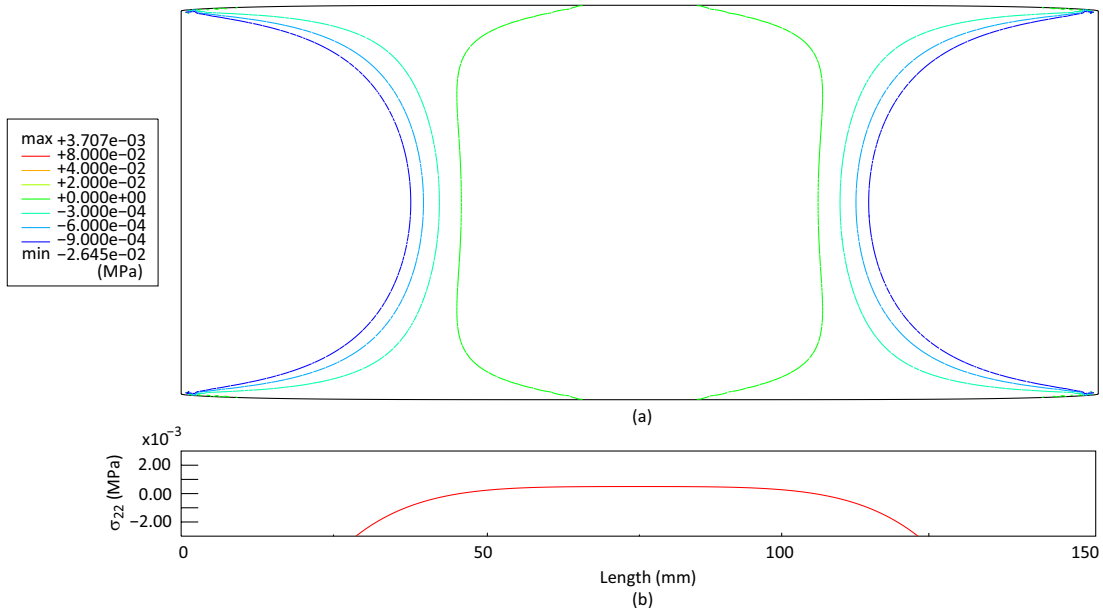
Figure 6.22: The distribution of the normal stress σ_{22} on a 127×63.5 mm (5×2.5 inch) membrane subjected to 20% tensile strain and 10 kV voltage subsequently. (a) isolines of σ_{22}, (b) σ_{22} along the horizontal centerline.

6.5.3 Wrinkling Profile

The finite element post-buckling analysis was carried out on the 127×63.5 mm (5×2.5 inch) membrane and presented in Figure 6.23. Prior to the electric field, membrane was first loaded uniaxially to 11% strain where the maximum wrinkle amplitude can be reached. The whole process can be divided into three stages. In the first stage for voltage less than 4000 V, the wrinkle amplitude is dramatically reduced though the wavelength does not change much. In the second stage for voltage between 4000 V and 7000 V, accompanied with the disappearance of the central crest, the two troughs in the center merge into one trough. As a consequence, the total number of wrinkles drop as well as wrinkle wavelength. In the last stage for voltage greater than 7000 V, the membrane is overexpanded laterally. The re-distribution of the compressive and tensile σ_{22} leads to the migration of wrinkles from the center towards the two clamped edges followed by a increase of wrinkle amplitude and wrinkle numbers.

These wrinkle behaviors are described in a more quantitative way by plotting the cross section along the transverse centerline of the membrane in Figure 6.24. The maximum wrinkle amplitude throughout is reduced by approximately 85% at 5 kV. In reality a higher electric field may not always be helpful in suppressing the wrinkling instability since it may break down the thin membrane. Figure 6.25 shows the wrinkle amplitude at the centroid of the membrane can be reduced by about 90% at 4 kV voltage, and central crest is almost removed at 5 kV.
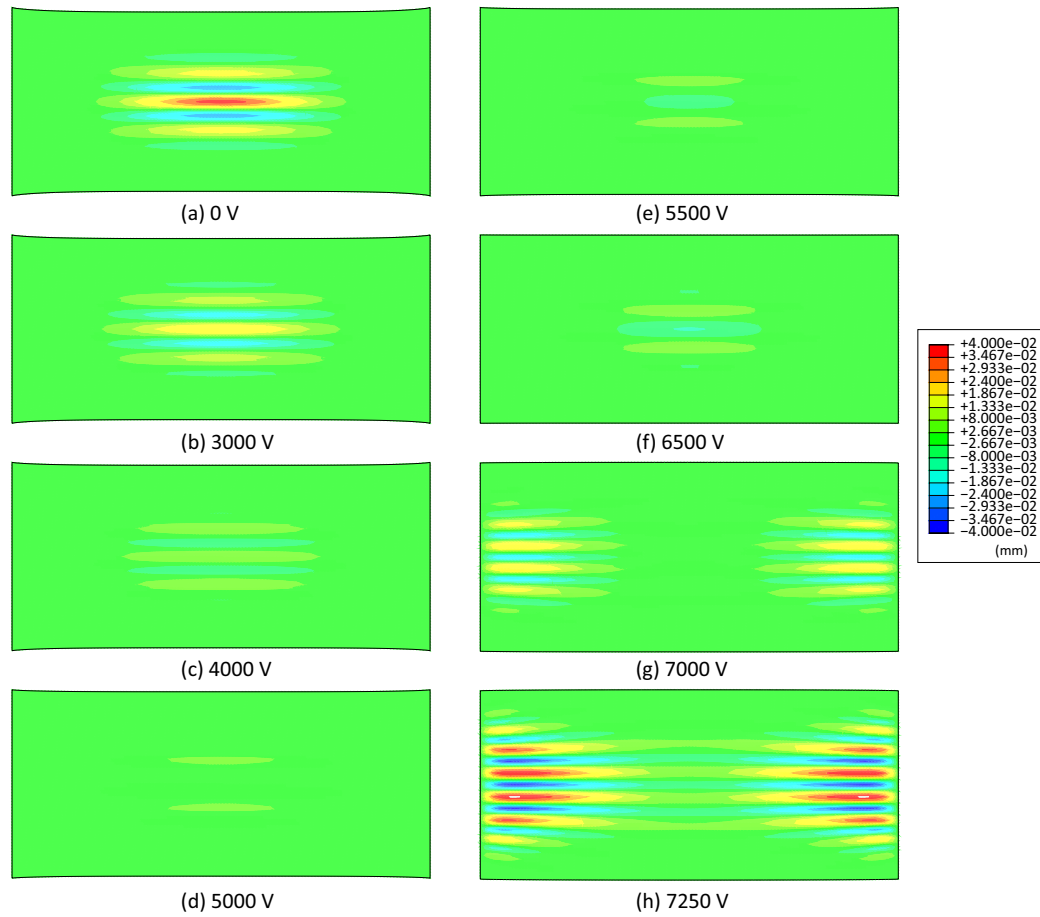
Figure 6.23: The wrinkle profiles of the 127×63.5 mm (5×2.5 inch) membrane under applied voltages of (a) 0 V, (b) 3000 V, (c) 4000 V, (d) 5000 V, (e) 5500 V, (f) 6500 V, (g) 7000 V, (h) 7250 V.
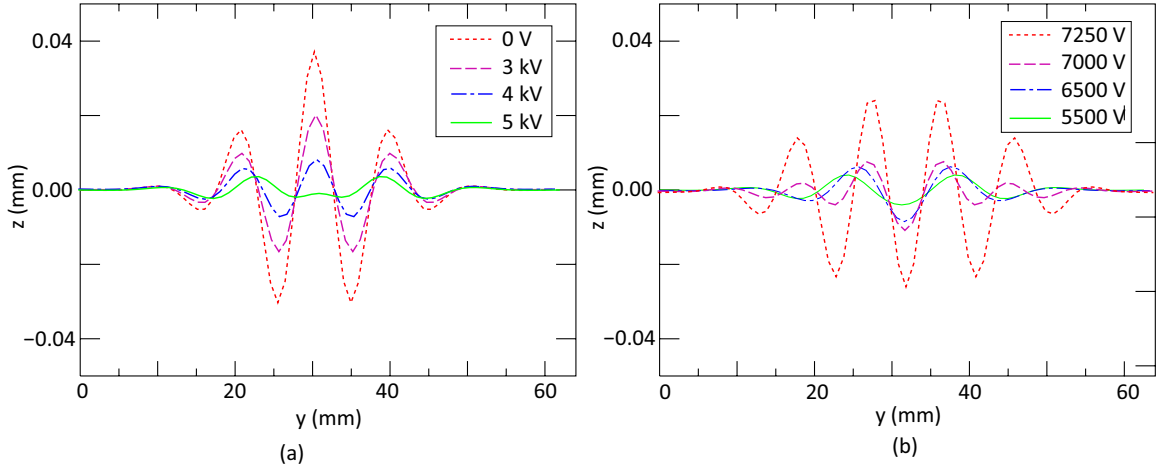
Figure 6.24: The cross-sectional plot of the wrinkle profile along the transverse centerline of the 127×63.5 mm (5×2.5 inch) membrane under voltages in the range of (a) 0-5000 V and (b) 5500-7250 V.
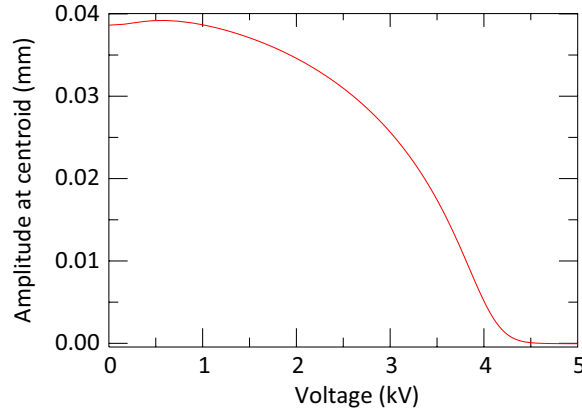
Figure 6.25: The out-of-plane displacement at centroid of the 127×63.5 mm (5×2.5 inch) membrane vs. the applied voltage up to 5 kV.

Interestingly, it is found that the lateral contraction of the membrane in the midplane linearly increases with the uniaxial tensile strain (up to 11%) and then quadratically decreases with the applied voltage as shown in Figures 6.26(a) and (b) respectively. At around 6600 V voltage, the membrane is brought to the original width by the applied electric field and starts to expand.
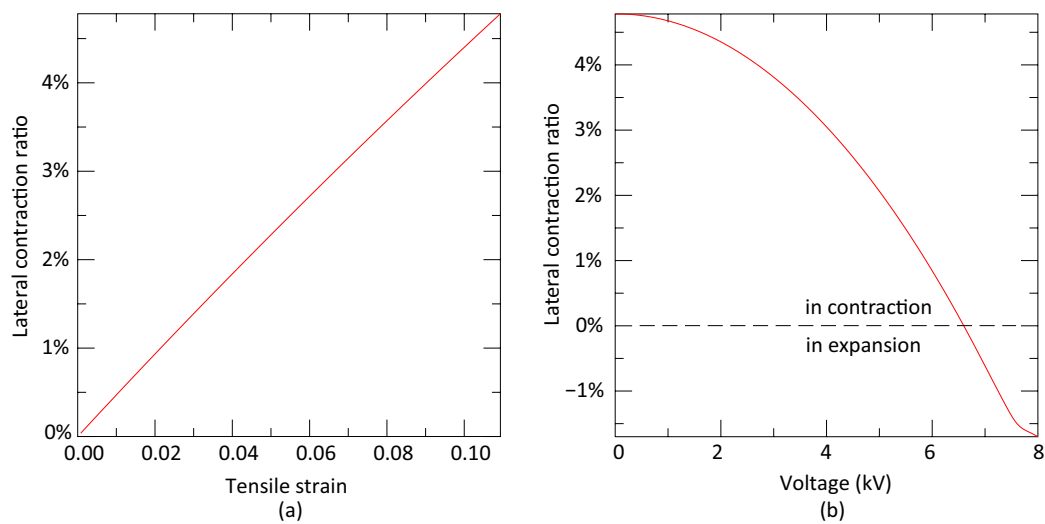
Figure 6.26: The lateral contraction ratio (lateral contraction over the original width of the membrane) vs. (a) the tensile strain, (b) the applied voltage.

Chapter 7

Conclusions and Future Work

This chapter summarizes the main achievements and conclusions of this study and recommends areas for further investigation.

7.1 Conclusions

The objectives of this study were to investigate the wrinkling behavior of thin silicone membranes subjected to uniaxial tension and post-wrinkling behavior of dielectric elastomer membranes subjected to electrostatic pressure. The study has identified various parameters that govern wrinkling behaviors by using both experimental and numerical approaches.

First, a series of experiments were conducted to gain insight into the wrinkling phenomenon, using physical models. Membrane samples were made from commercially fabricated silicone rubber sheets of 0.1 mm (0.004 inch). The silicone rubber was characterized through a conventional uniaxial tensile test using Instron testing machine, and was found to behave as a linear elastic material with small anisotropy. The Young's modulus of the silicone in the rolling direction is 1 MPa, which was determined directly from the stress-strain curve. The Poisson's ratio of the silicone is 0.5, which was determined by evaluating its compressibility by using the hyperelastic models in the finite element software ABAQUS.

An integrated optical method was implemented for measuring the full-field out-of-plane displacement of the membranes, which combines fringe projection method with four-frame phase-shifting technique, pre-conditioned conjugate gradient phase unwrapping algorithm and series-expansion carrier removal technique. The phase measured using this method is proportional to the height of the membrane surface and the proportionality was calibrated using a standard object with known geometry. An optical system was constructed, which is comprised of a LCD projector, a CCD cam-

era, a frame grabber card and a computer as well as an imaging processing software developed in MATLAB. The measurement sensitivity and accuracy of this system were optimized by adjusting the relative positions of the project and camera to the testbed. An accuracy of 0.1 mm for the out-of-plane displacement was achieved.

A series of uniaxial tensile tests was carried out on membranes in 27 different dimensions in order to investigate the effect of membrane dimension and aspect ratio on the structural instability in terms of the wrinkling onset; and a series of measurements of the quasi-static deformation were performed on each membrane at several desired strain levels for understanding the evolution of the wrinkling deformation. During the loading process, the two short edges of the membranes were clamped and thus refrained from contracting laterally, while the two long edges are completed free.

It is found that the wrinkle onset and the overall wrinkle patterns are strongly dependent on the inherent factors such as membrane dimension, thickness and aspect ratio, while the wrinkle details such as the amplitude and wavelength are dependent on the external factors such as boundary (mounting) conditions and tensile load. In experiments it was found that for some of the membranes the initial unstressed configuration can not be perfectly flat and wrinkles appeared spontaneously after the load was applied. Therefore it is very difficult to accurately determine the strain at which wrinkles first form on the membrane of each dimension. However, qualitatively, membranes with larger in-plane dimensions (relative to thickness) and intermediate aspect ratios around 2 exhibited lower structural instability.

Some common features were observed on all the membranes tested. Wrinkles form along the longitudinal loading direction. Wrinkle patterns were symmetric about the transverse midplane due to the symmetry of loading. Regarding the wrinkle details, the wrinkle amplitudes first increase and then decrease as the membrane is loaded, whereas the wrinkle wavelengths monotonically decrease.

Features dependent on the membrane dimension and aspect ratio were also observed. For example, wrinkle patterns were either symmetric or anti-symmetric about the longitudinal midplane of the membranes, whose profiles on the transverse midplane can be characterized by damped cosine function and damped sine function, respectively. For membranes with small aspect ratios, wrinkles initiated from the center of the membrane and the maximum wrinkle amplitude remained at the center as the membrane was stretched, while for those with large aspect ratios, wrinkles initiated at the two ends close to the clamped edges. For membranes with intermediate aspect ratios around 3, wrinkles initiated at the center and then grew toward the ends upon elongation.

A numerical study of rectangular membranes in uniaxial tension was carried out using the commercial finite element package ABAQUS aiming to capture the important characteristics of wrinkling of thin membranes observed in the physical model. Geometrically nonlinear finite element models of membrane structures were constructed using thin-shell elements. The boundary conditions were defined at the two short edges of the rectangular membrane. One edge was fully constrained in all its six degrees of freedom. On the other edge only translations along the longitudinal direction was allowed. The two long edges were completely free.

A three-step analysis procedure was introduced following the sequence of the initial step, the pre-buckling eigenvalue analysis and the post-buckling analysis. In the initial step, a small in-plane prestress was applied to stabilize the thin shell model by providing some initial bending stiffness. The next step was a linear perturbation analysis, in which incremental load was applied to the membrane in terms of edge displacement, and the eigenvalues and normalized eigenvectors of the incremental stiffness matrix were computed. The buckling load of each mode then was determined as the sum of the prestress and the product of the eigenvalue and incremental load, among which the critical buckling load is the smallest one corresponding to the lowest eigenvalue. In the final step, a static incremental analysis was performed to simulate the formation and growth of wrinkles on the membrane. A linear combination of some buckling modes selected from the eigenvectors previously computed was introduced into the structure as a geometric imperfection such that the bifurcation can be numerically dealt with. The stabilize function was activated to facilitate the solution by introducing pseudo-inertia and pseudo-viscous forces into the model and switching the quasi-static analysis to a transient analysis, and thus enabling the simulation of the actual dynamic response of the structure as it snaps. Preliminary analyses following this procedure were carried out to address several simulation issues related to modeling of thin membranes, such as material model, element type, mesh density, imperfection sensitivity and stabilizing factor. S4R thin-shell element was chosen for constructing the mesh at a density of 0.028 mm^{-2}. 1% of the membrane thickness was adopted as the magnitude of the geometric imperfection and 1×10^{-8} was adopted as the stabilizing factor unless a larger value was needed for accomplishing convergence.

A series of simulations was conducted up to the pre-buckling stage based on the models of 144 dimensions, spanning over the range of the physical models. A contour map of the critical buckling strain was generated by interpolating the values of the 144 data points. The effect of the membrane dimension and aspect ratios that were observed and qualitatively described was reproduced in a quantitative manner. The critical buckling strain normalized by the surface area of the membrane is a quadratic function of the membrane thickness. The critical buckling strain normalized by both the area and the square of the thickness is a nonlinear function of the aspect ratio and reaches its

minimum at aspect ratio around 2. It was also found in the eigenvalue analysis that corresponding to each eigenvalue there were always two eigenmodes, one symmetric and one anti-symmetric, indicating the membranes may have equal chance of deforming into either of the two wrinkle patterns.

Next, a few models with dimensions exactly the same as those of the physical models were selected for post-buckling analysis. Either the first symmetric mode or the first anti-symmetric mode was implemented as a geometric imperfection for each dimension according to the real wrinkle pattern it exhibited in experiment. The incremental analysis reproduced the continuous image of the deformation on wrinkled membranes, including the overall wrinkle pattern, the total number of wrinkles and the wrinkle wavelength, except that in simulation wrinkle amplitudes were slightly smaller than those measured in the experiments, and decreased more rapidly beyond the strain at which the maximum wrinkle amplitude occurred.

A significant immediate benefit of the numerical study is that one can probe the simulation results in order to gain additional insights into the characteristics of wrinkles and their evolution under varying loads or boundary conditions.

Finally, a concept for suppressing wrinkle instabilities of dielectric elastomer membranes was proposed using the electric field-induced actuation. The mechanism of the dielectric actuation is as follows. Prior to actuation, the elastomer film is coated on each side with a compliant electrode. An applied electric field promotes attraction of the oppositely charged electrodes, thereby introducing a compressive Maxwell stress along the thickness direction. A simple analytical model was developed to determine the voltage at which membrane lateral contraction due to mechanical tensile load is canceled by the expansion due to electrical load, as a function of the applied tensile strain using the Mooney-Rivlin model previously characterized. This model was then applied to the silicone rubber membrane with typical dielectric constant between 3.2 and 9.8.

Electric field of varying strength was applied to a wrinkled membrane through the compliant electrodes painted on both surfaces, and the dynamic structural response of the membrane were captured in the experiments. In the numerical study, a simulation technique was developed to overcome the inability to apply electrostatic pressure. The previous finite elements models and analysis procedures were employed with minor changes. Through the pre-buckling analysis we found that the buckling modes were not affected in the presence of electric field, but the critical buckling strains were significantly raised by 11%-610% for different dimensions. In other words, the wrinkling instability of thin membranes is suppressed by electric field in the sense that the wrinkle onset requires higher external loads. In the post-buckling analysis, the membrane was first stretched to reach a

maximum amplitude and subjected to an electric field through the thickness direction while the two clamped edges were fixed. Simulations predicted a significant decrease in the wrinkling amplitude and the magnitude of the compressive stress due to an increasing applied voltage.

7.2   Open Issues and Future Work

Several research areas were identified during the course of this study, in which further explorations could contribute to the future study of wrinkling of thin membrane structures.

On the experimental aspect, the uniaxial tension testbed was designed to test membranes of up to 10 inches long and 4 inches wide. Larger sizes will exceed the geometrical capability of the apparatus. A 10 inches long membrane can only be stretched to about 30% strain. Partial modification to the test frame, i.e., longer side rails or wider grips, would allow us to study larger membrane samples. Scaling implies that reducing the thickness and increasing the size of membranes have the equivalent effect on lowering the threshold of wrinkling instability. All of our experimental results were based on membrane samples cut from commercially fabricated silicone rubber sheets of thickness 0.004 inch. A thinner sheet of 0.002 inch (minimum thickness commercially available) made the sample preparation very difficult because it folded up as it was peeled off from the substrate carrier mainly due to chemical-induced self-adhesion and electrostatic forces generated at peeling, and also residual stress may be induced during the peeling. This suggested a very narrow range of thicknesses for testing.

There are several other issues associated with the silicone rubber material and sample mounting, such as anisotropy, imperfect initial unstressed configurations (partially slack and partially taut) induced by the sample preparation and mounting procedure, and irreversible material wrinkles after loading-unloading cycles. Membranes fabricated in the lab by spin-coating may resolve the material anisotropy.

In experiments 27 different membrane dimensions were tested among which 16 wrinkled. Two types of wrinkle patterns (symmetric and anti-symmetric) were observed among the tested membranes. In order to discover the membrane's behavior in choosing the wrinkle pattern from a statistical point of view, a large number of membranes in a wide range of sizes and aspect ratios need to be tested .

Due to electrical safety concerns all the components on the testbed are nonconductive and the

frame was placed on a wooden table rather than an optical table. The tensile load was applied by manually turning a plastic threaded rod connected to the upper grip, and the value of the tensile strain was determined by reading the position of the moving edge of the membrane from a ruler on the side rail. Manual control induced vibrations to the frame during the loading process and may have influenced the wrinkling configuration. A motor driven metal threaded rod would be a good alternative. In addition, a displacement gauge (i.e., a Linear variable differential transformer) will provide more accurate measurement on tensile strain and a load cell will allow us to directly quantify the tensile load. However, careful operations are necessary on these modules in the presence of electric field.

As for the measurement techniques, the fringe projection method can only measure the out-of-plane displacement and it has to be combined with several other techniques in order to extract the height information on the object surface. The phase shifting technique requires a static or quasi-static deformation process since it takes time for the fringes to be shifted and captured. The carrier removal technique requires a reference plane beneath or a self-reference on the object to be identified during the image processing, and thus requires human intervention. Therefore, automatic continuous measurements were not accomplished. Instead, wrinkle profiles at discrete strain levels were measured. In order to capture the wrinkle evolution, a fully automated optical method is needed. 3D digital image correlation (DIC) may be a solution, which also enables one to obtain the in-plane strain distribution. This will be helpful in understanding the driving force of the wrinkling instability.

In the finite element analysis, the membrane material, silicone rubber was defined as a linearly elastic model with the Young's modulus and Poisson's ratio extracted from the results of a uni-axial tension tests performed using the Instron testing machine. The loading curve exhibits small curvatures and hysteresis within a load-unload cycle indicating the hyperelastic and viscoelastic properties built in the material. These test results were imported into ABAQUS for hyperelastic material model evaluation. For more accurate characterization, other types of tests are needed, for instance bi-axial tension test and volume dilatation test. The hyperelastic material model is highly unstable in the computation and failed to provide a convergent solution in either the pre-buckling or the post-buckling regime. New analysis techniques need to be developed to overcome the convergence difficulties associated with hyperelastic materials.
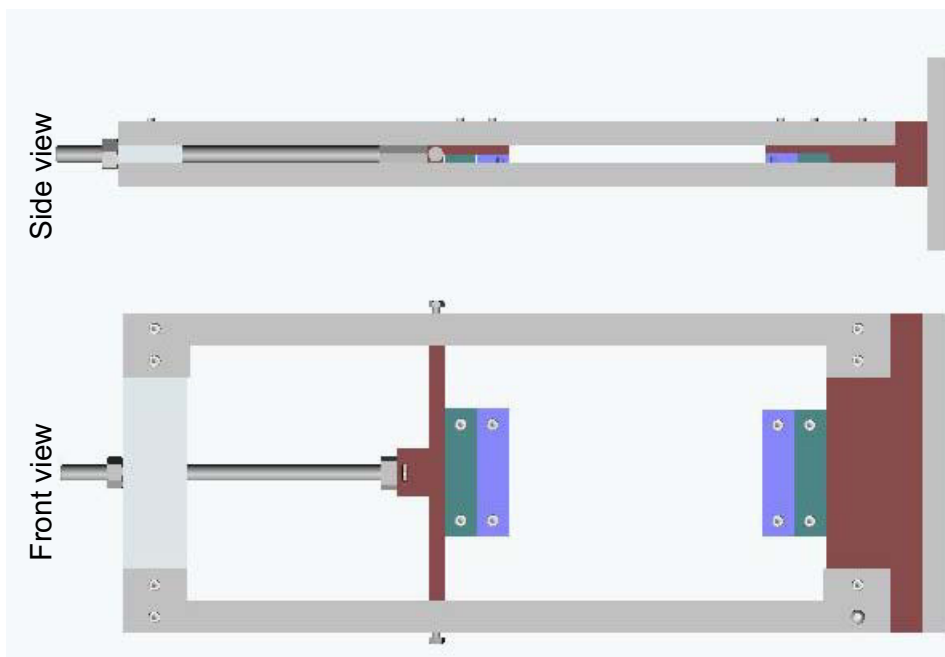
The compliant electrode is a big barrier to our study on suppressing membrane wrinkling by means of dielectric actuation. Ideally the electrode layer should be uniform and much thinner ($\sim$1/10th) than the thickness of the dielectric elastomer membrane. Currently there is no good way of controlling the thickness of the electrode layer since the traditional coating or printing techniques

are not applicable for soft elastomer membrane substrate especially when applied on both sides of the membrane. The black carbon grease also refrains us from using the fringe projection method for shape measurement. Seeking alternative compliant electrode materials and painting techniques is still an on-going area of research.

Appendix A

Construction Drawings for the Experimental set-ups

Fixture Assembly

Side view

Front view
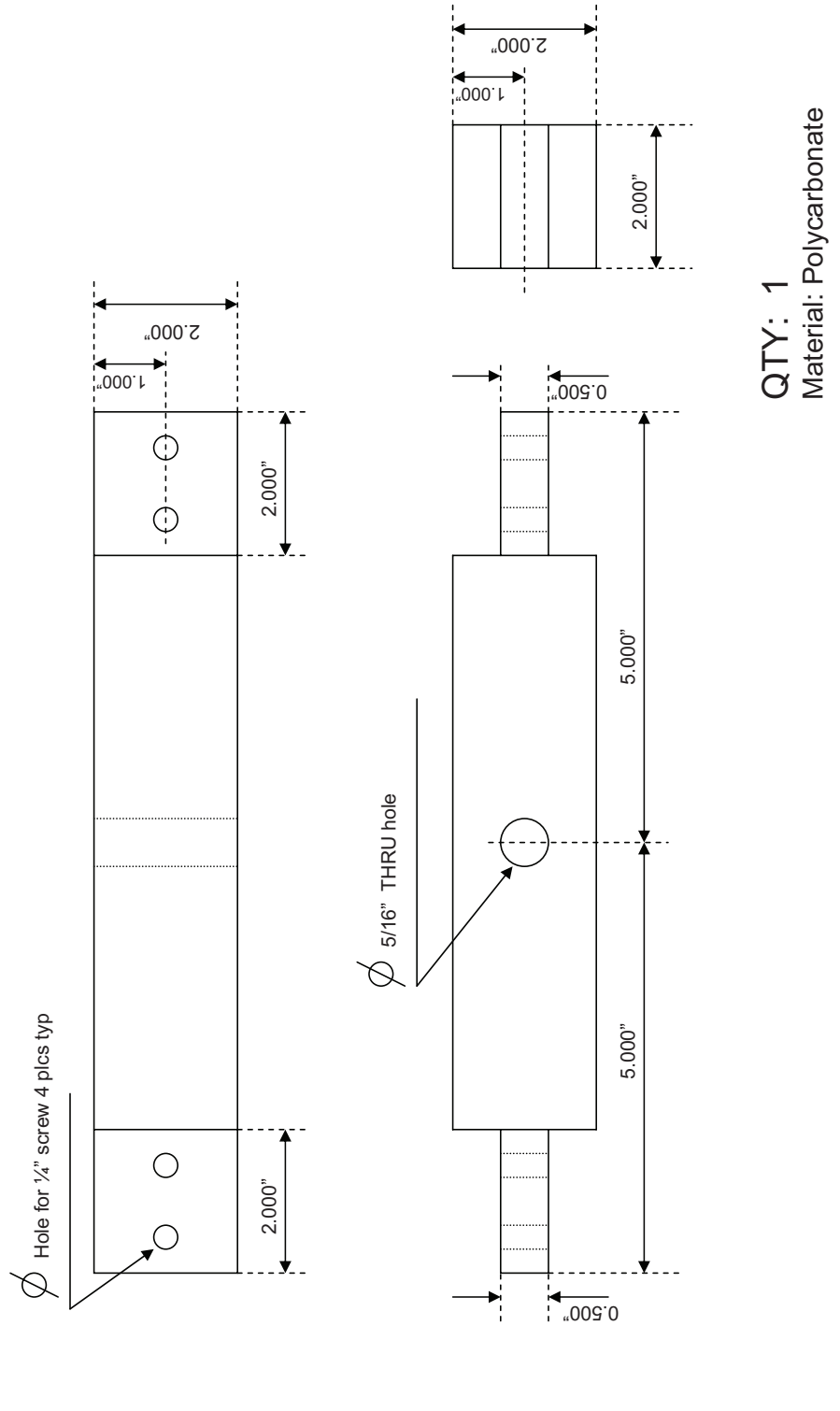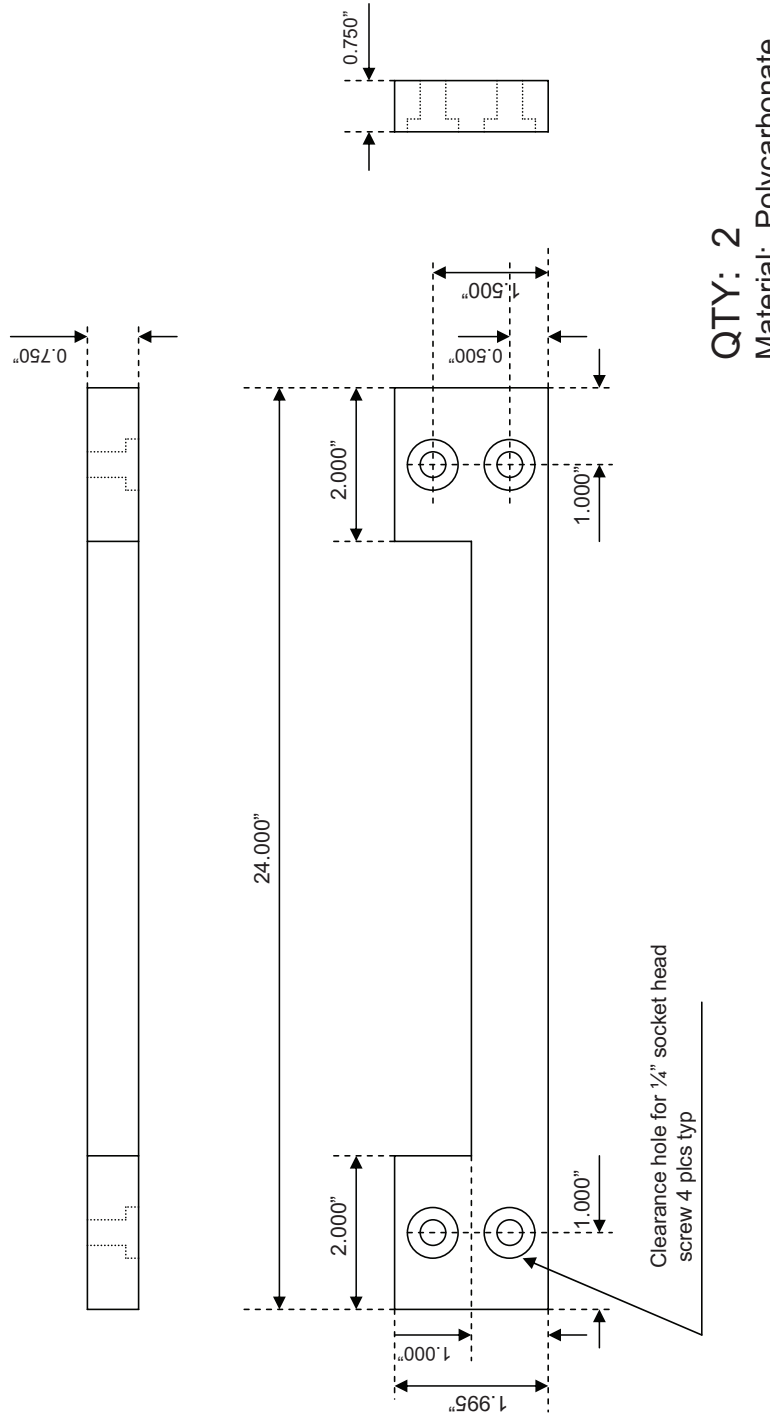
Part list

Part	Overall Dimension (inch)	Quantity	Material
Upper cross head	10 x 2 x2	1	Polycarbonate
Front side rail	24 x 2 x0.75	2	Polycarbonate
Back side rail	24 x 2 x0.75	2	Polycarbonate
Upper grip	9 x 3 x1	1	Polycarbonate
Pin pad	2 x 1 x0.5	1	Polycarbonate
Lower grip	4 x 1.75 x 0.75	1	Polycarbonate
Linear guide upper connector	2 x 0.7 x 0.75	1	Aluminum
Linear guide lower connector	1.5 x 0.5 x 0.25	1	Aluminum
Rail clamp	10 x 3 x 2	1	Polycarbonate
Grip pad	4 x 0.75 x 0.25	2	Polycarbonate
Grip electrode pad	4 x 0.75 x 0.25	2	Polycarbonate
Base	10 x 6 x 0.75	1	Polycarbonate

Upper Cross Head

2.000"

1.000"

2.000"

Hole for ¼" screw 4 plcs typ

2.000"

0.500"

5.000"

5.000"

⌀ 5/16" THRU hole

0.500"

2.000"

1.000"

2.000"

QTY: 1
Material: Polycarbonate

Front Side Rail

24.000"

2.000"

2.000"

1.000"

1.000"

1.500"

0.500"

1.000"

1.995"

0.750"

0.750"

Clearance hole for ¼" socket head screw 4 plcs typ

QTY: 2
Material: Polycarbonate

Back Side Rail

0.750"

0.750"

1.500"

0.500"

2.000"

1.000"

24.000"

2.000"

1.000"

¼-20 treads thru 4 plcs typ

1.000"

1.995"

QTY: 2

Material: Polycarbonate

Upper Grip

QTY: 1
Material: Polycarbonate

¼-20 0.50" deep 2 plcs

¼-20 threads 4 plcs typ

¼ clearance hole 3 plcs

3.000"

1.000"

1.500"

0.500"

0.250"

0.250"

1.000"

0.495"

1.000"

2.000"

9.000"

4.500"

1.000"

0.50"

0.500"

0.50"

0.50"

0.50"

1.000"

0.50"

3.000"

4.000"

0.375"

1.125"

Pin pad

3/8" threads (depth check with machine shop)

0.495"

2.000"

1.000"

0.250"

0.50"

0.50"

0.300"

¼ clearance hole 3 plcs

0.500"

1.000"

QTY: 1
Material: Polycarbonate

147

Lower Grip

QTY: 1
Material: Polycarbonate

0.100"
0.500"
0.700"
0.750"
0.100"
0.750"

0.750"
0.500"
2.000"

1.750"
0.250"
1.125"
0.375"
4.000"
3.000"

¼" threads 4 plcs typ

Linear guide upper connector

2.000"

0.100"

0.700"

Clearance hole for M2 socket head screw 4 plcs typ

Clearance hole for M2 socket head screw 4 plcs typ

0.100"

0.750"

QTY: 1
Material: Aluminum

Linear guide lower connector

0.500"

1.500"

20mm

Clearance hole for 1/4"socket head screw 2 plcs typ*

Clearance hole for M2 socket head screw 4 plcs typ*

0.250"

QTY: 1
Material: Aluminum

Rail Clamp

¼" threads (depth check with Machine shop) 2 plcs*

2.000"

0.500"

2.000"

1.500"

0.750"

2.000"

3.000"

2.000"

0.500"

1.500"

2.000"

¼-20 0.750" deep 3 plcs

¼ " hole thru 4 plcs typ

1.500"

10.000"

1.000"

0.500"

2.000"

QTY: 1

Material: Polycarbonate

Grip Pad

4.000"

3.000"

0.250"

0.370"

0.740"

¼-20 clearance holes for
Socket head screws 2 plcs typ

QTY: 2
Material: Polycarbonate

Grip Electrode Pad

0.250"

Thread for banana stud

Hole for electrode 0.375" deep
2 plcs typ

¼-20 clearance holes for
Socket head screws 2 plcs typ

4.000"

3.000"

0.250"

0.370"

0.740"

QTY: 2
Material: Polycarbonate

Base

3/4"

10.0"

8.000"

3.0"

3.500"

3.500"

6.0"

4.000"

QTY: 2
Material: Polycarbonate

Micro Frictionless Table NDN
1-30.20 ordered from SCHNEEBERGER

Layout of the standard attaching holes in the lower- and upper section NDN 05

Order No.	Dimensions (mm) A	B	B₁	Dw	H	L	L₃	L₄	d₁	s	t	x	b₁	°C in N	M_L in Ncm	M_o in Ncm	Weight in g
NDN 05-10.05	4	7	4	1	5	10	1 × 5	2.5	M 1.6	2.1	1.5	1.1	–	23	1.5	3	2
NDN 05-15.10					10	15	1 × 8	3.5						27	2.2	3.6	3
NDN 05-20.15					15	20	1 × 12	4						36	2.8	4.8	4
NDN 05-25.20					20	25	1 × 16	4.5						45	3.5	6	5
NDN 1-15.05	6	10	5	1.5	5	15	1 × 8	3.5	M 2	3	2.3	1.8	4	50	9	14	5
NDN 1-20.10					10	20	1 × 12	4						60	11	17	7
NDN 1-25.15					15	25	1 × 16	4.5						70	14	20	10
NDN 1-30.20					20	30	1 × 20	5						80	16	23	12
NDN 1-35.25					25	35	1 × 24	5.5						90	19	26	14
NDN 1-40.30					30	40	1 × 28	6						100	21	28	17
NDN 1-45.35					35	45	1 × 32	6.5						110	24	31	19
NDN 1-50.40					40	50	1 × 36	7						120	26	34	21
NDN 2-30.20	8	15	8	2.5	20	30	1 × 20	5	M 2.5	4.5	2.5	2.7	7	140	40	55	28
NDN 2-40.30					30	40	1 × 28	6						170	50	65	36
NDN 2-50.40					40	50	1 × 36	7						200	60	75	45
NDN 2-60.50					50	60	3 × 15	7.5						250	80	100	54
NDN 2-70.60					60	70	3 × 18	8						310	100	120	64
NDN 2-80.70					70	80	3 × 20	10						370	120	140	73

Material: corrosion resistant steel

Appendix B

ABAQUS Input Files

B.1 Input File, Initial and Eigenvalue Buckling Analysis

```
*Heading
 Rectangular membrane subjected to uniaxial tension load with two short edges
 clamped and two long edges free using S4R thin shell element.
*Preprint, echo=NO, model=NO, history=NO, contact=NO
** PARTS
*Part, name=Part-1
*Node, input=node_10x4.tex
*Nset, nset=_PickedSet2, internal, generate
    1,  6656,     1
*Element, type=S4R, input=element_10x4.tex
*Elset, elset=_PickedSet2, internal, generate
    1,  6477,     1
** Region: (Section-1:Picked)
*Elset, elset=_PickedSet2, internal, generate
    1,  6477,     1
** Section: Section-1
*Shell Section, elset=_PickedSet2, material=Linear
0.1, 7
*End Part
** ASSEMBLY
*Assembly, name=Assembly
*Instance, name=Part-1-1, part=Part-1
*End Instance
*Nset, nset=_PickedSet4, internal, instance=Part-1-1, generate
```

```
   1,  6529,   128
*Elset, elset=_PickedSet4, internal, instance=Part-1-1, generate
   1,  6351,   127
*Nset, nset=_PickedSet16, internal, instance=Part-1-1, generate
 128,  6656,   128
*Elset, elset=_PickedSet16, internal, instance=Part-1-1, generate
 127,  6477,   127
*Nset, nset=Set-1, instance=Part-1-1, generate
   1,  6656,     1
*Elset, elset=Set-1, instance=Part-1-1, generate
   1,  6477,     1
*Nset, nset=_PickedSet20, internal, instance=Part-1-1, generate
 128,  6656,   128
*Elset, elset=_PickedSet20, internal, instance=Part-1-1, generate
 127,  6477,   127
*End Assembly
** MATERIALS
*Material, name=Linear
*Elastic
 1., 0.5
*Expansion
 1e-06,
** BOUNDARY CONDITIONS
** Name: Clamping Type: Symmetry/Antisymmetry/Encastre
*Boundary
_PickedSet4, ENCASTRE
** ----------------------------------------------------------------
** STEP: Step-1
*Step, name=Step-1, nlgeom=YES
preload
*Static
1., 1., 1e-05, 1.
** BOUNDARY CONDITIONS
** Name: Preload Type: Displacement/Rotation
*Boundary
_PickedSet16, 1, 1, 3. _PickedSet16, 2, 2 _PickedSet16, 3, 3
```

```
_PickedSet16, 4, 4 _PickedSet16, 5, 5 _PickedSet16, 6, 6
** OUTPUT REQUESTS
*Restart, write, frequency=0
** FIELD OUTPUT: F-Output-1
*Output, field
*Node Output
CF, RF, U
*Element Output, directions=YES
ELEDEN, ELEN, ENER, LE, PE, PEEQ, PEMAG, S, STH, SVOL
*Contact Output
CDISP, CSTRESS
** HISTORY OUTPUT: H-Output-1
*Output, history, variable=PRESELECT
*End Step
** ----------------------------------------------------------------
** STEP: Step-2
*Step, name=Step-2, perturbation
*Buckle, eigensolver=lanczos
12, 0., ,
** BOUNDARY CONDITIONS
** Name: Clamping Type: Symmetry/Antisymmetry/Encastre
*Boundary, op=NEW, load case=1
_PickedSet4, ENCASTRE
*Boundary, op=NEW, load case=2
_PickedSet4, ENCASTRE
** Name: Preload Type: Displacement/Rotation
*Boundary, op=NEW, load case=1
** Name: live load Type: Displacement/Rotation
*Boundary, op=NEW, load case=1
_PickedSet20, 1, 1, 1. _PickedSet20, 2, 2 _PickedSet20, 3, 3
_PickedSet20, 4, 4 _PickedSet20, 5, 5 _PickedSet20, 6, 6
*Boundary, op=NEW, load case=2
_PickedSet20, 1, 1, 1. _PickedSet20, 2, 2 _PickedSet20, 3, 3
_PickedSet20, 4, 4 _PickedSet20, 5, 5 _PickedSet20, 6, 6
** OUTPUT REQUESTS
*Restart, write, frequency=0
```

```
** FIELD OUTPUT: F-Output-2
*Output, field, variable=PRESELECT
*NODE FILE
U,
*End Step
```

B.2 Input File, Post-buckling Analysis

```
*Heading
** Job name: static_10x4_electric
*Preprint, echo=NO, model=NO, history=NO, contact=NO
** PARTS
*Part, name=Part-1
*Node, input=node_10x4.tex
*Nset, nset=_PickedSet2, internal, generate
    1,  6656,     1
*Element, type=S4R5, input=element_10x4.tex
*Elset, elset=_PickedSet2, internal, generate
    1,  6477,     1
** Region: (Section-1:Picked)
*Elset, elset=_PickedSet2, internal, generate
    1,  6477,     1
** Section: Section-1
*Shell Section, elset=_PickedSet2, material=Linear
0.1, 7
*End Part
*IMPERFECTION,FILE=buckle_10x4,STEP=2
2,0.01
** ASSEMBLY
*Assembly, name=Assembly
*Instance, name=Part-1-1, part=Part-1
*End Instance
*Nset, nset=_PickedSet4, internal, instance=Part-1-1, generate
    1,  6529,   128
*Elset, elset=_PickedSet4, internal, instance=Part-1-1, generate
    1,  6351,   127
```

```
*Nset, nset=_PickedSet16, internal, instance=Part-1-1, generate
  128,  6656,   128
*Elset, elset=_PickedSet16, internal, instance=Part-1-1, generate
  127,  6477,   127
*Nset, nset=Set-1, instance=Part-1-1, generate
    1,  6656,     1
*Elset, elset=Set-1, instance=Part-1-1, generate
    1,  6477,     1
*Nset, nset=_PickedSet18, internal, instance=Part-1-1, generate
    1,  6656,     1
*Elset, elset=_PickedSet18, internal, instance=Part-1-1, generate
    1,  6477,     1
*Nset, nset=_PickedSet21, internal, instance=Part-1-1, generate
  128,  6656,   128
*Elset, elset=_PickedSet21, internal, instance=Part-1-1, generate
  127,  6477,   127
*End Assembly
** MATERIALS
*Material, name=Linear
*Elastic
1., 0.5
*Expansion
 1e-06,
** BOUNDARY CONDITIONS
** Name: Clamping Type: Symmetry/Antisymmetry/Encastre
*Boundary
_PickedSet4, ENCASTRE
** PREDEFINED FIELDS
** Name: Predefined Field-1   Type: Temperature
*Initial Conditions, type=TEMPERATURE
_PickedSet18, 0.
** ------------------------------------------------------------
** STEP: Step-1
*Step, name=Step-1, nlgeom=YES
preload
*Static
```

```
1., 1., 1e-05, 1.
** BOUNDARY CONDITIONS
** Name: Preload Type: Displacement/Rotation
*Boundary
_PickedSet16, 1, 1, 0.1 _PickedSet16, 2, 2 _PickedSet16, 3, 3
_PickedSet16, 4, 4 _PickedSet16, 5, 5 _PickedSet16, 6, 6
** OUTPUT REQUESTS
*Restart, write, frequency=0
** FIELD OUTPUT: F-Output-1
*Output, field
*Node Output
CF, RF, U
*Element Output, directions=YES
ELEDEN, ELEN, ENER, LE, PE, PEEQ, PEMAG, S, STH, SVOL
*Contact Output
CDISP, CSTRESS
** HISTORY OUTPUT: H-Output-1
*Output, history, variable=PRESELECT
*End Step
** ----------------------------------------------------------------
** STEP: Step-2
*Step, name=Step-2, nlgeom=YES, inc=100000
*Static, stabilize=1e-08
0.0001, 1., 1e-08, 0.01
** BOUNDARY CONDITIONS
** Name: Clamping Type: Symmetry/Antisymmetry/Encastre
*Boundary, op=NEW
_PickedSet4, ENCASTRE
** Name: Preload Type: Displacement/Rotation
*Boundary, op=NEW
** Name: stretch Type: Displacement/Rotation
*Boundary, op=NEW
_PickedSet21, 1, 1, 76.2 _PickedSet21, 2, 2 _PickedSet21, 3, 3
_PickedSet21, 4, 4 _PickedSet21, 5, 5 _PickedSet21, 6, 6
** OUTPUT REQUESTS
*Restart, write, frequency=0
```

```
** FIELD OUTPUT: F-Output-1
*Output, field
*Node Output
NT, U
*Element Output, directions=YES
E, S, STH, SVOL, TEMP
** HISTORY OUTPUT: H-Output-1
*Output, history, variable=PRESELECT
*End Step
** ----------------------------------------------------------------
** STEP: Step-3
*Step, name=Step-3, nlgeom=YES, inc=100000
*Static, stabilize=1e-08
0.0001, 1., 1e-08, 0.01
** PREDEFINED FIELDS
** Name: Predefined Field-1   Type: Temperature
*Temperature
_PickedSet18, 18647.
** OUTPUT REQUESTS
*Restart, write, frequency=0
** FIELD OUTPUT: F-Output-1
*Output, field
*Node Output
NT, U
*Element Output, directions=YES
E, S, STH, SVOL, TEMP
** HISTORY OUTPUT: H-Output-1
*Output, history, variable=PRESELECT
*End Step
```

Appendix C

Table of Critical Buckling Strains

Table C.1: Computation results of critical buckling strain without and with 5×10^7 V/m electric field for membranes of 0.1 mm (0.004 inch) thick. P_0 is the preload, λ is the eigenvalue, $P_{\text{crit}} = P_0 + \lambda P_\Delta$ is the critical buckling load in terms of edge displacement, where P_Δ is the incremental load and set to be 1, $\varepsilon_{\text{crit}}$ is the critical buckling strain.

L	W	L/W	Without electric field				With electric field			
(inch)	(inch)		P_0	λ	P_{crit}	$\varepsilon_{\text{crit}}$	P_0	λ	P_{crit}	$\varepsilon_{\text{crit}}$
			(inch)		(inch)		(inch)		(inch)	
1.75	0.9	2.00	0.01	0.9986	1.0086	57.1%	0.08	1.0332	1.1132	63.6%
2	1	1.60	0.01	0.8915	0.9015	44.6%	0.1	1.0226	1.1226	56.1%
2	1.25	2.20	0.01	1.0565	1.0665	52.8%	0.1	1.1667	1.2667	63.3%
2.75	1.25	1.83	0.03	0.9011	0.9311	32.8%	0.15	1.0317	1.1817	43.0%
2.75	1.5	2.40	0.03	0.6515	0.6815	23.7%	0.15	0.7663	0.9163	33.3%
3	1.25	2.00	0.03	1.0984	1.1284	36.6%	0.15	1.1842	1.3342	44.5%
3	1.5	1.71	0.03	0.6339	0.6639	21.1%	0.2	0.9099	1.1099	37.0%
3	1.75	1.50	0.03	0.6203	0.6503	20.7%	0.2	0.8844	1.0844	36.1%
3	2	2.80	0.03	1.1716	1.2016	39.1%	0.2	1.6075	1.8075	60.3%
3.5	1.25	2.33	0.03	1.7204	1.7504	49.2%	0.2	2.0801	2.2801	65.1%
3.5	1.5	2.00	0.03	0.8116	0.8416	23.2%	0.2	1.0463	1.2463	35.6%
3.5	1.75	1.75	0.03	0.5249	0.5549	15.0%	0.2	0.7131	0.9131	26.1%
3.5	2	1.56	0.03	0.4982	0.5282	14.2%	0.2	0.6764	0.8764	25.0%
3.5	2.25	3.20	0.03	0.743	0.773	21.2%	0.2	0.9406	1.1406	32.6%
4	1.25	2.67	0.03	2.4867	2.5167	62.2%	0.2	2.68	2.88	72.0%
									continued on next page	

continued from previous page										
			Without electric field				With electric field			
L	W	L/W	P_0	λ	P_{crit}	$\varepsilon_{\text{crit}}$	P_0	λ	P_{crit}	$\varepsilon_{\text{crit}}$
(inch)	(inch)		(inch)		(inch)		(inch)		(inch)	
4	1.5	2.00	0.03	1.1844	1.2144	29.6%	0.25	1.6496	1.8996	47.5%
4	2	1.60	0.03	0.448	0.478	11.2%	0.25	0.6858	0.9358	23.4%
4	2.5	1.45	0.03	0.5454	0.5754	13.6%	0.25	0.8049	1.0549	26.4%
4	2.75	3.00	0.03	1.1219	1.1519	13.6%	0.25	1.5469	1.7969	44.9%
4.5	1.5	2.25	0.03	1.6808	1.7108	37.4%	0.25	2.094	2.344	52.1%
4.5	2	1.80	0.03	0.53	0.56	11.8%	0.25	0.7652	1.0152	22.6%
4.5	2.5	1.50	0.01	0.3335	0.3435	7.4%	0.25	0.5603	0.8103	18.0%
4.5	3	1.38	0.01	0.6995	0.7095	15.5%	0.3	1.1359	1.4359	31.9%
4.5	3.25	3.33	0.03	1.9611	1.9911	44.2%	0.27	2.6335	2.9035	64.5%
5	1.5	2.86	0.03	2.204	2.234	44.1%	0.3	2.9461	3.2461	64.9%
5	1.75	2.50	0.03	1.2179	1.2479	24.4%	0.3	1.7097	2.0097	40.2%
5	2	2.22	0.03	0.6961	0.7261	13.9%	0.3	1.0424	1.3424	26.8%
5	2.25	2.00	0.03	0.4609	0.4909	9.2%	0.3	0.7199	1.0199	20.4%
5	2.5	1.82	0.01	0.3217	0.3317	6.4%	0.3	0.5791	0.8791	17.6%
5	2.75	1.67	0.01	0.2975	0.3075	6.0%	0.3	0.5425	0.8425	16.9%
5	3	1.54	0.01	0.3359	0.3459	6.7%	0.3	0.597	0.897	17.9%
5	3.25	1.43	0.03	0.5254	0.5554	10.5%	0.3	0.806	1.106	22.1%
5	3.5	3.67	0.03	1.0801	1.1101	21.6%	0.3	1.5148	1.8148	36.3%
5.5	1.5	3.14	0.03	2.69	2.72	48.9%	0.3	3.2946	3.5946	65.4%
5.5	1.75	2.75	0.03	1.5958	1.6258	29.0%	0.3	2.0485	2.3485	42.7%
5.5	2	2.44	0.03	0.93	0.96	16.9%	0.3	1.2793	1.5793	28.7%
5.5	2.25	2.20	0.03	0.5705	0.6005	10.4%	0.3	0.8545	1.1545	21.0%
5.5	2.5	2.00	0.03	0.392	0.422	7.1%	0.35	0.6778	1.0278	18.7%
5.5	2.75	1.83	0.01	0.291	0.301	5.3%	0.35	0.5582	0.9082	16.5%
5.5	3	1.69	0.01	0.269	0.279	4.9%	0.35	0.3712	0.7212	13.1%
5.5	3.25	1.57	0.01	0.2926	0.3026	5.3%	0.35	0.5596	0.9096	16.5%
5.5	3.5	1.47	0.03	0.4144	0.4444	7.5%	0.35	0.7054	1.0554	19.2%
5.5	3.75	1.38	0.03	0.7075	0.7375	12.9%	0.35	1.128	1.478	26.9%
5.5	4	4.00	0.03	1.7796	1.8096	32.4%	0.35	2.7809	3.1309	56.9%
6	1.5	3.43	0.05	3.3387	3.3887	55.6%	0.33	3.8674	4.1974	70.0%
6	1.75	3.00	0.03	1.9701	2.0001	32.8%	0.35	2.667	3.017	50.3%
6	2	2.67	0.03	1.2068	1.2368	20.1%	0.35	1.7184	2.0684	34.5%

			Without electric field				With electric field			
continued from previous page										
L	W	L/W	P_0	λ	P_{crit}	$\varepsilon_{\text{crit}}$	P_0	λ	P_{crit}	$\varepsilon_{\text{crit}}$
(inch)	(inch)		(inch)		(inch)		(inch)		(inch)	
6	2.25	2.40	0.03	0.7402	0.7702	12.3%	0.35	1.1275	1.4775	24.6%
6	2.5	2.18	0.03	0.4814	0.5114	8.0%	0.35	0.7913	1.1413	19.0%
6	2.75	2.00	0.01	0.3263	0.3363	5.4%	0.35	0.6112	0.9612	16.0%
6	3	1.85	0.01	0.2657	0.2757	4.4%	0.35	0.5219	0.8719	14.5%
6	3.25	1.71	0.01	0.2458	0.2558	4.1%	0.35	0.4915	0.8415	14.0%
6	3.5	1.50	0.01	0.2603	0.2703	4.3%	0.35	0.512	0.862	14.4%
6	4	1.41	0.03	0.5183	0.5483	8.6%	0.35	0.8268	1.1768	19.6%
6	4.25	4.33	0.03	1.0368	1.0668	17.3%	0.4	1.762	2.162	36.0%
6.5	1.5	3.71	0.03	3.5126	3.5426	54.0%	0.35	4.2839	4.6339	71.3%
6.5	1.75	3.25	0.03	2.3169	2.3469	35.6%	0.35	2.9234	3.2734	50.4%
6.5	2	2.60	0.03	1.4959	1.5259	23.0%	0.35	1.9809	2.3309	35.9%
6.5	2.5	2.17	0.03	0.6083	0.6383	9.4%	0.4	1.0062	1.4062	21.6%
6.5	3	2.00	0.01	0.2942	0.3042	4.5%	0.4	0.583	0.983	15.1%
6.5	3.25	1.86	0.01	0.2445	0.2545	3.8%	0.4	0.5042	0.9042	13.9%
6.5	3.5	1.73	0.01	0.2265	0.2365	3.5%	0.4	0.4748	0.8748	13.5%
6.5	3.75	1.63	0.01	0.2353	0.2453	3.6%	0.4	0.4886	0.8886	13.7%
6.5	4	1.53	0.01	0.2775	0.2875	4.3%	0.4	0.5556	0.9556	14.7%
6.5	4.25	1.44	0.03	0.4076	0.4376	6.3%	0.4	0.7189	1.1189	17.2%
6.5	4.5	1.37	0.03	0.6961	0.7261	10.7%	0.4	1.1308	1.5308	23.6%
6.5	4.75	4.67	0.05	1.7752	1.8252	27.3%	0.4	2.5161	2.9161	44.9%
7	1.5	3.50	0.03	3.8645	3.8945	55.2%	0.36	4.5515	4.9115	70.2%
7	2	2.80	0.03	1.7751	1.8051	25.4%	0.4	2.4488	2.8488	43.6%
7	2.5	2.33	0.03	0.7653	0.7953	10.9%	0.4	1.189	1.589	26.8%
7	3	2.00	0.03	0.3654	0.3954	5.2%	0.4	0.6655	1.0655	17.8%
7	3.5	1.75	0.01	0.2264	0.2364	3.2%	0.4	0.4878	0.8878	14.0%
7	4	1.56	0.01	0.2151	0.2251	3.1%	0.45	0.4657	0.9157	12.8%
7	4.5	1.40	0.01	0.3169	0.3269	4.5%	0.45	0.6401	1.0901	13.4%
7	5	5.00	0.05	1.0765	1.1265	15.4%	0.5	1.9639	2.4639	17.0%
7.5	1.5	3.75	0.03	4.1908	4.2208	55.9%	0.38	4.8962	5.2762	70.3%
7.5	2	3.00	0.03	2.0346	2.0646	27.1%	0.4	2.6486	3.0486	40.6%
7.5	2.5	2.50	0.03	0.9413	0.9713	12.6%	0.4	1.4794	1.8794	25.1%
7.5	3	2.14	0.03	0.4421	0.4721	5.9%	0.45	0.7964	1.2464	16.6%

			Without electric field				With electric field			
L	W	L/W	P_0	λ	P_{crit}	$\varepsilon_{\text{crit}}$	P_0	λ	P_{crit}	$\varepsilon_{\text{crit}}$
(inch)	(inch)		(inch)		(inch)		(inch)		(inch)	
7.5	3.5	2.00	0.01	0.2459	0.2559	3.3%	0.45	0.5284	0.9784	13.0%
7.5	3.75	1.88	0.01	0.2108	0.2208	2.8%	0.45	0.4718	0.9218	12.3%
7.5	4	1.67	0.01	0.1961	0.2061	2.6%	0.45	0.4475	0.8975	12.0%
7.5	4.5	1.50	0.01	0.2204	0.2304	2.9%	0.45	0.4866	0.9366	12.5%
7.5	5	1.36	0.03	0.4048	0.4348	5.4%	0.45	0.74	1.19	15.9%
7.5	5.5	5.33	0.05	1.5826	1.6326	21.1%	0.45	2.3119	2.7619	36.8%
8	1.5	4.00	0.03	4.4987	4.5287	56.2%	0.41	5.3263	5.7363	71.7%
8	2	3.20	0.03	2.273	2.303	28.4%	0.45	3.0843	3.5343	44.2%
8	2.5	2.91	0.03	1.124	1.154	14.1%	0.45	1.6716	2.1216	26.5%
8	2.75	2.67	0.03	0.7746	0.8046	9.7%	0.45	1.2311	1.6811	21.0%
8	3	2.46	0.03	0.5384	0.5684	6.7%	0.45	0.9257	1.3757	17.2%
8	3.25	2.29	0.03	0.3872	0.4172	4.8%	0.5	0.7398	1.2398	15.5%
8	3.5	2.00	0.01	0.2806	0.2906	3.5%	0.5	0.5958	1.0958	13.7%
8	4	1.78	0.01	0.1972	0.2072	2.5%	0.55	0.4459	0.9959	12.4%
8	4.5	1.60	0.01	0.1846	0.1946	2.3%	0.55	0.4215	0.9715	12.1%
8	5	1.45	0.01	0.2387	0.2487	3.0%	0.5	0.5268	1.0268	12.8%
8	5.5	1.33	0.01	0.4901	0.5001	6.1%	0.5	0.9332	1.4332	17.9%
8	6	5.67	0.05	2.2101	2.2601	27.6%	0.5	3.8425	4.3425	54.3%
8.5	1.5	4.25	0.05	5.0208	5.0708	59.1%	0.43	5.6385	6.0685	71.4%
8.5	2	3.40	0.05	2.6098	2.6598	30.7%	0.5	3.5101	4.0101	47.2%
8.5	2.5	2.83	0.05	1.3649	1.4149	16.1%	0.5	1.9773	2.4773	29.1%
8.5	3	2.43	0.03	0.6503	0.6803	7.7%	0.5	1.1095	1.6095	18.9%
8.5	3.5	2.13	0.03	0.3438	0.3738	4.0%	0.5	0.6803	1.1803	13.9%
8.5	4	2.00	0.01	0.2113	0.2213	2.5%	0.5	0.4951	0.9951	11.7%
8.5	4.25	1.89	0.01	0.1853	0.1953	2.2%	0.5	0.4522	0.9522	11.2%
8.5	4.5	1.70	0.01	0.173	0.183	2.0%	0.5	0.4316	0.9316	11.0%
8.5	5	1.55	0.01	0.1847	0.1947	2.2%	0.5	0.4507	0.9507	11.2%
8.5	5.5	1.42	0.01	0.27	0.28	3.2%	0.5	0.5885	1.0885	12.8%
8.5	6	6.00	0.01	0.6483	0.6583	7.6%	0.55	1.2428	1.7928	21.1%
9	1.5	4.50	0.05	4.763	4.813	52.9%	0.55	5.0796	5.6296	62.6%
9	2	3.60	0.05	2.8147	2.8647	31.3%	0.55	3.9327	4.4827	50.8%
9	2.5	3.00	0.05	1.5403	1.5903	17.1%	0.55	2.2904	2.8404	33.1%

continued from previous page										
			Without electric field				With electric field			
L	W	L/W	P_0	λ	P_{crit}	$\varepsilon_{\text{crit}}$	P_0	λ	P_{crit}	$\varepsilon_{\text{crit}}$
(inch)	(inch)		(inch)		(inch)		(inch)		(inch)	
9	3	2.57	0.05	0.8055	0.8555	8.9%	0.55	1.319	1.869	22.5%
9	3.5	2.25	0.03	0.4071	0.4371	4.5%	0.55	0.7914	1.3414	14.9%
9	4	2.00	0.01	0.2358	0.2458	2.6%	0.55	0.5416	1.0916	12.1%
9	4.5	1.80	0.01	0.1747	0.1847	1.9%	0.55	0.4365	0.9865	11.0%
9	5	1.64	0.01	0.1623	0.1723	1.8%	0.55	0.4144	0.9644	10.7%
9	5.5	1.50	0.01	0.1935	0.2035	2.1%	0.55	0.4698	1.0198	11.3%
9	6	1.38	0.03	0.332	0.362	3.7%	0.55	0.6793	1.2293	13.7%
9	6.5	4.75	0.03	0.944	0.974	10.5%	0.6	1.7618	2.3618	26.2%
9.5	2	3.80	0.08	3.1966	3.2766	33.6%	0.55	4.0205	4.5705	48.1%
9.5	2.5	3.17	0.05	1.7044	1.7544	17.9%	0.55	2.4329	2.9829	31.4%
9.5	3	2.71	0.05	0.9348	0.9848	9.8%	0.55	1.4707	2.0207	21.3%
9.5	3.5	2.38	0.03	0.4817	0.5117	5.1%	0.55	0.9021	1.4521	15.3%
9.5	4	2.11	0.01	0.2696	0.2796	2.8%	0.55	0.6108	1.1608	12.2%
9.5	4.5	2.00	0.01	0.1854	0.1954	2.0%	0.8	0.3804	1.1804	12.4%
9.5	4.75	1.90	0.01	0.1653	0.1753	1.7%	0.8	0.3275	1.1275	11.9%
9.5	5	1.73	0.01	0.155	0.165	1.6%	0.8	0.3005	1.1005	11.6%
9.5	5.5	1.58	0.01	0.16	0.17	1.7%	0.8	0.316	1.116	11.7%
9.5	6	1.46	0.01	0.2102	0.2202	2.2%	0.8	0.4593	1.2593	13.3%
9.5	6.5	1.36	0.01	0.3815	0.3915	4.0%	0.8	0.9753	1.7753	18.7%
9.5	7	5.00	0.05	1.2914	1.3414	13.6%	0.8	4.2752	5.0752	53.4%
10	2	4.00	0.05	3.1863	3.2363	31.9%	0.6	4.4097	5.0097	50.1%
10	2.5	3.64	0.05	1.8572	1.9072	18.6%	0.6	2.7186	3.3186	33.2%
10	2.75	3.33	0.05	1.4126	1.4626	14.1%	0.6	2.1441	2.7441	27.4%
10	3	3.08	0.03	1.0428	1.0728	10.4%	0.6	1.6859	2.2859	22.9%
10	3.25	2.50	0.03	0.7616	0.7916	7.6%	0.6	1.3239	1.9239	19.2%
10	4	2.22	0.03	0.324	0.354	3.2%	0.6	0.6879	1.2879	12.9%
10	4.5	2.00	0.01	0.2034	0.2134	2.0%	0.6	0.5074	1.1074	11.1%
10	5	1.82	0.01	0.1568	0.1668	1.6%	0.6	0.4253	1.0253	10.3%
10	5.5	1.67	0.01	0.1452	0.1552	1.5%	0.6	0.4042	1.0042	10.0%
10	6	1.54	0.01	0.164	0.174	1.6%	0.6	0.4386	1.0386	10.4%
10	6.5	1.43	0.01	0.2353	0.2453	2.4%	0.6	0.5639	1.1639	11.6%
10	7	1.33	0.03	0.499	0.529	5.0%	0.65	1.0106	1.6606	16.6%
									continued on next page	

			Without electric field				With electric field			
continued from previous page										
L	W	L/W	P_0	λ	P_{crit}	$\varepsilon_{\text{crit}}$	P_0	λ	P_{crit}	$\varepsilon_{\text{crit}}$
(inch)	(inch)		(inch)		(inch)		(inch)		(inch)	
10	7.5	1.33	0.03	1.6486	1.6786	16.5%	0.65	3.4776	4.1276	41.3%

Table C.2: Computation results of critical buckling strain without and with 5×10^7 V/m electric field for membranes of 0.05 mm (0.002 inch) thick. The $\varepsilon_{\text{crit}}$ in the case without electric field is calculated from the $\varepsilon_{\text{crit}}$ of the 0.1 mm thick membrane listed in Table C.1 based on the quadratic dependence of critical buckling strain on membrane thickness.

			Without electric field	With electric field			
L	W	L/W	$\varepsilon_{\text{crit}}$	P_0	λ	P_{crit}	$\varepsilon_{\text{crit}}$
(inch)	(inch)			(inch)		(inch)	
L	W	L/W	ε_{crit}	P_0	λ	P_{crit}	ε_{crit}
175	90	1.94	15.9%	10	36.231	46.231	26.4%
200	100	2.00	14%	11	33.358	44.358	22.2%
200	125	1.60	15.8%	11	37.791	48.791	24.4%
275	125	2.20	10.7%	16	33.664	49.664	18.1%
275	150	1.83	8.3%	16	26.046	42.046	15.3%
300	125	2.40	11.1%	17	40.231	57.231	19.1%
300	150	2.00	9.2%	17	26.427	43.427	14.5%
300	175	1.71	9%	18	26.087	44.087	14.7%
300	200	1.50	15.1%	18	42.499	60.499	20.2%
350	125	2.80	16.3%	20	61.221	81.221	23.2%
350	150	2.33	8.9%	20	33.878	53.878	15.4%
350	175	2.00	6.5%	20	24.699	44.699	12.8%
350	200	1.75	6.3%	21	23.655	44.655	12.8%
350	225	1.56	8.1%	19	90.175	109.175	31.2%
continued on next page							

			Without electric field	With electric field			
L	W	L/W	$\varepsilon_{\text{crit}}$	P_0	λ	P_{crit}	$\varepsilon_{\text{crit}}$
(inch)	(inch)			(inch)		(inch)	
400	125	3.20	18%	22	84.442	106.442	26.6%
400	150	2.67	11.9%	23	47.534	70.534	17.6%
400	200	2.00	5.8%	23	23.475	46.475	11.6%
400	250	1.60	6.6%	24	26.556	50.556	12.6%
400	275	1.45	11.2%	24	45.64	69.64	17.4%
450	150	3.00	13%	26	65.227	91.227	20.3%
450	200	2.25	5.6%	28	27.352	55.352	12.3%
450	250	1.80	4.5%	27	21.081	48.081	10.7%
450	300	1.50	8%	27	33.995	60.995	13.6%
450	325	1.38	16.1%	28	80.396	108.396	24.1%
500	150	3.33	16.2%	28	82.296	110.296	22.1%
500	175	2.86	10%	29	52.468	81.468	16.3%
500	200	2.50	6.7%	29	34.84	63.84	12.8%
500	225	2.22	5.1%	29	25.941	54.941	11%
500	250	2.00	4.4%	31	20.979	51.979	10.4%
500	275	1.82	4.2%	30	20.343	50.343	10.1%
500	300	1.67	4.5%	30	22.055	52.055	10.4%
500	325	1.54	5.5%	30	28.326	58.326	11.7%
500	350	1.43	9.1%	30	48.213	78.213	15.6%
550	150	3.67	16.3%	31	99.808	130.808	23.8%
550	175	3.14	10.7%	32	66.677	98.677	17.9%
550	200	2.75	7.2%	32	44.381	76.381	13.9%
550	225	2.44	5.2%	32	31.538	63.538	11.6%
550	250	2.20	4.7%	33	24.25	57.25	10.4%
550	275	2.00	4.1%	33	20.829	53.829	9.8%
550	300	1.83	3.3%	32	16.041	48.041	8.7%
550	325	1.69	4.1%	33	20.909	53.909	9.8%
550	350	1.57	4.8%	33	25.083	58.083	10.6%
550	375	1.47	6.7%	33	36.388	69.388	12.6%
550	400	1.38	14.2%	35	81.229	116.229	21.1%
600	150	4.00	17.5%	34	115.94	149.94	25%
600	175	3.43	12.6%	35	80.871	115.871	19.3%

continued from previous page

			Without electric field	With electric field			
L	W	L/W	$\varepsilon_{\text{crit}}$	P_0	λ	P_{crit}	$\varepsilon_{\text{crit}}$
(inch)	(inch)			(inch)		(inch)	
600	200	3.00	8.6%	35	55.392	90.392	15.1%
600	225	2.67	6.2%	35	38.965	73.965	12.3%
600	250	2.40	4.8%	35	29.189	64.189	10.7%
600	275	2.18	4%	36	23.221	59.221	9.9%
600	300	2.00	3.6%	36	20.353	56.353	9.4%
600	325	1.85	3.5%	36	19.381	55.381	9.2%
600	350	1.71	3.6%	36	20.104	56.104	9.4%
600	400	1.50	4.9%	36	30.292	66.292	11%
600	425	1.41	9%	37	50.901	87.901	14.7%
650	150	4.33	17.8%	37	130.75	167.75	25.8%
650	175	3.71	12.6%	37	93.012	130.012	20%
650	200	3.25	9%	38	66.843	104.843	16.1%
650	250	2.60	5.4%	38	35.147	73.147	11.3%
650	300	2.17	3.8%	39	22.425	61.425	9.5%
650	325	2.00	3.5%	39	19.972	58.972	9.1%
650	350	1.86	3.4%	39	19.057	58.057	8.9%
650	375	1.73	3.4%	39	19.523	58.523	9%
650	400	1.63	3.7%	39	21.671	60.671	9.3%
650	425	1.53	4.3%	39	26.688	65.688	10.1%
650	450	1.44	5.9%	39	38.531	77.531	11.9%
650	475	1.37	11.2%	41	78.723	119.723	18.4%
700	150	4.67	17.5%	40	144.48	184.48	24.6%
700	200	3.50	10.9%	41	78.012	119.012	15.9%
700	250	2.80	6.7%	41	42.216	83.216	11.1%
700	300	2.33	4.5%	42	25.634	67.634	9%
700	350	2.00	3.5%	42	19.662	61.662	8.2%
700	400	1.75	3.2%	42	19.091	61.091	8.1%
700	450	1.56	3.3%	42	24.36	66.36	9.5%
700	500	1.40	4.3%	43	52.227	95.227	13.6%
750	150	5.00	17.6%	42	155.07	197.07	26.3%
750	200	3.75	10.2%	44	88.561	132.561	17.7%
750	250	3.00	6.3%	44	49.957	93.957	12.5%

			Without electric field	With electric field			
L	W	L/W	$\varepsilon_{\text{crit}}$	P_0	λ	P_{crit}	$\varepsilon_{\text{crit}}$
(inch)	(inch)			(inch)		(inch)	
750	300	2.50	4.2%	45	29.81	74.81	10%
750	350	2.14	3.3%	45	21.288	66.288	8.8%
750	375	2.00	3.1%	45	19.413	64.413	8.6%
750	400	1.88	3%	45	18.608	63.608	8.5%
750	450	1.67	3.1%	45	19.995	64.995	8.7%
750	500	1.50	4%	46	27.88	73.88	9.9%
750	550	1.36	9.2%	47	76.496	123.496	16.5%
800	150	5.33	17.9%	47	172.29	219.29	27.4%
800	200	4.00	11%	46	97.561	143.561	17.9%
800	250	3.20	6.6%	47	57.928	104.928	13.1%
800	275	2.91	5.3%	47	44.719	91.719	11.5%
800	300	2.67	4.3%	48	34.792	82.792	10.3%
800	325	2.46	3.9%	49	27.569	76.569	9.6%
800	350	2.29	3.4%	48	23.706	71.706	9%
800	400	2.00	3.1%	46	46.52	92.52	11.6%
800	450	1.78	3%	48	18.513	66.513	8.3%
800	500	1.60	3.2%	49	20.964	69.964	8.7%
800	550	1.45	4.5%	49	33.65	82.65	10.3%
800	600	1.33	13.6%	52	121.58	173.58	21.7%
850	150	5.67	17.8%	48	179.46	227.46	26.8%
850	200	4.25	11.8%	49	106.71	155.71	18.3%
850	250	3.40	7.3%	50	65.797	115.797	13.6%
850	300	2.83	4.7%	51	40.371	91.371	10.7%
850	350	2.43	3.5%	51	26.805	77.805	9.2%
850	400	2.13	2.9%	51	20.544	71.544	8.4%
850	425	2.00	2.8%	51	19.044	70.044	8.2%
850	450	1.89	2.7%	51	18.327	69.327	8.2%
850	500	1.70	2.8%	52	18.328	70.328	8.3%
850	550	1.55	3.2%	52	23.352	75.352	8.9%
850	600	1.42	5.3%	52	41.916	93.916	11%
900	150	6.00	15.6%	49	152.84	201.84	22.4%
900	200	4.50	12.7%	52	115.32	167.32	18.6%

			Without electric field	With electric field			
L	W	L/W	$\varepsilon_{\text{crit}}$	P_0	λ	P_{crit}	$\varepsilon_{\text{crit}}$
(inch)	(inch)			(inch)		(inch)	
900	250	3.60	8.3%	53	73.379	126.379	14%
900	300	3.00	5.6%	54	46.308	100.308	11.1%
900	350	2.57	3.7%	54	30.494	84.494	9.4%
900	400	2.25	3%	54	22.46	76.46	8.5%
900	450	2.00	2.7%	54	18.907	72.907	8.1%
900	500	1.80	2.7%	55	17.397	72.397	8%
900	550	1.64	2.8%	55	19.411	74.411	8.3%
900	600	1.50	3.4%	55	26.595	81.595	9.1%
900	650	1.38	6.6%	56	54.284	110.284	12.3%
950	200	4.75	12%	55	123.5	178.5	18.8%
950	250	3.80	7.8%	56	80.593	136.593	14.4%
950	300	3.17	5.3%	56	52.631	108.631	11.4%
950	350	2.71	3.8%	57	34.665	91.665	9.6%
950	400	2.38	3.1%	57	24.882	81.882	8.6%
950	450	2.11	3.1%	57	20.036	77.036	8.1%
950	475	2.00	3%	58	18.014	76.014	8%
950	500	1.90	2.9%	58	17.364	75.364	7.9%
950	550	1.73	2.9%	58	17.741	75.741	8%
950	600	1.58	3.3%	58	20.993	78.993	8.3%
950	650	1.46	4.7%	58	30.91	88.91	9.4%
950	700	1.36	13.4%	60	73.777	133.777	14.1%
1000	200	5.00	12.5%	58	131.34	189.34	18.9%
1000	250	4.00	8.3%	59	87.426	146.426	14.6%
1000	275	3.64	6.9%	59	71.582	130.582	13.1%
1000	300	3.33	5.7%	59	58.607	117.607	11.8%
1000	325	3.08	4.8%	60	47.693	107.693	10.8%
1000	400	2.50	3.2%	60	27.75	87.75	8.8%
1000	450	2.22	2.8%	60	21.612	81.612	8.2%
1000	500	2.00	2.6%	61	17.911	78.911	7.9%
1000	550	1.82	2.5%	61	17.166	78.166	7.8%
1000	600	1.67	2.6%	61	18.496	79.496	7.9%
1000	650	1.54	2.9%	61	23.096	84.096	8.4%

continued from previous page

			Without electric field	With electric field			
L	W	L/W	$\varepsilon_{\mathrm{crit}}$	P_0	λ	P_{crit}	$\varepsilon_{\mathrm{crit}}$
(inch)	(inch)			(inch)		(inch)	
1000	700	1.43	4.2%	61	36.665	97.665	9.8%
1000	750	1.33	10.3%	65	104.61	169.61	17%

continued from previous page

Bibliography

Alder, A. L., Mikulas, M. M., and Hedgepeth, J. M. (2000). Static and dynamic analysis of partially wrinkled membrane structures. In *Proc. 41st AIAA/ASME/ASCE/AHS/ASC Structures, Structures Dynamics, and Material Conference and Exhibit.* Atlanta, GA. 3-6 April 2000, AIAA-2000-1810.

Barsotti, R. and Ligaro, S. S. (2000). An accurate wrinkled membrane model for analysing the post-critical behavior of stiffened plate-girders. In *Proc. IASS-IACM 2000 Computational Methods for Shell and Spatial Structures*, edited by M. Papadrakakis, A. Samartin and E. Onate.

Blandino, J. R., Johnston, J. D., Miles, J. J., and Soplop, J. S. (2001). Thin film membrane wrinkling due to mechanical and thermal loads. In *Proc. 42nd AIAA/ASME/ASCE/AHS/ASC Structures, Structured Dynamics, and Materials Conference and Exhibit.* Seattle, WA, USA. 16-19 April 2001, AIAA-2001-1345.

Blandino, J. R., Johnston, J. D. and Dharamsi, U. K. (2002). Corner wrinkling of a square membrane due to symmetric mechanical loads. *J. Spacecraft Rockets*, 39:717-724.

Blandino, J. R., Pappa, R. and Black, J. (2003). Model identification of membrane structures with videogrammetry and laser vibrometry. In *Proc. 44th AIAA/ASME/ASCE/AHS/ASC Structures, Structural Dynamics, and Material Conference and Exhibit*, AIAA-2003-1745.

Borges, A. F. (1989). Relaxed Skin Tension Lines. *Dermatol. Clin.*, 7(1):169-177.

Cerda, E., Ravi-chandar, K. and Mhadevan, L. (2003). Wrinkle of an elastic sheet under tension. *Nature*,419:579-580.

Cerda, E. and Mahadevan, L. (2003). Geometry and physics of wrinkling. *Physical Review Letters*, 90, 074302.

Cerda, E. (2005). Mechanics of Scars. *J. Biomech.*, 38: 159-1603.

Chen, L. and Tay, C. J. (2006). Carrier phase component removal: a generalized least-squares approach. *J. Opt. Soc. Am. A*, 23:435-443.

Coggrave, C. R. and Huntley, J. M. (2000). Optimisation of a shape-measurement system based on spatial light modulators. *Opt. Eng.*, 39:91-98.

Contri, P. and Schrefler, B. A. (1988). A geometrically nonlinear finite element anlaysis of wrinkled membrane surfaces by a no-compression material model. *Communications in Applied Numerical Methods*, 4:5-15.

Creath, K. (1988). Phase-measurement interferometry techniques. In *Progress in Optics XXVI*, edited by E. Wolf, North-Holland, Amsterdam, pp. 349-393.

Epstein, M. and Forcinito, M. A. (2001). Anisotropic membrane wrinkling: theory and analysis. *International Journal of Solids and Structures*, 38:5253-7272.

Epstein, M. (2003). Differential equation for the amplitude of wrinkles. *AIAA Journal*, 41:327-329.

Flynn, T. J. (1997). Two-dimensional phase unwrapping with minimum weighted discontinuity. *J. Opt. Soc. Am. A* 14:2692-2701.

Friedl, N., Rammerstorfer, F. G. and Fischer, F. D. (2000). Buckling of stretched strips. *Computers and Structures*, 78:185-190.

Ghiglia, D. C. and Romero, L. A. (1994). Robust two-dimensional weighted and unweighted phase unwrapping that uses fast transforms and iterative methods. *J. Opt. Soc. Am. A*, 11:107-117.

Hibbitt, Karlsson and Sorensen. Inc (2001). *ABAQUS Theory and User's Manual*, Version 6.5, Pawtucket, RI, USA.

Jenkins, C. H., Haugen, F., and Spicher, W. H. (1998). Experimental measurement of wrinkling in membranes undergoing planar deformation. *Experimental Mechanics*, 38:147-152.

Kornbluh, R., Pelrine, R., Pei, Q., Oh, S. and Joseph, J. (2000). In *Proc. SPIE-Int. Soc. Opt. Eng.*, 3987:51-64.

Leifer, J. and Belvin, W. K. (2003). Prediction of wrinkle amplitudes in thin fil membranes using finite element modeling. In *Proc. 44th AIAA/ASME/ASCE/AHS/ASC Structures*, Structural Dynamics and Materials Conference and Exhibit, 7-10 April 2003, Norfolk, VA. AIAA-2003-1983.

Liu, X., Jenkins, C. H., and Schur, W. W. (1998). Computational issues in the modeling of wrinkling during parachute deployment. In *IUTAM-IASS Symposium on Deployable Structures: Theory and Application*, edited by S. Pellegrino and S. D. Guest, Kluwer Academic Publishers, pp. 239-250.

Liu, X., Jenkins, C. H. and Schur, W. W. (2001). Large deflection analysis of pneumatic envelopes using a penalty paramter modified material model. *Finite Elements in Analysis and Design*, 37: 233-251.

Lochmatter, P., Kovacs, G. and Ermanni, P. (2007) Design and characterization of shell-like actuators based on soft dielectric electroactive polymers. *Smart Mater. Struct*, 16:1415-1422.

Mansfield, E. H. (1968). Tension field thoery, a new approach which shows its duality with inextensional theory. In *Proc. XII Int. Cong. Appl. Mech.*, pp. 305-320.

Mansfield, E. H. (1970). Load transfer via a wrinkled membrane. In *Proc. Roy. Soc. Lond. A.*, 316:269-289.

Mansfield, E. H. (1981). Gravity-induced wrinkle lines in vertical membrane. In *Proc. Roy. Soc. Lond. A.*, 375:307-325.

Mansfield, E. H. (1989). *The bending and stretching of plates.* Cambridge University Press. Cambridge, England. Second edition.

Behavior of a flat stretched membrane wrinkled by the rotation of an attached hub. *NASA TN D-2456.*

Miller, R. K. and Hedgepeth, J. M. (1982). An algorithm for finite element analysis of partly wrinkled membranes. *AIAA Journal*, 20:1761-1763.

Papa, A. and Pellegrino, S. (2005). Mechanics of systematically creased thin-film membrane structures. In *Proc. 46th AIAA/ASME/ASCE/AHS/ASC Structures*, Structural Dynamics and Materials Conference, 18-21 April 2005, Austin, TX. AIAA-2005-1975.

Pelrine, R., Kornbluh, R., Pei, Q. and Joseph, J. (2000). High-speed electrically actuated elastomers with strain greater than 100%. *Science*, 287:836-839.

Pelrine, R., Kornbluh, R., Joseph, J., Heydt, R., Pei Q. and Chiba, S. (2000). High-field deformation of elastomeric dielectrics for actuators. *Mater. Sci. Eng., C*, 11:89-100.

Pipkin, A. C. (1986). The relaxed energy density for isotropic elastic membrane. *IMA Journal of Applied Mathematics*, 36:85-99.

Quan, C., He, X. Y., Wang, C. F., Tay, C. J. and Shang, H. M. (2001). Shape measurement of small objects using LCD fringe projection with phase shifting. *Optics Communications*, 189:21-29.

Quan, C., Tay, C. J. and Chen, L. J. (2006). A study on carrier-removal techniques in fringe projection profilometry. *Optics & Laser Technology*, 39:1155-1161.

Reissner, E. (1938). On tension field theory. In *Proc. V Int. Cong. Appl. Mech.*, pp. 88-92.

Rimrott, F. P. J. and Cvercko, M. (1985). Wrinkling in thin plates due to in-plane body forces. In *Inelastic Behaviour of Plates and Shells*, edited by L. Bevilacqua, R. Feijoo and R. Valid. Springer-Verlag, pp. 19-48.

Roddeman, D. G., Drukker, J., Oomens, C. W. J., and Janssen, J. D. (1987). The wrinkling of thin membranes: Part I-Theory. *Journal of Applied Mechanical*, 54:884-887.

Sansoni, G., Corini, S. Lazzari, Rodella, R. and Docchio, F. (1997). Three-dimensional imaging based on Gray-code light projection: characterization of the measuring algorithm and development of a measuring system for industrial applications. *Appl. Opt*, 36:4463-4472.

Shankar, R., Ghosh, T. K. and Spontak, R. J. (2007). Dielectric elastomers as next-generation polymeric actuators. *Soft Matter*, 3:1116-1129.

Srinivasan, V., Liu, H. C. and Halious, M. (1984). Automated phase-measureing profilometry of 3-D diffuse objects. *Applied Optics*, 23:3105-3108.

Stamper, B., Angel, R., Burge, J. and Woolf, N. (2000). Flat membrane mirrors for space telescopes. *Imaging Technology and Telescopes*, edited by Breckinridge, *J., Proc. SPIE* 4091:126-136.

Steigmann, D. J. and Pipkin, A. C. (1989). Finite deformations of wrinkled membranes. *Quar. Jour. Mech. Appl. Math.*, 42:427-440.

Steigmann, D. J. and Pipkin, A. C. (1989). Wrinkling of pressurized membrnaes. *ASME J. Appl. Mech.*, 56:624-628.

Stein, M. and Hedgepeth, J. M. (1961). Analysis of partly wrinkled membranes. *NASA TN*, D-813.

Sun, Y., Choi, W. M. Jiang, H, Huang, Y. and Rogers, J. A. (2006) *Nature Nanotechnology*, 1:201-207.

Takeda, M. and Mutoh, K. (1883). Fourier transform profilometry for the automatic measurement of 3-D object shapes. *Applied Optics*, 22:3977-3982.

Tessler, A., Sleight, D. W. and Wang, J. T. (2003). Nonlinear shell modeling of thin membranes with emphasis on structural wrinling. In *Proc. 44th AIAA/ASME/ASCE/AHS/ASC Structures*, Structural Dynamics and Materials Conference and Exhibit, 7-10 April 2003, Norfolk, VA. AIAA-2003-1931.

Tessler, A., Sleight, D. W. (2004). Toward effective shell modeling of wrinkled thin-film membranes exhibiting stress concentrations. In *Proc. 45th AIAA/ASME/ASCE/AHS/ASC Structures*, Structural Dynamics and Materials Conference and Exhibit, 19-22 April 2004, Palm Springs, CA. AIAA-2004-1739.

TNO (1998). *DIANA-Finite Element Analysis User's Manual*. Release 7, Delft, The Netherlands.

Tomita, Y. and Shindo, A. (1988). Onset and growth of wrinkling in thin square plate subjected to diagonal tension. *Int. J. Mech. Sci.*, 30:921-931

UNIQ (2004). *UP-2000/UP-2000CL Progressive Scan CCD Camera User's Manual*, Version 1.3, Uniq Vision Inc.

Wagner, H. (1929). Flat sheet metal girder with very thin metal web, *Zeitschrift für Flugtechnik und Motorluftschiffahrt*, 20.

Wang, Z. (2003). Development and application of computer-aided fringe anlaysis. PhD Dessertation, University of Maryland at College Park.

Wong, Y. W. and Pellegrino, S. (2002). Comoputation of wrinkle amplitudes in thin membranes. In *Proc. 43rd AIAA/ASME/ASCE/AHS/ASC Structures*, Structures Dynamics and Material Conference and Exhibit, 22-25 April 2002, Denver, CO. AIAA-2002-1369.

Wong, Y. W., Pellegrino, S. and Park, K. C. (2003). Prediction of wrinkle amplitudes in square solar sails. In *Proc. 44th AIAA/ASME/ASCE/AHS/ASC Structures*, Structural Dynamics and Materials Conference and Exhibit, 7-10 April 2003, Norfolk, VA. AIAA-2003-1980.

Wong, Y. W. and Pellegrino, S. (2006). Wrinkled membranes I: experiments. *J. of Mechanics of Materials and Structures*, 1:2-23.

Wong, Y. W. and Pellegrino, S. (2006). Wrinkled membranes II: analytical models. *J. of Mechanics of Materials and Structures*, 1:25-59.

Wong, Y. W. and Pellegrino, S. (2006). Wrinkled membranes III: numerical simulations. *J. of Mechanics of Materials and Structures*, 1:61-93.

Wu, C. H. and Canfield, T. R. (1981). Wrinkling in finite plan-stress theory. *Q. Appl. Math.*, 39, 2, 179-199.

Xu, W. and Cumming, I. (1996). A region growing algorithm for InSAR phase unwrapping. In *Proc. IGARSS*, Lincoln, Nebraska, pp. 2044-2046.